

Studies on Bismuth Sodium Titanate-based Lead-Free Piezoelectric Bulk Ceramics and Thin Films

*A Thesis Submitted to
Indian Institute of Technology Guwahati
for the Degree of*

Doctor of Philosophy

By

Srinivas Pattipaka



**Department of Physics
Indian Institute of Technology Guwahati
Assam, India
January 2020**



INDIAN INSTITUTE OF TECHNOLOGY GUWAHATI
Department of Physics
Guwahati – 781039

STATEMENT

The present thesis entitled, “**Studies on Bismuth Sodium Titanate-based Lead-Free Piezoelectric Bulk Ceramics and Thin Films**” has been carried out by me under the supervision of Dr. D. Pamu, Department of Physics, Indian Institute of Technology Guwahati. This work has not been submitted elsewhere for the award of any degree.

January, 2020

Srinivas Pattipaka

Department of Physics,

Indian Institute of Technology Guwahati,

Guwahati – 781 039



INDIAN INSTITUTE OF TECHNOLOGY GUWAHATI
Department of Physics
Guwahati – 781039

CERTIFICATE

It is certified that the work described in this thesis, entitled “**Studies on Bismuth Sodium Titanate-based Lead-Free Piezoelectric Bulk Ceramics and Thin Films**”, done by Mr. Srinivas Pattipaka, a Ph.D. student of Department of Physics, Indian Institute of Technology Guwahati, for the award of degree of *Doctor of Philosophy* has been carried out under my supervision. This work has not been submitted elsewhere for the award of any degree.

January, 2020.

Dr. D. Pamu

Associate Professor,
Department of Physics,
Indian Institute of Technology Guwahati,
Guwahati – 781 039.



Dedicated to my family

ACKNOWLEDGEMENTS

Almost five and half years of hard work and the innumerable help and support from the people around me made it possible in completion the thesis work.

First, I express my sincere gratitude to my research supervisor Dr. D. Pamu for his constant support, guidance, encouragement, advice, and valuable discussions, which helped me to improve an understanding of the subject along with skills and the successful culmination of my thesis work. I must acknowledge him for providing the unconditional freedom to work, think and express on whatever I have done in my research work by keeping the faith on my capabilities.

I am highly thankful to my doctoral committee members, Prof. Dilip Pal (Chairman), Prof. S. Ravi and Prof. Roy Paily Palathinkal for their continuous academic guidance and checking my work progress and seminars during my Ph.D. Their valuable discussions and suggestions helped me to understand the basics of the subject and along with skills and also improve the quality of my research work.

I would like to express my sincere gratitude to Prof. Subhradip Ghosh, head of the Department of the Physics, and former head of the departments, Prof. Saurabh Basu, and Prof. Poulouse Poulouse, for giving me the opportunity to work in the department and to use departmental facilities. I am also grateful to all the faculty members of the Physics department. I would also like to thank Dr. Sidananda Sarma for his technical assistance and friendly discussions. My special thanks to all scientific officers and staff members in our department, central instruments facility and centre for nanotechnology.

My sincere thanks to collaborators Prof. K. C. James Raju (University of Hyderabad) for providing pulsed laser deposition facility, Dr. A. R. James (DMRL, Hyderabad) for providing dielectric measurements and Prof. Alikea Khare for providing nonlinear optical measurements facility. I acknowledge Prof. Roy Paily Palathinkal and Mrs. S. Josephine for providing the microwave dielectric measurement facility, without their help I would not be able to complete my thesis work.

The financial support for this thesis is provided by the Indian Institute of Technology Guwahati and Ministry of Human Resource and Development. Also, I would like to express my heartfelt thanks to Science and Engineering Research Board (SERB)/Department of Science and Technology (DST), New Delhi; Board of Research in Nuclear Sciences (BRNS), Mumbai; Defense Research and Development Organization

(DRDO), New Delhi; and Board of Research in Fusion Science & Technology (BRFST), Gandhinagar, Gujarat through research projects for various experimental facilities. The XRD facility provided by DST, New Delhi, through the FIST program [SR/FST/PSII-020/2009] is also acknowledged.

I am also grateful to my seniors Dr. T. Santhosh Kumar, Dr. Mahesh Peddigari, Dr. Anil Kumar C, Dr. Pallabi Gogoi, and Dr. Ranjan Kumar Bhuyan for sharing their knowledge and useful discussions. I would like to thank my research team members and colleagues Susmita, Apurba, Prajna, Radhika, Shashi Priya, Sunil, Anil, Sweety, S. S. Budha, Gobinda, Sasmita, Indu, Ranjan, Aakansha, Pratap, Dr. Bibhuti, Dr. Deep and Dr. Vishwajit Gaikwad for their help, suggestions and enjoyable company.

I would like to thank my best friends at IIT Guwahati, especially, Jagan Mohan, Dr. Venkatanna, Dr. Sanjib Nayak, Dr. Ranganatha, Dr. Rajender, Dr. Patta Ravi, Dr. Ramakrishna, Dr. Vikky bio, and Dr. Gyan Prakash, Dr. Harikrishna, Lathakka, Dr. Ramesh bhukya and Sahithi Bhukya for creating a friendly and homely atmosphere. I would also like to thank my village and other best friends Sathih Vodnala, Rajesh Suddala, Santhosh kadakuntla, Praveen Nayak, Madhav Kumar, Sathish T, Saru, Sumalatha, Bheem Raj and Pundareekam Goud for their support in every step of my life.

Finally, I would like to express my deepest gratitude to my family, especially, my better half (Hari Priya), My Son (Vihaan), parents (Padma and Rajanna), brother, sister-in-law and daughter (Mahesh, Rajitha & Shainisri), sister, brother-in-law and nephews (Shireesha and Vekatesh, Cherry (Krishna), Sahashra and Nanditha), uncle and aunty (Venkata Ramaiah and Baghya laxmi), Anil annaiah, Anjali vadhina, Adwaith and Nihanth and all other family members, who gave blessings, moral support and continuous encouragement.

Srinivas Pattipaka

Abstract

Ferroelectric materials play a significant role in modern science and technology for various electronic device applications such as capacitors for tunable capacitance due to their nonlinear response, ferroelectric non-volatile dynamic random-access memory (DRAM) for computers, radio-frequency identification (RFID) cards due to memory function, etc. These ferroelectric materials possess spontaneous polarization in the absence of an electric field, and they have the ability to switch the direction of polarization. Besides, ferroelectric materials can display simultaneously piezoelectric and pyroelectric properties. Piezoelectric materials tend to produce electrical polarization when mechanical stress is applied i.e., direct piezoelectric effect. Conversely, a mechanical strain is created when an electric field is applied, i.e., converse piezoelectric effect. These materials are widely used in sensors, actuators, accelerators, ultrasonic motors, transducers, filters, buzzers, and resonators and micro-electromechanical systems (MEMS) device applications.

In addition, the demand for ferroelectric thin films is also increasing day by day due to their superior properties suitable for integrated electronic applications. Thin films play a key role in miniaturizing electrical components and devices. These are widely used in the capacitor, non-volatile memory, energy storage, micro-sensors, micro-actuator, pulsed power systems, microwave tunable, nonlinear photonic devices and MEMS applications, etc. Thin film properties are important for the applications: ferroelectric and piezoelectric nonlinearity of thin films are also relevant in microsystems; nonlinear optical properties are promising for photonic device applications and high permittivity and low dielectric loss in films important for the all applications and essential for high-frequency devices.

The ferroelectric materials are classified into four categories based on the structure of the unit cell: (i) Perovskite, (ii) bismuth layered, (iii) tungsten bronze and (iv) pyrochlore Non-perovskite. The perovskite structured (ABO_3) materials have received giant significance in materials science due to their fascinating dielectric, ferroelectric, piezoelectric, pyroelectric, and optical properties for technological applications. The lead-based perovskite structured piezoelectric materials such as $Pb(ZrTi)O_3$ (PZT), $Pb(ZnNb)O_3$ (PZN), $Pb(MgNb)O_3$ (PMN), $Pb(NiNb)$ (PNN) and etc. are extensively investigated and have been attracted much attention due to their promising properties for the above application. However, the toxicity of the lead causes a serious problem for human health and the environment. Environmental legislation in the European Union, US, and few countries of Asia demands the elimination of toxic lead, which encouraged a great effort in the research community for the development of lead-free piezoelectric materials. In the last decade, three main lead-free piezoelectric materials have drawn the most attention, such as $BaTiO_3$ (BT), $(K_{0.5}Na_{0.5})NbO_3$ (KNN) and $(Bi_{0.5}Na_{0.5})TiO_3$ (BNT) due to their superior ferroelectric, piezoelectric properties and are comparable to the PZT.

Among these lead-free piezoelectric ceramics, BNT is a promising candidate for such applications and is discovered by Smolenski et al. The crystal structure of the BNT system is a rhombohedral with $R3c$ space group at room temperature (RT), which exhibits two structural phase transitions: (i) ferroelectric rhombohedral to anti-ferroelectric tetragonal phase at 200 °C (i.e. depolarization temperature, T_d) and (ii) anti-ferroelectric tetragonal to paraelectric cubic phase at 320 °C (Curie transition temperature, T_C). It also exhibits a maximum relative permittivity (~ 3000) at T_C , larger remnant polarization ($P_r = 38 \mu C/cm^2$ @ $E_c=73$ kV/cm), and best dielectric properties ($\epsilon_r = 692$ and $\tan\delta = 0.045$ at 1 kHz) at RT and interesting piezoelectric properties ($d_{33}=79$ pC/N, $k_p \sim 48\%$). The scientific community has explored BNT due to its strong ferroelectric response and higher

T_C . However, BNT ceramics possess few drawbacks like (i) inferior piezoelectric properties (ii) difficult to pole electrically due to its high coercive field ($E_c = 73$ kV/cm) and (iii) high electrical conductivity, which makes the BNT ceramics less applicable for the above/practical applications. Also, it is challenging to densify BNT ceramics due to the volatile nature of Na and Bi during the sintering process, which causes the increment of the leakage current and degradation in the dielectric, ferroelectric, and piezoelectric properties.

Successful efforts have made to overcome such drawbacks and improve the dielectric, ferroelectric and piezoelectric properties of BNT ceramics with the various synthesis methods, suitable dopants and compositions. The BT, KNN, NaNbO₃ (NN) and SrTiO₃ (ST) compositions and etc. were added to BNT, which have displayed improved dielectric, ferroelectric and piezoelectric properties and also eased the polling process at morphotropic phase boundary (MPB). Further, considerable efforts have also been made with the substitution of dopants (isovalent, donor and/or acceptor) either in A or B-site of BNT ceramics to enhance the ferroelectric and piezoelectric properties due to difference between the ionic radius of doping elements and lattice ions. The donor substitution of more positive ions (Li³⁺, La³⁺ and Nd³⁺) at A-site (Na⁺ and Bi³⁺) or Ta⁵⁺, Nb⁵⁺ and Sb⁵⁺ at B-site (Ti⁴⁺), which could improve the dielectric, ferroelectric and piezoelectric properties due to the formation of A-site vacancies facilitating the motion of domain and domain walls. The isovalent dopants normally reduce the T_C and increase the electrical properties. On the other hand, the acceptor substitution of the lower valence ions could create the oxygen vacancies, which lead to a decrease in the dielectric constant, loss, and enhance the mechanical quality factor and coercive field. Most of the properties are enhanced in BNT systems with donor or isovalent dopants and other perovskite composites at MPB. To date, there are few reports available on donor/rare-earth oxide doped Gd₂O₃ and CeO₂

onto BNT ceramics. In present thesis work, we aim to study the Ce^{+3} , Gd^{+3} , K^+ and KNN based compositions on the structural, morphological, dielectric, and piezoelectric properties of BNT ceramics and to address the issues related to densification, leakage current, and difficulties in the polling process.

So far, BNT based ceramics have been explored more in the bulk form due to its excellent ferroelectric and piezoelectric properties, which leads to fabricate thin-film devices for the sensors, actuators, energy harvesters, and MEMS applications, etc. BNT thin films have been deposited using various deposition techniques, such as RF magnetron sputtering, sol-gel process and pulsed laser deposition (PLD). Among these, the PLD technique is a highly versatile tool and widely used for fabricating thin films and multilayer structures. It offers film growth of oxides, good stoichiometry control of the film composition and chemical homogeneity, porosity control, better crystallinity, excellent adhesion, low cost, and etc. Therefore, the underlying benefits of PLD motivated us to deposit BNT thin films to study the structural, morphological, optical, dielectric and ferroelectric properties systematically. Moreover, microwave dielectric and nonlinear optical properties of films have been widely investigated for microwave communication, radiofrequency, and photonic devices due to their fast response, lower operation voltage, better compatibility, and larger nonlinearity. Nevertheless, there are limited studies available involving with microwave dielectric and nonlinear optical properties of BNT films, which suggested to study the microwave dielectric and nonlinear optical properties of BNT thin films systematically.

The background and objective of the present study are motivated us to prepare lead-free ceramics, to understand the fundamental issues, to study and improve the structural and dielectric, ferroelectric and piezoelectric properties of the pure, doped (Ce, Gd and K) BNT and its compositions. The pure BNT and best-doped composition chosen

to deposit thin films by the PLD technique to study their optical, dielectric, and ferroelectric properties. Further, the nonlinear optical and microwave dielectric properties of the thin films investigated for nonlinear photonic and microwave tunable device applications. The present thesis has been divided into six chapters as follows.

Chapter 1 describes the introduction of dielectric, ferroelectric and piezoelectric phenomena. The origin of the perovskites and lead-free piezoelectric materials are discussed. This chapter also discusses some of the technologically important piezoelectric systems with their applications. The motivation behind choosing the lead-free BNT, brief outline, and literature survey are presented. Further, the outstanding performance of the BNT ceramics and thin films for the in piezoelectric applications and their drawbacks are also discussed. The emphasis is given to bismuth sodium titanate system based compositionally modified through KNN, alkaline, and rare-earth-doped K^+ and Ce^{+3} , Gd^{+3} at the A-site of the BNT system.

Chapter 2 presents a detailed overview of various experimental techniques for the synthesis and characterization of bulk BNT ceramics and thin films. The pure and modified BNT ceramics were synthesized by using a conventional solid-state reaction method. High energy ball milling parameters, calcination, and sintering temperatures are optimized to achieve the desired phase and maximum relative density. Archimedes's principle is used to measure the density of prepared samples. Pulsed laser deposition technique is used for the deposition of thin films. The structural characterization of all the bulk ceramics and thin films is performed by X-ray diffraction (XRD). The phase purity and crystal structure of prepared samples are confirmed by employing the Rietveld refinement method using Fullprof software. Surface morphology and elemental analysis are characterized using field emission scanning electron microscopy (FESEM), field emission transmission electron microscopy (FETEM), atomic force microscope (AFM),

and energy dispersive analysis of X-ray (EDAX). The Raman spectra are recorded by using a Raman spectrometer. The UV-Vis-NIR spectrometer was used for optical characterization. Spectroscopic ellipsometry (SE) measurements were performed by variable angle spectroscopic ellipsometer, followed by spectroscopy ellipsometry analyzer (SEA) software was used to extract the optical parameters. The modified z-scan technique is used to study the nonlinear optical properties of the films. Frequency and temperature-dependent dielectric properties are measured by using an LCR meter and impedance analyzer. Microwave dielectric properties of the thin films estimated using a split post dielectric resonator (SPDR) technique. The ferroelectric properties are obtained by using the ferroelectric tester. A Keithley parameter analyzer was used to measure the leakage current with an applied voltage.

Chapter 3 deals with the synthesis of pure BNT, Ce^{+3} , and Gd^{+3} doped ceramics with various concentrations, and its structural, microstructural, dielectric, and AC-conductivity studies are presented systematically. The processing parameters such as milling time, milling speed, the ball to powder ratio, calcination, sintering temperatures, and sintering duration were optimized. The effect of sintering temperature on structural, microstructural, dielectric and AC-conductivity behavior of BNT ceramics studied. These properties are significantly enhanced with the sintering temperature, the samples sintered at 1100 °C showed a high dielectric constant ($\epsilon_r = 692$ @ 1 kHz), and low dielectric loss ($\tan\delta = 0.045$) due to the maximum relative density (~94%), dense microstructure (grain size of 1.40 μm) with larger crystallite size (52 nm). The high-frequency dielectric analysis revealed that weak relaxor behavior is observed in the system.

Further, the structural, microstructural, and dielectric properties of the $\text{Bi}_{0.5}\text{Na}_{1-x}\text{Ce}_{x0.5}\text{TiO}_3$ ($x = 0 - 0.035$) and $\text{Bi}_{1-x}\text{Gd}_{x0.5}\text{Na}_{0.5}\text{TiO}_3$ ($x = 0.02 - 0.06$) lead-free ceramics

have been investigated. Rietveld refinement of both Ce and Gd doped BNT ceramics revealed the rhombohedral crystal with improved dielectric properties of the Gd ($\epsilon_r = 809$ and $\tan\delta = 0.201$ at 1 kHz) and Ce ($\epsilon_r = 775$ and $\tan\delta = 0.032$ at 1 kHz) doped BNT ceramics improved for the composition of $x = 0.025$ and 0.06 , respectively. In both cases, the average grain size reduced and improved density with substitution of Ce and Gd concentrations. The temperature-dependent of AC-conductivity is analyzed using a variable range hopping (VRH) model to study the hopping conduction mechanism in terms of the density of states ($N(E_F)$), hopping length (R_H), and hopping energies (W_H). It has been observed that both R_H and W_H values decreased with Gd and Ce doping, which is due to the enhancement of defect states near the Fermi level. It indicates that Gd^{3+} and Ce^{3+} assisted the hopping of charge carriers from one localized state to another in the BNT system.

Chapter 4 presents the structural, microstructural, piezoelectric, dielectric and AC conductivity studies of $Bi_{0.5}(Na_{1-x}K_x)_{0.5}TiO_3$ (BNKT; $x=0, 0.1, 0.2$ and 0.3) and $(1-x)$ BNT $-x [(K_{0.5}Na_{0.5})NbO_3 + 0.01 \text{ wt.}\% Gd_2O_3]$ (BNT-KNNG; $x=0-0.02$) piezoelectric ceramics systematically. The XRD and Raman analysis revealed that $Bi_{0.5}(Na_{0.8}K_{0.2})_{0.5}TiO_3$ and $Bi_{0.5}(Na_{0.7}K_{0.3})_{0.5}TiO_3$ ceramics exhibited a mixture of rhombohedral and tetragonal structures. The segregation of K at the grain boundary is confirmed by transmission electron microscopy (TEM) and is co-related with typical microstructural local compositional mapping analysis. Two transitions at $\sim 330^\circ\text{C}$ and 150°C were observed from ϵ' versus T curve in pure BNT are associated with the ferroelectric tetragonal to paraelectric cubic phase (T_C) and ferroelectric rhombohedral to ferroelectric tetragonal phase (T_d), respectively. Further, the T_C and T_d shifted towards the lower temperature with a rise K concentration. Frequency dispersion of T_d and T_C suggests that BNKT ceramics exhibit a weak-relaxor behavior with a diffuse phase

transition, which is confirmed by Uchino-Nomura criteria and Vogel-Fulcher law. The AC-resistivity $\rho_{ac}(T)$ follows the Mott's variable range hopping (VRH) conduction mechanism. A significant enhancement of dielectric and piezoelectric properties were observed for $x = 0.2$ system: dielectric constant ($\epsilon' = 1273$), dielectric loss ($\tan \delta = 0.047$) at 1 kHz, electromechanical coupling coefficients (k_{ij} : k_{33} , $k_t \sim 60\%$, $k_{31} \sim 62\%$ and $k_p \sim 46\%$), elastic coupling coefficients ($S_{33}^D = 6.40 \times 10^{-13} \text{ m}^2/\text{N}$ and $S_{33}^E = 10.06 \times 10^{-13} \text{ m}^2/\text{N}$) and piezoelectric constants ($d_{33} = 64.23 \text{ pC/N}$ and $g_{33} = 5.69 \times 10^{-3} \text{ Vm/N}$).

Further, the structural, morphological, and electric properties of BNT-KNNG ceramics were investigated in detail. XRD studies revealed the rhombohedral phase, which is also confirmed by HRTEM. The diffuse phase transition of BNT-KNNG samples exhibited a relaxor behavior supported by modified Curie Weiss law and Vogel-Fulcher law. The AC-Conductivity of BNT-KNNG ceramics in terms of hopping length, hopping energy, and density of states across the Fermi level was analyzed by Mott's variable range hopping mechanism. The addition of KNNG effectively reduced grain size, transition temperature, leakage current and improved dielectric ($\epsilon' = 1074$ and $\tan \delta = 0.059$ @ 1 kHz) and piezoelectric properties; electromechanical coupling factors (k_{33} , k_{31} , $k_t \sim 48\%$ and $k_p = 53\%$), and piezoelectric constants ($d_{33} = 108 \text{ pC/N}$ and $g_{33} = 1.14 \times 10^{-2} \text{ Vm/N}$) are observed for $x = 0.01$ sample, which is a potential candidate for high power electromechanical applications.

Chapter 5 presents the deposition of pure BNT and BNT-KNNG composite thin films grown by PLD technique on Pt(111)/Ti/SiO₂/Si and quartz substrates. BNT thin films are grown at different oxygen partial pressures (P) and investigated their structural, morphological, linear, and nonlinear optical, dielectric, and microwave dielectric properties in detail. The suitable O₂ pressure is optimized to obtain a pure BNT phase. The growth dynamics of BNT thin films are studied by scaling theory as a function of P

using height–height correlation function analysis from atomic force microscopy images. All the films exhibited a local roughness exponent; $\alpha_{loc} = 0.85 \pm 0.08$. The linear optical properties of the films extracted from ellipsometric analysis using a Tauc-Lorentz dispersion model and are in the same order extracted from the Swanepoel envelope and Tauc relation. The thickness, refractive index, extinction coefficient, packing density values increased, whereas the bandgap energy values reduced with a rise in oxygen pressure due to the improvement in crystallinity and reduction in the oxygen vacancies. The third-order nonlinear optical and microwave dielectric properties are enhanced with O₂ pressure. The film (50 Pa) with a rich BIT phase displayed self-defocusing behavior for the application in the protection of optical sensor devices. The film deposited at 10 Pa exhibited higher nonlinearity ($n_2 = 4.62 \times 10^{-6}$ cm²/W), strong absorbance ($\beta = 0.755$ cm/W) and higher dielectric constant ($\epsilon_r = 336$) with lower loss tangent ($\tan\delta = 0.0093$ @ 5 GHz) which makes it suitable for nonlinear optical and high frequency tunable device applications.

BNT-KNNG composite thin films are deposited at various O₂ pressures (0.1 Pa to 10 Pa) and investigated their structural, optical, dielectric, and ferroelectric properties. X-ray diffraction patterns revealed a single phase with rhombohedral symmetry. The increase in the refractive index and a decrease in optical bandgap is observed with O₂ pressure and are in the range of 2.18-2.28, and 4.08-3.70 eV, respectively. The obtained nonlinear optical properties revealed improved nonlinear refractive index ($n_2 = 5.775 \times 10^{-6}$ cm²/W) and absorption coefficient ($\beta = 0.973$ cm/W). The temperature-dependent dielectric response displayed two structural phase transitions from rhombohedral to tetragonal phase at 165 °C and tetragonal to cubic phase at 298 °C. The enhanced dielectric ($\epsilon_r = 411$, $\tan\delta = 0.156$), ferroelectric ($P_r = 25.31$ μC/cm², $E_C = 42.62$ kV/cm at 1kHz) with low leakage current are observed for 10 Pa deposited film.

Chapter 6 deals with a brief summary, important findings, and highlights of the thesis work and their potential applications in devices. In this chapter, the future scope of the work is also presented.



CONTENTS

List of Figures	i
List of Tables	x
List of Symbols and Abbreviations	xii
1. Introduction to Ferroelectric and Piezoelectric Ceramics and Thin Films	1-38
1.1 Introduction and motivation	1
1.2 Theory and fundamental concepts	2
1.2.1 Dielectrics	2
1.2.2 Piezoelectricity	6
1.2.3 Pyroelectricity	10
1.2.4 Ferroelectricity	10
1.2.5 Perovskite structure and stability	15
1.2.6 Relaxor ferroelectrics	17
1.3 Lead-based piezoelectric ceramics	18
1.3.1 Lead zirconium titanate - morphotropic phase boundary	18
1.3.2 Doping of PZT	20
1.4 Lead-free piezoelectric ceramics	20
1.4.1 Barium titanate (BaTiO_3)	21
1.4.2 Sodium potassium niobate ($\text{K}_{0.5}\text{Na}_{0.5}\text{NbO}_3$)	22
1.4.3 Bismuth sodium titanate ($\text{Bi}_{0.5}\text{Na}_{0.5}\text{TiO}_3$)	23
1.4.4 BNT thin films	26
1.5 Objective of the present work	28
1.6 References	30
2. Synthesis and characterization techniques	39-78

2.1 Synthesis of bulk BNT ceramics	39
2.1.1 Conventional solid-state reaction method	39
2.1.2 Stoichiometric Weighing of starting materials	40
2.1.3 Uniform mixing of starting materials	41
2.1.4 Calcination	41
2.1.5 Particle size reduction	42
2.1.6 Pelletization	42
2.1.7 Sintering	43
2.2 Thin-film preparation	45
2.2.1 Preparation of BNT target	45
2.2.2 Pulsed laser deposition (PLD)	45
2.2.3 Description of PLD	46
2.2.4 Film growth	46
2.2.5 Substrate temperature	47
2.2.6 Energy of the deposition flux	48
2.2.7 Deposition rate, vacuum quality and background gas	48
2.3 Characterization techniques	49
2.3.1 Thermal analysis	49
2.3.2 X-Ray diffraction	50
2.3.3 Density measurement	52
2.3.4 Raman spectroscopy	53
2.3.5 Scanning electron microscopy	55
2.3.6 Field emission transmission electron microscopy	57
2.3.7 Dielectric measurements and impedance spectroscopy	58
2.3.8 Ferroelectric measurements	61
2.3.9 Piezoelectric measurements	62

2.3.9.1 Polling	62
2.3.9.2 Piezoelectric coefficients	63
2.3.10 Atomic force microscope	65
2.3.11 Optical characterization	66
2.3.11.1 Linear optical properties	66
2.3.11.2 Nonlinear optical characterization	70
2.3.12 Microwave dielectric characterization	73
2.3.13 I-V characteristics	75
2.4 References	76
3. Structural and Dielectric Properties of Ce-BNT and Gd-BNT Doped Ceramics	79-109
3.1 Introduction	79
3.2 Sample preparation of Ce and Gd doped BNT ceramics	80
3.3 Results and discussion: Effect of sintering temperature on the densification of BNT ceramics	81
3.4 Results and discussion: Ce doped BNT ceramics	89
3.5 Results and discussion: Gd doped BNT ceramics	99
3.6 Conclusions	106
3.7 References	107
4. Dielectric, Piezoelectric and AC-Conductivity Studies of BNKT and BNT-KNNG Ceramics	110-161
4.1 Introduction	110
4.2 Sample preparation of K doped BNT and BNT-KNNG ceramics	112
4.3 Results and discussion of K doped BNT ceramics	113
4.4 Results and discussion of BNT-KNNG composite ceramics	134
4.5 Conclusions	156

4.6 References	157
5. Nonlinear Optical and Microwave Dielectric Studies of BNT and BNT-KNNG Thin Films	162-205
5.1 Introduction	162
5.2 Deposition of thin films	163
5.3 Results and discussions of BNT thin films	164
5.4 Results and discussions of BNT-KNNG thin films	184
5.5 Conclusions	199
5.6 References	201
6. Summary and future scope of work	206-213
6.1 Summary	206
6.1.1 Pure $\text{Bi}_{0.5}\text{Na}_{0.5}\text{TiO}_3$, $\text{Bi}_{0.5}(\text{Na}_{(1-x)}\text{Ce}_x)_{0.5}\text{TiO}_3$, and $\text{Bi}_{1-x}\text{Gd}_{x0.5}\text{Na}_{0.5}\text{TiO}_3$ ceramics	206
6.1.2 $\text{Bi}_{0.5}(\text{Na}_{1-x}\text{K}_x)_{0.5}\text{TiO}_3$ and $(1-x)$ BNT – x [$(\text{K}_{0.5}\text{Na}_{0.5})\text{NbO}_3 + 0.01$ wt.% Gd_2O_3] ceramics	207
6.1.3 BNT and BNT-KNNG composite thin films	209
6.2 Future scope of work	211
List of Publications	214

LIST OF FIGURES

Figure no.	Figure description	Page no.
<i>Chapter 1</i>		
1.1	Schematic diagram of polarization mechanisms.	4
1.2	Classification of dielectric, piezoelectric, pyroelectric and ferroelectric ceramics.	5
1.3	Direct and converse piezoelectric effect in piezoelectric ceramics.	6
1.4	The classification of point groups of crystals based on their symmetry.	8
1.5	Representation of the axes and directions of the piezoelectric system	9
1.6	The typical polarization-electric field (<i>P-E</i>) loop of ferroelectric ceramics.	11
1.7	Free energy versus polarization for (a) $T > T_C$ and (b) $T < T_C$.	13
1.8	(a) Free energy versus polarization. Temperature dependence of (b) spontaneous polarization, and (c) dielectric susceptibility in first-order phase transition.	13
1.9	(a) Free energy versus polarization. Temperature dependence of (b) spontaneous polarization, and (c) dielectric susceptibility in the second-order phase transition.	14
1.10	Schematic diagram of ideal cubic structure with ABO_3 perovskite.	16
1.11	Phase diagram of PZT.	19
1.12	(a) ϵ_r (b) d_{33} , and (c) k_{33} as a function of Curie temperature of different piezoelectric ceramics, measured at room temperature.	21
1.13	Temperature dependence of relative permittivity for single crystal $BaTiO_3$.	22
<i>Chapter 2</i>		
2.1	Flowchart of the various steps of synthesis procedure in conventional solid-state reaction.	40

Figure no.	Figure description	Page no.
2.2	Photograph of the planetary ball mill.	41
2.3	Photograph of the conventional furnace.	43
2.4	(a) Initial (b) intermediate and (c) final stages of the sintering process.	44
2.5	Schematic diagram of the PLD process.	46
2.6	Different growth modes in thin film deposition, (a) Volmer-Weber growth, (b) Frank – van der Merwe growth and (c) mixed growth.	47
2.7	Pulsed laser deposition system.	49
2.8	Photographic image of the DSC-TGA system.	50
2.9	(a) Bragg's law for X-ray diffraction and (b) schematic diagram of X-ray diffractometer.	51
2.10	Photograph image of the X-ray diffractometer.	52
2.11	Energy level diagram for Rayleigh and Raman Scattering.	53
2.12	Photograph of Raman spectrometer (LBRAM HR800).	55
2.13	The schematic diagram of a scanning electron microscope.	55
2.14	Photograph of field emission scanning electron microscope.	56
2.15	The schematic outline of a FETEM.	57
2.16	Photograph of FETEM instrument.	58
2.17	Photographs of the (a) LCR meter and (b) RF impedance material analyzer equipped with temperature control systems.	60
2.18	(a) Photograph of the ferroelectric $P - E$ tester and (b) Sawyer-Tower circuit diagram.	62
2.19	DC polling unit.	63
2.20	Impedance as a function of the frequency curve for measuring the resonance frequency and anti-resonance frequency.	64

Figure no.	Figure description	Page no.
2.21	Schematic diagram of the atomic force microscope.	65
2.22	Photograph of atomic force microscope.	66
2.23	Schematic diagram of refractive index in different mediums of the thin film.	67
2.24	Typical transmittance spectrum of a thin film.	67
2.25	(a) Photograph of UV-VIS-NIR spectrophotometer and (b) Spectroscopic ellipsometer.	70
2.26	Schematic diagram of the z-scan technique.	72
2.27	The cross-sectional view of SPDR fixture	74
Chapter 3		
3.1	DSC and TGA curves of the BNT precursor powder.	82
3.2	XRD pattern of calcined BNT ceramics at (a) 600 °C, (b) 700 °C, and (c) 800 °C for 3 hours.	82
3.3	Rietveld refined XRD pattern of the BNT samples sintered at (a) 1050 °C, (b) 1100 °C and (c) 1150 °C for 3 h.	83
3.4	Raman spectra of BNT samples sintered at (a) 1050 °C, (b) 1100 °C and (c) 1150 °C.	85
3.5	FESEM micrographs of the BNT ceramics sintered at (a) 1050 °C, (b) 1100 °C and (c) 1150 °C.	86
3.6	The temperature variation of dielectric constant (ϵ_r) and dissipation factor	86
3.7	The temperature variation of dielectric constant (ϵ_r) and dissipation factor ($\tan\delta$) of BNT ceramics, sintered at 1100 °C and measured at different frequencies.	87

Figure no.	Figure description	Page no.
3.8	Frequency variation of dielectric constant (a) and dissipation factor (b) of BNT samples measured at different temperatures.	88
3.9	Rietveld refined XRD pattern of the BNTC ceramics for (a) $x = 0.00$, (b) 0.005 , (c) $x = 0.015$, (d) $x = 0.025$, (e) $x = 0.035$ and (f) magnified image of (110) diffraction peak of all BNTC samples.	89
3.10	Raman spectra of BNTC ceramics for (a) $x = 0$ (b) $x = 0.005$ (c) $x = 0.015$ (d) $x = 0.025$ and (e) $x = 0.035$.	91
3.11	FESEM micrograph for (a) $x = 0$, (b) $x = 0.005$, (c) $x = 0.015$, (d) $x = 0.025$, (e) $x = 0.035$ of BNTC ceramics and (f) Ce concentration versus average grain size of BNTC samples.	93
3.12	The temperature dependence of (a) ϵ_r and (b) $\tan\delta$ of BNTC ceramics, measured at 1 MHz.	94
3.13	(a) The variation of $\log(1/\epsilon_r - 1/\epsilon_m)$ as a function of $\log(T - T_m)$ measured at 1 MHz and (b) γ versus Ce concentration of BNTC ceramics.	95
3.14	Variation of logarithmic σ_{ac} with a reciprocal temperature of (a) actual data, and fitted with Arrhenius relation in (b) Regime 1 (c) Regime 2, and (d) Ce concentration versus E_A of BNTC ceramics calculated in different regimes.	95
3.15	Fitting of VRH mechanism in pure ($x = 0$) and Ce^{3+} doped BNT ($x = 0.025$) ceramics.	96
3.16	Temperature variation of Mott's variable range hopping parameters pure ($x = 0$) and doped ($x = 0.025$) ceramics.	98
3.17	Rietveld refined XRD pattern of the BGNT ceramics ($x = 0.00$ to 0.06), sintered at $1150^\circ C$ for 3 h.	99
3.18	Raman spectra of BGNT ($x = 0.00$ to 0.06) samples.	99
3.19	FESEM micrographs of the BGNT samples (a) 0.00 , (b) 0.02 , (c) 0.04 and (d) 0.06 .	100
3.20	The temperature variation of ϵ_r (a) and $\tan\delta$ (b) of BGNT ceramics ($x = 0.00$ to 0.06) measured at 1 MHz.	101

Figure no.	Figure description	Page no.
3.21	Temperature-dependent of AC-conductivity of BGNT ceramics fitted with Arrhenius equation for (a) $x = 0$ (inset), (b) $x = 0.02$, (c) $x = 0.04$ and (d) $x = 0.06$.	103
3.22	The $\ln[\ln(\rho_{ac}/\rho_0)]$ versus $\ln[T(K)]$ of BNGT ceramics for (a) $x = 0$ and (b) $x = 0.06$.	104
3.23	Temperature variation of Mott's variable range hopping parameters (R_H and W_H) of BGNT ceramics for (a) $x = 0$ and (b) $x = 0.06$.	104
Chapter 4		
4.1	(a) XRD pattern of $\text{Bi}_{0.5}(\text{Na}_{(1-x)}\text{K}_x)_{0.5}\text{TiO}_3$ ceramics in the 2θ range of $20 - 80^\circ$ and (b) Splitting of (021) and (122) peaks in the 2θ range of $39.2 - 41.5^\circ$ and $56.5 - 60^\circ$, respectively.	113
4.2	Raman spectra of $\text{Bi}_{0.5}(\text{Na}_{(1-x)}\text{K}_x)_{0.5}\text{TiO}_3$ ceramics for (a) $x = 0$, (b) $x = 0.1$, (c) $x = 0.2$ and (d) $x = 0.3$.	114
4.3	FESEM micrographs of $\text{Bi}_{0.5}(\text{Na}_{(1-x)}\text{K}_x)_{0.5}\text{TiO}_3$ ceramics for (a) $x = 0$, (b) $x = 0.1$, (c) $x = 0.2$ and (d) $x = 0.3$.	116
4.4	FETEM images of $\text{Bi}_{0.5}(\text{Na}_{(1-x)}\text{K}_x)_{0.5}\text{TiO}_3$ ceramics for (a) $x = 0$ and (b) 0.2 samples.	117
4.5	The typical microstructure, elemental mapping and composition distribution for (a ₁), (a ₂), (a ₃) and (b ₁), (b ₂), (b ₃) for $x = 0$ and 0.2 samples, respectively.	118
4.6	The temperature dependence of ϵ_r and $\tan\delta$ of $\text{Bi}_{0.5}(\text{Na}_{(1-x)}\text{K}_x)_{0.5}\text{TiO}_3$ ceramics for (a) $x = 0$, (b) $x = 0.1$, (c) $x = 0.2$ and (d) $x = 0.3$, measured at 100 Hz – 1 MHz, respectively. Insets of (a), (b), (c) and (d) show the variation of depolarization temperature (T_d) at 1 MHz.	119
4.7	The logarithmic variation of $(1/\epsilon_r - 1/\epsilon_r^m)$ as a function of $\log(T - T_m)$ of $\text{Bi}_{0.5}(\text{Na}_{(1-x)}\text{K}_x)_{0.5}\text{TiO}_3$ ceramics for (a) $x = 0$, (b) $x = 0.1$, (c) $x = 0.2$ and (d) $x = 0.3$.	121
4.8	Frequency variation of critical temperature of BNKT ceramics, for (a) $x = 0$ and (b) $x = 0.2$ samples fitted with Vogel-Fulcher law.	122

Figure no.	Figure description	Page no.
4.9	Temperature-dependent of AC-conductivity of $\text{Bi}_{0.5}(\text{Na}_{(1-x)}\text{K}_x)_{0.5}\text{TiO}_3$ ceramics, analyzed with Arrhenius relation in R1 (302 – 392K) and R2 (562 – 592K) regimes.	123
4.10	The $\ln(\rho_{ac})$ versus reciprocal temperature of $\text{Bi}_{0.5}(\text{Na}_{(1-x)}\text{K}_x)_{0.5}\text{TiO}_3$ ceramics for (a) $x = 0$ and (b) $x = 0.2$ in R1 (302 – 392K) and R2 (562 – 592K) regimes. Insets of (a) and (b) show the VRH linear fit parameters in tabular form.	124
4.11	The $\ln[\ln(\rho_{ac}/\rho_0)]$ versus $\ln[T(K)]$ of $\text{Bi}_{0.5}(\text{Na}_{(1-x)}\text{K}_x)_{0.5}\text{TiO}_3$ ceramics for (a) $x = 0$ and (b) $x = 0.2$ in R1 (302 – 392K) and R2 (562 – 592K) regimes. Insets of (a) and (b) show the VRH linear fit parameters in tabular form.	126
4.12	Temperature variation of Mott's variable range hopping parameters (R_H and W_H) of $\text{Bi}_{0.5}(\text{Na}_{(1-x)}\text{K}_x)_{0.5}\text{TiO}_3$ ceramics, for (a) $x = 0$ and (b) $x = 0.2$ in R1 (302 – 392K) and R2 (562 – 592K) regimes.	127
4.13	Resonance and anti-resonance curve for $\text{Bi}_{0.5}(\text{Na}_{(1-x)}\text{K}_x)_{0.5}\text{TiO}_3$ ceramics with (a) $x = 0$, (b) $x = 0.1$, (c) $x = 0.2$ and (d) $x = 0.3$, measured at room temperature.	128
4.14	(a) Leakage current density (J) versus electric field (E), (b) $\ln(E)$ versus $\ln(J)$ of BNKT ceramics for $x = 0$ and 0.2, measured at RT.	132
4.15	Rietveld refined XRD patterns of BNT-KNNG composites for (a) $x = 0$, (b) $x = 0.005$, (c) $x = 0.01$ and (d) $x = 0.02$. Inset of figure (a) represents the shift in (110) diffraction peak in 2θ range of 30° to 36° .	134
4.16	FESEM micrographs of BNT-KNNG composites for (a) $x = 0$, (b) $x = 0.005$, (c) $x = 0.01$ and (d) $x = 0.02$.	136
4.17	The typical microstructure and elemental mapping for (a) $x = 0$ and (b) $x = 0.01$ of BNT-KNNG ceramics.	137
4.18	The EDAX spectra of BNT-KNNG composites for (a) $x = 0$ and (b) $x = 0.021$ samples.	138
4.19	(a) and (e) represents the bright field TEM images, (b) and (f) the SAED patterns, (c) and (g) HRTEM images, (d) and (h) the IFFT images (insets) of BNT-KNNG ceramics for $x = 0$ and 0.01, respectively.	140

Figure no.	Figure description	Page no.
4.20	Raman spectra of BNT-KNNG composites for (a) $x = 0$, (b) $x = 0.005$, (c) $x = 0.01$ and (d) $x = 0.02$.	141
4.21	The temperature dependence of ϵ_r and $\tan\delta$ of BNT-KNNG composites for (a) $x = 0$, (b) $x = 0.005$, (c) $x = 0.01$ and (d) $x = 0.02$, measured from 1 kHz – 1 MHz. The inset of figure (a) represents the temperature dependence of ϵ_r at 100 kHz for all the compositions.	144
4.22	The logarithmic variation of $(1/\epsilon_r - 1/\epsilon_r^m)$ as a function of $\log(T-T_m)$ of BNT-KNNG composites for (a) $x = 0$, (b) $x = 0.005$, (c) $x = 0.01$ and (d) $x = 0.02$.	145
4.23	Frequency variation of critical temperature of BNT-KNNG ceramics for (a) $x = 0$ and (b) $x = 0.01$ fitted with Vogel-Fulcher law.	145
4.24	Temperature-dependent of AC-conductivity of BNT-KNNG composites fitted with Arrhenius equation for (a) $x = 0$, (b) $x = 0.005$, (c) $x = 0.01$ and (d) $x = 0.02$.	146
4.25	The $\ln(\rho_{ac})$ versus reciprocal temperature of BNT-KNNG composites for (a) $x = 0$ and (b) $x = 0.01$ in different regimes (R1 and R2).	147
4.26	The $\ln[\ln(\rho_{ac}/\rho_0)]$ versus $\ln[T(K)]$ of BNT-KNNG composites for (a) $x = 0$ and (b) $x = 0.01$ in different regimes (R1 and R2).	148
4.27	Temperature variation of Mott's variable range hopping parameters (R_H and W_H) of BNT-KNNG composites for (a) $x = 0$ and (b) $x = 0.01$ in different regimes (R1 and R2).	149
4.28	Resonance and anti-resonance frequency characteristics of capacitance and loss tangent of poled BNT-KNNG composites for (a) $x = 0$, (b) $x = 0.005$, (c) $x = 0.01$ and (d) $x = 0.02$.	152
4.29	(a) Leakage current density (J) versus electric field (E), (b) $\ln(E)$ versus $\ln(J)$ of BNT-KNNG composites for (a) $x = 0$, (b) $x = 0.005$, (c) $x = 0.01$ and (d) $x = 0.02$, measured at RT.	153
Chapter 5		
5.1	Rietveld refinement XRD pattern of BNT films for (a) 1 Pa (b) 5 Pa, (c) 10 Pa and (d) 50 Pa. Inset of Figure 5.1(c) represents the simulated structure of BNT system for the film deposited at 10 Pa.	164

Figure no.	Figure description	Page no.
5.2	AFM 3D (left side) and 2D (centre) images of BNT films for (a) 1 Pa (b) 5 Pa, (c) 10 Pa and (d) 50 Pa. Height profile of each image is shown at the right side of respective images.	167
5.3	(a) log-log plot of HHCF, $H(r)$ as a function of distance r with fitted theoretical curve for BNT thin films at various pressures from 1 – 50 Pa. The plot of (b) roughness exponent α_{loc} , (c) surface roughness ω and (d) correlation length ζ as a function of pressure (P).	169
5.4	(a) Raman spectra and (b) Wavenumber versus oxygen partial pressure of BNT films, deposited at 1 Pa, 5 Pa, 10 Pa and 50 Pa.	170
5.5	(a) Optical transmittance spectra, inset of Figure 5.5(a) optical bandgap energy of BNT films deposited at various pressures. (b) d , α , n , P_0 , and E_g values as a function of oxygen pressure.	172
5.6	(a) and (b) The measured real and imaginary part of the dielectric permittivity of BNT thin films for various pressures. (c - f) The real part of the dielectric function of BNT thin films along with the fitted curve. (g) A schematic diagram of layer structure for SE analysis. (h) n , d and E_g as a function of oxygen pressure.	174
5.7	(a-d) Open apertures, (e-h) closed apertures normalized transmittance as a function of film position for (a) 1 Pa (b) 5 Pa, (c) 10 Pa and (d) 50 Pa. (i) and (j) β , n_2 , $\chi_R^{(3)}$, $\chi_I^{(3)}$ and $ \chi^{(3)} $ values as a function of oxygen partial pressures.	176
5.8	(a) and (b) The frequency variation of (a) ϵ_r and (b) $\tan\delta$ of BNT films deposited under various pressures and measured at RT. (c) The ϵ_r and $\tan\delta$ values as a function of O ₂ pressure. (d) The temperature variation of ϵ_r and $\tan\delta$ of BNT films deposited at 10 Pa pressure and measured at different frequencies.	180
5.9	(a) Resonance curve of Split Post Dielectric Resonator of nominal frequency 5 GHz with the investigated substrate (quartz) and film (10 Pa). (b) and (c) are the magnified image of Figure 5.9(a) for BNT film and substrate, respectively.	181
5.10	XRD pattern of BNT-KNNG thin films for (a) BNT-KNNG target (b) 0.1 Pa, (c) 1 Pa (d) 5 Pa and (e) 10 Pa.	184

Figure no.	Figure description	Page no.
5.11	FESEM micrographs of BNT-KNNG films for (a) 0.1 Pa, (b) 1 Pa (c) 5 Pa and (d) 10 Pa. Inset AFM images represents the BNT-KNNG films for various pressures.	186
5.12	Optical transmittance spectra of BNT-KNNG films for (a) 0.1 Pa, (b) 1 Pa (c) 5 Pa and (d) 10 Pa.	187
5.13	Optical bandgap energy of BNT-KNNG films deposited at (a) 0.1 Pa, (b) 1 Pa (c) 5 Pa and (d) 10 Pa.	189
5.14	The normalized transmittance as a function of film position in (a) open apertures and (b) closed apertures for the deposited films at 1 and 10 Pa.	191
5.15	The frequency variation of (a) ϵ_r and (b) $\tan\delta$ of BNT-KNNG films for various O ₂ pressures measured.	193
5.16	Temperature dependence of (a) ϵ_r and (b) $\tan\delta$ of BNT-KNNG film deposited at 10 Pa.	193
5.17	Hysteresis loops of BNT-KNNG thin film at a different voltage for the films deposited at (a) 1 Pa and (b) 10 Pa film.	196
5.18	(a) Current density (J) versus Electric field (E) and (b) linear fitting of $\ln(J)$ versus $\ln(E)$ for films deposited at 1 and 10 Pa.	198

LIST OF TABLES

Table no.	Table description	Page no.
Chapter 1		
1.1	Literature survey of BNT based ceramics.	24
1.2	Literature survey of BNT based thin films.	26
Chapter 3		
3.1	Rietveld refined parameters of BNT ceramics at different sintering temperatures.	84
3.2	Rietveld refinement parameters of $\text{Bi}_{0.5}(\text{Na}_{1-x}\text{Ce}_x)_{0.5}\text{TiO}_3$ ceramics.	90
3.3	Rietveld refinement parameters of $(\text{Bi}_{1-x}\text{Gd}_x)_{0.5}\text{Na}_{0.5}\text{TiO}_3$ ceramics.	98
Chapter 4		
4.1	Raman shift and FWHM of the modes for $\text{Bi}_{0.5}(\text{Na}_{(1-x)}\text{K}_x)_{0.5}\text{TiO}_3$ ceramics ($x = 0 - 0.3$).	115
4.2	Activation Energy (E_A) and Mott's parameters of $\text{Bi}_{0.5}(\text{Na}_{(1-x)}\text{K}_x)_{0.5}\text{TiO}_3$ ($x = 0 - 0.3$) ceramics, in R1 (302 – 392K) and R2 (562 – 592K) regimes.	127
4.3	Dielectric, electromechanical, elastic and piezoelectric parameters of $\text{Bi}_{0.5}(\text{Na}_{(1-x)}\text{K}_x)_{0.5}\text{TiO}_3$ ceramics ($x = 0 - 0.3$).	131
4.4	Lattice parameters and average grain sizes of BNT-KNNG ceramics ($x = 0 - 0.02$).	135
4.5	Crystal planes and corresponding inter planer spacing (d) of BNT-KNNG ceramics for $x = 0$ and 0.01 compositions.	139
4.6	Raman shift and FWHM of the modes for BNT-KNNG ceramics ($x = 0 - 0.02$).	142
4.7	Activation energy (E_A) and Mott's parameters of BNT-KNNG ($x = 0 - 0.02$) ceramics, in different regimes (R1 and R2).	150

Table no.	Table description	Page no.
4.8	Dielectric, electromechanical, elastic and piezoelectric parameters of BNT-KNNG ceramics ($x = 0 - 0.02$).	151
Chapter 5		
5.1	Lattice constants, lattice volume, and phase fraction of BNT thin films deposited at various oxygen pressures.	166
5.2	The estimated refractive index (n_f), absorption coefficient (α), and bandgap (E_g) of BNT films.	173
5.3	Nonlinear optical parameters of BNT films deposited under different O ₂ pressures.	179
5.4	Microwave dielectric properties of BNT films for various O ₂ pressures.	182
5.5	The refractive index (n_f), absorption coefficient (α), extinction coefficient (k) and bandgap (E_g) of BNT-KNNG composite thin films deposited at various pressures.	188
5.6	Microwave dielectric properties of BNT-KNNG composite thin films for various pressures.	195

List of Symbols and Abbreviations

Units of measurement

m	Meter
cm	Centimeter
μm	Micrometer
nm	Nanometer
Å	Angstrom
°C	Centigrade (degree)
kHz	Kilo Hertz
MHz	Mega Hertz
GHz	Giga Hertz
h	Hour
F	Farad
pC	Pico Coulomb
μC	Micro Coulomb
N	Newton
V	Volt
eV	Electron-volt
GPa	Giga Pascal
g	Gram
W	Watt
esu	Electrostatic unit
A	Ampere

Electrical measurements

ϵ_r	Relative permittivity
$\tan \delta$	Loss tangent
A	Area of the electrodes
ϵ'	Real part of permittivity
ϵ''	Imaginary part of permittivity

ϵ_0	Permittivity of vacuum
σ_{ac}	AC-conductivity
χ_e	Electric susceptibility
J	Leakage current density
k_{ij}	Electromechanical coupling coefficient
k_p	Planar electromechanical coupling coefficient
k_{33}	Thickness of electromechanical coupling coefficient
d_{ij}	Piezoelectric charge coefficient
E	Electric field
C	Capacitance
d	Thickness
σ	Stress
s	Strain
S	Electric compliance
g_{ij}	Piezoelectric voltage coefficient
P	Polarization
p	Dipole moment
V	Unit cell volume
Z	Impedance
Z'	Resistance
Z''	Reactance
f_r	Resonant frequency
f_a	Anti-resonance frequency
Q	Quality factor
P_s	Saturation polarization
P_r	Remnant polarization
E_c	Coercive field
τ	Relaxation time
DC	Direct current
AC	Alternating current
γ	Degree of diffuseness

E_A	Activation energy
ω	Angular frequency
k_B	Boltzmann constant
T_f	Freezing temperature
T_{CW}	Curie-Weiss temperature
T_d	Depolarization temperature
T_C	Curie temperature
ρ_{ac}	AC-resistivity
ζ	Decay length
$N(E_F)$	Density of states
R_H	Hopping length
W_H	Hopping energy

Optical measurements

α	Absorption coefficient
n	Refractive index
n_{633}	Refractive index at 633 nm
n_b	Bulk refractive index
P_0	Optical packing density
E_g	Optical bandgap
h	Planck's constant
ω_0	Beam waist
z_0	Rayleigh length
n_2	Nonlinear refractive index
β_{eff}	Nonlinear absorption coefficient
$\chi^{(2)}$	Second order nonlinear susceptibility
$\chi^{(3)}$	Third order nonlinear susceptibility
$\chi_R^{(3)}$	Real part of third order nonlinear susceptibility
$\chi_I^{(3)}$	Imaginary part of third order nonlinear susceptibility
L_{eff}	Effective thickness of the thin film
λ	Wavelength

c	Velocity of light
$h\nu$	Photon energy

Other parameters

θ	Angle
D	Crystallite size
FWHM	Full width at half maximum
a, b, c	Lattice parameters
χ^2	Chi-square
R_{Bragg}	Bragg factor
R_f	Profile factor
F	Orientation factor
ρ	Density
wt.	Weight
rms	Root mean square
TD	Theoretical density
EU	European union
WEEE	Waste of electrical and electronic equipment
RoHS	Restriction of hazardous substances
CSSR	Conventional solid-state reaction
RT	Room temperature
RF	Radio frequency
FE	Ferroelectric
RFE	Relaxor ferroelectric
PNR	Polar nanoregions
O_2	Oxygen partial pressure
VRH	Variable range hopping
CCD	Charge coupled device
SCLC	Space charge limited conduction
SE	Spectroscopic ellipsometry
SEA	Spectroscopy ellipsometry analyzer

NLO	Nonlinear optical
MWD	Microwave dielectric
SPDR	Split post dielectric resonator
MIM	Metal-insulator-metal
DSC	Differential scanning calorimetry
TGA	Thermal gravimetric analysis
XRD	X-Ray diffraction
AFM	Atomic force microscopy
SEM	Scanning electron microscopy
FESEM	Field emission scanning electron microscopy
FETEM	Field emission transmission electron microscope
HRTEM	High resolution transmission electron microscope
SAED	Selected area electron diffraction
EDS	Energy dispersive X-ray spectrometer
BNT	$\text{Bi}_{0.5}\text{Na}_{0.5}\text{TiO}_3$
BNTC	$\text{Bi}_{0.5}(\text{Na}_{(1-x)}\text{Ce}_x)_{0.5}\text{TiO}_3$
BGNT	$(\text{Bi}_{1-x}\text{Gd}_x)_{0.5}\text{Na}_{0.5}\text{TiO}_3$
BNKT	$\text{Bi}_{0.5}(\text{Na}_{1-x}\text{K}_x)_{0.5}\text{TiO}_3$
KNNG	$(\text{K}_{0.5}\text{Na}_{0.5})\text{NbO}_3 + 0.01 \text{ wt.}\% \text{ Gd}_2\text{O}_3$
BT	BaTiO_3
KNN	$\text{K}_{0.5}\text{Na}_{0.5}\text{NbO}_3$

Introduction to Ferroelectric and Piezoelectric Ceramics and Thin Films

1.1 Introduction and motivation

Piezoelectric materials play a significant role in modern science and technology due to their electromechanical responses. They can transform the mechanical energy into electrical energy and vice versa based on the piezoelectric effect that leads to the development of piezoelectric devices such as sensors, actuators, transducers, accelerators, ultrasonic motors, filters, buzzers, resonators and micro-electromechanical systems (MEMS) [1–5]. The perovskite piezoelectric materials have proven to be an abundant research field due to their fascinating functional properties for the applications in electronic, microelectronic devices, industrial production, etc. Hence, they have attracted much attention. The lead-based perovskite piezoelectric materials such as PbZrTiO_3 (PZT), PbZnNbO_3 (PZnN), PbMgNbO_3 (PMN), PbNiNb (PNN) and etc. were thoroughly investigated and have been used extensively due to their promising properties for the above application [6–10]. However, the toxicity of the lead causes a serious problem for human health and the environment [11]. Therefore, it is necessary to develop lead-free piezoelectric materials in order to replace Pb-based materials.

Besides, the demand for ferroelectric thin films is also increasing day by day due to their superior properties suitable for integrated electronic applications. Thin films play a key role in miniaturizing electrical components and devices. These are widely used in the capacitor, non-volatile memory, energy storage, micro-sensors, micro-actuator, pulsed

power systems, microwave tunable, nonlinear photonic devices and MEMS applications, etc. [12–14]. The ability to tune the thin film properties by changing the deposition parameters and fabrication process is a great advantage. Thin-film properties are important for the applications: ferroelectric and piezoelectric nonlinearity of thin films are also relevant in microsystems, nonlinear optical properties are promising for photonic device applications and high permittivity and low dielectric loss in films are important for applications in high-frequency devices [13,15].

The background and objective of the present study have been motivated to prepare lead-free perovskite ceramics, to understand fundamental issues, study the structural and electric properties, and aimed to improve the piezoelectric properties for high-performance electromechanical applications. Further, the optimized composition has been chosen to deposit thin films by the pulsed laser deposition technique, to study their nonlinear optical and microwave dielectric properties of the films for nonlinear photonic and microwave tunable device applications. The present chapter describes the introduction, fundamental theory, and concept of dielectric, ferroelectricity, and piezoelectricity. The origin of the perovskite piezoelectric materials is discussed. It also describes some of the technologically critical piezoelectric bulk ceramics and thin films with their applications. The motivation behind choosing the lead-free ceramics and thin films, brief outline, literature survey, and objectives of the work is given in detail.

1.2 Theory and fundamental concepts

1.2.1 Dielectrics

Dielectric materials are electrical insulators or very poor conductors that do not have free charge carriers, and they are tightly bound to the nucleus/atoms. When dielectric materials are placed in an external electric field, the charge carriers do not move through the sample, unlike the conductor. But, they can slightly shift away from their

equilibrium position in the sample, which results in a net dipole moment. The net dipole moment ($\vec{\mu}$) per unit volume (V) of the dielectric material is known as polarization ($\vec{P} = \Sigma(\vec{\mu}/V)$). The positive charge carriers (nucleus) are displaced in the field direction and negatively charge carriers (electrons) are shifted in the opposite direction to the field. The atoms or molecules can remain neutral in charge until they form an electric dipole moment. These materials have the ability to store the electric charge (energy), which acts as a capacitor. The energy storage of a capacitor varies from one material to another, depending on the polarization's intrinsic and extrinsic contributions.

There are four types of polarization mechanisms in dielectric materials depending on the frequency: electronic (\vec{P}_e), ionic (\vec{P}_i), orientational (\vec{P}_{dp}) (dipolar) and space charge (\vec{P}_{sc}) polarizations [16]. The schematic diagram of polarization mechanisms is shown in Figure 1.1. The electronic polarization occurs if the applied electric field causes the distortion of the negative cloud of an electron around positive atomic nuclei, which responds to the frequency in the range of 10^{12} and 10^{15} Hz. The relative displacement of positive and negative ions with an applied electric field is called ionic polarization; it responds to the frequency in the range of 10^9 and 10^{12} Hz. The alignment of permanent dipoles in the applied electric field is called as orientational polarization; it responds to the frequency in the range of 10^6 and 10^9 Hz. The space charge polarization is generated by an accumulation of charge carriers at an interface between electrodes and material surface and grain and grain boundary, and it occurs at a low frequency around 10^3 Hz. Therefore, the contribution of all individual types of polarization will give total polarization of dielectric material can be written as,

$$\vec{P}_{total} = \vec{P}_e + \vec{P}_i + \vec{P}_{dp} + \vec{P}_{sc} \quad (1.1)$$

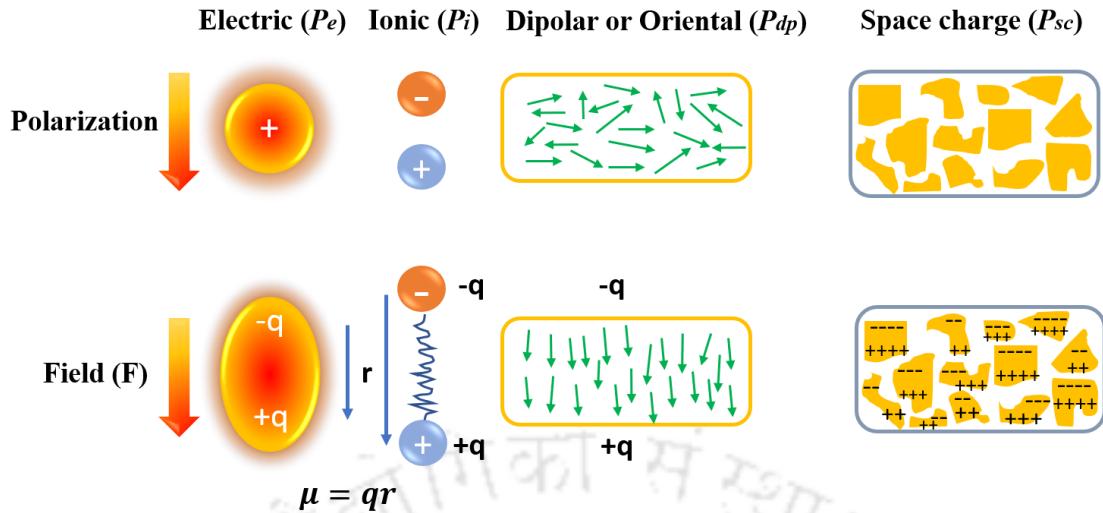


Figure 1.1: Schematic diagram of polarization mechanisms.

In linear dielectrics, the polarization \vec{P} is directly proportional to the applied electric field is given by the following equation,

$$\vec{P} = \chi_e \epsilon_0 \vec{E} \quad (1.2)$$

where χ_e is the electric susceptibility which is dependent on all polarization mechanisms and frequency, and ϵ_0 is the permittivity of the free space. For linear dielectrics: $\chi_e = \epsilon_r - 1$ where, ϵ_r the relative permittivity of the dielectric material, which is the ratio of the permittivity of the dielectric material (ϵ) to the permittivity of the free space (ϵ_0). It gives the ability of the energy storage in the dielectric sample by the application of the electric field. The relative permittivity is generally estimated using parallel plate capacitance method by the following equation,

$$\epsilon_r = \frac{\epsilon}{\epsilon_0} = \frac{Cd}{\epsilon_0 A} \quad (1.3)$$

where C is the capacitance, d , and A is the thickness of the sample and area of the electrodes, respectively. These materials have different dielectric constants at room temperature. A low dielectric constant material has a low ability to polarize and store a

charge. The high dielectric constant materials are good at storing a higher amount of charge. Dielectric properties of the materials include dielectric constant and dielectric loss (loss tangent/dissipation factor), in which the dielectric loss is the dissipation of energy in dielectric material under an electric field. It is defined as the ratio of the imaginary (ϵ'') part of the dielectric permittivity to the real permittivity (ϵ'), i.e., $\tan \delta = \frac{\epsilon''}{\epsilon'}$. Therefore, the high dielectric constant and low dielectric loss materials are key parameters for the electrical/electronics industry applications.

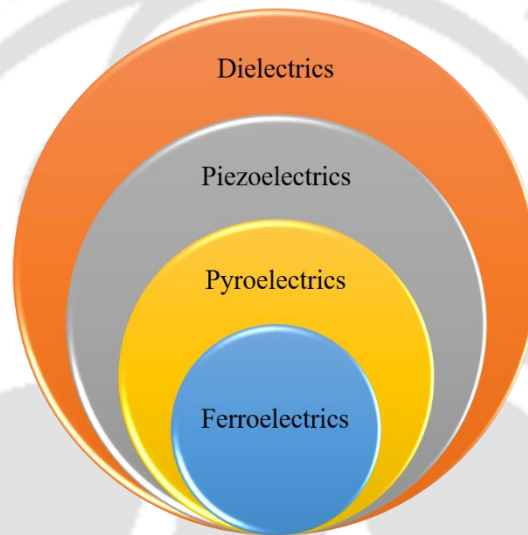


Figure 1.2: Classification of dielectric, piezoelectric, pyroelectric and ferroelectric ceramics.

Dielectric materials are divided into two main categories such as linear dielectric and nonlinear dielectrics. The linear dielectric materials exhibit a linear response between the polarization and the applied electric field. The nonlinear dielectric materials exhibit a spontaneous polarization even in the absence of an external electric field. The appearance of spontaneous polarization in nonlinear dielectrics is basically dependent on the crystal structure. The existence of non-centre of symmetrical structure is a necessary condition for a solid to belong to the nonlinear dielectric class of materials. The dielectric materials

are a subgroup of piezoelectric, pyroelectric, ferroelectric materials as shown in Figure 1.2.

1.2.2 Piezoelectricity

The piezoelectricity phenomena were discovered by Jacques and Pierre Curie in 1880 [17]. The material can be piezoelectric only if there is the centre of inversion in the unit cell. Piezoelectricity is the generation of electric charge with the application of mechanical force or stress or vibration. Piezoelectric materials exhibit a direct piezoelectric effect and a converse piezoelectric effect. Figure 1.3 shows the schematic diagram of the direct and converse piezoelectric effect. The ability to generate electric potential by application mechanical stress is known as a direct piezoelectric effect. It is utilized for sensor applications (e.g., quartz clock, gas igniter, transformer, and automotive devices). The generation of mechanical strain due to the deformation of material by applying the external electric field is known as a converse piezoelectric effect and is being used in actuator applications (e.g., sonar, buzzer, microphone, and transducer).

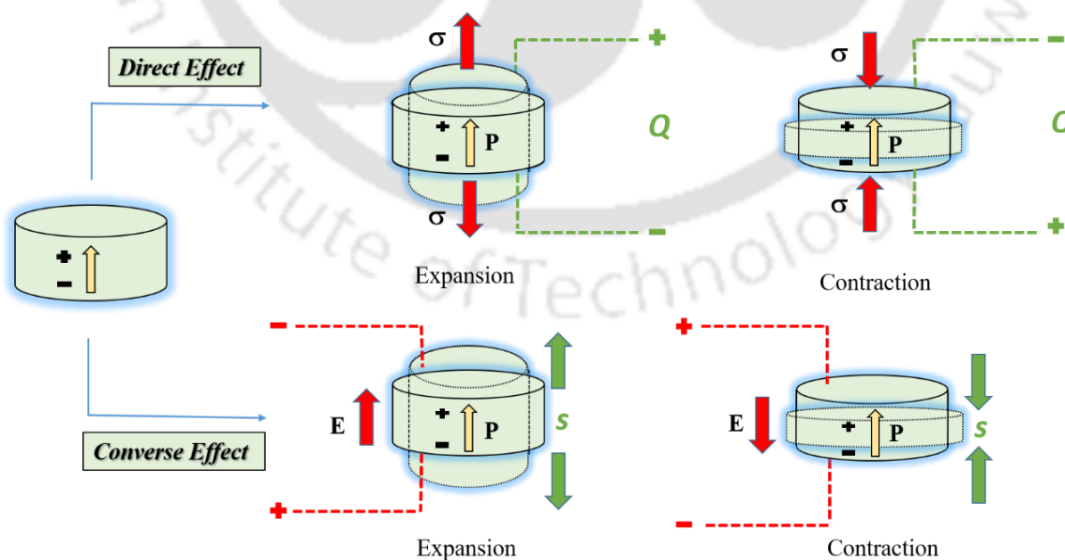


Figure 1.3: Direct and converse piezoelectric effect in piezoelectric ceramics.

In other words, the piezoelectricity depends upon the crystal symmetry and is explained using the crystallographic principles. There are 32 classes of crystal point groups [16–18], as shown in Figure 1.4. Among these, 21 are non-centrosymmetric, of which 20 exhibits the piezoelectric effect, and the remaining 11 possesses centrosymmetric structures. The 10-point groups only exhibit spontaneous polarization out of 20. The crystals of these point groups are known as polar, which means that the permanent dipole moment exists even in the absence of an electric field. These materials possess a spontaneous polarization known as ferroelectricity.

In the direct piezoelectric effect, the electric potential can be generated by the application of mechanical stress by the following equation,

$$D = d\sigma + \varepsilon^\sigma E \quad (1.4)$$

where D is the electric polarization (C/m^2), d is the piezoelectric charge coefficient (C/N), σ is the stress (N/m^2), ε is the dielectric permittivity (F/m), and E is the electric field (V/m). The superscript σ denotes that the permittivity is measured under zero stress (short-circuit condition). If the applied field is zero, the above equation can be written as,

$$D_i = d_{ijk}\sigma_{jk} \quad (1.5)$$

where, D_i , d_{ijk} , and σ_{jk} are the first rank vector, third rank tensor, and second rank tensor.

In the converse piezoelectric effect, the strain will be induced in response to the applied electric field by the following equation,

$$s = S^E \sigma + dE \quad (1.6)$$

where, s is the strain component, S is the electric compliance; T is stress (N/m^2), d is the piezoelectric voltage coefficient (m/V), and E is the electric field (V/m). The superscript E denotes that the elastic compliance which is measured under the constant electric field

(short-circuit condition). The above equation can be written in the following form if the mechanical stress is zero,

$$s_{jk} = d_{ijk}E_i \quad (1.7)$$

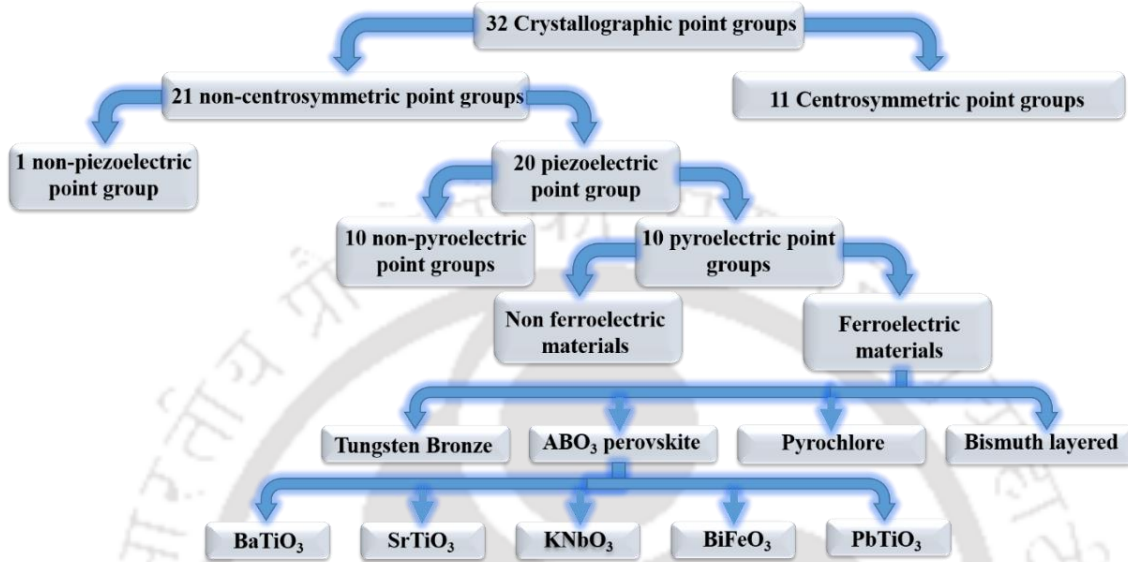


Figure 1.4: The classification of point groups of crystals based on their symmetry [18].

The charge displacement and strain are directional dependent parameters. Piezoelectric materials are anisotropic; i.e., they do not exhibit the same properties in all directions. Therefore, the directions must be defined to understand the piezoelectric properties. The lower subscripts i , j , and k represent the directions of stress, strain, or electric field in the above constitutive equations (1.4 – 1.7). The polarization or poling direction is usually preferred along the Z-axis with the two other orthogonal directions (X and Y-axis) of the system. The directions of X, Y, and Z are denoted by the subscript 1, 2, and 3, respectively, and the shears around these axes are denoted by 4, 5, and 6, respectively, and are shown in Figure 1.5. The first subscript indicates the input directions, whereas the second subscript indicates the response direction. For example, the parameter M_{32} is considered as a material property. For direct piezoelectric effect, M is measured by the stress in 3 direction inducing polarization in 2 direction or by the

external electric field in 3 direction produce strain in 2 direction for converse piezoelectric effect.

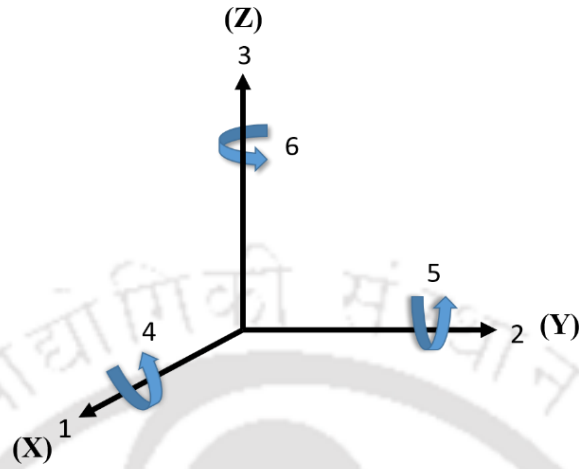


Figure 1.5: Representation of the axes and directions of the piezoelectric system.

The electromechanical coupling coefficient (k) is one of the most important parameters in piezoelectric materials; it is the efficiency of the energy conversion between electrical energy into mechanical energy and vice versa. There are few other coupling coefficients introduced by considering the effect in specific directions such as planar (k_p) (planar), thickness (k_t), longitudinal (k_{33}), transverse (k_{31}), shear (k_{15}) [19]. The electromechanical coupling coefficient can be defined by the following equation.

$$k^2 = \frac{\text{stored mechanical (electrical)-energy}}{\text{applied electrical,(mechanic)al energy}} \quad (1.8)$$

The mechanical quality factor (Q_m) is the ratio of the stored mechanical energy to the dissipated energy per cycle. Larger Q_m gives less mechanical loss should be employed for highly efficient actuators and transducers. The Q_m is defined by the following equation,

$$Q_m = 2\pi \frac{\text{stored mechanical energy}}{\text{dissipated energy per cycle}} \quad (1.9)$$

1.2.3 Pyroelectricity

Pyroelectricity is the generation of electric charge on the material in response to temperature. Ten of the 20 point groups are polar, which exhibit pyroelectricity [20]. In pyroelectric materials, the spontaneous polarization can be generated by the application of temperature and forms the dipoles without any stress or external electric field, unlike the normal piezoelectric materials. A change in spontaneous polarization (dP_s) with temperature (dT) is given by the following equation,

$$dP_s = p dT \quad (1.10)$$

$$p = \left(\frac{\partial P_s}{\partial T} \right)_{\sigma, E} \quad (1.11)$$

where, p is the pyroelectric coefficient (C/m²K), electric field (E), and stress (σ) are constants.

1.2.4 Ferroelectricity

Ferroelectric materials are a subgroup of piezoelectric and pyroelectric materials and exhibit the spontaneous electric polarization that can be reversed by the application of electric field; this phenomenon is known as ferroelectricity. Ferroelectric materials exhibit nonlinear polarization with applied electric field is known as a hysteresis loop of polarization (P) versus applied electric field (E) ($P - E$ loop). A typical hysteresis loop of ferroelectrics is shown in Figure 1.6. Initially, the polarization varies linearly to the applied electric field due to insufficient field for the orientation of the domain. The polarization rises to saturation with an increase in the field, i.e., the maximum number of domains oriented in the field direction, which is known as saturation polarization (P_s). As the electric field decreases to zero, some of the domains can't orient along the original direction (i.e., non-zero polarization), which turns to remnant polarization (P_r) even in absence of electric field. The field with the opposite direction required to reduce the

polarization to zero is known as the coercive field (E_c). If this field continues to increase in a negative direction, then the polarization will reverse and reaches to negative saturation polarization ($-P_r$). And similarly, a positive coercive electric field is required to reset the negative polarization ($-P_s$). The area of the hysteresis loop signifies the energy dissipated inside the sample as heat during each cycle.

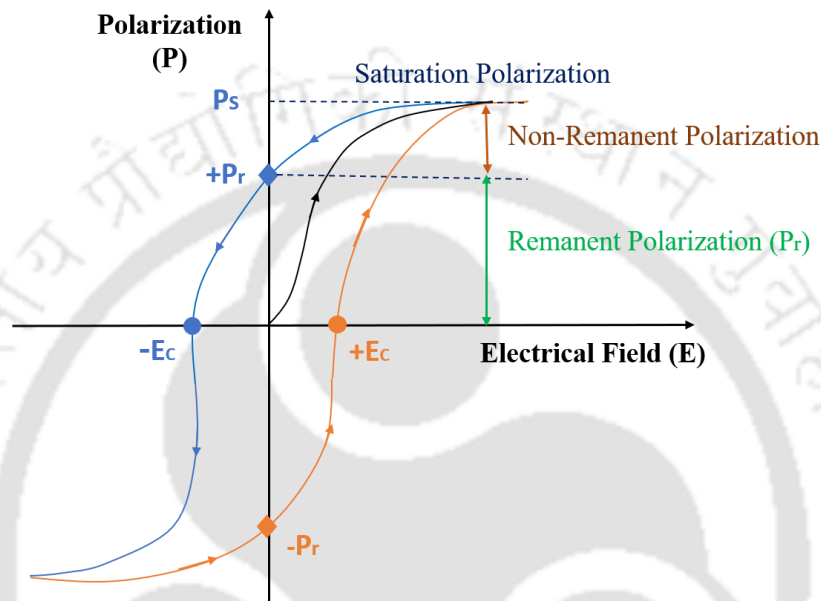


Figure 1.6: The typical polarization–electric field (P - E) loop of ferroelectric ceramics.

The orientation states can be defined as the various possible orientation of polarization in the ferroelectric material. The non-ferroelectric materials do not show the switchable polarization in the presence of an electric field due to only one equilibrium orientation state for the spontaneous polarization. Ferroelectric materials possess two or more equilibrium orientation states of the spontaneous polarization vector, and it can be switched from one to another in response to various orientations of sufficient electric field. The spontaneous polarization is the atomic displacement from their centrosymmetric positions, and it disappears above the Curie temperature (T_c). Usually, ferroelectric materials show the polycrystalline nature, and each unit cell has a net dipole moment. Nevertheless, this moment does not lead to macroscopic polarization because of

the randomly orientated domains in the polycrystalline material. The domain is another important feature of ferroelectric materials, which is a small area of ferroelectric crystal in which adjacent unit cells possess homogeneous and uniform polarization. The origin of the domains is attributable to the electrostatic energy minimization. The polarization directions of domains are $\langle 001 \rangle$, $\langle 110 \rangle$, $\langle 111 \rangle$, and angles between the dipoles of adjacent domains are 71° , 90° , and 180° , respectively for high-temperature symmetry axes. It can be modified slightly by ferroelectric deformation. Crystallographically, domain structure has a twinning nature [21]. The domain structure consists of several domains with different orientations, and a boundary between two neighbor domains is known as domain wall, typically they have 1-10 nm of width. The domain walls can be switched by 91° or 180° with the application of a sufficient high electric field, yielding processes like domain wall motion, domain nucleation and domain switching. Hence, ferroelectricity is considered to have a spontaneous and switchable alignment of dipoles in polar materials by an external electric field. In ferroelectrics, the ability to switch bipolar states electrically can enable ultrafast write-erase operations.

The phenomena of ferroelectricity in a ferroelectric material were described by Landau- Ginzburg-Devonshire (LGD) theory [22,23]. According to LGD theory, the free energy (F) of the system can be expanded as a function of polarization and strain in the vicinity of phase transition temperature (T_0) and is given by the following expression.

$$F(P, T) = \frac{1}{2} \alpha P^2 + \frac{1}{4} \beta P^4 + \frac{1}{6} \gamma P^6 + \dots \quad (1.12)$$

where, α , β , and γ are temperature-dependent parameters and determine the nature of phase transitions and dielectric behavior in the vicinity of T_C . The symbols α and γ are positive for the ferroelectric phase.

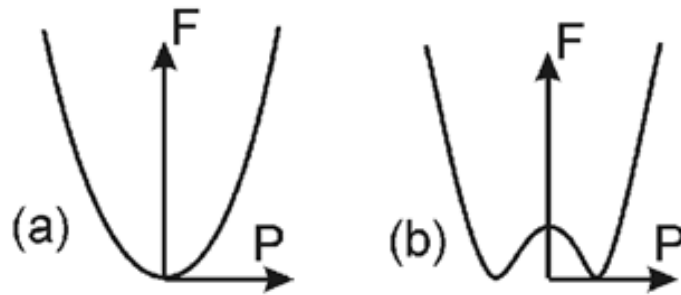


Figure 1.7: Free energy versus polarization for (a) $T > T_C$ and (b) $T < T_C$ [23].

Figure 1.7 shows the polarization as a function of free energy in the paraelectric region at $T > T_C$ and the ferroelectric region at $T < T_C$. The sign of β represents the transformation of free energy from one to another phase and the nature of ferroelectric to paraelectric transition (continuous or discontinuous). The sign of β is negative and positive for the first-order and second-order phase transitions, respectively.

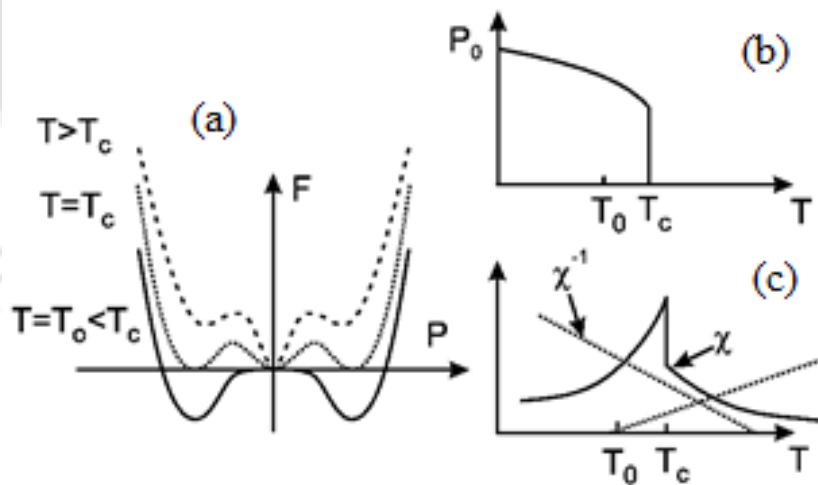


Figure 1.8: (a) Free energy versus polarization. Temperature dependence of (b) spontaneous polarization, and (c) dielectric susceptibility in first-order phase transition [23].

For first-order phase transitions ($\beta < 0$), the free energy is minimum when temperature is above T_0 . While temperature decreases, the free energy is further decreased

and is favored thermodynamically. This will occur at T_C and exceed T_0 . In this phase transition, the order parameter is polarization, and the linear susceptibility jumps at T_C discontinuously (Figure 1.8). Both the phases (ferro and para) coexist at T_C and are correlated with the latent heat. For the second-order phase transition ($\beta > 0$), the transition takes place at $T = T_0$, and no discontinuity change in the polarization is found. As the temperature reduces below T_0 , the free energy and spontaneous polarization continuously increase (Figure 1.9). The dielectric susceptibility at $T = T_0$ is found to diverge, and the dielectric stiffness will disappear. The two phases do not coexist, and the atomic displacements are relatively smaller than the first-order phase transition. The heat capacity indicates discontinuity without latent heat in the second-order phase transition. However, the limitations of this theory are (i) the macroscopic atomic interpretation was not explained (ii) minimal explanation of hysteresis phenomena and (iii) intrinsic, quasi-static, and single domain properties were described without considering the extrinsic contribution. In comparison, most ferroelectrics are polycrystalline materials, and the frequency response of the polycrystalline materials was not analyzed.

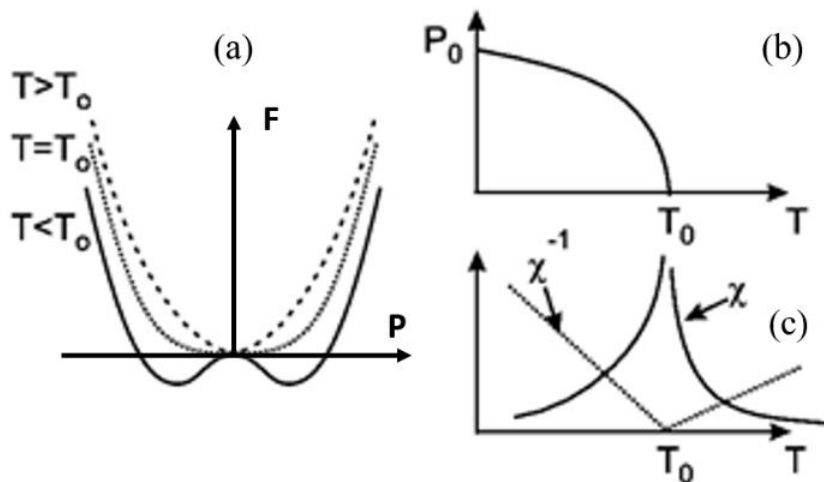


Figure 1.9: (a) Free energy versus polarization. Temperature dependence of (b) spontaneous polarization, and (c) dielectric susceptibility in the second-order phase transition [23].

1.2.5 Perovskite structure and stability

The perovskite family of materials has enormous technological importance in the areas of solid-state Physics, Optics, Chemistry and Materials science due to their fascinating functional properties such as dielectric, ferroelectric (multi), piezo-pyroelectricity, magnetic, linear and nonlinear electro-optical, superconducting properties for technological applications [24–27]. Many of these properties vary from one perovskite to another due to the differences in the crystal structure. The perovskite has a crystal structure similar to that of calcium titanium oxide (CaTiO_3). It was first discovered by German chemist Gustav Rose in 1839 and named after the Russian mineralogist L. A. Perovski (1792-1856) [28]. The general chemical formula for perovskite materials is ABO_3 , where 'A' and 'B' are two cations with different sizes. The atomic size of 'A' is larger than 'B.' The A-site cations have 12-fold cuboctahedral coordination with the anions whereas B-site cation in 6-fold coordination, surrounded by octahedral of oxygen (O) anions. The schematic diagram of the ideal cubic structure with ABO_3 perovskite per unit cell is shown in Figure 1.10. The A-site cations occupy at the corners (8) of the cube, B-site cation sits in the body center position (1), and oxygen anions are sitting at face centers (6). In order to achieve charge balance and stoichiometry in the perovskite composition, the combination ($\text{A}^{2+}\text{B}^{4+}\text{O}_3$, $\text{A}^{1+}\text{B}^{5+}\text{O}_3$, and $\text{A}^{3+}\text{B}^{3+}\text{O}_3$) of A and B site-cations should satisfy the condition, i.e., the sum of the valency of all cations is +6 to balance the negative charge of the three oxygen anions (-6). Thus, it permits the formation of complex perovskites. Non-centrosymmetric perovskite materials are essential to obtain piezoelectric properties, which have a non-zero net charge in each unit cell of the crystal. Nevertheless, an electrical polarity occurs as a result of the B-site cation sitting slightly off-centre inside the unit cell, thus effectively turning the unit cell into an electrical dipole. Among them, $\text{A}^{2+}\text{B}^{4+}\text{O}_3$

perovskite structures (Titanates/Zirconates) are the most common useful compounds (BaTiO_3 , PbTiO_3 , and PbZrO_3) because of their high dielectric, ferroelectric, and piezoelectric properties. $\text{A}^{\text{I}}\text{B}^{\text{5+}}\text{O}_3$ perovskite compounds (KNbO_3 , NaNbO_3 , and LiTaO_3) are of particular interest for their piezoelectric properties. The $\text{A}^{\text{3+}}\text{B}^{\text{3+}}\text{O}_3$ perovskite group (BiFeO_3 and LaAlO_3) are having a lower symmetry structure (rhombohedral/orthorhombic).

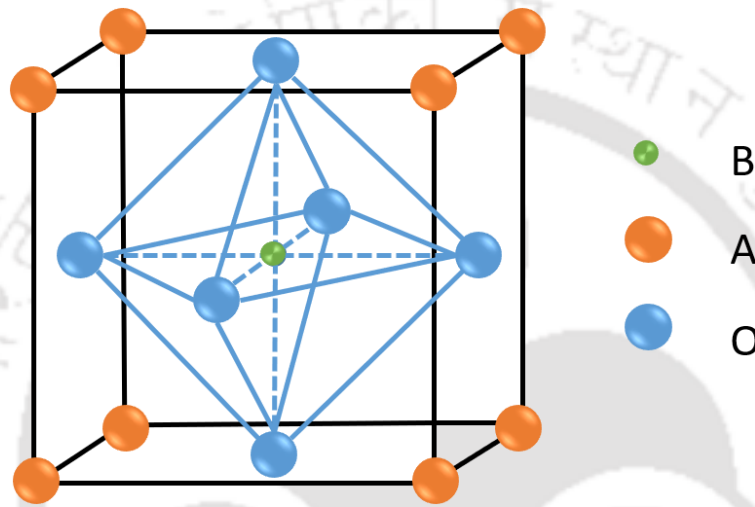


Figure 1.10: Schematic diagram of ideal cubic structure with ABO_3 perovskite.

Goldschmidt proposed a simple geometrical relation between cations and anions that provides stability and distortion of perovskite structures. Goldschmidt's tolerance factor (t) is calculated based on the ionic radii by following relation [29].

$$t = \frac{r_A + r_O}{\sqrt{2}(r_B + r_O)} \quad (1.13)$$

where, r_A , r_B , and r_O are the ionic radii of the A-site, B-site cations, and oxygen anions, respectively. $t = 1$ for the ideal cubic structures (SrTiO_3), $t < 1$ for lower symmetry phase (rhombohedral/orthorhombic), and $t > 1$ for hexagonal or tetragonal phases. The increase in t value is attributed to the increase in the A-site cation radius and decrease in the B-site cation radius and vice versa.

1.2.6 Relaxor ferroelectrics

The relaxor properties of ferroelectrics were first discovered by Smolenskii et al. [30,31] in 1959. Relaxor ferroelectrics or relaxors are a special class of disorder ferroelectrics that have peculiar structure and properties in which the ferroelectric state occurs only in nanoscale regions. The origin of relaxor ferroelectric (RFE) behavior is due to the compositional disorder in the complex perovskite structure with the general formula of $A'A''B'B''O_3$, especially with end-member compound (B-site). The variation in A and/ or B site valences and ionic radii lead to the formation of the local electric fields due to local charge imbalance and local elastic fields due to distortions of local structure preventing the long-range dipole alignment, which results in the existence of polar nanoregions (PNR) [32–34]. Therefore, the PNR strongly affects the behaviors of the ferroelectric sample.

The RFE's are different from normal ferroelectrics (NFE's) in several characteristics features as follows:

- NFE's exhibit a sharp phase transitions at T_C , while RFE's exhibit the diffuse phase transitions at a temperature of maximum permittivity (T_{max}).
- NFE's show weak frequency dependence at T_C , while RFE shows the strong frequency dependence at T_{max} and shifts towards high temperature with an increase in frequency.
- NFE follows the Curie-Weiss law above the T_C . In contrast, RFE's deviate from the Curie-Weiss behavior at Burns temperature (T_B) defined as the high permittivity that occurs from local polarizations and nano-sized domains, which nucleate and grow below a specific temperature and follows the modified Curie-Weiss law.
- NFE's exhibit the significant P_r with fat hysteresis loop, and RFE's exhibit the small P_r and large P_s with a slim hysteresis loop.

- NFE shows the strong anisotropy response to light, whereas RFE shows the weak anisotropic response to the light.

To date, several models were proposed to understand the mechanism of relaxor ferroelectric behavior, such as the super-paraelectric model, first-principle method, order-disorder transition model, microdomain, and macrodomain switching model, dipolar glass model and random field theory [35–39].

1.3 Lead-based piezoelectric ceramics

1.3.1 Lead zirconium titanate - morphotropic phase boundary

The piezoelectric materials can convert electrical energy into mechanical energy and vice versa. This feature becomes much dominating in the research as well as the industrial application of piezoelectrics, which produce macroscopic strain by the application of the electric field. Therefore, these materials and their functionality can be used in many applications such as sensor, actuator, transducer, strain gauge, ultra-sonar, microphone, phonograph pickups, accelerometer, fuel jet valve, an imaging device, and etc. [11,40,41]. Generally, the piezoelectric materials are classified into four categories: (i) Perovskite, (ii) bismuth layered, (iii) tungsten bronze, and (iv) pyrochlore non-perovskite. The perovskite structured (ABO_3) materials have received giant significance in materials science due to their fascinating dielectric, ferroelectric, piezoelectric, pyroelectric, and optical properties for technological applications [42]. To date, perovskite structure lead zirconium titanate $PbZr_{1-x}Ti_xO_3$ (PZT) is one of the best piezoelectric materials and widely investigated for the above applications due to their superior dielectric, ferroelectric, and piezoelectric properties. PZT is a solid solution of ferroelectric lead titanate $PbTiO_3$ (PT) and antiferroelectric lead zirconate $PbZrO_3$ (PZ) [40,43]. At room temperature, PT has a tetragonal phase with $P4mm$ symmetry and PZ

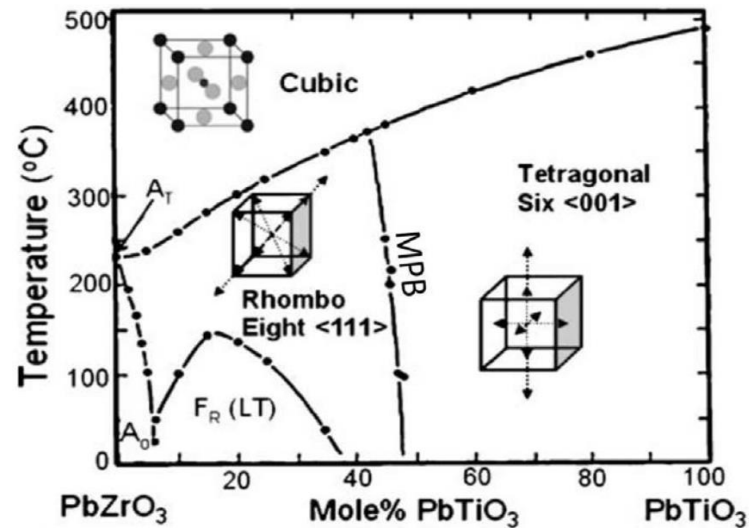


Figure 1.11: Phase diagram of PZT [44].

has a rhombohedral phase with $R3m$ symmetry. PZT has a perovskite structure of ABO_3 , where Pb ions occupy at the A site, and Zr and Ti ions occupy at the B site and Figure 1.11 shows the phase diagram of PZT. It is well-established that the improved properties are strongly dependent on composition and temperature near the morphotropic phase boundary (MPB). At MPB, an abrupt structural change happens between the tetragonal and rhombohedral phases allow more polarization directions [17,44]. Therefore, more polarization directions across the unit cell could increase ease of domain reorientation, which improves the piezoelectric properties near MPB [48-49]. The PZT exhibits the higher dielectric constant and low dielectric loss ($\epsilon_r = 730$, $\tan\delta = 0.004$) and high T_C (386 °C) and larger piezoelectric charge coefficient ($d_{33} = 220$ pC/N and electromechanical coupling coefficient ($k_{33} = 67\%$) [45]. Further, many other lead-based perovskite systems (binary and ternary) were synthesized in order to enhance the properties. For example, $PbZn_{1/3}Nb_{2/3}O_3 - PbTiO_3$ (PZN-PT) and $PbMg_{1/3}Nb_{2/3}O_3 - PbTiO_3$ (PMN-PT) exhibited the improvement in dielectric ($\epsilon_r = 5000$, $\tan\delta = 0.01$ at 1kHz), ferroelectric ($P_r = 43$ $\mu C/cm^2$, $E_c = 3$ kV/cm) and piezoelectric properties ($d_{33} > 2500$ pC/N, $k_{33} = 0.94$ and strain level $> 0.6\%$) [46]. The higher piezoelectric charge coefficient, induced strain, and

electromechanical coupling coefficient are making the material suitable for the high-performance actuator, transducer, and energy conversion device (energy harvesters) applications, respectively [47–49].

1.3.2 Doping of PZT

Doping is an approach used for improving dielectric, ferroelectric, piezoelectric properties, etc. The doping can be done by mainly three types, such as isovalent, donor, and acceptor doping at A and/or B sites [17]. First, the isovalent dopants such as Ba^{2+} , Sr^{2+} , Ca^{2+} , etc. in A-site (Pb^{2+}) and Sn^{4+} , Hf^{4+} , etc. in B-site (Zr^{4+} and Ti^{4+}) of PZT leads to reduce in T_C and increase in the dielectric and piezoelectric properties [50,51]. Secondly, the donor dopants with higher charges such as La^{3+} , Nd^{3+} , and Bi^{3+} in Pb^{2+} site and Nb^{5+} , Sb^{5+} , and Ta^{5+} in Zr^{4+} sites are compensated by the formation of the cation vacancies can be either A or/and B sites. Hence, the electrical resistivity of the PZT tends to increase [18,52,53]. Such dopants can enhance the ϵ_r , $\tan\delta$, P_r , and k , whereas the E_c reduces (i.e., soft PZT). Lastly, the acceptor type dopants with a lower charge such as K^+ , Na^+ , etc. in A-site and Mg^{2+} , Fe^{3+} , Co^{3+} , etc. in B-site are compensated by the formation the oxygen vacancies [54,55]. Nevertheless, such dopants reduce the ϵ_r , $\tan\delta$, P_r , and k , whereas the E_c increases (i.e., hard PZT).

1.4 Lead-free piezoelectric ceramics

The lead-based perovskite piezoelectric materials such as PZT, PZnN , PMN , PNN , etc. are extensively investigated and have attracted much attention due to their promising properties for the applications in sensor, actuator, transducer, MEMS, and etc. However, the toxicity of the lead causes a severe problem for human health and the environment [56]. Environmental legislation in the European Union, US, and few countries of Asia demands the elimination of toxic lead, which encouraged a great effort

in the research community for the development of lead-free piezoelectric ceramics [11]. Therefore, three main lead-free ceramics have drawn the most attention, such as barium titanate (BT) based, sodium potassium niobate (KNN) based, and bismuth sodium titanate (BNT) based ferroelectrics. Figure 1.12 shows dielectric constant, piezoelectric coefficient and coupling factor versus Curie temperature of these three-lead free based materials and PZT material.

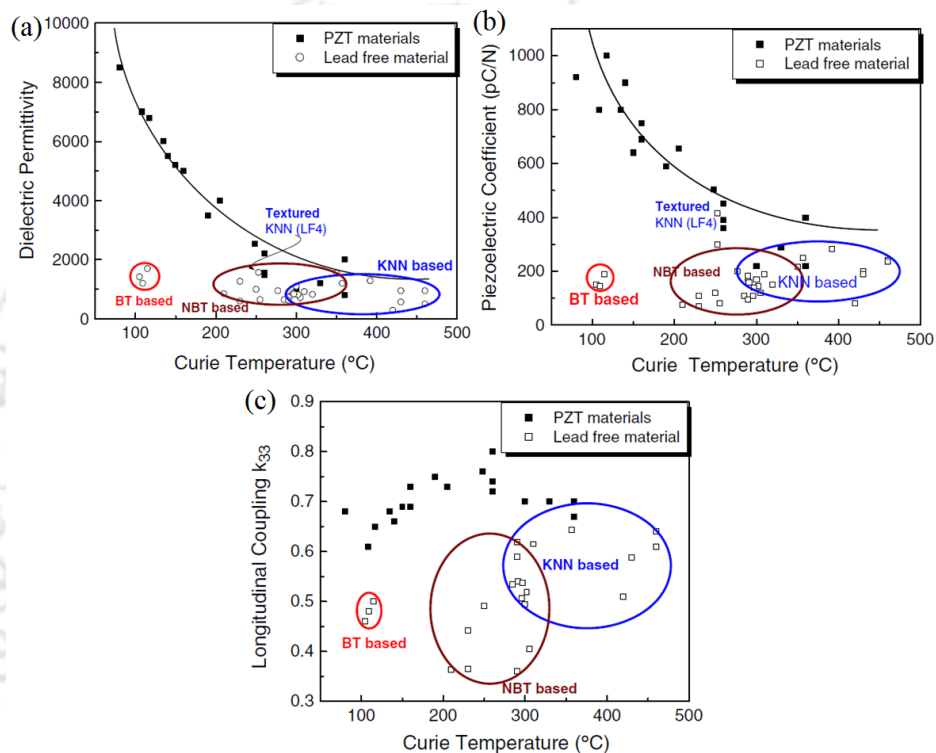


Figure 1.12: (a) ϵ_r (b) d_{33} , and (c) k_{33} as a function of Curie temperature of different piezoelectric ceramics, measured at room temperature [44].

1.4.1 Barium titanate (BaTiO₃)

The discovery of barium titanate BaTiO₃ (BT) was a milestone of piezoelectric materials development. It has a perovskite structure (ABO₃) like PT. In this structure, Ba²⁺ ions occupy the corners of the cube (A-site), oxygen ions (O²⁻) possess the face-centered positions, and Ti⁴⁺ sits the body center position (B-site). $T > T_c$, it has cubic symmetry whereas the centers of the positive and negative charges are coincident, i.e.,

zero dipole moment. When $T < T_c$, a relative shift between the Ba^{2+}/Ti^{4+} ions and the O^{2-} octahedra, destroying the cubic symmetry, i.e., spontaneous polarization. The relative shift produces different phases (non-cubic) such as orthorhombic, rhombohedral and tetragonal. Here, temperature and ionic size are the driving forces to determine the phase [11,40]. Figure 1.13 shows the Dielectric constant as a function of temperature for single crystal $BaTiO_3$ [53]. It is utilized in many applications due to its superior dielectric ($\epsilon_r = 1500-1600$ @ 1kHz), ferroelectric and piezoelectric properties ($d_{33} = 190$ pC/N). However, it is limited for high-temperature piezoelectric applications (actuators) due to low Curie temperature ($120^\circ C$).

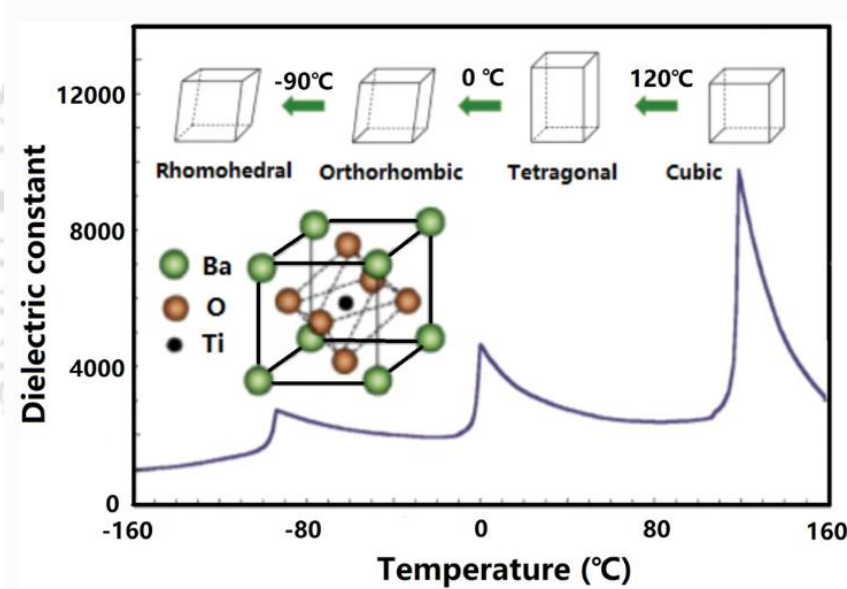


Figure 1.13: Dielectric constant as a function of temperature for single crystal $BaTiO_3$ [57].

1.4.2 Sodium potassium niobate ($K_{0.5}Na_{0.5}NbO_3$)

The sodium-potassium niobate $K_{0.5}Na_{0.5}NbO_3$ (KNN) is also a similar structure of BT (ABO_3) but exhibits high T_c . It is a solid solution of ferroelectric KN and anti-ferroelectric $NaNbO_3$ (NN) and is orthorhombic crystal symmetry at RT [58]. The KNN exhibits an MPB with K/Na ratio of 50/50, resulting enhanced dielectric ($\epsilon_r \sim 200-500$),

ferroelectric ($P_r = 9 \mu\text{C}/\text{cm}^2$) and piezoelectric properties ($d_{33} = 70\text{-}110 \text{ pC}/\text{N}$, and $k_{33} = 0.2\text{-}0.5$) near MPB [58–60]. In addition, KNN exhibits three structural phase transitions, such as (i) rhombohedral to orthorhombic at $-80 \text{ }^\circ\text{C}$ (T_{R-O}), (ii) orthorhombic to tetragonal at $200 \text{ }^\circ\text{C}$ (T_{O-T}) and (iii) tetragonal to cubic phases at $400 \text{ }^\circ\text{C}$ (T_C). However, the main drawback of KNN is very difficult to prepare a densified sample due to the volatilization of K and Na during sintering temperature which leads to the deterioration in the properties [61].

1.4.3 Bismuth sodium titanate ($\text{Bi}_{0.5}\text{Na}_{0.5}\text{TiO}_3$)

The $\text{Bi}_{0.5}\text{Na}_{0.5}\text{TiO}_3$ (BNT) is also a perovskite ferroelectric, and it was first discovered by Smolenskii et al. [62] in 1960. However, it did not attract much attention until the rapid increase in the development of lead-free ceramics over the past 20 years because of its inferior piezoelectric response as compared to the Pb or PZT ceramics. The Pb-based ceramics exhibit the best piezoelectric response based on the concept of stereochemical activity of $6s^2$ lone pair electrons on the Pb^{+2} , which are the origin of large structural distortions that promotes a strong coupling between the electronic and structural degrees of freedom [63,64]. Bismuth-based ceramics are also similar to the Pb-based ceramics, where the stereochemically active $6s^2$ lone pair is associated with Bi^{3+} , which are the driving forces, promote large ferroelectricity. BNT is considered to be one of the good candidates for lead-free piezoelectric materials due to its strong ferroelectric response (remnant polarization (P_r) = $38 \mu\text{C}/\text{cm}^2$) at room temperature (RT), high transition temperature (T_C) and good dielectric properties ($\epsilon_r = 692$ and $\tan\delta = 0.045$ at 1 kHz) [30,65]. However, the BNT ceramics possess few drawbacks like (i) inferior piezoelectric properties (ii) difficult to pole electrically due to its high coercive field ($E_c = 73 \text{ kV}/\text{cm}$) and (iii) high electrical conductivity, which makes the BNT ceramics limited for the practical applications. Also, it is challenging to densify BNT due to the volatile

nature of Na and Bi during the sintering process, which causes deterioration in the piezoelectric properties. Moreover, it exhibits two phase transitions (i) paraelectric to ferroelectric around 320°C (T_C) and (ii) depolarization temperature \sim 200°C (T_d). These transitions are also associated with the structural deformation of BNT i.e., from tetragonal to cubic (T_C) and rhombohedral to tetragonal phase (T_d), respectively [30,66]. Therefore, considerable efforts have been made with the addition of dopants in A and/or B-site of BNT system or other composite solid solutions (ABO_3) to enhance the dielectric, ferroelectric, and piezoelectric properties [67–73]. The suitable dopants such as isovalent, donor, and acceptor can modify the transition temperature, dielectric constant, ferroelectric, and piezoelectric properties of BNT and its crystal structure. Table 1 shows a variety of dopants and compositions of BNT based ceramics, and their properties have been reported in the literature. Among the lead-free ceramics, BNT is one of the best ferroelectric material with special properties that drives the research work of the present thesis is presented.

Table 1: Literature survey of BNT based ceramics.

Systems	T_C (°C)	T_d (°C)	ϵ_r	$\tan\delta$	P_r ($\mu C/cm^2$)	E_c (kV/cm)	d_{33} (pC/N)	k_{33}/k_p	Ref.
BNT	340	200	700	0.044	38	73	92	0.47	[74,75]
BNT	310	-	302	0.017	-	-	64	-	[76]
BNT	325	-	343	-	-	-	72.9	0.16	[77]
$Bi_{0.5}(Na_{0.7}K_{0.25}Li_{0.05})_{0.5}TiO_3$	-	-	1276	0.041	-	-	145	-	[78]
$(Bi_{1-x-y}Nd_xNa_{1-y})_{0.5}Ba_yTiO_3$; x/y =0.02/0.06	-	-	-	-	-	-	150	0.30	[79]

0.94(Bi_{0.5}Na_{0.5})Ba_{0.06}TiO₃ + x wt% CeO₂; (0-1)	-	-	891	0.018	-	-	128	0.28	[80]
(Na_{1-x}Li_x)_{0.5}Bi_{0.5}TiO₃; (BNLT; 0≤x≤0.20)	365	-	480	0.036	-	-	95	0.18	[81]
(Bi_{1/2}Na_{1/2})_{1-x}Ba_xTiO₃	288	105	826	0.25	40	34	155	0.36	[82]
Er₂O₃ doped 0.82Bi_{0.5}Na_{0.5}TiO₃- 0.18Bi_{0.5}K_{0.5}TiO₃; 0-0.8 wt%	-	-	936	-	-	-	138	0.23	[83]
0.2Bi_{0.5}Na_{0.5}TiO₃- (0.8- x)BaTiO₃-xBaZrO₃ +0.3 wt% Li₂CO₃; (0≤x≤0.08)	150	-	661	-	18.5	34.1	72	0.15	[84]
[(Bi_{1/2}Na_{1/2})_{0.95}Ba_{0.05}]_{1-x} La_xTiO₃; x = 0.02	~275	~40	ε _r > 2000	-	39	45	151	-	[85]
BNT-BKT	280	130	945	0.02	38	40	190	0.56	[86]
BNT-BKT-BT	290	125	700	0.02	40	29	148	0.49	[87]
BNT-BKT-KNN	-	125	-	-	41	46	60	-	[88]
(1-x)(Bi_{1/2}Na_{1/2})TiO₃-x Bi(Mg_{2/3}Nb_{1/3})O, x=0.07/0.2	370	200	1350	-	-	-	94	0.46	[89]
1-x) BNT-x) NaNbO₃ x = 0.2	~150	-	~16 00	-	-	-	88	0.15	[90,91]
(1-x)(Bi_{0.5}Na_{0.5})TiO₃- xKNbO₃, x=0.05	~260	75	~19 00	~0.04	32	32	132	0.20	[92]
(1-x) Bi_{0.5}Na_{0.5}TiO₃- xK_{0.47}Na_{0.47}Li_{0.06} Nb_{0.74}Sb_{0.06}Ta_{0.2}O₃, x=0.03	340	180	3900	-	40	42	169	0.49	[93]

1.4.4 BNT thin films

BNT has been explored extensively in the bulk form due to its excellent dielectric, ferroelectric and piezoelectric properties, which have received much attention in fabrication of thin-film for the sensors, non-volatile memories, actuators, optical coatings, electro-optic devices, high frequency tunable and energy harvesting devices due to their outstanding dielectric, ferroelectric and piezoelectric performance [94–97]. So far, BNT thin films have been deposited using various deposition techniques, such as RF magnetron sputtering [98], sol-gel process (SG) [96,99], chemical solution deposition (CSD) [100], and pulsed laser deposition (PLD) [101,102]. Among these, the PLD technique is a highly versatile technique widely used for fabricating thin films and multilayer structures. It is an exquisite technique for high-quality oxide film of good stoichiometry, control of the film composition and chemical homogeneity, porosity control, better crystallinity, excellent adhesion, low cost, etc. [103]. However, to deposit the single/pure phase of BNT thin film by maintaining its stoichiometry, and better crystallinity in the film is a challenging task due to the volatile nature of the elements in the present composition. Therefore, the unique advantages of PLD motivated us to deposit pure phase BNT thin films with an excess of Bi and Na to compensate for their loss during sintering as well as in the deposition process. Table 2 summarises a review of the properties of BNT based thin films from literature.

Table 2: Literature survey of BNT based thin films.

Systems	ϵ_r	$\tan\delta$	P_r ($\mu\text{C}/\text{cm}^2$)	E_c (kV/cm)	d_{33} (pm/V)	k_{33}/k_p	Ref.
BNT (RFMS)	520	0.032	12	125	80	-	[104]
BNT(Sg)	420	0.07	12	120	-	-	[105]
BNT	754	0.21	20	160	-	-	[101]

Bi_{0.5}(Na_{0.85}K_{0.15})_{0.5}TiO₃	-	-	-	-	63.6	-	[106]
Bi_{0.5}(Na_{0.80}K_{0.20})_{0.5}TiO₃ (CSD)	-	-	9.2	-	-	-	[107]
Na_{0.5}Bi_{0.5}(Ti_{0.98}Zr_{0.02})O₃	263	0.067	12.3	-	-	-	[108]
K_{0.5}Bi_{0.5}TiO₃	57	0.08					[109]
Na_{0.5}Bi_{0.5}Ti_{0.98}Mn_{0.02}O₃	-	-	38	200	-	-	[110]
BNT - 0.11 BT (SG)	164	0.095	1.06	53.39	29	-	[111]
0.85Bi_{0.5}Na_{0.5}TiO₃ - 0.15Bi_{0.5}K_{0.5}TiO₃ (CSD)	510	0.003	34	~100	75	-	[112]
0.96 (0.8Bi_{0.5}Na_{0.5}Ti_{0.5}O₃- 0.2Bi_{0.5}K_{0.5}TiO₃)-0.04 BiZn_{0.5}Ti_{0.5}O₃	560	-	10	-	40	-	[113]
0.88(Bi_{0.5}Na_{0.5})TiO₃- 0.08(Bi_{0.5}K_{0.5})TiO₃- 0.04BaTiO₃	645	-	30	85	-	-	[114]

The electrical properties of BNT thin films were extensively reported (at low frequency, ≤ 1 MHz), unlike optical properties in the diverse form, which are rather scarce. These properties of BNT thin films are essential not only for theoretical studies of phase transition mechanisms and nature of electronic transitions but also for potential applications in optoelectronic devices. In addition, BNT thin films display better nonlinear optical responses make these films suitable for nonlinear photonic and electro-optical device applications. However, there are no reports available for the third-order nonlinear optical and microwave dielectric study of BNT thin films for high-frequency tunable devices. In the present thesis, the structural and physical properties will be investigated for the best composition in bulk form. Further, the BNT, along with the best composition, was chosen to deposit the thin films. In ferroelectric oxide ceramics, oxygen

deficiency can play a crucial role in tailoring the properties of the films. Therefore, it is necessitated fabricating the BNT thin films in an oxygen atmosphere. The effect of oxygen partial pressure on the linear, nonlinear, and microwave dielectric and nonlinear optical properties pure BNT and its best composition of thin films will be identified and investigated in detail.

1.5 Objective of the present work

The challenges associated with the lead-free piezoelectric materials to replace lead-based materials, the approaches to improve and understand the dielectric, ferroelectric and piezoelectric response of lead-free BNT ceramics and developing new BNT-based piezoelectric ceramics for high performance and high T_C of piezoelectric applications will be investigated in this thesis work.

The objectives of the present work are as follows:

- Synthesis of pure BNT ceramics by conventional solid-state reaction (CSSR) method and optimization of calcination and sintering temperatures to obtain superior electric properties will be explored.
- The effect of donor (CeO_2 and Gd_2O_3) substitutions on the dielectric and AC-conductivity behavior of BNT ceramics will be investigated.
- The formation of a morphotropic phase boundary (MPB) with the addition of a suitable substitution can improve the dielectric and piezoelectric properties. Thus, the alkaline K will be studied to enhance the piezoelectric properties at MPB and to understand AC-conductivity response in the BNT ceramics in detail.
- Similarly, the BNT-KNN based composite ceramics will be studied to enhance piezoelectric performance and to study AC-conductivity behavior.

- To study the effect of oxygen partial pressure on optical, dielectric, and microwave dielectric properties of BNT thin films will be deposited by PLD.
- The best optimized BNT-KNN based composite will be explored to deposit thin films using a PLD technique for microwave tunable and nonlinear optical device applications.



1.6 References

- [1] S. Takagi, A. Subedi, V. R. Cooper, and D. J. Singh, *Phys. Rev. B - Condens. Matter Mater. Phys.* **82**, 19 (2010).
- [2] J. F. Scott, *Science (80-.)*. **315**, 954 (2007).
- [3] S. T. Lau, C. H. Cheng, S. H. Choy, D. M. Lin, K. W. Kwok, and H. L. W. Chan, *J. Appl. Phys.* **103**, 14 (2008).
- [4] S. G. Kim, S. Priya, and I. Kanno, *MRS Bull.* **37**, 1039 (2012).
- [5] L. Luo, B. Wang, X. Jiang, and W. Li, *J. Mater. Sci.* **49**, 1659 (2014).
- [6] Z. Kutnjak, R. Blinc, and Y. Ishibashi, *Phys. Rev. B - Condens. Matter Mater. Phys.* **76**, 104102 (2007).
- [7] Y. Saito, H. Takao, T. Tani, T. Nonoyama, K. Takatori, T. Homma, T. Nagaya, and M. Nakamura, *Nature* **432**, 84 (2004).
- [8] F. Li, D. Lin, Z. Chen, Z. Cheng, J. Wang, C. Li, Z. Xu, Q. Huang, X. Liao, L. Q. Chen, T. R. Shrout, and S. Zhang, *Nat. Mater.* **17**, 349 (2018).
- [9] Q. Wang, C. R. Bowen, W. Lei, H. Zhang, B. Xie, S. Qiu, M. Y. Li, and S. Jiang, *J. Mater. Chem. A* **6**, 5040 (2018).
- [10] G. gui Peng, D. yi Zheng, C. Cheng, J. Zhang, and H. Zhang, *J. Alloys Compd.* **693**, 1250 (2017).
- [11] J. Rödel, W. Jo, K. T. P. Seifert, E. M. Anton, T. Granzow, and D. Damjanovic, *J. Am. Ceram. Soc.* **92**, 1153 (2009).
- [12] P. Muralt, *J. Micromechanics Microengineering* **10**, 136 (2000).
- [13] N. Setter, D. Damjanovic, L. Eng, G. Fox, S. Gevorgian, S. Hong, A. Kingon, H.

- Kohlstedt, N. Y. Park, G. B. Stephenson, I. Stolitchnov, A. K. TagansteV, D. V Taylor, T. Yamada, and S. Streiffer, *J. Appl. Phys.* **100**, 51606 (2006).
- [14] G. H. Haertling, *J. Vac. Sci. Technol. A* **9**, 414 (1991).
- [15] Y. H. Wang, B. Gu, G. D. Xu, and Y. Y. Zhu, *Appl. Phys. Lett.* **84**, 1686 (2004).
- [16] A. J. Moulson and J. M. Herbert, *Electroceramics: Materials, Properties, Applications* (Wiley, 2003).
- [17] W. R. C. and J. M. H. B. Jafe, *Piezoelectric Ceramics* (Academic Press London and New York, 1971).
- [18] G. H. Haertling, *J. Am. Ceram. Soc.* **82**, 797 (1999).
- [19] J. Fialka and P. Beneš, *IEEE Trans. Instrum. Meas.* **62**, 1047 (2013).
- [20] C. B. Carter and M. G. Norton, *Ceramic Materials: Science and Engineering* (Springer, New York, 2007).
- [21] G. Arlt, *J. Mater. Sci.* **25**, 2655 (1990).
- [22] H. Ehrenreich and F. Spaepen, *Solid State Physics Advances in Research and Applications* (Academic Press, San Diego, 2001).
- [23] P. Chandra and P. B. Littlewood, *In A Landau Primer for Ferroelectrics: Physics of Ferroelectrics: A Modern Perspective*, Rabe K., Ahn CH, and Triscone J.-M., Eds (Springer-Verlag, Berlin, 2007).
- [24] Y. Moritomo, A. Asamitsu, H. Kuwahara, and Y. Tokura, *Nature* **380**, 141 (1996).
- [25] H. Fu and R. E. Cohen, *Nature* **403**, 281 (2000).
- [26] G. Sághi-Szabó, R. E. Cohen, and H. Krakauer, *Phys. Rev. Lett.* **80**, 4321 (1998).
- [27] S. Kanno, Y. Imamura, and M. Hada, *Phys. Rev. Mater.* **3**, 75403 (2019).

- [28] J. P. Attfield, P. Lightfoot, and R. E. Morris, *Dalt. Trans.* **44**, 10541 (2015).
- [29] V. M. Goldschmidt, *Naturwissenschaften* **14**, 477 (1926).
- [30] K. N. N. Smolenskii G.A., Isupov V.A., Agranovskaya A.I., *Sov. Phys. Solid State* **2**, 2651 (1961).
- [31] R. A. Cowley, S. N. Gvasaliya, S. G. Lushnikov, B. Roessli, and G. M. Rotaru, *Adv. Phys.* **60**, 229 (2011).
- [32] Z. Raddaoui, S. El Kossi, J. Dhahri, N. Abdelmoula, and K. Taibi, *RSC Adv.* **9**, 2412 (2019).
- [33] L. E. Cross, *Ferroelectrics* **151**, 305 (1994).
- [34] A. A. Bokov and Z.-G. Ye, *J. Mater. Sci.* **41**, 31 (2006).
- [35] L. E. Cross, *Ferroelectrics* **76**, 241 (1987).
- [36] D. Viehland, S. J. Jang, L. E. Cross, and M. Wuttig, *J. Appl. Phys.* **68**, 2916 (1990).
- [37] D. Viehland, M. Wuttig, and L. E. Cross, *Ferroelectrics* **120**, 71 (1991).
- [38] V. Westphal, W. Kleemann, and M. D. Glinchuk, *Phys. Rev. Lett.* **68**, 847 (1992).
- [39] M. D. Glinchuk and R. Farhi, *J. Phys. Condens. Matter* **8**, 6985 (1996).
- [40] B. Jaffe, R. S. Roth, and S. Marzullo, *J. Appl. Phys.* **25**, 809 (1954).
- [41] K. Uchino, *Piezoelectric Actuators and Ultrasonic Motors* ((edited: Tuller H. L.), Kluwer Academic Publishers, USA, 1997).
- [42] P. K. Panda, *J. Mater. Sci.* **44**, 5049 (2009).
- [43] B. Noheda, D. E. Cox, G. Shirane, J. A. Gonzalo, L. E. Cross, and S.-E. Park, *Appl. Phys. Lett.* **74**, 2059 (1999).

- [44] T. R. ShROUT and S. J. Zhang, *J. Electroceramics* **19**, 113 (2007).
- [45] C. A. Randall, N. Kim, J.-P. Kucera, W. Cao, and T. R. ShROUT, *J. Am. Ceram. Soc.* **81**, 677 (1998).
- [46] S.-E. Park and T. R. ShROUT, *J. Appl. Phys.* **82**, 1804 (1997).
- [47] H. Fan and H.-E. Kim, *J. Appl. Phys.* **91**, 317 (2002).
- [48] P. Rakbamrung, M. Lallart, D. Guyomar, N. Muensit, C. Thanachayanont, C. Lucat, B. Guiffard, L. Petit, and P. Sukwisut, *Sensors Actuators A Phys.* **163**, 493 (2010).
- [49] S. E. Moon, S.-K. Lee, Y.-G. Lee, K. M. Kim, Y.-S. Yang, W. S. Yang, and J. Kim, *J. Korean Phys. Soc.* **60**, 230 (2012).
- [50] K. Ramam, M. Lopez, and K. Chandramouli, *Philos. Mag. Lett.* **88**, 429 (2008).
- [51] P. K. Panda and B. Sahoo, *Ferroelectrics* **474**, 128 (2015).
- [52] S.-Y. Chu, T.-Y. Chen, I.-T. Tsai, and W. Water, *Sensors Actuators A Phys.* **113**, 198 (2004).
- [53] A. Garg and D. C. Agrawal, *Mater. Sci. Eng. B* **86**, 134 (2001).
- [54] J. F. Fernández, C. Moure, M. Villegas, P. Durán, M. Kosec, and G. Drazic, *J. Eur. Ceram. Soc.* **18**, 1695 (1998).
- [55] M. I. Morozov and D. Damjanovic, *J. Appl. Phys.* **104**, 34107 (2008).
- [56] L. A. Schmitt, H. Kungl, M. Hinterstein, L. Riekehr, H. J. Kleebe, M. J. Hoffmann, R. A. Eichel, and H. Fuess, *J. Am. Ceram. Soc.* **98**, 269 (2015).
- [57] J. Su and J. Zhang, *J. Mater. Sci. Mater. Electron.* **30**, 1957 (2019).
- [58] L. Liang, Y. L. Li, L.-Q. Chen, S. Y. Hu, and G.-H. Lu, *J. Appl. Phys.* **106**, 104118

- (2009).
- [59] R. E. JAEGER and L. EGERTON, *J. Am. Ceram. Soc.* **45**, 209 (1962).
- [60] G. H. HAERTLING, *J. Am. Ceram. Soc.* **50**, 329 (1967).
- [61] M. D. Maeder, D. Damjanovic, and N. Setter, *J. Electroceramics* **13**, 385 (2004).
- [62] G. A. Smolenskii, V. A. Isupov, A. I. Agranovskaya, and N. N. Krainik, *Fiz. Tverd. Tela Sanktpeterbg.* **2**, 2982 (1960).
- [63] N. A. Hill and K. M. Rabe, *Phys. Rev. B* **59**, 8759 (1999).
- [64] P. Baettig, C. F. Schelle, R. LeSar, U. V. Waghmare, and N. A. Spaldin, *Chem. Mater.* **17**, 1376 (2005).
- [65] J. Rödel, K. G. Webber, R. Dittmer, W. Jo, M. Kimura, and D. Damjanovic, *J. Eur. Ceram. Soc.* **35**, 1659 (2015).
- [66] E. Aksel, J. S. Forrester, B. Kowalski, M. Deluca, D. Damjanovic, and J. L. Jones, *Phys. Rev. B - Condens. Matter Mater. Phys.* **85**, 21 (2012).
- [67] P. Y. Chen, C. C. Chou, T. Y. Tseng, and H. Chen, *Jpn. J. Appl. Phys.* **49**, 0615061 (2010).
- [68] N. D. Quan, V. N. Hung, N. Van Quyet, H. V. Chung, and D. D. Dung, *AIP Adv.* **4**, 17122 (2014).
- [69] A. M. Balakt, C. P. Shaw, and Q. Zhang, *J. Alloys Compd.* **709**, 82 (2017).
- [70] V. Chauhan, S. K. Ghosh, A. Hussain, and S. K. Rout, *J. Alloys Compd.* **674**, 413 (2016).
- [71] F. Han, J. Deng, X. Liu, T. Yan, S. Ren, X. Ma, S. Liu, B. Peng, and L. Liu, *Ceram. Int.* **43**, 5564 (2017).

- [72] J. Yin, X. Lv, and J. Wu, *Ceram. Int.* **43**, 13541 (2017).
- [73] A. Hussain, C. W. Ahn, J. S. Lee, A. Ullah, and I. W. Kim, *Sensors Actuators, A Phys.* **158**, 84 (2010).
- [74] Y. Hiruma, Y. Watanabe, H. Nagata, and T. Takenaka, in *Electroceramics Japan X* (Trans Tech Publications Ltd, 2007), pp. 93–96.
- [75] J. Suchanicz, K. Roleder, A. Kania, and J. Hańderek, *Ferroelectrics* **77**, 107 (1988).
- [76] J. Yoo, D. Oh, Y. Jeong, J. Hong, and M. Jung, *Mater. Lett.* **58**, 3831 (2004).
- [77] Y. Hiruma, H. Nagata, and T. Takenaka, *J. Appl. Phys.* **105**, 84112 (2009).
- [78] J. Yoo, J. Hong, H. Lee, Y. Jeong, B. Lee, H. Song, and J. Kwon, *Sensors Actuators A Phys.* **126**, 41 (2006).
- [79] D. Lin and K. W. Kwok, *Curr. Appl. Phys.* **10**, 422 (2010).
- [80] J. Shi and W. Yang, *J. Alloys Compd.* **472**, 267 (2009).
- [81] W. Lu, Y. Wang, G. Fan, X. Wang, and F. Liang, *J. Alloys Compd.* **509**, 2738 (2011).
- [82] T. Takenaka, K. Maruyama, and K. Sakata, *Jpn. J. Appl. Phys.* **30**, 2236 (1991).
- [83] P. Fu, Z. Xu, H. Zhang, R. Chu, W. Li, and M. Zhao, *Mater. Des.* **40**, 373 (2012).
- [84] F. Zhou, L. Wu, N. Liu, Y. Teng, Y. Li, J. Wen, and X. Ren, *J. Alloys Compd.* **512**, 52 (2012).
- [85] X. Liu, H. Guo, and X. Tan, *J. Eur. Ceram. Soc.* **34**, 2997 (2014).
- [86] K. Yoshii, Y. Hiruma, H. Nagata, and T. Takenaka, *Jpn. J. Appl. Phys.* **45**, 4493 (2006).

- [87] X. X. Wang, X. G. Tang, and H. L. W. Chan, *Appl. Phys. Lett.* **85**, 91 (2004).
- [88] Z. Yao, H. Liu, L. Chen, and M. Cao, *Mater. Lett.* **63**, 547 (2009).
- [89] C. Zhou and X. Liu, *J. Mater. Sci.* **43**, 1016 (2008).
- [90] H. Qi and R. Zuo, *J. Mater. Chem. A* **7**, 3971 (2019).
- [91] T. Wada, K. Toyoiike, Y. Imanaka, and Y. Matsuo, *Jpn. J. Appl. Phys.* **40**, 5703 (2001).
- [92] X. Jiang, B. Wang, L. Luo, W. Li, J. Zhou, and H. Chen, *J. Solid State Chem.* **213**, 72 (2014).
- [93] A. Singh and R. Chatterjee, *J. Am. Ceram. Soc.* **96**, 509 (2013).
- [94] E. Aksel, J. S. Forrester, J. C. Nino, K. Page, D. P. Shoemaker, and J. L. Jones, *Phys. Rev. B - Condens. Matter Mater. Phys.* **87**, 1 (2013).
- [95] M. Peddigari, H. Palneedi, G. T. Hwang, and J. Ryu, *J. Korean Ceram. Soc.* **56**, 1 (2019).
- [96] T. Yu, K. W. Kwok, and H. L. W. Chan, *Thin Solid Films* **515**, 3563 (2007).
- [97] Y. Kitanaka, H. Matsuo, Y. Noguchi, and M. Miyayama, *J. Asian Ceram. Soc.* **3**, 160 (2015).
- [98] Z. H. Zhou, J. M. Xue, W. Z. Li, J. Wang, H. Zhu, and J. M. Miao, *Appl. Phys. Lett.* **85**, 804 (2004).
- [99] X.-G. Tang, J. Wang, X.-X. Wang, and H. L.-W. Chan, *Chem. Mater.* **16**, 5293 (2004).
- [100] Z. Cao, A. L. Ding, X. He, W. Cheng, and P. Qiu, *J. Cryst. Growth* **270**, 168 (2004).

- [101] A. S. Daryapurkar, J. T. Kolte, and P. Gopalan, *Thin Solid Films* **579**, 44 (2015).
- [102] J.-R. Duclère, C. Cibert, A. Boulle, V. Dorcet, P. Marchet, C. Champeaux, A. Catherinot, S. Députier, and M. Guilloux-Viry, *Thin Solid Films* **517**, 592 (2008).
- [103] D. H. Lowndes, D. B. Geohegan, A. A. Poretzky, D. P. Norton, and C. M. Rouleau, *Science (80-.)*. **273**, 898 (1996).
- [104] S. Quignon, C. Soyer, and D. Remiens, *J. Am. Ceram. Soc.* **95**, 3180 (2012).
- [105] S. A. Dargham, F. Ponchel, Y. Zaatar, J. Assaad, D. Remiens, and D. Zaouk, *Mater. Today Proc.* **3**, 810 (2016).
- [106] S. S. Won, C. W. Ahn, and I. W. Kim, *J. Korean Phys. Soc.* **61**, 928 (2012).
- [107] N. D. Co, L. V. Cuong, B. D. Tu, P. D. Thang, L. X. Dien, V. N. Hung, and N. D. Quan, *J. Sci. Adv. Mater. Devices* (2019).
- [108] H. Sui, C. Yang, F. Geng, and C. Feng, *Mater. Lett.* **139**, 284 (2015).
- [109] C. H. Yang, Z. Wang, H. Y. Xu, Z. H. Sun, F. Y. Jiang, and J. P. Z. J. R. Han, *J. Cryst. Growth* **262**, 304 (2004).
- [110] C. Feng, C. H. Yang, S. X. Li, Y. J. Han, X. Q. Hu, F. Y. Jiao, J. Qian, and X. B. Du, *Ceram. Int.* **41**, 14179 (2015).
- [111] M. Cernea, A. C. Galca, M. C. Cioangher, C. Dragoi, and G. Ioncea, *J. Mater. Sci.* **46**, 5621 (2011).
- [112] C. W. Ahn, S. S. Won, A. Ullah, S. Y. Lee, S. D. Lee, J. H. Lee, W. Jo, and I. W. Kim, *Curr. Appl. Phys.* **12**, 903 (2012).
- [113] W. Li, H. Zeng, K. Zhao, J. Hao, and J. Zhai, *Ceram. Int.* **40**, 7947 (2014).
- [114] M. Hejazi, B. Jadidian, and A. Safari, *IEEE Trans. Ultrason. Ferroelectr. Freq.*

Control **59**, 1855 (2012).



Synthesis and characterization techniques

The present chapter describes the synthesis methods of investigated samples and various experimental measurement techniques that are implemented in this thesis work to characterize the bulk ceramics and their thin films. First, the synthesis methods, sintering mechanism was used to prepare pure BNT ceramics and various characterization techniques were implemented to study the structural, microstructural, dielectric, ferroelectric and piezoelectric properties. Later, the pulsed laser deposition technique was used to fabricate BNT based thin film and various characterization techniques are used to study the structural, microstructural, optical and electrical properties of thin films that are presented in this chapter.

2.1 Synthesis of bulk BNT ceramics

Several methods have been developed for the synthesis of polycrystalline samples with good purity, homogeneity and finer particle size, such as conventional solid-state reaction (CSSR) method, sol-gel method, co-precipitation method, and wet (semi-wet) chemical method, etc. In this thesis, we have employed a conventional solid-state reaction method for the synthesis of BNT based ceramics.

2.1.1 Conventional solid-state reaction method

The CSSR method is the most versatile technique and widely used for the synthesis of polycrystalline samples. The main advantage of the CSSR provides a wide range of selection starting materials (like oxides, carbonates, etc.), thermodynamically

stable, environment-friendly, cost-effectiveness, the reaction takes place without any solvents, the structurally pure final product and simplicity. In this method, two main steps are involved that are the uniform mixing of starting materials for better homogenization and heat treatment process at high temperatures for phase formation. The starting materials do not react with each other at room temperature, sufficient temperature with proper heating and cooling rates are required for the phase formation and densification. Various steps were involved in this method which is explained in the following sections. The flowchart of the various steps of the synthesis procedure by CSSR is shown in Figure 2.1.

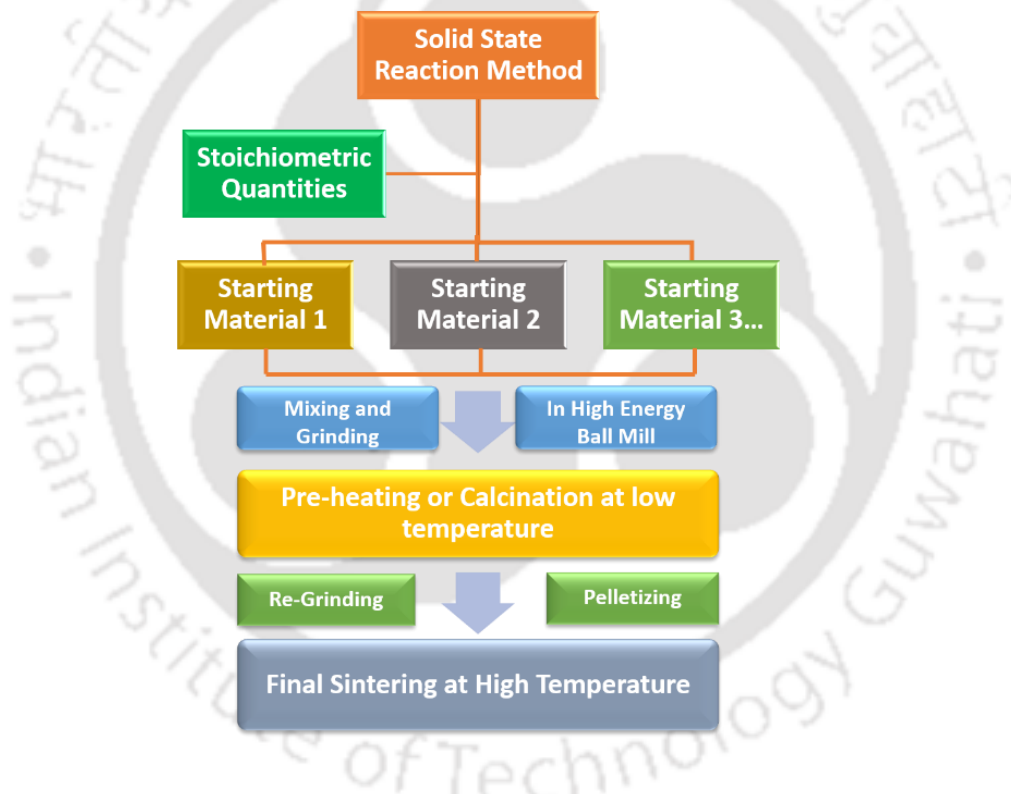
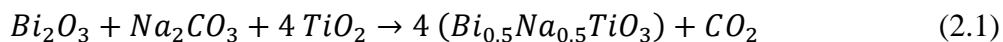


Figure 2.1: Flowchart of the various steps of the synthesis procedure in a conventional solid-state reaction.

2.1.2 Stoichiometric weighing of starting materials

The high purity of starting materials (> 99.99%) is very important to get the desired phase. The starting materials of $\text{Bi}_{0.5}\text{Na}_{0.5}\text{TiO}_3$ ceramics are weighed (AG135,

Mettler Toldo), accuracy ~0.01 mg) as per the stoichiometric ratio using the following equation.



2.1.3 Uniform mixing of starting materials

The weighed powders were uniformly mixed using a planetary ball mill (Pulverisette 6, Fritsch GmbH, Germany) in a zirconium jar with zirconia balls of 5 mm diameter, where distilled water used as milling media. The powders were milled at a speed of 120 rotations per minute for 5h. Figure 2.2 shows photograph of the planetary ball mill was used in the present study.



Figure 2.2: Photograph of the planetary ball mill.

2.1.4 Calcination

To obtain the desired phase formation, the samples must be heated to an appropriate temperature, called the calcination temperature. Calcination is a thermal treatment of mixed starting materials at lower temperatures prior to the sintering. The calcination process produces a new solid phase and eliminates unwanted reagents like carbonates, and nitrides, sulfates, etc. In this process, the calcination temperature, duration

and atmospheres are important parameters that play a key role in the phase formation of the ceramics. Generally, the phase formation temperature of the sample is confirmed from differential scanning calorimetry and thermogravimetric analysis. The phase purity of the calcined powder sample can be identified from the X-ray diffraction pattern.

2.1.5 Particle size reduction

The surface to a volume ratio is higher for smaller size particles as compared to the larger particles, where the smaller size particles possess high chemical reactivity. As the initial particle sizes decrease, the sintering temperature reduces and improves the density of the samples. Therefore, it is important to decrease the particle size after the calcination process. In this study, we have employed the planetary ball mill twice; the first time is for the uniform mixing of the initial reagents and the second time is for the particle size reduction. All the processing parameters (milling time, rotations per minute, ratio of balls with respect to powders) are optimized to obtain smaller particle sizes without any secondary phase formation.

2.1.6 Pelletization

After the process of ball milling, the slurry was dried at 120 °C for 24 h to obtain the fine powders. The organic binder polyvinyl alcohol was added to the fine powders and pressed into cylindrical shaped discs of 10 mm in diameter and 1 mm in thickness using KBr hydraulic press (M-20, Technosearch Instruments, India). The applied pressure on the upper part of the die is given by the following equation,

$$P_x = P_a \exp \frac{-4\mu KL}{D} \quad (2.2)$$

where P_x is the pressure gradient; P_a is the applied pressure, μ is the friction coefficient, K is a constant, L and D are the length and diameters of the die, respectively [1]. In this study, the pressure was applied in uniaxial pressing to prepare the green cylindrical discs.

2.1.7 Sintering

Sintering is the process of compacting and forming a solid mass of material by heat and/or pressure without melting the material. The main purpose of sintering is densifying the ceramics and reducing porosity. Density and porosity are very important parameters, which can directly impact the dielectric, ferroelectric and piezoelectric properties of the samples. Hence, it is important to optimize the sintering temperature to achieve maximum density and minimum porosity in the material. In this thesis, the calcination and sintering temperature of prepared samples are optimized by using conventional furnace (LHT 04/18, Nabertherm GmbH, Germany; Temperature range: 25°C-1800°C). Figure 2.3 shows a photograph of the conventional furnace that was used in the present study.



Figure 2.3: Photograph of the conventional furnace.

Basically, the sintering process can be categorized into two types: (a) solid-state sintering and (b) liquid phase sintering. In solid-state sintering, the densification occurs by changing in the particle shape without any rearrangement, while some dopants are added to the material to form a liquid phase during the sintering process which enhances densification in the liquid phase sintering. In this study, we have employed the solid-state sintering process for all the prepared samples. The sintering process of the samples can be completed in three stages: (a) initial, (b) intermediate and (c) final stage as shown in Figure 2.4 [2]. In the first stage, surface smoothing of grains (or particles), neck growth and rounding of interconnected pores take place. The relative density of the green discs reaches around 60-65% at the end of the first stage. The grain growth and rapid densification occur in an intermediate stage. A number of transport and diffusion mechanisms such as surface diffusion, lattice diffusion, grain boundary diffusion are involved in this stage, which leads to the densification by neck growth between the particles. The relative density increases from 65% to 90% of theoretical density at the end of the intermediate stage.

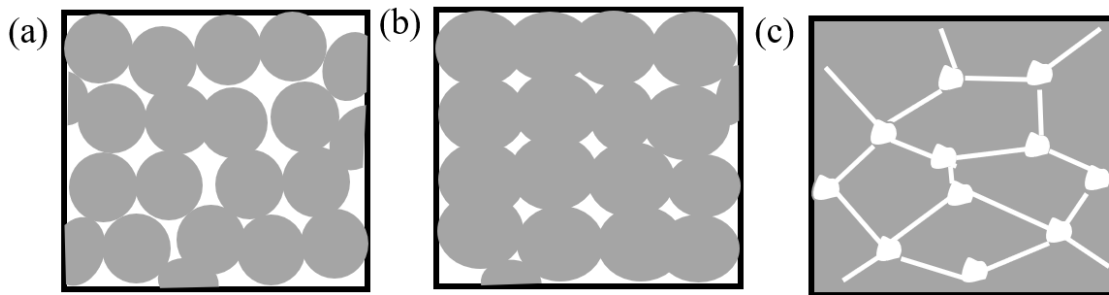


Figure 2.4: (a) Initial (b) intermediate and (c) final stages of the sintering process.

The final stage of sintering is much slower than the initial and intermediate stages. In this stage, isolated pores in the grain boundaries and within the grains are removed through the process of grain boundary diffusion and lattice diffusion, respectively. The maximum removal of porosity is possible when all of the void spaces are connected to fast

and short diffusion paths along the grain boundaries. The final stage of sintering begins around 90 - 95 % of theoretical density.

2.2 Thin-film preparation

2.2.1 Preparation of BNT target

The BNT ceramic target was prepared by a conventional solid-state reaction method. High purity starting materials Bi_2O_3 (Alfa-Aesar, USA, 99.999%) Na_2CO_3 and TiO_2 (Sigma-Aldrich, USA, 99.99%) are used and weighed according to the $\text{Bi}_{0.5}\text{Na}_{0.5}\text{TiO}_3$ stoichiometric ratios (Eq. 2.1). The 5 mol % of excess Bi and Na added to BNT powder to minimize the loss of Bi and Na during the deposition process. The mixed powders are subsequently milled with the ZrO_2 balls and vessel in isopropanol by using a high energy planetary ball mill (Pulverisette 6, Fritsch GmbH, Germany) for 5h. Further, the grounded powder was calcined at 800°C for 3h. The calcined powder was again ball milled for 10 h to reduce the particle size to enhance the densification process. The organic binder polyvinyl alcohol was added to the fine powder and prepared the BNT target by using KBr Press (M-20, Techno Search Instruments, India) with 20 mm diameter and 4 mm thickness. The prepared target was sintered at the optimized temperature 1100°C for 3h with a heating rate of $5^\circ\text{C}/\text{min}$ in a conventional furnace.

2.2.2 Pulsed laser deposition (PLD)

There are many methods and techniques that have been developed for the deposition of thin films such as sol-gel technique, sputtering, chemical vapor deposition, physical vapor deposition, thermal evaporator, pulsed laser deposition and etc. Among these, the PLD technique is a versatile tool and widely used for the deposition of complex oxide thin films due to stoichiometry control of the film composition, control of film thickness,

chemical homogeneity, porosity control, control of film crystallinity, excellent adhesion, low cost, etc. [3].

2.2.3 Description of PLD

In PLD, a pulsed laser beam is focused onto a target of the deposited material which can be placed in a high vacuum chamber or a low pressure of background gas. The sufficient laser energy density on the target surface causes the ejection of neutral and ionized material via thermal, chemical and mechanical mechanisms. The ejected material from a target that occurs after laser irradiation, i.e. ablation plume, which consist of plasma, gas and a particulate component. Then the flux of material impinges upon a substrate on which deposition occurs. The block diagram of the PLD process is given in Figure 2.5.

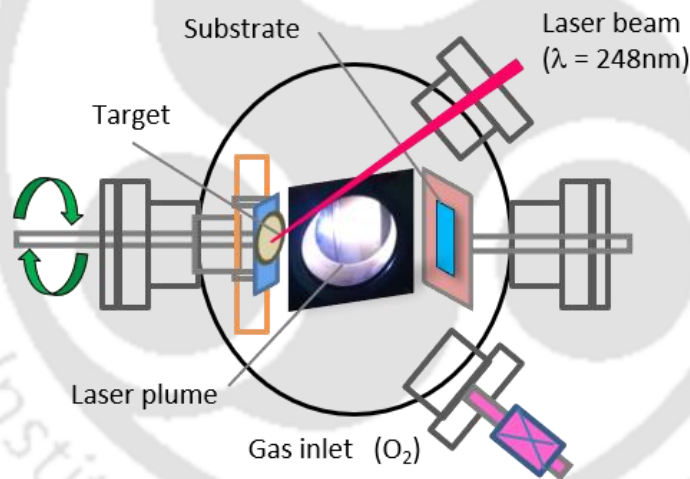


Figure 2.5: Schematic diagram of the PLD process.

2.2.4 Film growth

The film growth and quality basically depending on a few fundamental parameters, such as substrate temperature, the kinetic energy of the deposition flux, deposition rate, vacuum quality and background gas [4]. The importance of these parameters is discussed below.

2.2.5 Substrate temperature

The substrate temperature is the most important parameter, which highly influences the phase formation, crystallinity and morphology of the film. In the initial stages of film growth, the flux deposited on the substrate may re-evaporate from the surface, nucleate into a cluster, be consumed by forming clusters or be trapped on a surface defect site. Not only PLD but all the deposition processes also relied on the mobility of deposited atoms on the surface and each has its characteristic activation energies. These surface rearrangements are probable at higher temperatures, whereas they are inhibited at low temperature.



Figure 2.6: Different growth modes in thin film deposition, (a) Volmer-Weber growth, (b) Frank – van der Merwe growth and (c) mixed growth.

Generally, three growth modes (island, layer-by-layer, and mixed growth) can be distinguished and are shown in Figure 2.6 [5]. The Island (Volmer-Weber) growth is a formation of isolated islands on the surface. It happens when the cohesive energy of the atoms within the film is greater than the cohesive energy between the film and atoms on the surface. In layer-by-layer (Frank - van der Merwe) growth, the deposition of one monolayer at the time, resulting in a very smooth epitaxial film. It happens when there is greater cohesive energy between the film and the surface atoms than the cohesive energy of the film atoms. As each layer of film is added, the cohesive energy will be decreased monotonically. In the case of mixed growth, the growth of islands is successfully formed after the first monolayer. This happens when other factors such as strain due to lattice

mismatch energetically override the monotonic decrease in binding energy, this leads to island formation.

2.2.6 Energy of the deposition flux

The impact of high kinetic energy ion bombardment of the substrate includes ballistic collisions, ion mixing and thermally induced exchange mixing. Such effects produce similar results in raising the temperature of the substrate and control the film properties like film stress, crystallinity and crystal structure. An important correlation between the temperature and incident kinetic energy is that high-quality films can be deposited at lower substrate temperatures using high energy of the deposition flux.

2.2.7 Deposition rate, vacuum quality and background gas

The rate of the material impinging upon the surface is known as deposition rate which is mostly dependent on the deposited material. A very high rate of deposition causes film deterioration due to the decreased opportunity for relaxation of film. On the other hand, a very small rate of deposition leads to unacceptably long runs of deposition. The rate of deposition is also related to the quality of the vacuum available inside the chamber. There are more chances to reach the film with unwanted gaseous impurities (e.g. H₂O, CO₂, H₂ and N₂) at a lower deposition rate.

The introduction of a background gas (e.g. oxygen) is most important in PLD, especially for oxide thin films. The kinetic energy of deposited fluxes can be controlled by the introduction of the gas. If the deposition flux has not high kinetic energy and directionality, it will be scattered by collisions with the gas. In such cases, the film thickness drops dramatically as either the source-substrate distance or the pressure is increased. Figure 2.7 shows a photograph of the PLD system by employing an excimer laser that was used in the present study. Here, 20 ns pulse width KrF Excimer laser of

wavelength 248 nm (COMPexPro 102 F, Coherent) was used with 5 Hz repetition rate. The deposition process of BNT films is carried out in a spherical chamber (Excel Instruments, India). Initially, the chamber is evacuated to 6×10^{-6} mbar using Turbo and backing (Rotary) pumps. The distance between the target and substrate is maintained at 5 cm. The target is set to rotate with a specific speed of 10 rpm.

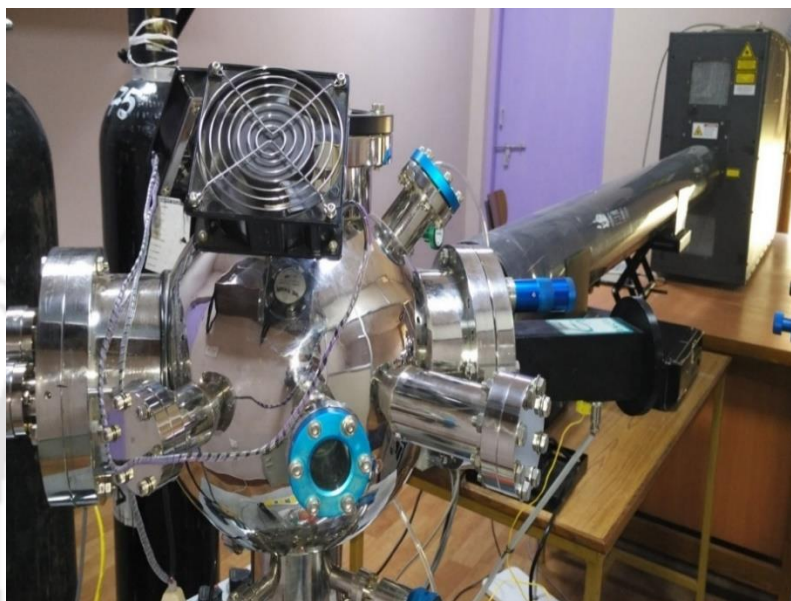


Figure 2.7: Pulsed laser deposition system.

2.3 Characterization techniques

2.3.1 Thermal analysis

The differential scanning calorimetry (DSC) and thermal gravimetric analysis (TGA) methods are employed to study the heat flow and weight changes in a material as a function of time and temperature [6]. The DSC analysis gives information about the change in energy of a material as a function of temperature and time. Based on the material behavior, the change in energy can be endothermic (heat absorption) and exothermic (heat release) to the reference material. The advantages of DSC are: a small amount of sample ($\sim 3 - 15$ mg) is needed, sample preparation is much simpler and calculation for quantitative

or qualitative studies is readily measured. The crystallization, melting, and phase transition temperature can be estimated from DSC studies.

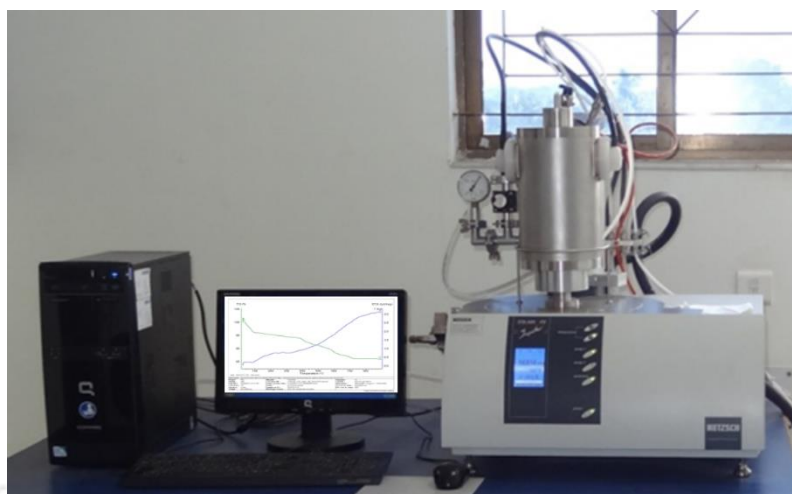


Figure 2.8: Photographic image of the DSC-TGA system.

The TGA analysis provides information about the change in the mass of the material as a function of temperature and time. The change in mass of the material might be due to the evaporation of moisture, decomposition of material, other solvent residues and oxidation of metals. Therefore, the TGA technique is used to determine the reaction temperature of the chemical process. In this work, the DSC/TGA system (STA449F3A00, Netzsch) was employed for the thermal analysis of the BNT ceramic powders. Figure 2.8 shows the photography of the DSC-TGA system was used in the present study.

2.3.2 X-Ray diffraction

X-ray diffraction (XRD) is a versatile tool and non-destructive technique for the determination of the phase purity and crystal structure of materials. The wavelength of X-ray is comparable to the size of atoms around a few Å to 0.1 Å. Therefore, X-rays are more suitable to investigate the structural arrangement of atoms in various materials. The general relationship between the wavelength of the incident X-rays, angle of incidence and spacing

between the crystal lattice planes of atoms is known as Bragg's Law and is given by the following expression [7].

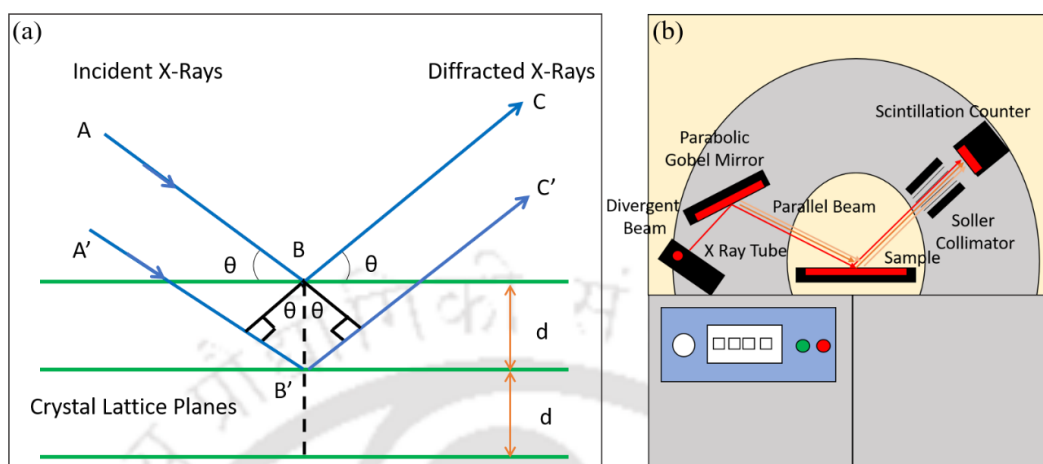


Figure 2.9: (a) Bragg's law for X-ray diffraction and (b) schematic diagram of X-ray diffractometer.

$$n\lambda = 2d \sin \theta \quad (2.3)$$

where, n is (integer) the order of reflection, λ is the wavelength of incident X-rays, d is the interplanar spacing of the crystal and θ is the angle of incident. Figure 2.9 shows the Bragg's Law reflection and schematic diagram of the X-ray diffractometer. The diffracted X-rays exhibit constructive interference when the distance between ABC and A'B'C' paths ($2d \sin \theta$) is differ by an integer number of λ .

In this thesis, X-ray diffractometer (TTRAX-III 18 kW, Rigaku,) with $\text{CuK}\alpha$ ($\lambda = 1.5406 \text{ \AA}$) radiation was used to characterize the BNT based ceramics and thin films. Figure 2.10 shows the photographic image of the X-ray diffractometer employed in the present work. The XRD patterns of the prepared BNT based ceramics and thin films were measured with scanning step size 0.03° and scanning rate $3^\circ/\text{minute}$ between the 2θ range of $20-80^\circ$. The 2θ calibration was performed using a standard Si sample to account for the instrumental line broadening approximately equal to the 0.15° . The XRD patterns of the BNT based

ceramics and thin films were analyzed using the Rietveld refinement method using Fullprof software [8].



Figure 2.10: Photograph image of the X-ray diffractometer.

2.3.3 Density measurement

The Archimedes' method was employed to determine the relative density of the sintered discs of BNT based ceramics. According to this method, when an object is partially or fully immersed in a fluid, there is an upward force (buoyance force) produced by the fluid on the object. The force acts upward and has the magnitude equal to the weight of the fluid displaced by it. The apparent weight of the object is equal to the difference between the actual weight of the object and the magnitude of the buoyance force. The apparent density (ρ_a) of the sintered pellets is estimated using the following expression,

$$\rho_a = \left(\frac{w_1}{w_2 - w_3} \right) \times \rho_w \text{ gm/cm}^3 \quad (2.4)$$

where, w_1 is the weight of the pellet in air, w_2 is the weight of the discs immersed in the liquid medium, and w_3 is the weight of the pellet after removed from the liquid medium, and ρ_w is the density of the liquid used. In the present study, the distilled water ($\rho_w = 1$

gm/cm³) used as the liquid medium. Further, the percentage in relative density of the samples was estimated using the following expression,

$$\text{relative density (\%)} = \frac{\rho_a}{\text{theoretical density}} \quad (2.5)$$

2.3.4 Raman spectroscopy

Raman scattering phenomenon was first discovered by Sir Chandrasekhara Venkata Raman in 1928 [9]. Raman spectroscopy is a versatile technique and is the measurement of the wavelength and intensity of inelastically scattered light from molecules, which observe the molecule vibration of the sample [10]. Raman spectroscopy is sensitive to the crystal structure, bonding and chemical composition of the material and does not require any sample preparation [11]. Such characteristics make it a very important tool for identifying the material in any physical form; solids, liquids, and gases.

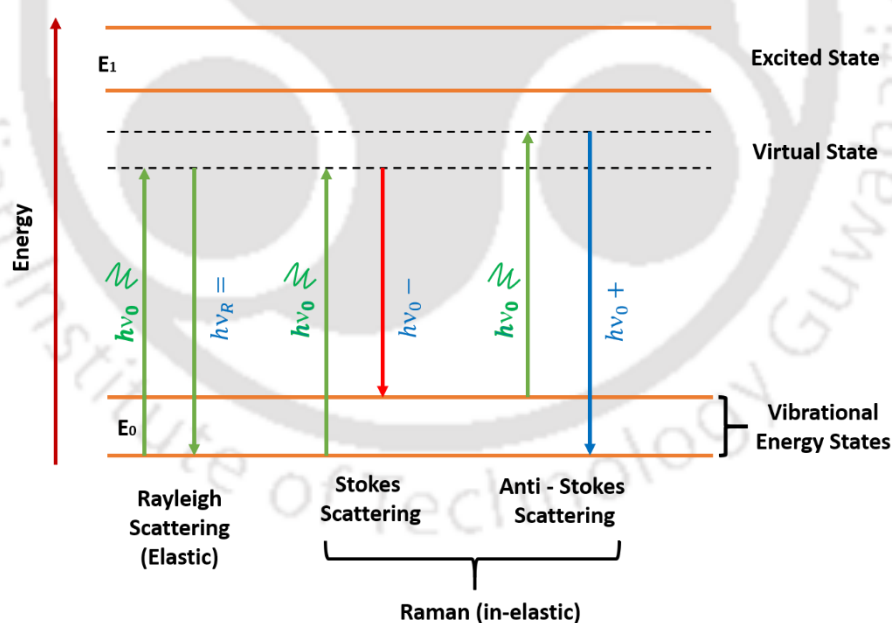


Figure 2.11: Energy level diagram for Rayleigh and Raman Scattering.

In Raman spectroscopy, the monochromatic laser beam falls and interacts with the molecule of the sample and a small fraction of light may be scattered either elastically or

inelastically. Therefore, the energy of the scattered light is either higher or lower than incoming light, which is called a Raman effect. The Raman spectra can be classified as Stokes and anti-Stokes (Figure 2.11). The Stokes and anti-Stokes lines exhibit lower and higher energy, respectively. However, if the scattered radiation energy is equal to the energy of the incident radiation is known as Rayleigh scattering (elastic scattering) is shown in Figure 2.11. The Stokes lines are more intense than anti-Stokes lines. Hence, Stokes is used to measure the conventional Raman spectroscopy where anti-Stokes bands are measured with fluorescing samples due to fluorescence causes interference with Stokes bands. The magnitude of the Raman shift is basically independent of the wavelength of the incident radiation. Since, the Raman scattering is low due to water, which is used as an ideal solvent for dissolving liquid samples. The solid samples can directly mount on a glass substrate and perform the measurements by mean of the optical components (mirror, lens, sample cell) in Raman spectrophotometer [10,12,13]. In the present thesis, the room temperature Raman spectra of BNT based ceramics and thin films were performed using the LABRAM HR800 Raman spectrometric analyzer developed by Horiba Jobin Yvon with an excitation wavelength of 488 nm of an Ar-ion laser is shown in Figure 2.12. This instrument is equipped with a dedicated heating/cooling sample stage (THMS600, Linkam). All the spectra were recorded in a backscattered geometry furnished with a 50× objective, an appropriate edge filter and a Peltier-cooled charge-coupled device detector. An Ar⁺ ion excitation laser source in a high-resolution dispersive geometry was used for these low-temperature micro-Raman measurements with $\lambda = 514 \text{ nm}$ and an 1800 mm^{-1} grating. The spectral resolution of the system is 1 cm^{-1} . The grating was fixed during the entire temperature scan for the high degree of positional accuracy.



Figure 2.12: Photograph of Raman spectrometer (LBRAM HR800).

2.3.5 Scanning electron microscopy

In the present thesis, the microstructural images and chemical composition of the BNT based ceramics and thin films have been performed by the scanning electron microscopy (SEM) (1430 VP, LEO) equipped with energy dispersive X-ray spectrometer (EDS) and field emission scanning electron microscope (FESEM) (Sigma, Zeiss,). The schematic diagram of the SEM is shown in Figure 2.13.

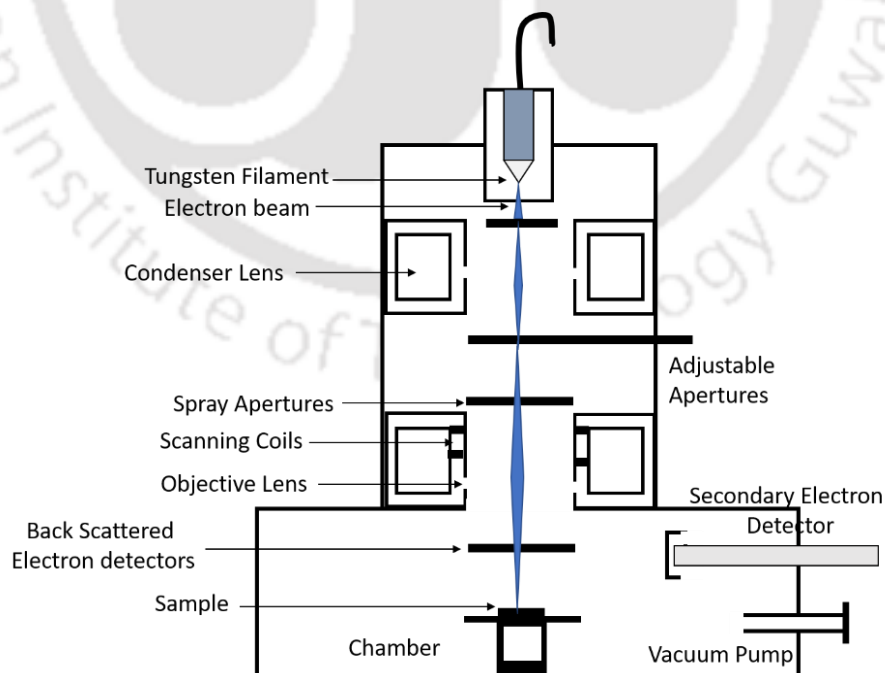


Figure 2.13: The schematic diagram of a scanning electron microscope.

In SEM, the surface of a material is scanned by high energy electrons and are thermionically emitted from a tungsten filament and accelerated towards an anode with sufficient kinetic energy. In FESEM, electrons are emitted from field emission. The energy of an electron beam is dissipated as different signals depending on the interactions between the electrons and samples. Among these signals, secondary electrons and backscattered electrons are used to obtain the surface morphology and photons are used for elemental analysis, and others are cathode luminescence and heat. Secondary electrons can produce the classic topographic images, whereas the backscattered electrons provide the information about the variations in the composition. The EDS is an analytical technique employed for the chemical characterization of a sample. The EDS spectrum shows the peaks correspond to the energy levels for which the X-rays had been received. Each peak of the spectrum is unique to an atom (element) and the intensity of the peak defines the concentration of elements presented in the sample. Figure 2.14 shows a photograph of the field emission scanning electron microscope that was used in the present study.



Figure 2.14: Photograph of field emission scanning electron microscope.

2.3.6 Field emission transmission electron microscopy

A field emission transmission electron microscope (FETEM) is one type of electron microscope with high resolution than other microscopes. In FETEM, a high energy electron beam is used to detect the crystal structure, dislocation, grain boundaries of nanoparticles or nanocrystals. It has four major parts as shown in Figure 2.15: (a) electron gun; it consists of cathode and anode usually tungsten filament is used which emits electrons, (b) electromagnetic lens system; consists of an electromagnetic lens and metal aperture, (c) the sample holder; is a platform equipped with a mechanical arm to hold and controlling its position of the specimen, (d) imaging system. The FETEM functions like a slide projector. A projector shines a beam of light that transmits through the slide. The patterns painted on the slide only allow certain parts of the light beam to pass through. Thus, the transmitted beam replicates the patterns on the slide, producing an enlarged image of the slide when it falls on the screen.

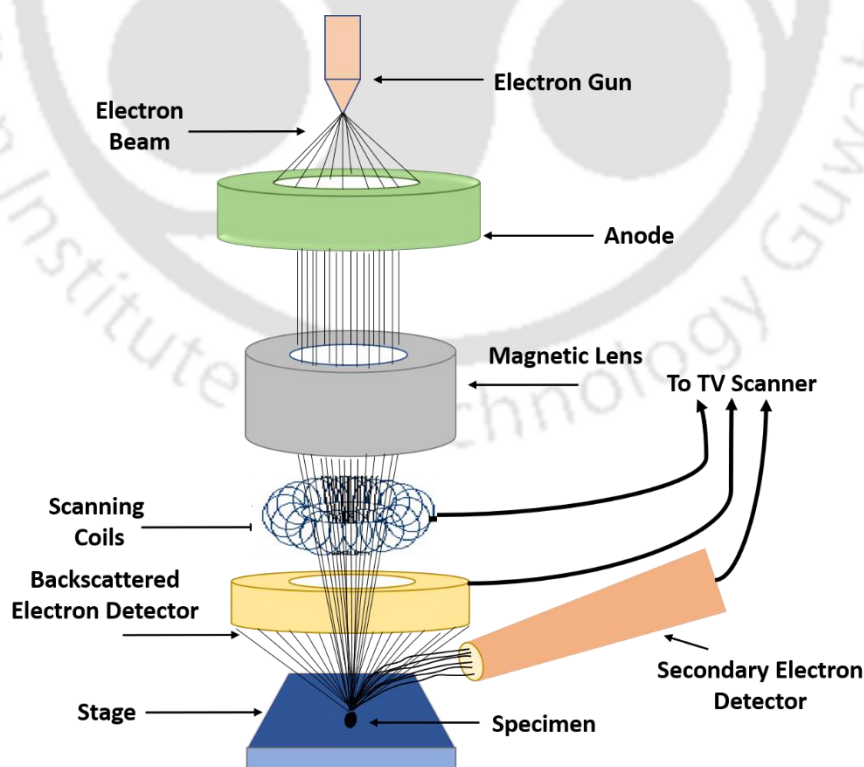


Figure 2.15: The schematic outline of a FETEM.

In the present thesis, the FETEM instrument (2100F, JEOL) is employed to study morphology and the crystallographic structure of the prepared samples was analyzed by bright-field TEM image, high-resolution transmission electron microscopy (HRTEM) and selected area electron diffraction (SAED) in some of the papers. Figure 2.16 shows the TEM instrument was used in the present study. The figures themselves explain in details of the individual parts of the instrument and its arrangements of the TEM instrument. The resolution of the instrument is 1.9 Å to 1.4 Å (lattice) with accelerating voltage 60 to 200 kV in 50 V steps and a tilt of $\pm 25^\circ$. The magnification range of standard specimens goes from 50 X to 1,500,000 X which is a very sophisticated instrument for the characterization of nanomaterial. It also has a high-resolution CCD (charge-coupled device) camera with 2.672 x 2.672 K resolution provides very high-resolution images of the samples.



Figure 2.16: Photograph of FETEM instrument.

2.3.7 Dielectric measurements and impedance spectroscopy

The dielectric properties such as the relative permittivity (ϵ_r) and loss tangent ($\tan\delta$) are the most important parameters to understand the structural phase transitions,

relaxation behavior, various types of polarization mechanisms and etc. For the dielectric measurements, the silver paste was coated on both sides of the samples to make metal-insulator-metal (MIM) capacitors.

Impedance spectroscopy is a versatile technique for investigating the electrical properties of the materials [14–16]. The AC voltage and current of an electrical network is given by,

$$V(t) = V_0 \exp(j\omega t) \quad (2.6)$$

$$I(t) = I_0 \exp(j\omega t + \varphi) \quad (2.7)$$

where, $j = \sqrt{-1}$, ω is an angular frequency and φ is the phase angle. The complex impedance (Z^*) can be expressed in terms of both magnitude ($|Z|$) and phase angle (φ) as,

$$Z^*(\omega) = |Z| \exp(-j\varphi) \quad (2.8)$$

$$Z^*(\omega) = |Z| \cos(\varphi) - j|Z| \sin(\varphi) \quad (2.9)$$

$$Z^*(\omega) = Z'(\omega) - jZ''(\omega) \quad (2.10)$$

where, $Z'(\omega)$ and $Z''(\omega)$ are the real and imaginary parts of complex impedance, and

$$|Z| = \sqrt{[Z'(\omega)^2 + Z''(\omega)^2]} \quad (2.11)$$

The complex admittance (Y^*), complex permittivity (ϵ^*), and complex modulus (M^*) of the sample can be estimated using impedance values by following expressions,

$$Y^*(\omega) = Y'(\omega) + jY''(\omega) = 1/Z^* \quad (2.12)$$

$$\epsilon^*(\omega) = \epsilon'(\omega) - j\epsilon''(\omega) = 1/j\omega C_0 Z^* \quad (2.13)$$

$$M^*(\omega) = M'(\omega) + jM''(\omega) = j\omega C_0 Z^* \quad (2.14)$$

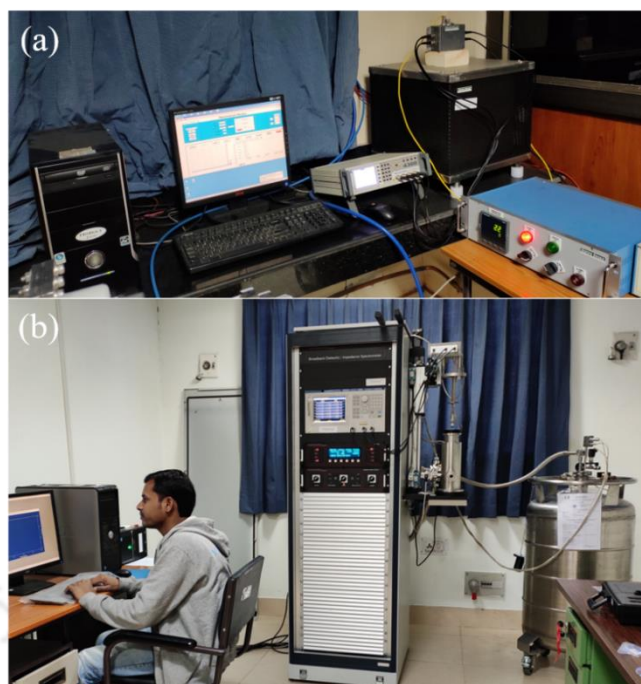


Figure 2.17: Photographs of the (a) LCR meter and (b) RF impedance material analyzer equipped with temperature control systems.

In the present thesis, we have employed low and high-frequency instruments for the dielectric studies. The low frequency (20 Hz -1 MHz) dielectric properties of the prepared BNT bulk ceramics and thin films measured in the temperature range 25 °C - 500 °C employing LCR meter (1J43100, Wayne Kerr Electronics Pvt. Ltd.) controlled by PID controller (3216, Eurotherm) with an accuracy of ± 1.5 °C. The low and high frequency (3 μ Hz – 40 MHz) dielectric properties of the BNT based ceramics were measured by employing the RF Impedance analyzer (E4991A, Keysight Technologies) in the wide temperature range of -160 °C – 1200 °C with stability of 0.01 °C due to the 4 channel Quatro controller containing PID control algorithms (Concept 70, Novocontrol). The high frequency (1 MHz -1 GHz) dielectric properties of the BNT based ceramics were measured using the RF impedance material analyzer (E4991A, Agilent Technologies,) in the wide temperature range of -160 °C – 400 °C with stability of 0.01 °C due to the 4 channel Quatro controller containing PID control algorithms (Novocontrol, Concept 70). The low-

temperature measurements were carried out using liquid nitrogen as a cooling or heating medium. Figure 2.17 shows a photograph image of the LCR meter and RF material analyzer being used in this study.

2.3.8 Ferroelectric measurements

Ferroelectric property is the most important property of ferroelectric materials and measured by the reversal of polarization or switching in response to the applied electric field. Figure 2.18 (b) shows a schematic modified Sawyer-Tower circuit developed for the investigations on P-E loops, whereas a step voltage (V) is applied across the two electrodes on the surfaces of a sample capacitor (C_s , with thickness d) in the circuit [17]. Therefore, the electric field can be estimated by dividing the voltage by the thickness ($E=V/d$) across the sample. The magnitude of the applied field is plotted on the horizontal X-axis. The sample is coupled in series with a parallel RC circuit, which compensates for any phase shift due to dielectric loss or conductivity in the sample. The voltage (V_r) across the reference capacitor (C_r) is measured and the charge on the reference capacitor will be the same as the charge over the sample capacitor due to the two capacitors are connected in series. The charge per unit surface area i.e. density of flux on the ferroelectric sample can be determined by the following equation,

$$D = \epsilon_0 E + P \quad (2.15)$$

where, $P = Q/A$, the polarization can be measured using the above equation (2.15) when the charge on the sample is predictable. In this work, the polarization versus electric field (P - E) hysteresis loop of BNT based ceramics and thin films were measured at room temperature using ferroelectric tester (Precision LCII 10kV HVI-SC, Radiant Technologies). Figure 2.18 (a) shows a photograph of the P-E tester was used in present work.

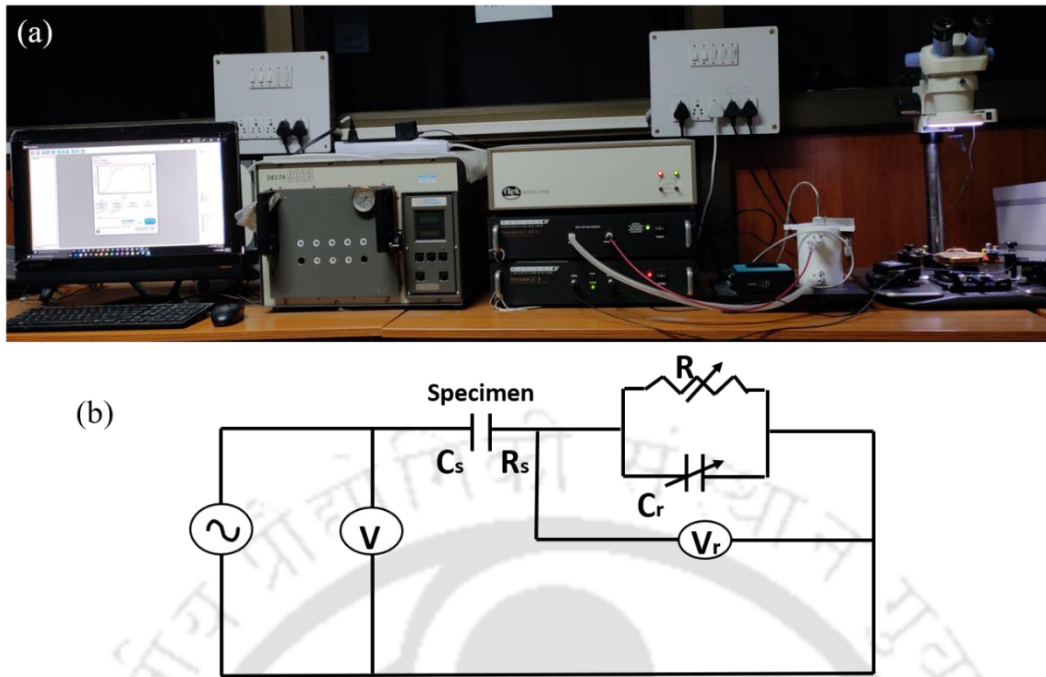


Figure 2.18: (a) Photograph of the ferroelectric P - E tester and (b) Sawyer-Tower circuit diagram.

2.3.9 Piezoelectric measurements

2.3.9.1 Polling

In order to make the material much more piezoelectric sensitive has to initially orient the domains in the direction of the applied electric field. This process is called poling. The electrical properties of piezoelectric materials have been greatly influenced by the various polling parameters: (a) poling electric field, (b) poling time, and (c) poling temperature. Before polling, the ferroelectric materials do not possess proper piezoelectric and pyroelectric response due to the random orientation of the ferroelectric domains. Therefore, a poling field must be applied to the sample and maintained for a certain time to reorient the domain and for better rearrangement of the domain polling temperatures, but lower than transition temperature T_c . It occurs due to the anisotropy nature of piezoelectric material and the coercive field (E_c) reduces with the increase in poling temperature. Space charges, which act against domain motion, are also reduced with a rise in temperature.

However, if poling temperature is much high, problems arise as the electrical conductivity and leakage current increases, which results in degradation of the sample during the poling process. The sample is allowed naturally cool down to room temperature with the electric field applied and the electric field is removed at room temperature. After poling, the remanent polarization and residual strain are preserved in the material and the piezoelectric and pyroelectric effects begin to appear. Figure 2.19 shows a photograph of DC Poling unit (DC-01, Marine, India) that was used for BNT based bulk ceramics in present work.



Figure 2.19: DC polling unit.

2.3.9.2 Piezoelectric coefficients

The basic fundamentals and their notations were already explained in the introduction part of piezoelectricity. In present thesis, the piezoelectric properties such as piezoelectric charge constants (d_{33} and d_{11}), piezoelectric voltage constants (g_{33} and g_{11}), electromechanical coupling factors (k_{33} , k_{31} , k_p and k_t), and elastic compliance (S_{33} and S_{11}) of BNT based ceramics have been determined from resonance and anti-resonance frequency using impedance analyzer (E4991A, Keysight Technologies) (i.e. indirect method) and ANSI/IEEE standards on piezoelectricity expressions [18–20].

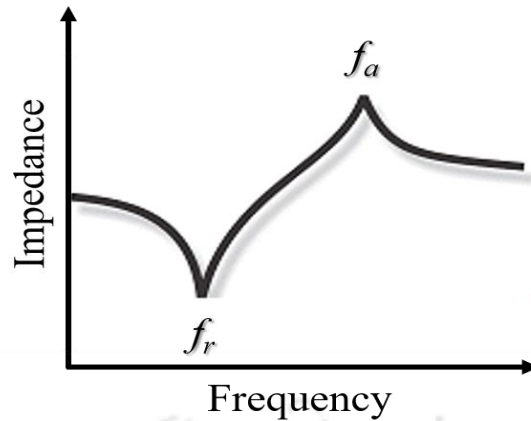


Figure 2.20: Impedance as a function of the frequency curve for measuring the resonance frequency and anti-resonance frequency.

The dimensions of the piezoelectric material changes when it is subjected to an AC-electric field. The frequency at which the material vibrates more readily and most effectively transforms the electrical energy into mechanical energy, which is known as the resonance frequency. With increasing the frequency, the oscillations of the material first approach a frequency with minimum impedance (maximum admittance). This minimum impedance frequency (f_m) approximates the series resonance frequency (f_s), the frequency at which impedance in an electrical circuit is zero if resistance caused by mechanical losses are avoided. The minimum impedance frequency is called the resonance frequency (f_r). It can be estimated by the composition of material, shape and volume of the material. Generally, a material with higher thickness has a lower resonance frequency than a material with a lower thickness of the same shape. Further as the frequency increases, the impedance reaches to maximum (minimum admittance) and the maximum impedance frequency f_n approximates the parallel resonance frequency (f_p). The frequency at which parallel resistance in the electrical circuit is infinite if resistance caused by mechanical losses is avoided. The maximum impedance frequency is called the anti-resonance frequency (f_a).

The f_r , and f_a values can be estimated by measuring the impedance as a function of the frequency plot is shown in Figure 2.20.

2.3.10 Atomic force microscope

Atomic force microscope (AFM) is a powerful imaging technique to produce topographical images that quantify surface morphology, size, the surface roughness of nanoscale samples. It can also produce a 3D image profile of the sample surface [21,22]. AFM consists of a flexible cantilever with a sharp tip (silicon or silicon nitride), scanner, controller and signal processing unit. The tip scans the sample surface and produces the surface topography depends on the interactions between the tip atoms and surface atoms. The Van der Waals forces between atoms at the tip and the sample surface leads to a deflection of the cantilever according to Hooke's law. This deflection is measured using a laser reflected back from the top surface of the cantilever to a photodetector shown in Figure 2.21. Further, the detected signals send to the signal processing unit to produce the topography image along with amplitude and phase.

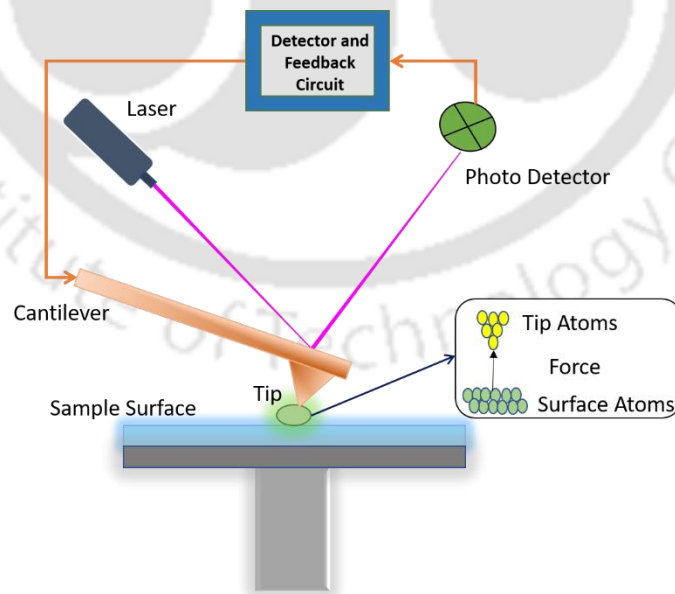


Figure 2.21: Schematic diagram of the atomic force microscope.

In this thesis, the atomic force microscope (Cypher, Oxford) was used to obtain AFM images of the BNT based thin films and further the surface roughness, 3D and 2D image processing were done using WSxM 4.0 Beta software [23]. The photograph of the atomic force microscope was used in the present work as shown in Figure 2.22.



Figure 2.22: Photograph of atomic force microscope.

2.3.11 Optical characterization

2.3.11.1 Linear optical properties

In the present work, the linear optical properties of the fabricated thin films have been investigated by employing a UV-VIS-NIR spectrophotometer (UV 3101PC, SHIMADZU) and Spectroscopic Ellipsometer (GES5E, SEMILAB). It is a more popular and easy way to calculate the optical properties of thin films using transmittance spectra by the Swanepoel envelop technique [24]. The fundamental optical constants such as linear refractive index (n), packing density (p), absorption coefficient (α) and optical bandgap (E_g) can be calculated from transmission spectra. In addition, the film thickness can also be calculated by this method. In general, a film of refractive index n with the thickness d deposited onto any transparent substrate having the refractive index n_s and thickness d_s as shown in Figure 2.23. When a light incident on the film, then some fraction of an incident is reflected and the rest is transmitted at the interfaces of air-film, film-substrate and substrate-air. The reflected and transmitted light exhibit the interference pattern since the beams originated

from a single coherent source. The typical transmittance spectrum of a film deposited onto a transparent substrate measured in the wavelength range of 200 -1000 nm is shown in Figure 2.24.

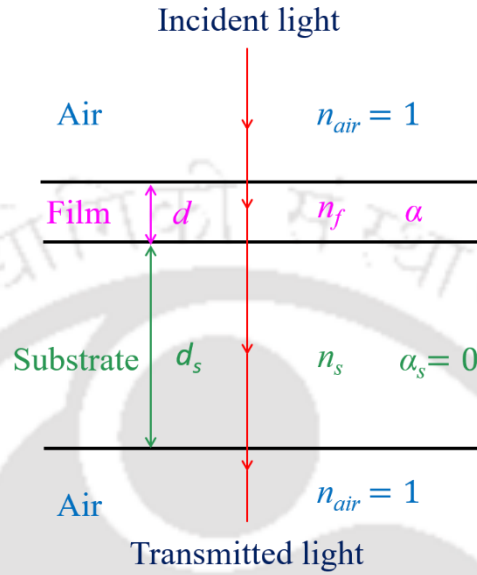


Figure 2.23: Schematic diagram of refractive index in different mediums of the thin film.

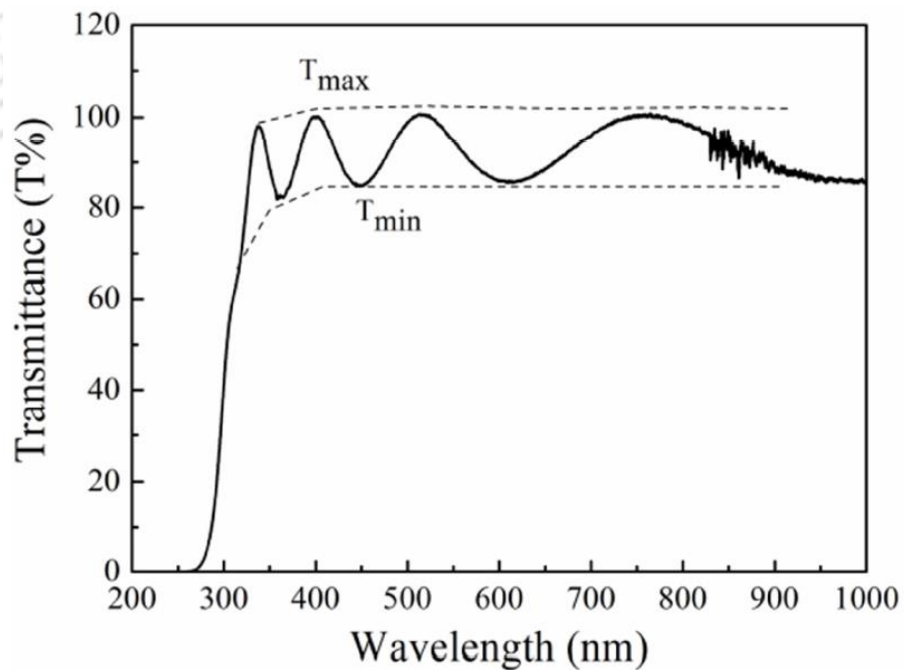


Figure 2.24: Typical transmittance spectrum of a thin film.

The refractive index (n) of the film can be calculated by using the Swanepoel's envelop method based on the following expressions [24,25],

$$n = \sqrt{N + \sqrt{N^2 - n_s^2}} \quad (2.16)$$

where,
$$N = 2n_s \frac{T_M - T_m}{T_M T_m} + \frac{n_s^2 + 1}{2} \quad (2.17)$$

$$n_s = \frac{1}{T_s} + \sqrt{\frac{1}{T_s^2} - 1} \quad (2.18)$$

here, n_s is the substrate refractive index, T_M and T_m are the transmittances at maxima and minima at certain wavelength λ .

The thickness of the film (d) can be estimated by the following expression,

$$d = \frac{\lambda_1 \lambda_2}{2(n_1 \lambda_2 - n_2 \lambda_1)} \quad (2.19)$$

where, n_1 and n_2 are the refractive indices of two adjacent maximum and minimum at wavelengths λ_1 and λ_2 , respectively.

The optical packing density (p) of the films can be estimated by the following expression,

$$P_0 = \left(\frac{n_f^2 - 1}{n_f^2 + 2} \right) \left(\frac{n_b^2 + 2}{n_b^2 - 1} \right) \quad (2.20)$$

where, n_b and n_f are the refractive indices of the bulk sample and film, respectively.

From the Beer-Lambert's law [26],

$$I = I_0 \exp(-\alpha d) \quad (2.21)$$

where, I_0 is the incident light intensity, I is the intensity of the light at wavelength λ , d is the thickness of the film and α is the absorption coefficient, which can be related to the transmittance as,

$$\alpha = \frac{-\ln T_{\alpha}}{d} \quad (2.22)$$

where, $T_{\alpha} = (T_M T_m)^{0.5}$.

The optical bandgap (E_g) of the films can be estimated using the Tauc relation by following relation [27,28],

$$(\alpha h\nu)^m = B(h\nu - E_g) \quad (2.23)$$

where, $h\nu$ is the incident photon energy, m determines the type of electronic transition between the valence band and conduction band and B is the measure of crystalline order. The E_g of the films can be calculated from the extrapolated linear portion of $(\alpha h\nu)^m$ versus $(h\nu)$ curve, In the present thesis, the E_g has been calculated by assuming an allowed direct electronic transition ($m=2$). The error associated with the measurement of n and d is ± 0.02 and ± 10 nm, respectively.

Moreover, the fundamental optical constants of the deposited films were also characterized using a spectroscopic ellipsometer. It is one of the best techniques to estimate the optical properties of films by an adequate optical model with more accuracy. The spectroscopic ellipsometry (SE) measurements have been performed to investigate the relevance of linear optical properties of BNT thin films in terms of complex dielectric function ($\varepsilon^* = \varepsilon_1 + i\varepsilon_2$) and refractive index ($n^* = n + ik$). The characteristics of SE is related to surface morphology, crystallinity, chemical composition, and conductivity of the films [29]. In the present study, the measured ε_1 and ε_2 of spectra were fitted with the Tauc-Lorentz dispersion model by using Spectroscopy ellipsometry analyzer (SEA) software. Figure 2.25 shows the photograph of UV-VIS-NIR spectrophotometer and spectroscopic ellipsometer that were employed in the present work.



Figure 2.25: (a) Photograph of UV-VIS-NIR spectrophotometer and (b) Spectroscopic ellipsometer.

2.3.11.2 Nonlinear optical characterization

Nonlinear optics is a well-known and most powerful tool to investigate the properties of the materials. In this thesis, we have employed an important nonlinear optical (NLO) technique is known as electric field induced second harmonic generation to study the hyperpolarizability of various molecular objects. For example, the second-harmonic generation occurs as a result of the atomic response that scales quadratically with the amplitude of the applied optical field. Consequently, the intensity of the light generated at the second-harmonic frequency increases as the square of the intensity of the applied laser light.

Usually, the NLO phenomena occur at higher intense fields. The induced electric polarization (P) in the material by the applied electromagnetic field (laser) can be written as a Taylor series expression [30,31],

$$P = \varepsilon_0 \chi^{(1)} E + \varepsilon_0 \chi^{(2)} E^2 + \varepsilon_0 \chi^{(3)} E^3 + \dots \quad (2.24)$$

where, ε_0 is the vacuum permittivity, E is the electric field, $\chi^{(1)}$ is the linear susceptibility of the material, $\chi^{(2)}$ and $\chi^{(3)}$ are the second and third-order nonlinear susceptibilities of the sample, respectively. The second-order nonlinear susceptibility ($\chi^{(2)}$) is related to the electro-optic effect, second-harmonic generation, and other sums as well as difference-frequency generation. The third-order nonlinear susceptibility ($\chi^{(3)}$) is related to the intensity-dependent third-order nonlinear effect and third harmonic generation. The intensity-dependent nonlinear refraction and absorption can be written by the following equations [32],

$$\alpha(I) = \alpha + \beta_{eff} I \quad (2.25)$$

$$n(I) = n_0 + n_2 I \quad (2.26)$$

where, α is the linear absorption coefficient, β_{eff} is the nonlinear absorption coefficient, n_0 is the linear refractive index, n_2 is the nonlinear refractive index and I is the intensity of the laser beam.

In this thesis, the nonlinear optical properties of the BNT based thin films were measured employing a modified single beam z-scan technique [33–35]. This technique basically depends on the spatial beam broadening and narrowing of the focused Gaussian beam in the far-field region which results in the optical nonlinear response present in the sample. The sample transmittance is measured as a function of sample position with respect to the focal plane, in the longitudinal direction. As shown in Figure 2.26, a continuous wave

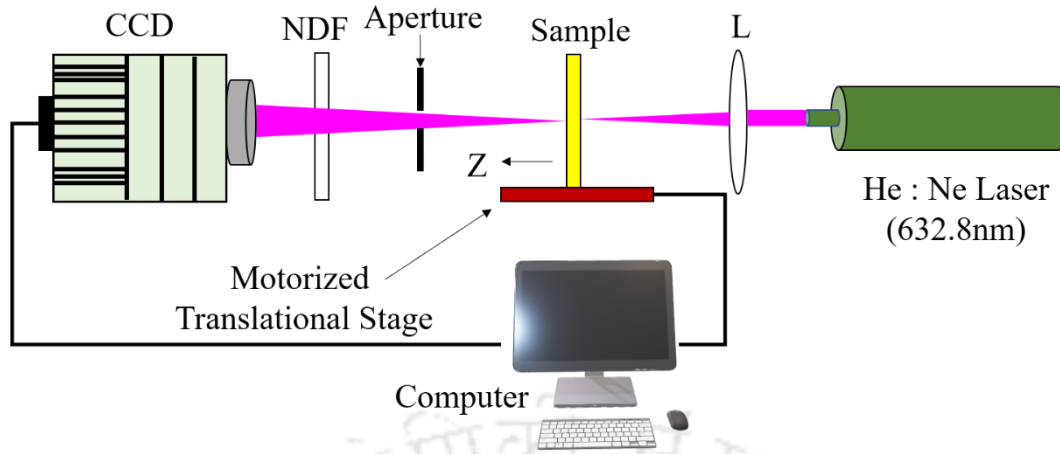


Figure 2.26: Schematic diagram of the z-scan technique.

(cw) He:Ne laser ($\lambda = 632.8 \text{ nm}$) beam is used to illuminate the sample by focusing with 5 cm focal length lens onto the sample mounted on the motorized translational stage. The sample is translated along the beam propagation direction and the corresponding transmitted image will be recorded using a charged coupled device (CCD) camera. In order to avoid the saturation of CCD, a neutral density filter (NDF) of 3.0 optical density (OD) is placed in front of CCD. An iris diaphragm is placed after the sample to prevent the multiple reflected and scattered light into the detectors. The Rayleigh length (z_0) should be greater than the sample thickness to satisfy the thin sample approximation for z-scan. The signals corresponding to the open aperture (OA) and closed aperture (CA) z-scan are simultaneously extracted from the single scanned images obtained from CCD camera. The open aperture z-scan curve measured from the integrated intensity over the entire image as a function of sample position with respect to the focal plane, which provides the nonlinear absorption coefficient (β_{eff}). The closed aperture z-scan curve is measured from the integrated intensity of the partially masked images of open z-scan by placing a suitable synthetic aperture in the central region using a MATLAB program.

The nonlinear absorption coefficient (β_{eff}) and nonlinear refractive index (n_2) are calculated by the following equations [27],

$$T_{open}(z) = 1 - \frac{\beta_{eff} I_0 L_{eff}}{2^{3/2} [1 + (z/z_0)^2]} \quad (2.27)$$

$$T_{closed}(z) = 1 - \frac{4n_2 I_0 L_{eff} (z/z_0) k}{[1 + (z/z_0)^2][9 + (z/z_0)^2]} \quad (2.28)$$

where, $T_{Open}(z)$ and $T_{Closed}(z)$ are the normalized open and closed aperture transmittances, respectively. $L_{eff} = [1 - \exp(-\alpha L)]/\alpha$ is the effective thickness of the film, α is the linear absorption coefficient, L is the film thickness, k is the magnitude of the wave vector.

The real as well as the imaginary part of the third-order nonlinear susceptibilities, $\chi_R^{(3)}$ and $\chi_I^{(3)}$, were evaluated from the following relations [36,37],

$$\chi_R^{(3)}(esu) = 10^{-4} \frac{\epsilon_0 n_0^2 c^2}{\pi} n_2 (cm^2/W) \quad (2.29)$$

$$\chi_I^{(3)}(esu) = 10^{-2} \frac{\epsilon_0 n_0^2 c^2 \lambda}{4\pi^2} \beta_{eff} (cm/W) \quad (2.30)$$

where, ϵ_0 , c , and λ are the vacuum permittivity, speed of light in vacuum, and wavelength of the laser used, respectively.

2.3.12 Microwave dielectric characterization

The split post dielectric resonator (SPDR) technique is a well-established, non-destructive and accurate technique for the measurement of complex permittivity of low loss dielectric substrates and thin films at spot frequencies in the microwave region of 5, 10 and 15 GHz [38,39]. In the present thesis, the microwave dielectric properties such as dielectric permittivity and loss of the prepared films were measured in the frequency range of 5 - 15 GHz using a vector network analyzer (8722 ES, Agilent Technologies,) and (ZVA24,

Rohde & Schwarz) by employing SPDR technique. The dielectric resonators are typically operated with $TE_{01\delta}$ mode, that mode has only an azimuthal electric field component. Thus, the electric field remains continuous across the dielectric interfaces, which makes the measurement insensitive to the presence of air gaps perpendicular to the z-axis of the fixture [40]. Figure 2.27 shows the typical cross-section of an SPDR.

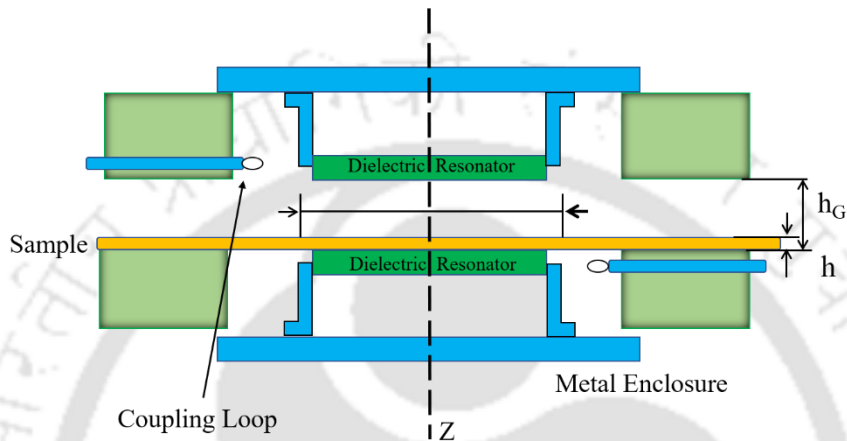


Figure 2.27: The cross-sectional view of SPDR fixture [30-31].

The relative permittivity (ϵ_r) and loss tangents ($\tan\delta$) of the films and substrates are mainly dependent on the resonant frequency and quality factor. Initially, the resonant frequency and quality factor of the empty resonator (f_{01} , Q_{01}) and resonant frequency and quality factor of the substrate (f_0 , Q_0) is measured before the deposition of the film. When the deposited film placed in SPDR, which results shift in resonant frequency. The shift of resonant frequency and its quality factor (f_s , Q_s) of the film is measured. The Rayleigh-Ritz method was employed to calculate the resonant frequencies, unloaded Q-factors, and other parameters. Therefore, the relative permittivity and loss tangent of the films were calculated based on the thickness and resonant frequencies by following equations [38],

$$\epsilon_r = 1 + \frac{(f_0 - f_s)}{hf_0 K_s(\epsilon_r, h)} \quad (2.31)$$

where, h is the thickness of the film, f_0 and f_s are the resonance frequencies of the bare substrate and film-coated substrate of the SPDR. K_s is a slowly varying function of the samples ϵ_r and h .

$$\tan \delta = \frac{Q^{-1} - Q_{Dr}^{-1} - Q_c^{-1}}{P_{es}} \quad (2.32)$$

where, Q is related to the unloaded quality factor of SPDR containing dielectric thin film, Q_{Dr} is related to the dielectric losses in the empty resonators, and Q_c belongs to the metal losses for the resonant cavity containing the thin film. The uncertainty in ϵ_r and $\tan \delta$ is calculated as,

$$\frac{\Delta \epsilon_r}{\epsilon_r} \leq 0.15\% + T \frac{\Delta h}{h} \quad (2.33)$$

where, $1 < T < 2$, and $\Delta \tan \delta = \pm 2.0 \times 10^{-5}$.

2.3.13 I-V characteristics

The leakage currents analysis is one of the most important characterizations for device applications. Most of the applications are based on the application of an external voltage on the ferroelectric capacitors either bulk ceramics or thin films, leading to the occurrence of leakage current. The leakage current might be the larger due presence of defects (oxygen vacancies, nonstoichiometric, defect states, and etc.) which leads to degradation in properties. The solutions to reduce the leakage current can be found by understanding the conduction mechanism in the samples. Therefore, it is very important to study the charging mechanism in samples to identify the conduction mechanisms responsible for the leakage current. In this thesis, the Keithley parameter analyzer (4200A-SCS, Tektronix, USA) was used to measure the leakage current versus applied voltage at room temperature.

2.4 References

- [1] S.-J. L. Kang, *Sintering: Densification, Grain Growth and Microstructure* (Elsevier, 2004).
- [2] R. L. Coble, *J. Appl. Phys.* **32**, 787 (1961).
- [3] D. H. Lowndes, D. B. Geohegan, A. A. Puretzky, D. P. Norton, and C. M. Rouleau, *Science* (80-.). **273**, 898 (1996).
- [4] D. B. Geohegan, D. B. Chrisey, and G. K. Hubler, Chrisey GK Hubler (Eds), Wiley, New York 59 (1994).
- [5] K. G. Weil, *Berichte Der Bunsengesellschaft Für Phys. Chemie* **84**, 1274 (1980).
- [6] P. K. Gallagher, M. E. Brown, and R. B. Kemp, *Handbook of Thermal Analysis and Calorimetry* (Elsevier New York, 1998).
- [7] B. D. Cullity, *Elements of X-Ray Diffraction by BD Cullity* (Addison-Wesley Publishing Company, 1978).
- [8] R. A. Young, *The Rietveld Method* (International union of crystallography, 1993).
- [9] R. Singh, *Phys. Perspect.* **4**, 399 (2002).
- [10] D. A. Skoog, F. J. Holler, and S. R. Crouch, *Principles of Instrumental Analysis*, 6th ed. (Cengage learning, 2017).
- [11] A. W. Varnes and F. A. Settle, *Handb. Instrum. Tech. Anal. Chem. Up.* Saddle River, New Jersey, Prentice Hall 419 (1997).
- [12] H. H. Willard, L. L. Merritt Jr, J. A. Dean, and F. A. Settle Jr, *Instrumental Methods of Analysis*, 7th ed. (CBS Publisher & Distributors, New Delhi, 1988).
- [13] E. Smith and G. Dent, *Modern Raman Spectroscopy: A Practical Approach* (John

- Wiley & Sons, England, Chichester, 2005).
- [14] J. R. Macdonald, *Ann. Biomed. Eng.* **20**, 289 (1992).
- [15] V. F. Lvovich, *Impedance Spectrosc.* New York Wiley 1 (2012).
- [16] M. E. Orazem and B. Tribollet, *Electrochemical Impedance Spectroscopy* (John Wiley & Sons, 2017).
- [17] C. B. Sawyer and C. H. Tower, *Phys. Rev.* **35**, 269 (1930).
- [18] A. H. Meitzler, H. Tiersten, A. Warner, D. Berlincourt, G. Couquin, and F. Welsh III, *Inst. Electr. Electron. Eng. Inc* (1987).
- [19] J. G. Smits, *IEEE Trans. Sonics Ultrason.* **23**, 393 (1976).
- [20] X.-H. Du, Q.-M. Wang, and K. Uchino, *IEEE Trans. Ultrason. Ferroelectr. Freq. Control* **50**, 312 (2003).
- [21] S. Hembacher, F. J. Giessibl, J. Mannhart, and C. F. Quate, *Phys. Rev. Lett.* **94**, 56101 (2005).
- [22] G. Binnig, H. Rohrer, C. Gerber, and E. Weibel, *Phys. Rev. Lett.* **50**, 120 (1983).
- [23] I. Horcas, R. Fernández, J. M. Gómez-Rodríguez, J. Colchero, J. Gómez-Herrero, and A. M. Baro, *Rev. Sci. Instrum.* **78**, 13705 (2007).
- [24] R. Swanepoel, *J. Phys. E.* **16**, 1214 (1983).
- [25] M. H. Saleh, N. M. Ershaidat, M. J. A. Ahmad, B. N. Bulos, and M. M. A.-G. Jafar, *Opt. Rev.* **24**, 260 (2017).
- [26] D. F. Swinehart, *J. Chem. Educ.* **39**, 333 (1962).
- [27] J. Tauc, *Opt. Prop. Solids* 277 (1972).
- [28] F. Abelès, *Optical Properties of Solids* (North-Holland Pub. Co., 1972).

- [29] H. Fujiwara, *Spectroscopic Ellipsometry: Principles and Applications* (John Wiley & Sons, 2007).
- [30] R. W. Boyd, in *Nonlinear Opt.*, edited by R. W. Boyd (Elsevier Science Academic Press, 2008).
- [31] R. W. Boyd, S. G. Lukishova, and Y. R. Shen, *Self-Focusing: Past and Present: Fundamentals and Prospects* (Springer Science & Business Media, 2008).
- [32] M. Sheik-Bahae, A. A. Said, T. H. Wei, D. J. Hagan, and E. W. Van Stryland, *IEEE J. Quantum Electron.* **26**, 760 (1990).
- [33] G. P. Bharti, P. P. Dey, and A. Khare, *Mater. Chem. Phys.* **216**, 206 (2018).
- [34] F. Z. Henari and A. A. Dakhel, *J. Appl. Phys.* **108**, 1 (2010).
- [35] Y. H. Wang, B. Gu, G. D. Xu, and Y. Y. Zhu, *Appl. Phys. Lett.* **84**, 1686 (2004).
- [36] K. K. Nagaraja, S. Pramodini, A. S. Kumar, H. S. Nagaraja, P. Poornesh, and D. Kekuda, *Opt. Mater. (Amst)*. **35**, 431 (2013).
- [37] Y. S. Zhou, E. B. Wang, J. Peng, J. Liu, C. W. Hu, R. D. Huang, and X. You, *Polyhedron* **18**, 1419 (1999).
- [38] J. Krupka, *J. Eur. Ceram. Soc.* **23**, 2607 (2003).
- [39] J. Krupka, A. P. Gregory, O. C. Rochard, R. N. Clarke, B. Riddle, and J. Baker-Jarvis, *J. Eur. Ceram. Soc.* **21**, 2673 (2001).
- [40] W. C. Oliver and G. M. Pharr, *J. Mater. Res.* **19**, 3 (2004).

Structural and Dielectric Properties of Ce-BNT and Gd-BNT Doped Ceramics

3.1 Introduction

The BNT ceramics have been considered as a good candidate for lead-free perovskite (ABO_3) family because of their excellent dielectric, ferroelectric and piezoelectric properties [1,2]. The rare-earth doping is believed to compensate for the volatility issue of BNT and inherent defects could be improved significantly. Further, considerable efforts have made with the substitution of dopants (donor and/or acceptor) either in A or B-site of BNT ceramics to enhance the ferroelectric and piezoelectric properties due to difference between the ionic radius of doping elements and lattice ions. The donor substitution of more positive ions (Li^{3+} , La^{3+} and Nd^{3+}) at A-site (Na^+ and Bi^{3+}) or Ta^{5+} , Nb^{5+} and Sb^{5+} at B-site (Ti^{4+}), which could improve the dielectric, ferroelectric and piezoelectric properties due to the formation of A-site vacancies facilitating the motion of domain and domain walls [3]. The rare-earth dopants are known to exhibit useful functions of stabilizing and lowering the dielectric loss due to low diffusivity characteristics [4]. Recently, Yi and Watcharapasorn et al. [5,6] reported that La and Dy-doped BNT ceramics induces A-site vacancies and improved grain growth inhibition and densification. Vijayeta et al. [7,8] investigated the Nd and Gd doped BNT ceramics using a semi-wet technique and improved ferroelectric properties. Moneim et al. [9] investigated the enhancement in energy-storage density (0.85 J cm^{-3} at 413 K) with the substitution of Gd into BNT, which is suitable for energy storage applications. Min C and Yueming L et al. [10,11] reported that the appropriate amount of CeO_2 on $(Na_{0.5}Bi_{0.5})_{0.93}Ba_{0.07}TiO_3$ and

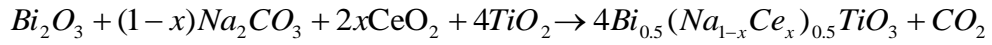
$\text{Bi}_{0.5}\text{Na}_{0.44}\text{K}_{0.06}\text{TiO}_3$ perovskite ceramics enhanced dielectric and piezoelectric properties. Moreover, BNT ceramics with relaxor behavior have attracted in industrial applications due to their larger dielectric constant in the broad temperature range and diffuse phase transition [12]. The origin of the relaxor behavior is might be due to the compositional disorder that arises from the substitution of different ions occupying the equivalent crystallographic sites [13]. It is observed that rare-earth-doped lead-free piezoelectric ceramics have shown the relaxor behavior by inducing the crystallographic distortion with improved dielectric properties [14]. A high dielectric constant (ϵ_r) and low loss tangent ($\tan\delta$) are the crucial parameters for the high-performance piezoelectric applications. However, there are only a few reports available on the rare-earth-doped BNT ceramics. According to the author's knowledge, there is no systematic study on the dielectric and AC-conductivity analysis of Ce and Gd doped BNT ceramics. In the present chapter, our aim is to study the effect of Ce^{+3} -BNT (BNTC) and Gd^{+3} -BNT (BGNT) doped ceramics on their structural, morphological, dielectric properties. This chapter classified into three parts. The first part describes the pure BNT with the effect of different sintering temperatures on structural, microstructural and dielectric properties. The second and third parts investigate the substitution of Ce and Gd into BNT on structural, microstructure, dielectric, and AC- conductivity studies, respectively.

3.2 Sample preparation of Ce and Gd doped BNT ceramics

Lead-free BNT ($x = 0$), $\text{Bi}_{0.5}(\text{Na}_{(1-x)}\text{Ce}_x)_{0.5}\text{TiO}_3$ (BNTC; $x = 0.015, 0.025$ and 0.035) and $(\text{Bi}_{1-x}\text{Gd}_x)_{0.5}\text{Na}_{0.5}\text{TiO}_3$ (BGNT; $x = 0.02, 0.04$ and 0.06) piezoelectric ceramics have been prepared by using a conventional solid-state reaction method. The high purity chemicals of Bi_2O_3 (Alfa-Aesar, 99.975%), Na_2CO_3 (Sigma Aldrich, 99.99%), TiO_2 (M/s Sigma-Aldrich, 99.99%) and CeO_2 (Sigma-Aldrich, 99.99%) and Gd_2O_3 (Alfa-Aesar,

99.99%), were used as starting materials and weighted according to their stoichiometry.

The BNTC and BGNT were prepared by the following chemical equations.



These powders were mixed for 5 h using a planetary ball mill (Pulverisette 6, Fritsch GmbH) and distilled water used as grinding media. The mixed slurry was dried at 120 °C and calcined at 800 °C for 3 h. These calcined powders were again grounded for 10 h to reduce the initial particle size. Then, the organic binder polyvinyl alcohol was added to the fine powders and pressed into cylindrical discs with dimensions of 10 mm in diameter and 1 mm of thickness. Further, these samples were sintered in the range of 1050 to 1150 °C for 3 h to obtain maximum density. The density of sintered pellets was measured using Archimedes's principle. The pure BNT, BNTC and BGNT ceramics sintered at 1100 and 1150 °C showed maximum relative density, uniform microstructure and better electrical properties. For electrical measurements, the silver paste was used as electrodes for both sides of the samples and heated at 150 °C for 10 minutes to dry the samples.

3.3 Results and discussion: Effect of sintering temperature on the densification of BNT ceramics

Figure 3.1 shows the DSC and TGA curves of BNT precursor powders synthesized by the solid-state reaction method. The total weight loss of BNT powder is ~11.3% observed in the temperature range of 25 °C–1150 °C. The decomposition process of BNT powders is divided into three distinct steps. The TGA curve of the first step shows ~3.5% weight loss from room temperature (RT) to 118 °C, which corresponds to the endothermic peak at 110 °C in the DSC curve, which occurs due to the evaporation of water molecules from the BNT powders. In the second step, TGA curve revealed ~2.3% of weight loss between 110 to 530 °C with one endothermic peak at 294 °C in the DSC curve is attributed

to the decomposition of starting precursors and release of CO₂ gas. The last step involved with maximum weight loss is around 5.5% in between 530 to 800 °C with two endothermic peaks at 604 °C and 748 °C due to secondary phase elimination and one exothermic peak at 800 °C is due to the crystallization. The weight loss is almost stable at ~800 °C with rising temperature indicates the formation of pure phase and corresponding exothermic peak confirmed the crystallization of BNT.

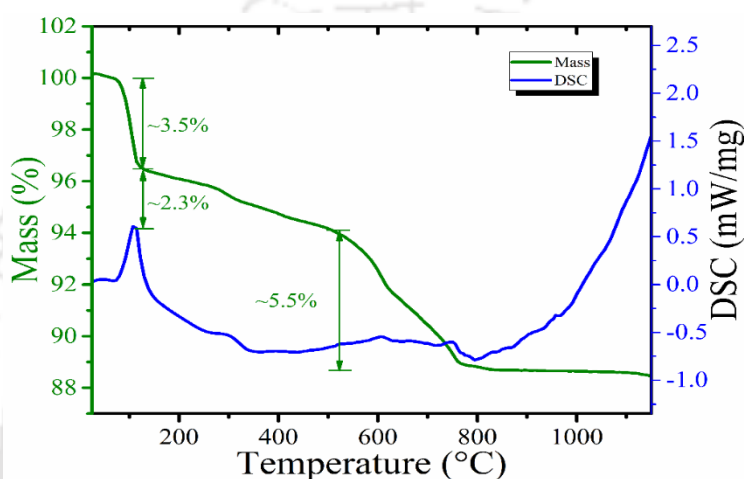


Figure 3.1: DSC and TGA curves of the BNT precursor powder.

Figure 3.2 shows the XRD patterns of BNT powders calcined at various temperatures from 600, 700 and 800 °C for 3h. The sample calcined at 600 and 700 °C revealed the BNT phase with a small secondary phase (* Bi₄Ti₃O₁₂), and further increasing temperature, a pure BNT phase is observed at 800 °C, which is also confirmed from the DSC-TGA analysis.

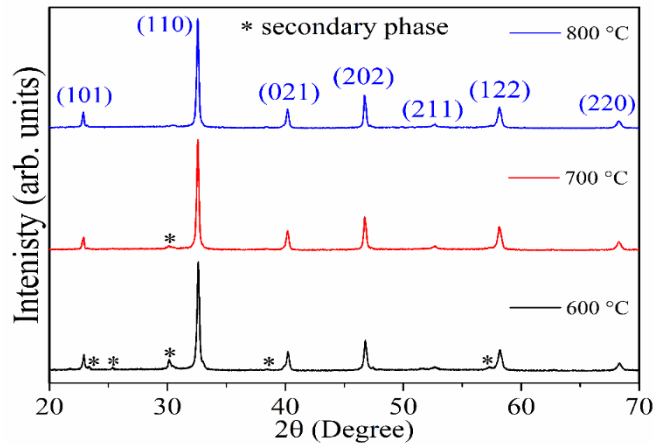


Figure 3.2: XRD pattern of calcined BNT ceramics at (a) 600 °C, (b) 700 °C, and (c) 800 °C for 3 hours.

The Rietveld refined XRD patterns of the sintered BNT ceramics are shown in Figure 3.3. The XRD analysis revealed the formation of a single-phase with rhombohedral crystal symmetry ($R3c$ space group) at room temperature. The lattice parameters, atomic positions and occupancy of the Bi, Na, Ti, and O atoms were refined by using Fullprof software, considering $R3c$ space group. The obtained lattice parameters and unit cell volumes are listed in Table 3.1. The lattice volume and density of sintered samples increased with sintering temperature up to 1100 °C and decreased beyond that. The density of the prepared samples was found to be in the range of 90-95 % of the theoretical density. The density and lattice volume decreased as the sintering temperature increases to 1150 °C. The grain boundary movements improve with sintering temperature. As a result, some closed pores remain inside the grains. Hence, the density of the ceramics sintered at 1150 °C is lower than 1100 °C.

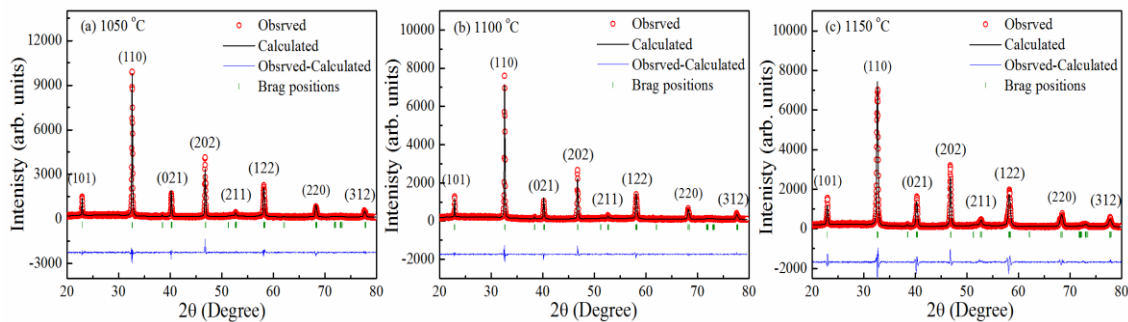


Figure 3.3: Rietveld refined XRD pattern of the BNT samples sintered at (a) 1050 °C, (b) 1100 °C and (c) 1150 °C for 3 h.

The crystallite size (D) of all sintered samples was calculated by using the Scherrer's equation [15,16]:

$$D = \frac{0.89\lambda}{\beta \cos \theta} \quad (3.1)$$

where, λ is the wavelength of the incident X-ray ($\text{Cu-K}\alpha = 1.5406 \text{ \AA}$), β is the full width at half maximum (FWHM) of the diffraction peak and θ is the Bragg angle. The crystallite sizes are found to be in the range of $48\text{-}52 \pm 2.5 \text{ nm}$. The larger crystalline size (52nm) with a maximum relative density of 95 % was obtained for the sample, sintered at 1100 °C.

Table 3.1: Rietveld refined parameters of BNT ceramics at different sintering temperatures.

Sintering temperature (°C)	χ^2	$a = b$ (Å)	c (Å)	Volume (Å ³)
1050	3.57	5.49	13.43	351.75±0.08
1100	2.33	5.50	13.44	352.44±0.03
1150	5.17	5.49	13.40	351.15±0.06

Raman spectroscopy is the most useful technique to study the structural deformation of perovskite systems. Figure 3.4 shows the Raman spectra of BNT ceramics (sintered at (a) 1050, (b) 1100 and (c) 1150 °C for 3 h measured over the range of 50 – 1000 cm^{-1}). The Raman spectrum is fitted with Origin software by using Gaussian function. There are nine vibrational modes observed at 83, 131, 227, 291, 371, 530, 599, 772 and 862 cm^{-1} , which are shown in Figure 3.4. The obtained results are in good agreement with the earlier reports [8, 9].

The BNT ceramics possess rhombohedral crystal symmetry with R3c space group. According to the group theory, R3c space group consists of 13 Raman active optical modes ($\Gamma_{\text{Raman}} = 4A_1 + 9 E$), where A_1 and E modes are Raman and IR active. These Raman active optical modes are due to disorder in the A- site of the BNT system associated with BiO_6 and NaO_6 clusters [17]. The scattering of light with respect to incoming polarization is responsible for splitting of optical modes into transverse (TO) and longitudinal (LO) components. The Raman active A_1 (TO_1) modes at 83 cm^{-1} and 131 cm^{-1} are related to the BiO_6 and NaO_6 clusters, respectively. The Raman active E (TO_2) modes at 227, 291 and 371 cm^{-1} are associated with the octahedral TiO_6 clusters and were observed in many perovskites [18]. The Raman-active LO_2 modes are responsible for low-intensity peaks and are related to short-range electrostatic forces associated with the lattice ionicity [19]. The TO_3 mode located around 530 cm^{-1} and 599 cm^{-1} corresponds to the (O-Ti-O) stretching symmetric vibrations of the TiO_6 clusters. The LO_3 modes observed at 772 and 862 cm^{-1} are due to the presence of sites within the rhombohedral lattice containing distorted octahedral TiO_6 clusters. These results indicate that the intensity of all the Raman modes increased with sintering temperature due to enhancement in disorder of A-site in BNT ceramics. However, no

significant changes observed in the Raman shift as well as the full width at half maximum (FWHM) in the spectra for sintered samples.

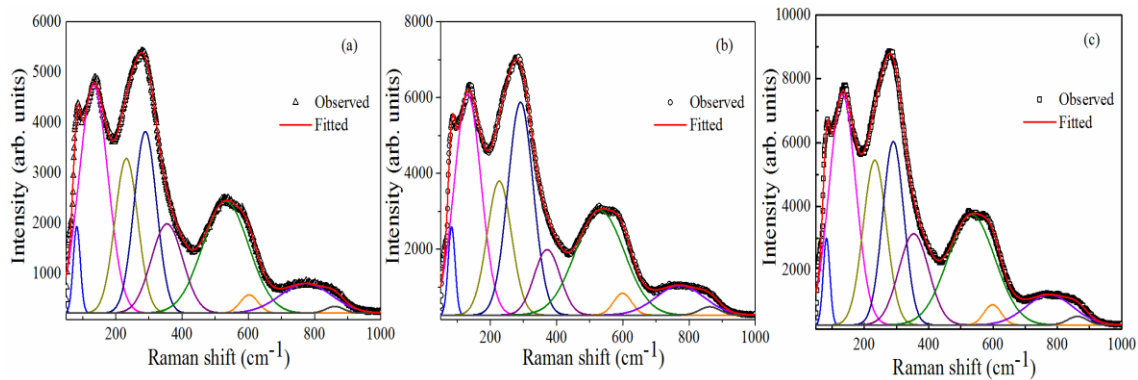


Figure 3.4: Raman spectra of BNT samples sintered at (a) 1050 °C, (b) 1100 °C and (c) 1150 °C.

Figure 3.5 shows the FESEM micrograph of the BNT ceramics, sintered at 1050, 1100 and 1150 °C for 3 h. The average grain size has been calculated using the linear intercept method and is found to increase from 1.09 to $1.98 \pm 0.52 \mu\text{m}$ with a rise in sintering temperature. The sample sintered at 1100 °C, exhibits rectangular shape grains with

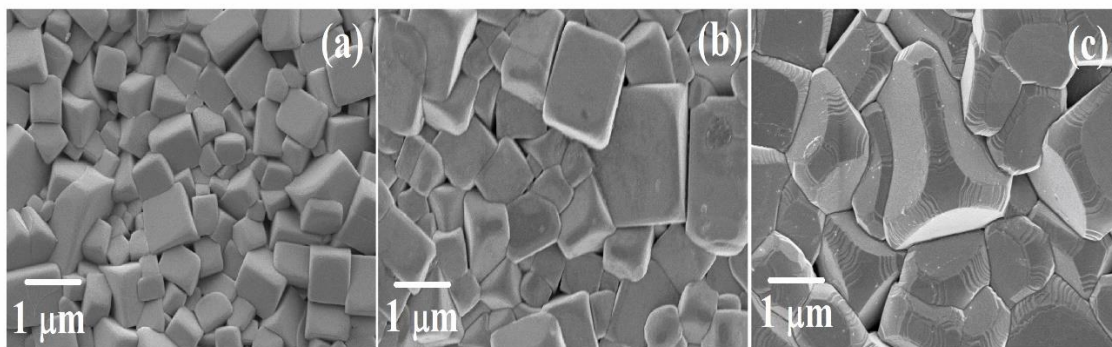


Figure 3.5: FESEM micrographs of the BNT ceramics sintered at (a) 1050 °C, (b) 1100 °C and (c) 1150 °C.

the average grain size of 1.40 μm . This sample showed well-defined grain boundaries and less porosity, which indicates that the sintered (1100 $^{\circ}\text{C}$) BNT ceramics having a high dense microstructure.

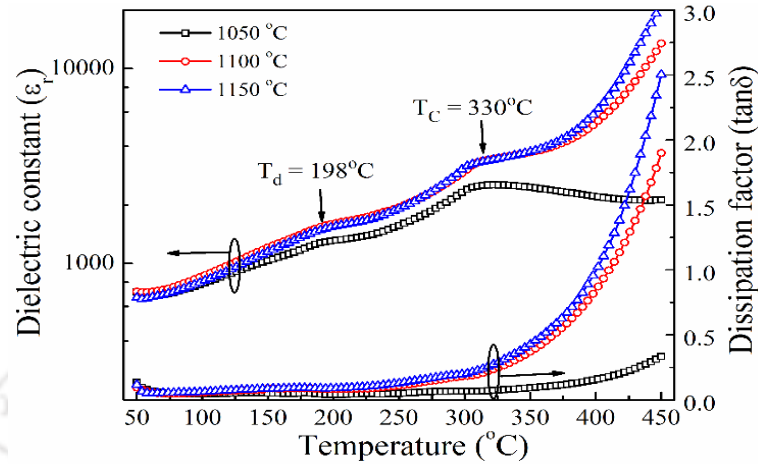


Figure 3.6: The temperature variation of dielectric constant (ϵ_r) and dissipation factor ($\tan\delta$) of BNT ceramics sintered at different temperatures, measured at 1 kHz.

The temperature dependence of ϵ_r and $\tan\delta$ for BNT ceramics sintered at different temperatures from 1050 $^{\circ}\text{C}$ to 1150 $^{\circ}\text{C}$ are shown in Figure 3.6. It is observed that the anomaly of dielectric constant around 198 $^{\circ}\text{C}$ is corresponding to the transition from ferroelectric to anti-ferroelectric phase transition, i.e., depolarization temperature (T_d) [20]. The Curie temperature T_C (330 $^{\circ}\text{C}$) of maximum dielectric constant ($\epsilon_r = 3524$) corresponds to the anti-ferroelectric to para electric phase transition. The ϵ_r start decreases above the T_C , it suggested that weakened dielectric properties in the cubic phase due to the increasing of randomness with the temperature in the unit cell of the BNT system. The sample sintered at 1100 $^{\circ}\text{C}$ showed the enhanced dielectric properties ($\epsilon_r = 694$, $\tan\delta = 0.103$) at 1 kHz and high Curie temperature (330 $^{\circ}\text{C}$). Further, with an increase in the sintering temperature (>1100 $^{\circ}\text{C}$) the dielectric properties were decreased due to the lower density and an increase in the porosity.

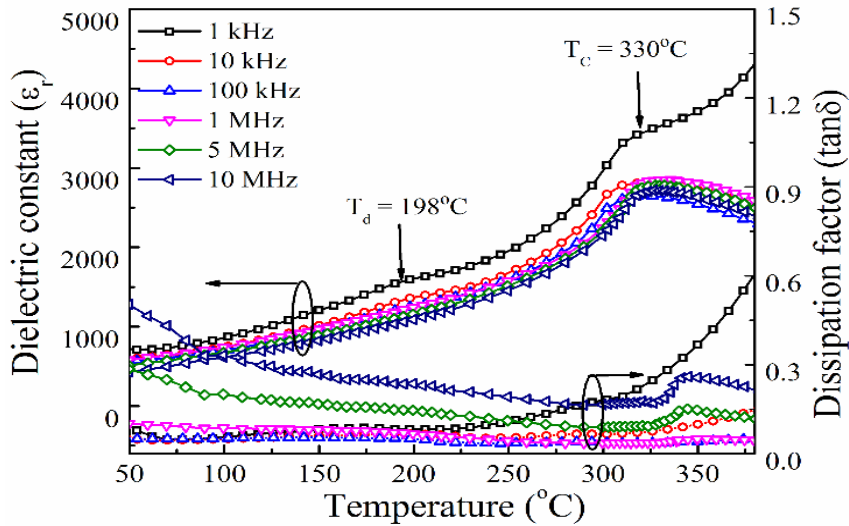


Figure 3.7: The temperature variation of dielectric constant (ϵ_r) and dissipation actor ($\tan\delta$) of BNT ceramics, sintered at 1100 °C and measured at different frequencies.

Figure 3.7. shows the temperature dependence of ϵ_r and $\tan\delta$ of BNT ceramics sintered at 1100 °C, measured at different frequencies from 1 kHz to 10 MHz. At low frequencies (1 kHz), the depolarization temperature clearly observed, as compared to the higher frequencies (10 MHz). However, the Curie temperature clearly observed for all the measured frequencies, and there is no significant change in the T_C is observed. The ϵ_r found to be decreased (466 at 10 MHz) with increasing the frequency due to the decrease in polarization. The higher values of ϵ_r at low frequencies might be due to the easy response of all the polarization mechanisms to the time varying electric field. As the frequency of the electric field increases, different polarization contributions filter out, and the net polarization of the material decreases. As a result, ϵ_r found to be decreased with an increase in the frequency. Initially, the dissipation factor found to be decreased up to 100 kHz and then increased with the frequency (10 MHz) due to the enhancement in the ionic conductivity within the sample.

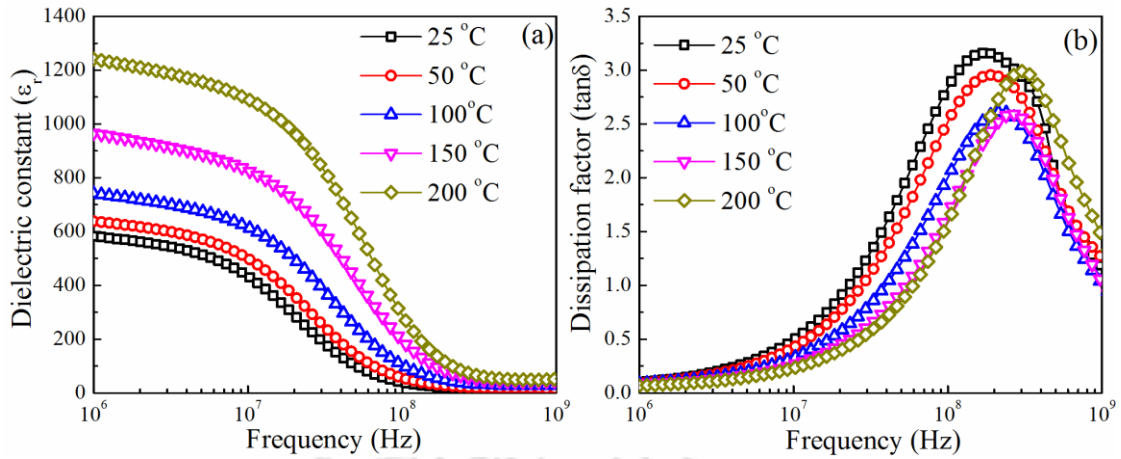


Figure 3.8: Frequency variation of dielectric constant (a) and dissipation factor (b) of BNT samples measured at different temperatures.

The high-frequency dependence of ϵ_r and $\tan\delta$ of BNT samples, sintered at 1100 °C and measured at different temperatures are shown in Figure 3.8. The ϵ_r is found to be increased whereas the $\tan\delta$ decreased with increasing the temperature. This is due to the fact that the molecules cannot orient themselves at room temperature. As the temperature increases, the orientation of dipoles facilitated, which leads to enhancement in the ϵ_r and decrement in the $\tan\delta$ was observed. From the Figure 3.8., it is observed that with increasing the temperature from 25 °C to 200 °C, the frequency of the maximum $\tan\delta$ shifted from 168.6 MHz to 301.9 MHz, which is the typical signature of relaxor ferroelectrics. Normally, the existence of the relaxor ferroelectric behavior is due to the formation of polar nano regions, which possess different relaxation times [21]. Due to the delay in the dielectric response of such frozen polar nano regions, the frequency corresponds to the maxima of $\tan\delta$ shifts towards high-temperature side.

3.4 Results and discussion: Ce doped BNT ceramics

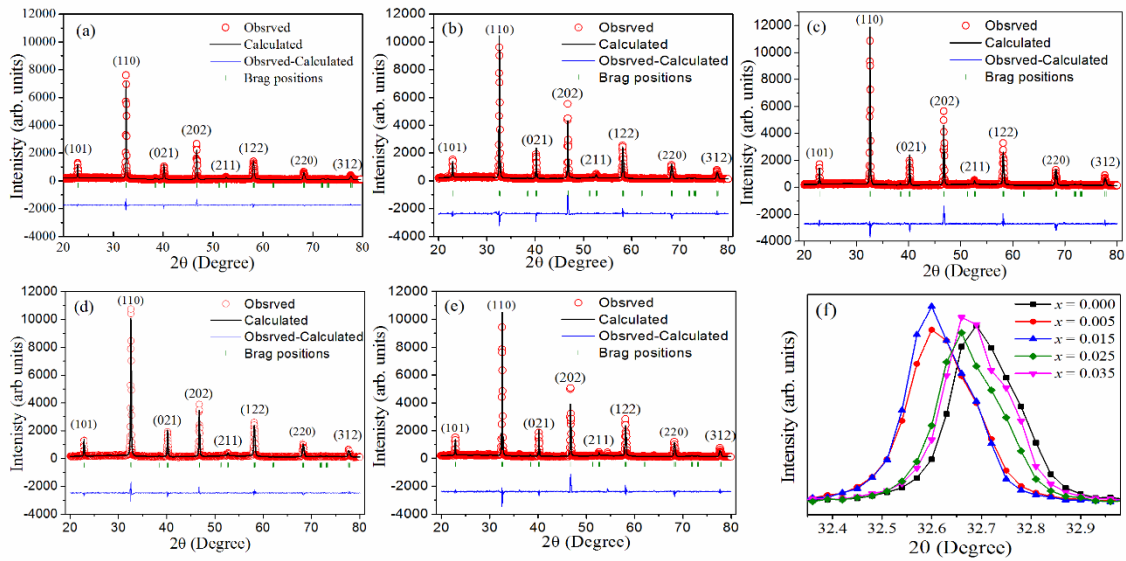


Figure 3.9: Rietveld refined XRD pattern of the BNTC ceramics for (a) $x = 0.00$, (b) 0.005 , (c) $x = 0.015$, (d) $x = 0.025$, (e) $x = 0.035$ and (f) magnified image of (110) diffraction peak of all BNTC samples.

The room temperature XRD patterns along with the Rietveld refinement of the BNTC ceramics, sintered at $1150\text{ }^{\circ}\text{C}$ for 3 h shown in Figure 3.9. All the BNTC ceramics exhibited a pure perovskite phase with rhombohedral crystal symmetry, which indicates that the Ce ions diffused into the BNT lattice and formed a solid solution. The lattice parameters (a , b , and c) and atomic positions of the Bi, Ce, Na, Ti, and O atoms were refined using Fullprof software by considering the R3c space group (JCPDS No. 01-085-0530) [22]. The obtained lattice parameters and unit cell volumes were listed in Table 3.2. It is observed that the unit cell volume found to be increased up to $x = 0.015$ and further it decreases above $x = 0.025$ sample. The expansion and compression of the unit cell volume with Ce doping might be due to the occupation of Ce ions in different sites of perovskite structure at different concentrations.

Table 3.2: Rietveld refinement parameters of $\text{Bi}_{0.5}(\text{Na}_{1-x}\text{Ce}_x)_{0.5}\text{TiO}_3$ ceramics.

x	χ^2	$a = b$ (Å)	c (Å)	Volume (Å ³)
0	5.43	5.491	13.430	350.551±0.06
0.005	5.38	5.495	13.449	351.790±0.05
0.015	6.10	5.502	13.451	352.353±0.04
0.025	2.35	5.489	13.439	352.047±0.07
0.035	5.19	5.492	13.430	351.073±0.06

The crystalline size of all the samples was calculated by using the Scherrer equation (Eq. 3.1). It is found to be increased from 47 nm to $48 \text{ nm} \pm 2.37 \text{ nm}$ with increasing Ce concentration up to $x = 0.015$ and further decreased to 46 nm for $x = 0.035$ sample. A similar trend was observed for the lattice parameters, density and grain size. From Figure 3.9f, it can be clearly seen that as the Ce concentration increases, the position of the (110) diffraction peak shifted towards the lower Bragg angle side up to $x = 0.015$, then after it shifted back to higher Bragg's angle side. It can be attributed to Ce occupancy. Initially, Ce occupied in the B (Ti) site, then after it occupied in A (Na) site due to mismatch in the ionic radii and valance. For the low concentration of $x (\leq 0.015)$, the Ce^{3+} (1.01 Å) ions occupied the Ti^{4+} (0.605 Å) site, whereas the Ce^{3+} ions occupied the Na^{1+} (1.02 Å) site at higher concentrations of $x (\geq 0.025)$ [23]. These obtained results are also co-related with microstructural analysis.

The back-scattered Raman spectra of BNTC ceramics, recorded at room temperature were depicted in Figure 3.10. All the BNTC ceramics exhibited the rhombohedral crystal symmetry with R3c space group. In this work, nine Raman active modes observed and were fitted with Lorentz function using Magic plot software. According to the group theory, R3c space group consists of 13 Raman active modes ($\Gamma_{\text{Raman}} = 4A_1 + 9 E$), which is proposed to be due to the disorder in A- site of BNTC ceramics.

Where, A_1 and E modes are Raman and IR active [17]. These optical modes are split into and transverse (TO) and longitudinal (LO) components, on the basis of scattered light with respect to incoming polarization. The Raman active A_1 (TO_1) modes appeared below 159 cm^{-1} are corresponding to the displacement of octahedral BiO_6 and NaO_6 clusters. The Raman active E (TO_2) modes at 212 cm^{-1} to 295 cm^{-1} , which are assigned as stretching modes arising from the bonds due to the presence of TiO_6 clusters in the short-range and which was observed in many perovskites [18]. The wavenumber above 212 cm^{-1} (Ti-O and oxygen-related) modes can be influenced by cationic substitution with different sizes at the A-site produces a distortion of the unit cell of BNTC [24]. The TO_3 mode located at around 487 cm^{-1} to 582 cm^{-1} due to the (O-Ti-O) stretching and symmetric vibrations of the TiO_6 clusters. The LO_3 mode was observed at 615 to 856 cm^{-1} are due to the presence of the sites within the rhombohedral lattice containing distorted TiO_6 clusters. The Raman-active (LO_2) modes with low intensity and related to short-range electrostatic forces associated with the lattice ionicity [19].

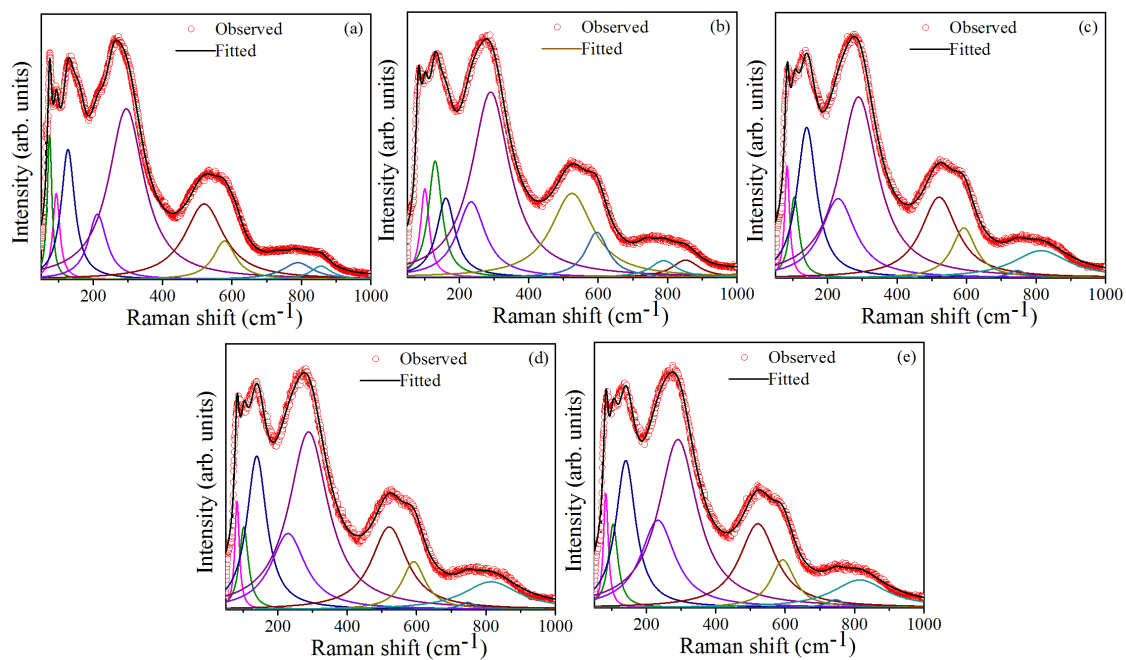


Figure 3.10: Raman spectra of BNTC ceramics for (a) $x = 0$ (b) $x = 0.005$ (c) $x = 0.015$ (d) $x = 0.025$ and (e) $x = 0.035$.

However, there is very small difference observed in the spectra of BNTC samples. We have interpreted this due to the small amount of Ce doping. The FWHM and shift of Raman modes is a distinctive characteristic of the short-range order/disorder state of a material [25]. The modes appeared in the range of 212–295 cm^{-1} , are found to be shifted toward a lower wavenumber (295 – 288 cm^{-1}) with increasing x up to 0.015 and further, shifted to higher wavenumber (290 cm^{-1}). Whereas, the FWHM of all modes found to be increased with x up to 0.015 and further it is decreased. The modes in-between 212–295 cm^{-1} correspond to the vibrations of TiO_6 octahedra. The changes in shift and FWHM of these modes related to octahedral distortion caused by the incorporation of Ce^{3+} ions [24]. Due to the substitution of larger ions in the A- site of perovskite, the shifting of the frequency mode towards the lower wavenumber side is expected from the relation between the optical phonon frequency and the reduced mass of ion [26].

Figure 3.11 display the surface micrographs of the BNTC ceramics, sintered at 1150 $^{\circ}\text{C}$ for 3 h. All the samples showed the homogenous grains with well-defined grain boundaries with rectangular shape, less porosity. The average grain size of all the samples was calculated using the linear intercept method and is found to be $1.4 \pm 0.39 \mu\text{m}$ for the pure BNT sample ($x = 0$). With an increase in the Ce concentration, the grain size ($2.2 \pm 0.93 \mu\text{m}$) was found to be increased up to $x = 0.015$ and further decreased to $1.1 \pm 0.31 \mu\text{m}$ for $x = 0.035$ sample. The grain size of the BNTC ceramics also showed similar behavior to that of the volume of the unit cell and crystalline size. However, a further increase in the Ce concentration ($x > 0.015$) inhibits the grain growth, which leads to the reduction of grain size. Consequently, the segregation of the excess oxide near the grain boundaries decreases their mobility. The reduction in grain boundary mobility, as well as mass transportation causes, inhibited grain growth [27]. The relative density (90 - 95 %) of the samples improved with increasing the Ce concentration, which is due to the

enhancement in the activity of the atoms in the crystal structure and facilitation of migrated atoms.

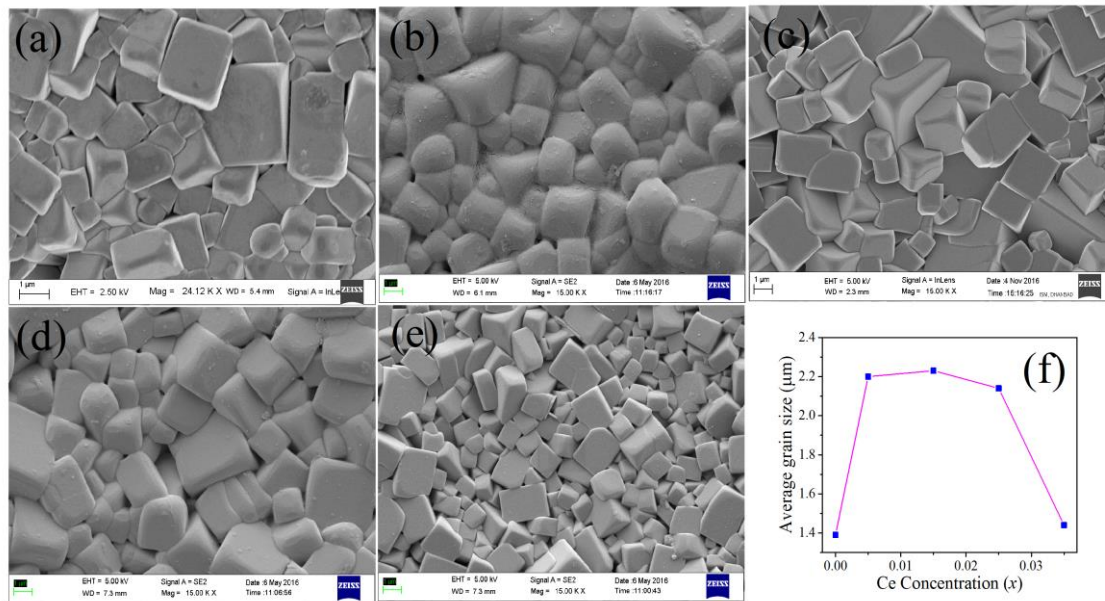


Figure 3.11: FESEM micrograph for (a) $x = 0$, (b) $x = 0.005$, (c) $x = 0.015$, (d) $x = 0.025$, (e) $x = 0.035$ of BNTC ceramics and (f) Ce concentration versus average grain size of BNTC samples.

The dielectric properties of BNTC ceramics were measured in the temperature range of 30 °C to 400 °C at 1 MHz are shown in Figure 3.12. The undoped and Ce doped BNT ceramics exhibited the structural transitions from ferroelectric rhombohedral to antiferroelectric tetragonal structure around 200 °C, which also called depolarization temperature (T_d), and another transition from antiferroelectric tetragonal to paraelectric cubic structure around 330 °C. At room temperature, the undoped system exhibited the ϵ_r and $\tan\delta$ of 461 and 0.30 at 1MHz, respectively. With an increase in the Ce concentration, ϵ_r increases and $\tan\delta$ decreases. The enhanced ϵ_r (775) and low $\tan\delta$ (0.032) @ 1 kHz were obtained for $x = 0.025$ sample. Beyond the T_C , the ϵ_r found to be decreased due to the increase in the randomness of dipoles in BNTC with temperature and weakens the dielectric properties in the cubic phase. The dielectric loss also showed a clear anomalies

at phase transitions. The temperature-dependent dielectric constant of BNTC ceramics exhibited the diffuse phase transitions near the transition temperature around 330 °C, which is the typical behavior of relaxor ferroelectrics [28]. Therefore, a modified Curie-Weiss law proposed by Uchino and Nomura [29], was used to describe the relaxor behavior of the BNTC ceramics.

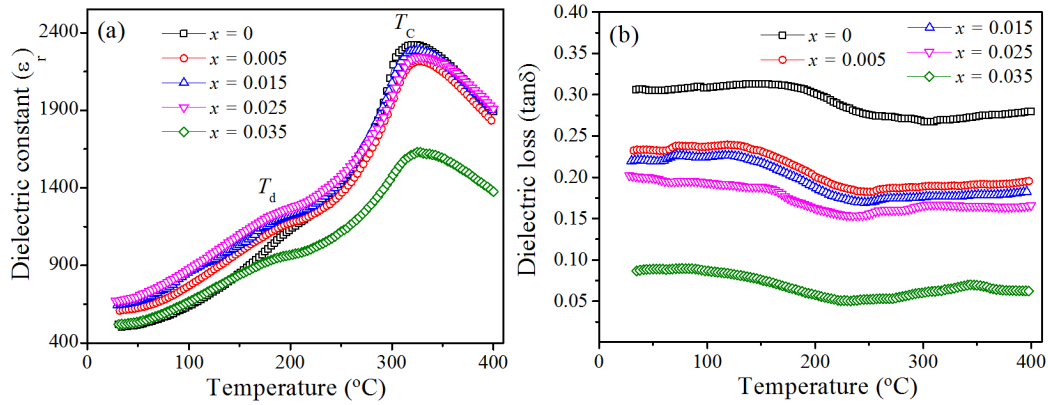


Figure 3.12: The temperature dependence of (a) ϵ_r and (b) $\tan\delta$ of BNTC ceramics, measured at 1 MHz.

$$(1/\epsilon_r) - (1/\epsilon_r^m) = (T - T_m)^\gamma / C \quad (3.2)$$

where, ϵ_r^m represents the maximum dielectric constant at a temperature T_m , C is the Curie constant and γ is the diffuseness coefficient. The value of γ should be equal to the unity for normal ferroelectrics and for relaxor ferroelectrics γ varies from 1 to 2. The value of γ has been calculated for all the samples by finding the slope of the Eq. 3.2 as shown in Figure 3.13 (a). The calculated γ values lie in the range of 1.63-1.83 (Figure 3.13 (b)), which indicates that the BNTC system exhibited relaxor behavior. The pure BNT sample shows the γ value 1.72 and it is found to be increased to 1.83 for the $x = 0.015$ sample. It can be understood as the substitution of Ce^{3+} for Ti^{4+} leads to an increase of disorder distribution and disturbance of long-range ferroelectric ordering [21]. Further, with an increase in x concentration, γ value found to be decreased due to the substitution of Ce^{3+} in Na^+ site.

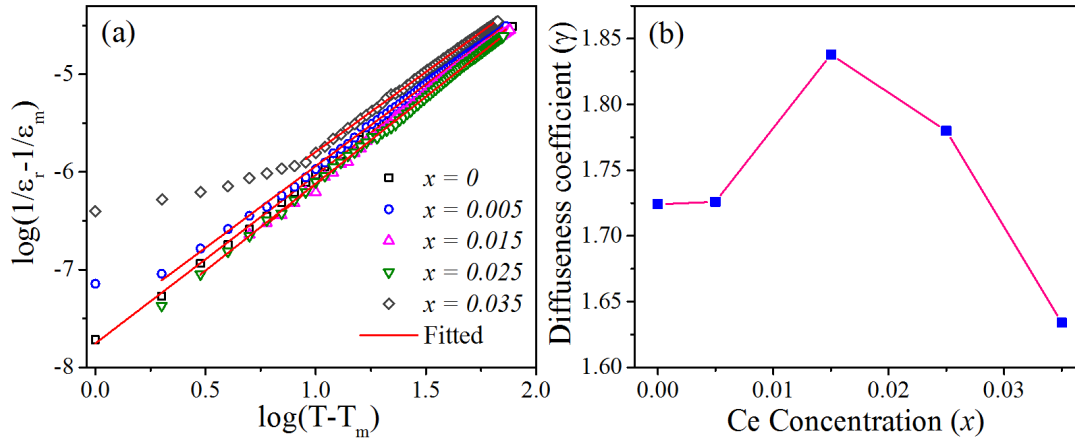


Figure 3.13: (a) The variation of $\log(1/\epsilon_r - 1/\epsilon_m)$ as a function of $\log(T - T_m)$ measured at 1 MHz and (b) γ versus Ce concentration of BNTC ceramics.

The AC-conductivity (σ_{ac}) measurements of BNTC ceramics are measured in the temperature range of 30 °C - 400 °C at 1 MHz. The activation energy (E_A) of the BNTC ceramics have been calculated by using Arrhenius relation [30],

$$\sigma_{ac} = \sigma_0 \exp(E_A / k_B T) \quad (3.3)$$

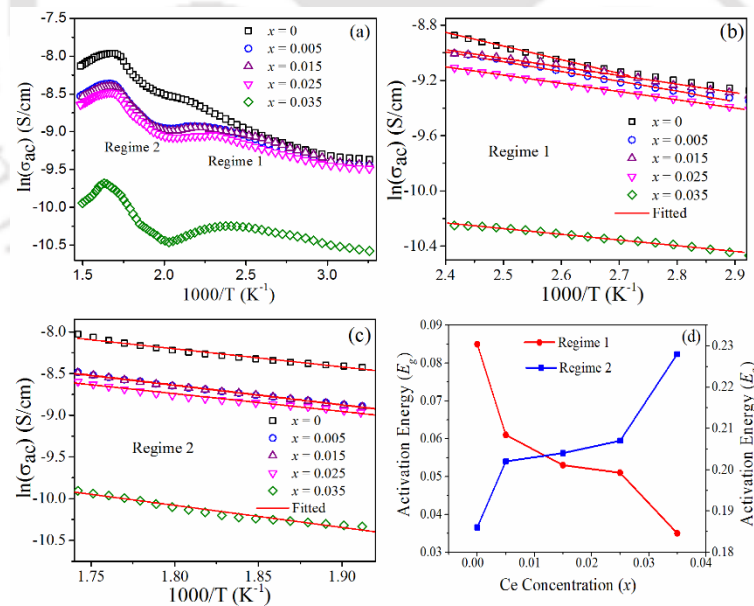


Figure 3.14: Variation of logarithmic σ_{ac} with the reciprocal temperature of (a) actual data, and fitted with Arrhenius relation in (b) Regime 1 (c) Regime 2, and (d) Ce concentration versus E_A of BNTC ceramics calculated in different regimes.

where, σ_0 is the pre-exponential factor, k_B is the Boltzmann constant, and T is the absolute temperature. The activation energy (E_A) calculated from the slope of the $\ln\sigma_{ac}$ versus $1000/T$ which is shown in Figure 3.14 (a). Two different temperature regimes were identified where the $\ln\sigma_{ac}$ versus $1000/T$ exhibits linear behavior. The calculated E_A values are in the range 0.035- 0.085 eV for the regime 1 (356-434 K) and 0.183- 0.228 eV for regime 2 (520 - 581 K), as shown in Figure 3.14 (a-b). The variation of activation energy values calculated as a function Ce Concentration was shown in Figure 3.14(d). The activation energy found to be decreased with a rise in Ce concentration in regime 1, it can be understood as the increasing of random hopping of charge carrier between the localized states. Whereas, the E_A values are found to be higher in regime 2 as compared to regime 1 due to the release more of charge carriers from the oxygen vacancies, excess amount electrons available in the A-site and phase change from anti-ferroelectric to paraelectric phase, which can strongly affect the AC-conductivity.

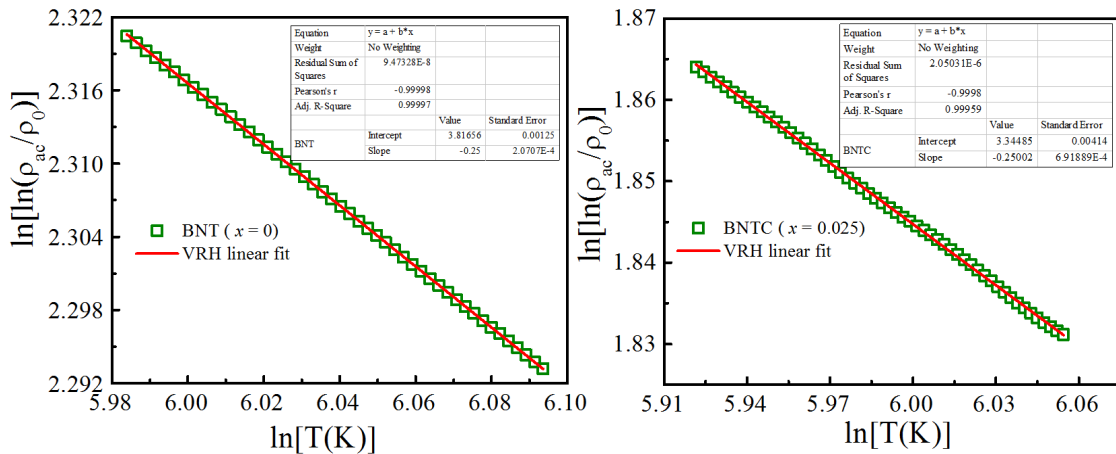


Figure 3.15: Fitting of VRH mechanism in pure ($x = 0$) and Ce^{3+} doped BNT ($x = 0.025$) ceramics.

In order to understand, the effect of Ce on the AC-conductivity of BNT ceramics was analyzed the AC-resistivity by using variable range hopping (VRH) model for

undoped ($x = 0$) and doped BNT samples ($x = 0.025$). Therefore, the resistivity data is fitted to the following equation [31,32],

$$\rho_{ac} = \rho_0 \exp(T_0 / T)^{1/4} \quad (3.4)$$

where, ρ_0 and T_0 represent the pre-exponential factor and characteristic temperature coefficient, respectively [33]. The linear variation in the $\ln\rho_{ac}$ versus $T^{-1/4}$ in a temperature range can provide the typical signature of the VRH process. The $\ln[\ln(\rho_{ac})]$ versus $\ln(T)$ plot for the both samples $x = 0$ and $x = 0.025$ in the regime 1 have been displayed in the Figure 3.15. Interestingly, both the samples exhibited the linear behavior with the slope exactly equal to -0.25 and it indicates that the VRH mechanism is the dominant conduction mechanism in the BNTC system. By using the fitted parameter T_0 and decay length α^{-1} , the density of states near the Fermi level ($N(E_F)$) can be extracted using the following formula [34].

$$N(E_F) = 16\alpha^3 / k_B T_0 \quad (3.5)$$

Where K_B is Boltzmann constant. The estimated value of $N(E_F)$ for the pure BNT system is $2.016 \times 10^{20} \text{ eV}^{-1} \text{ cm}^{-3}$, whereas it was increased to $1.330 \times 10^{21} \text{ eV}^{-1} \text{ cm}^{-3}$ for the doped system. Further, the average hopping length (R_H) between energy levels and the average hopping energy (W_H) was calculated using the following Equations [34] [35],

$$R_H = 0.75 \times [3 / (2\pi\alpha N(E_F) k_B T)]^{1/4} \quad (3.6)$$

$$W_H = [3 / (4\pi R_H^3 N(E_F))] \quad (3.7)$$

The obtained parameters for the VRH conduction mechanism for both samples satisfied the condition $W_H \geq k_B T$ and $\alpha R_H \geq 1$. From Figure 3.16, the R_H found to be decreased whereas W_H increases with an increase in the temperature and is attributed to the rise in disorder in the system. It has been observed that both R_H and W_H decreased with Ce doping, which is due to the enhancement of defect states near the Fermi level. It indicates

that Ce^{3+} assisted the hopping of charge carriers from one localized state to another in the BNT system.

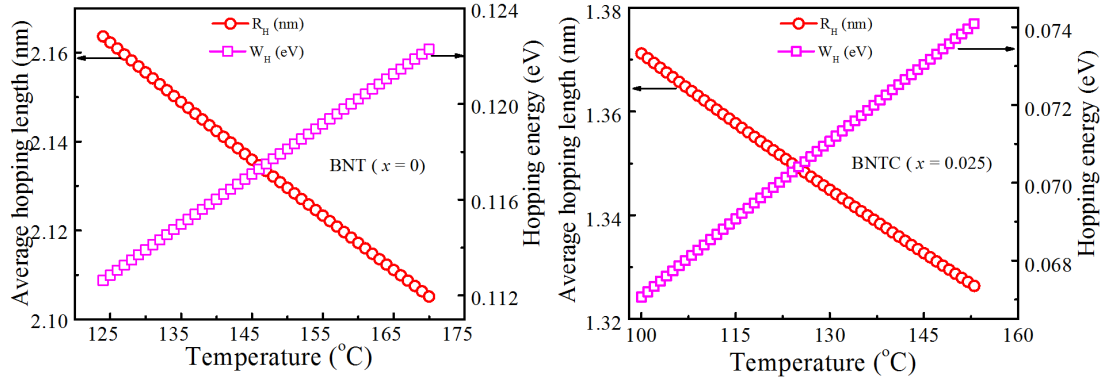


Figure 3.16: Temperature variation of Mott's variable range hopping parameters pure ($x = 0$) and doped ($x = 0.025$) ceramics.

3.5 Results and discussion: Gd doped BNT ceramics

The XRD pattern along with Rietveld refinement of BGNT ceramics, sintered at 1150 °C for 3 h is shown in Figure 3.17. XRD analysis of all the samples revealed the formation of a single-phase with rhombohedral crystal symmetry RT. The lattice parameters, atomic positions and occupancy of the Bi, Gd, Na, Ti, and O atoms were refined by using Fullprof software by considering R3c space group was listed in Table 3.3. It is observed that the lattice volume of the BGNT system found to be decreased with increasing Gd concentration due to radii of Gd^{3+} (0.938 Å) as compared to Bi^{3+} (1.03 Å).

Table 3.3: Rietveld refinement parameters of $(Bi_{1-x}Gd_x)_{0.5}Na_{0.5}TiO_3$ ceramics.

x	χ^2	Brag R factor	R_f factor	$a = b$ (Å)	c (Å)	Volume (Å ³)
0	2.36	2.98	3.81	5.49	13.44	352.44±0.03
0.02	3.16	5.37	4.78	5.50	13.45	352.41±0.05
0.04	2.91	8.52	8.41	5.49	13.43	351.59±0.06
0.06	2.91	5.86	5.58	5.49	13.44	350.52±0.05

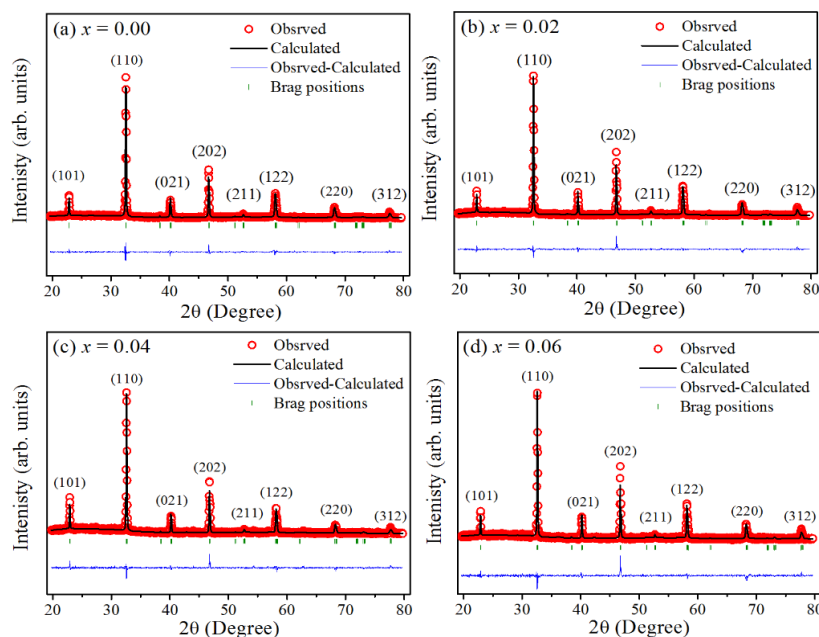


Figure 3.17: Rietveld refined XRD pattern of the BGNT ceramics ($x = 0.00$ to 0.06), sintered at $1150\text{ }^{\circ}\text{C}$ for 3 h.

The BGNT ceramics exhibited the rhombohedral crystal symmetry with the $R3c$ space group. Figure 3.18 shows the Raman spectra of BGNT ($x = 0.00$ to 0.06) samples. According to the group theory, the $R3c$ space group consists of 13 Raman active modes ($\Gamma_{\text{Raman}} = 4A_1 + 9E$), which is due to the disorder in the A- site of BGNT ceramics [17,36].

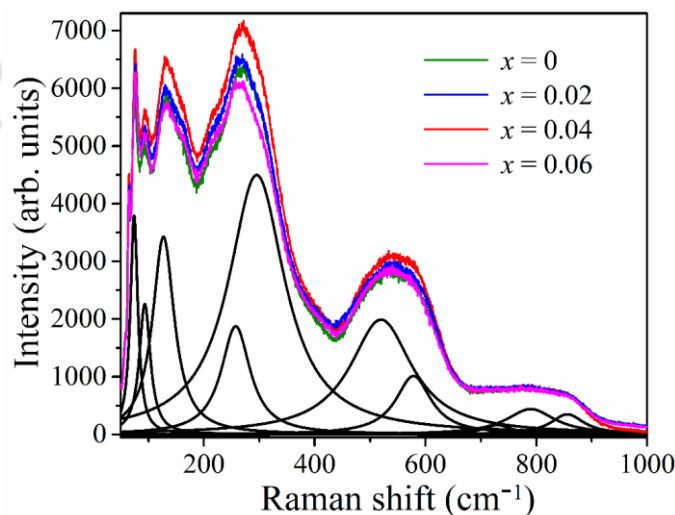


Figure 3.18: Raman spectra of BGNT ($x = 0.00$ to 0.06) samples.

The Raman modes that appeared below 159 cm^{-1} are corresponding to the distorted octahedral BiO_6 , and NaO_6 clusters, respectively. The Raman active E (TO2) mode at 210 cm^{-1} to 396 cm^{-1} , which are assigned as stretching modes arising from the bonds due to the presence of octahedral TiO_6 clusters in the short-range [18]. The Raman-active (LO2) mode with low intensity recognized to short-range electrostatic forces associated with the lattice ionicity [19]. The TO3 mode located at around 487 cm^{-1} to 582 cm^{-1} increasing due to the (O-Ti-O) stretching symmetric vibrations of the octahedral TiO_6 clusters. The LO3 mode was observed at 615 to 856 cm^{-1} are due to the presence of the sites within the rhombohedral lattice containing distorted TiO_6 clusters. These optical modes are split into longitudinal (LO) and transverse (TO) components due to the electric structure with the polar character of a lattice. It observed that the intensity of the peaks found to rise with Gd concentration due to the increase of disorder in the A-site of BGNT ceramics.

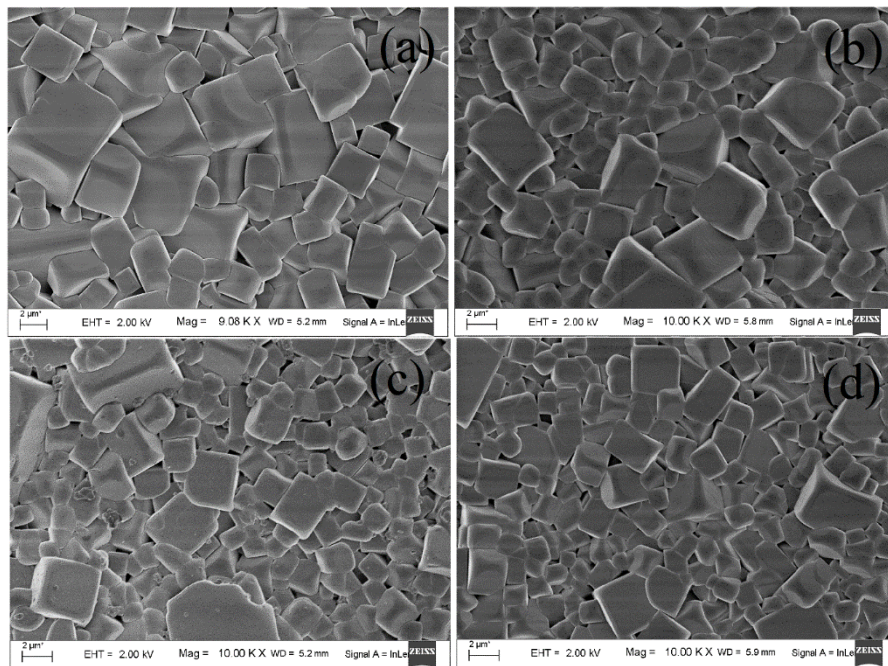


Figure 3.19: FESEM micrographs of the BGNT samples (a) 0.00, (b) 0.02, (c) 0.04 and (d) 0.06.

Figure 3.19 shows the FESEM micrograph of the BGNT ceramics, sintered at 1150 °C for 3 h. All the samples showed the homogenous grains with rectangular shape, less porosity and well-defined grain boundaries which indicates that the sintered BGNT ceramics have dense microstructure. The average grain size calculated using the linear intercept method and is found to be $3.2 \pm 0.91 \mu\text{m}$ to $1.2 \pm 0.34 \mu\text{m}$. The observed smaller grain size at higher concentrations of Gd might be due to the reduction in the grain boundary mobility as well as mass transportation [27].

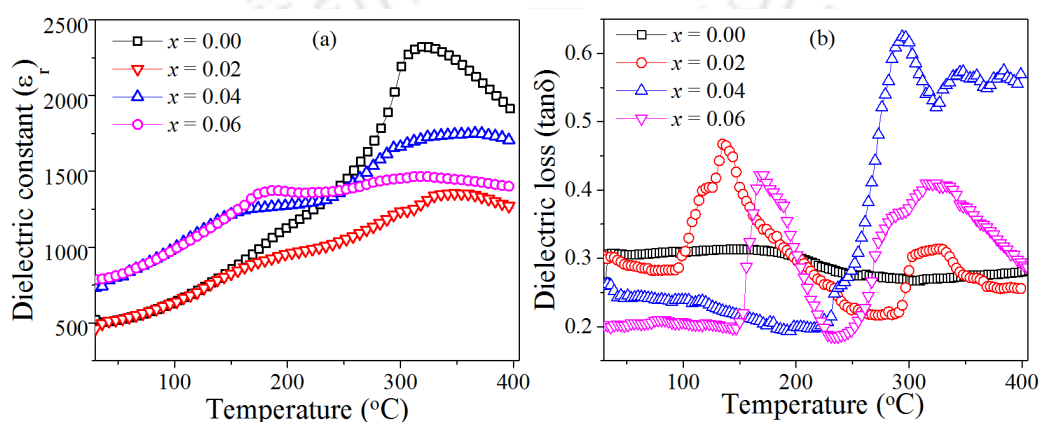


Figure 3.20: The temperature variation of ϵ_r (a) and $\tan\delta$ (b) of BGNT ceramics ($x = 0.00$ to 0.06) measured at 1 MHz.

The dielectric properties of BGNT ceramics were measured in the temperature range of 30 °C to 400 °C at 1 MHz are shown in Figure 3.20. The pure and Gd doped BNT ceramics exhibited the structural transitions from ferroelectric rhombohedral to antiferroelectric tetragonal phase transition around 160 - 200 °C, which is called as depolarization temperature (T_d), and another transition from antiferroelectric tetragonal to paraelectric cubic phase transition around 317 - 345 °C (i.e., Curie temperature, T_C). The T_C is shifted towards higher temperature (345 °C) for $x = 0.02$ and further, it shifted towards lower temperature (317 °C) for $x = 0.06$, where T_d shifted towards lower temperature for all the samples. The T_C and T_d were shifted towards lower temperatures with the incorporation of smaller Gd^{3+} ions at the A-site of the BNT system. It is due to the

heterovalent cation distribution on the same crystallographic site, which results in short-range polar order/random electric fields at the nano-scale. It causes a small distortion in the crystallographic unit cell and an increase of short-range harmonic restoring force in the system. The decrease in T_C and T_d can be understood by the following equation.

$$T_C = \frac{K_L - K_S}{B} \quad (3.8)$$

where, K_L is the long-range force constant, K_S is the short-range harmonic restoring force constant, and B is the anharmonic coefficient [37]. With an increase in Gd concentration, the ϵ_r enhanced and $\tan\delta$ decreased. The enhanced ϵ_r (809) and low $\tan\delta$ (0.201@1kHz) were obtained for $x = 0.06$ sample. Beyond the T_C , the ϵ_r found to be decreased due to the increasing the randomness of dipoles in BGNT with temperature and weakens the dielectric properties in the cubic phase. The dielectric loss also has shown the clear anomalies at phase transitions.

The activation energies (E_A) of all samples were estimated from the temperature dependence of ac conductivity (σ_{ac}) by using the Arrhenius equation by Eq. 3.3 [38]. The E_A values estimated from the slope of $\ln\sigma_{ac}$ versus $1000/T$ plots at different regimes were shown in Figure 3.21. For pure BNT, the activation energy is found to 0.085 eV in regime 1 (333 – 414 K) and 0.186 eV in regime 2 (518 – 542K). The E_A values are found to be increased from 0.032 – 0.043 eV for $x = 0.02$ to 0.06 in regime 1. This behavior can be understood from the enhancement in a random distribution of hopping charge carriers between the localized states. In regime 2 (518 – 542K), the activation energy values are found to be decreased from 0.86 – 0.37 eV for $x = 0.02$ to 0.06, which are higher than pure BNT (0.186 eV) and in regime 1 values and is attributed to the redistribution of oxygen vacancies and other charge carriers such as electrons and holes. However, the obtained activation energy values are less than 1 eV which signifies the presence of oxygen

vacancies due to the relaxation of charge carriers or defects of ion in complexes in the system.

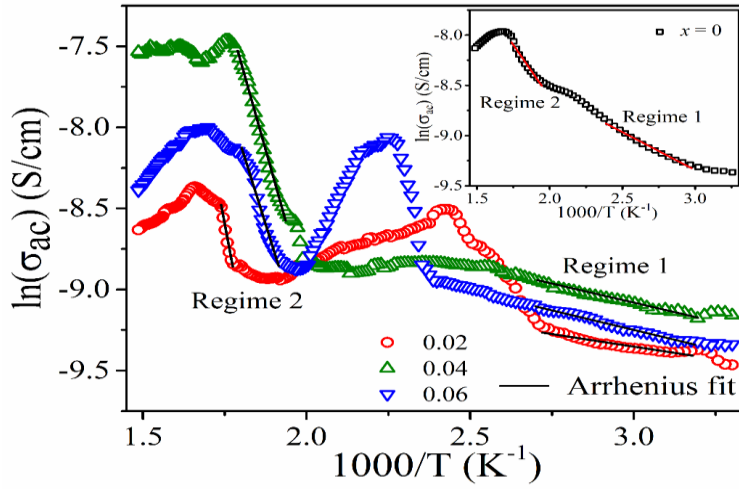


Figure 3.21: Temperature-dependent of AC-conductivity of BGNT ceramics fitted with Arrhenius equation for (a) $x = 0$ (inset), (b) $x = 0.02$, (c) $x = 0.04$ and (d) $x = 0.06$.

Further, the temperature dependence of AC-resistivity in BGNT ceramics were analyzed using Mott's variable-range-hopping (VRH) mechanism [32,33]. The linear plots of $\ln[\ln(\rho_{ac})]$ versus $\ln(T)$ for BNGT ceramics ($x = 0$ and 0.06) measured at 1 MHz in the temperature range of 531 – 572 K and are fitted with the Eq. 3.4, shown in Figure 3.22. It can be seen that both the samples exhibited the linear behavior with the slope of '-0.25', which indicates the signature of the VRH mechanism in the vicinity of the transition temperature. Further, the density of states across the Fermi level ($N(E_F)$) has been estimated by using the Eq. 3.5. In the R2 regime, the $N(E_F)$ values are enhanced from 8.053×10^{18} to $2.897 \times 10^{20} \text{ eV}^{-1} \text{ cm}^{-3}$ with Gd concentration due to the increase in crystal distortion and defect states across the Fermi level.

Moreover, the hopping length (R_H) and hopping energy (W_H) between localized states of the BGNT ceramics have been calculated by the Eq. 3.6 and 3.7 [34]. The R_H and W_H values for both compositions satisfied the VRH mechanism condition, i.e. $W_H \geq k_B T$ (0.025 eV) and $\alpha R_H \geq 1$ [39,40]. Temperature variation of Mott's variable range hopping

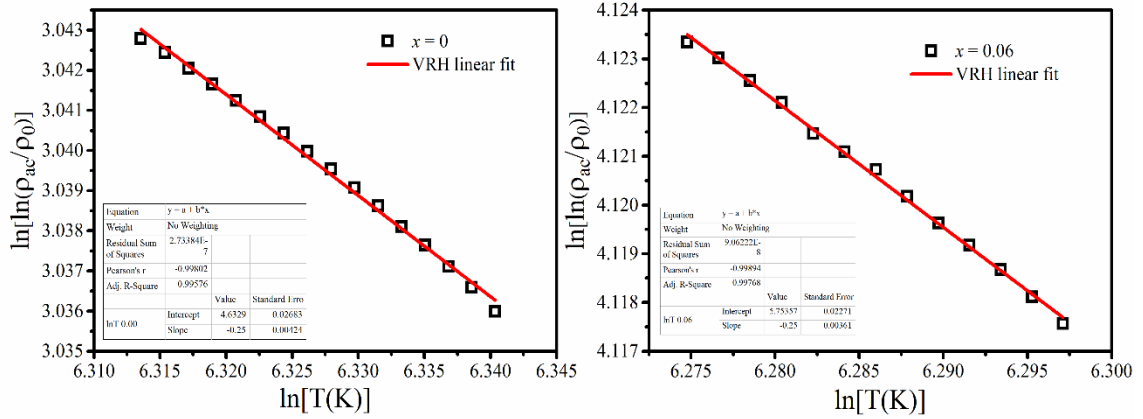


Figure 3.22: The $\ln[\ln(\rho_{ac}/\rho_0)]$ versus $\ln[T(K)]$ of BNT ceramics for (a) $x = 0$ and (b) $x = 0.06$.

parameters (R_H and W_H) of BNT ceramics for $x = 0$ and 0.06 are shown in Figure 3.23. The R_H values decreased and W_H values increased with the temperature, which is attributed to the increase in disorder in the BGNT system. With an increase in x concentration, both the R_H and W_H values reduced from 3.92 to 1.61 nm and 0.48 to 0.19 eV whereas $N(E_F)$ values increased. The reduction in average hopping length and hopping energy with the Gd concentration signifies the formation of additional localized states due to the incorporation of Gd into the BNT system.

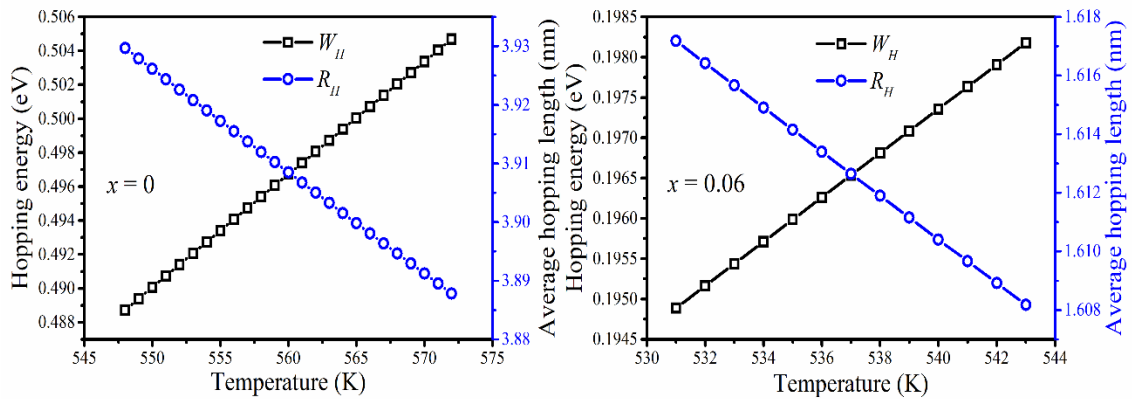


Figure 3.23: Temperature variation of Mott's variable range hopping parameters (R_H and W_H) of BGNT ceramics for (a) $x = 0$ and (b) $x = 0.06$.

3.6 Conclusions

In this present chapter, the structural, microstructural, dielectric and AC-conductivity studies of pure BNT, BNTC and BGNT ceramics were investigated in detail. The Rietveld refinement XRD and Raman spectroscopy of all samples revealed the rhombohedral crystal symmetry with the R3c space group. The average grain size of the BNTC and BGNT ceramics found to be decreased with Ce and Gd which inhibited grain growth as compared to pure BNT ceramics. The pure BNT ceramics calcined at 800 °C and sintered at 1100 °C showed enhanced dielectric properties ($\epsilon_r = 692$ and $\tan\delta = 0.045$ at 1 kHz) and weak relaxor behavior. The dielectric studies of pure BNT ceramics as a function of temperature exhibited two phase transitions correspond to the ferroelectric to antiferroelectric ($T_d \sim 198^\circ\text{C}$) and anti-ferroelectric to paraelectric phase ($T_C \sim 330^\circ\text{C}$). In BGNT ceramics, the T_d and T_C shifted towards the lower temperature for $x \geq 0.04$ samples. However, there is no change in transition temperature observed in BNTC ceramics. The dielectric response of the Ce and Gd doped BNT ceramics improved significantly ($\epsilon_r = 775$ and $\tan\delta = 0.032$ at 1 kHz) and ($\epsilon_r = 809$ and $\tan\delta = 0.201$ at 1 kHz) for $x = 0.025$ and 0.06 , respectively. The existence VRH process in both the BNTC and BGNT systems is confirmed by obtaining the slope value -0.25 . The reduction in average hopping length and hopping energy signifies the formation of additional localized states due to the incorporation of Gd and Ce into the BNT system.

3.7 References

- [1] G. A. Smolenskii, V. A. Isupov, A. I. Agranovskaya, and N. N. Krainik, *Fiz. Tverd. Tela Sanktpeterbg.* **2**, 2982 (1960).
- [2] M. Li, M. J. Pietrowski, R. A. De Souza, H. Zhang, I. M. Reaney, S. N. Cook, J. A. Kilner, and D. C. Sinclair, *Nat. Mater.* **13**, 31 (2014).
- [3] M. Li, L. Li, J. Zang, and D. C. Sinclair, *Appl. Phys. Lett.* **106**, 0 (2015).
- [4] J.-H. Kim, Y.-M. Kang, M.-S. Byun, and K.-T. Hwang, *Thin Solid Films* **520**, 1015 (2011).
- [5] J. Y. Yi, J.-K. Lee, and K.-S. Hong, *J. Am. Ceram. Soc.* **85**, 3004 (2002).
- [6] A. Watcharapasorn and S. Jiansirisomboon, *Ceram. Int.* **34**, 769 (2008).
- [7] V. Pal, R. K. Dwivedi, and O. P. Thakur, *Curr. Appl. Phys.* **14**, 99 (2014).
- [8] V. Pal, R. K. Dwivedi, and O. P. Thakur, *Mater. Res. Bull.* **51**, 189 (2014).
- [9] M. Zannen, A. Lahmar, H. Khemakhem, and M. El Marssi, *Solid State Commun.* **245**, 1 (2016).
- [10] M. Chen, Q. Xu, B. H. Kim, B. K. Ahn, and W. Chen, *Mater. Res. Bull.* **43**, 1420 (2008).
- [11] Y. Li, W. Chen, Q. Xu, J. Zhou, Y. Wang, and H. Sun, *Ceram. Int.* **33**, 95 (2007).
- [12] S. Xiao, S. Deng, J. Zhang, Y. Zhou, J. Tang, Y. Wang, L. Wang, H. Qi, and J. Wang, *Ceram. Int.* **38**, 6071 (2012).
- [13] L. E. Cross, *Ferroelectrics* **151**, 305 (1994).
- [14] Z. Wang, Y. Zhuo, D. Xiao, W. Wu, C. Zhang, X. Huang, and J. Zhu, *Curr. Appl. Phys.* **11**, S143 (2011).
- [15] U. Holzwarth and N. Gibson, *Nat. Nanotechnol.* **6**, 534 (2011).
- [16] A. L. Patterson, *Phys. Rev.* **56**, 978 (1939).
- [17] J. Petzelt, S. Kamba, J. Fábry, D. Noujny, V. Porokhonsky, A. Pashkin, I. Franke,

- K. Roleder, J. Suchanicz, R. Klein, and G. E. Kugel, *J. Phys. Condens. Matter* **16**, 2719 (2004).
- [18] M. Zannen, A. Lahmar, M. Dietze, H. Khemakhem, A. Kabadou, and M. Es-Souni, *Mater. Chem. Phys.* **134**, 829 (2012).
- [19] A. Chaves, R. S. Katiyar, and S. P. S. Porto, *Phys. Rev. B* **10**, 3522 (1974).
- [20] K. Roleder, A. Kania, and J. Handerek, *Ferroelectrics* **77**, 107 (1988).
- [21] and Z.-G. Y. A. A. Bokov, *J. Mater. Res.* **41**, 31 (2006).
- [22] Y. Hiruma, H. Nagata, and T. Takenaka, *J. Appl. Phys.* **105**, 84112 (2009).
- [23] R. D. Shannon, *Acta Crystallogr. Sect. A* **32**, 751 (1976).
- [24] J. Kreiselt, A. M. Glazer, G. Jones, P. A. Thomas, L. Abello, and G. Lucazeau, *J. Phys. Condens. Matter* **12**, 3267 (2000).
- [25] E. Husson, in *Key Eng. Mater.* (Trans Tech Publications Ltd, 1998), pp. 1–40.
- [26] V. Pal, O. P. Thakur, and R. K. Dwivedi, *J. Phys. D. Appl. Phys.* **48**, 55301 (2015).
- [27] P. Fu, Z. Xu, R. Chu, W. Li, Q. Xie, Y. Zhang, and Q. Chen, *J. Alloys Compd.* **508**, 546 (2010).
- [28] H. Yu and Z.-G. Ye, *J. Appl. Phys.* **103**, 34114 (2008).
- [29] K. Uchino and S. Nomura, *Ferroelectrics* **44**, 55 (1982).
- [30] C. C. Homes, T. Vogt, S. M. Shapiro, S. Wakimoto, and A. P. Ramirez, *Science* (80-.). **293**, 673 (2001).
- [31] R. M. Hill, *Phys. Status Solidi* **34**, 601 (1976).
- [32] S. Ke, P. Lin, H. Fan, H. Huang, and X. Zeng, *J. Appl. Phys.* **114**, 104106 (2013).
- [33] J. J. Hauser, *Phys. Rev. B* **9**, 2623 (1974).
- [34] I. Rawal and A. Kaur, *J. Appl. Phys.* **115**, 43717 (2014).
- [35] S. Upadhyay, O. Parkash, and D. Kumar, *J. Phys. D. Appl. Phys.* **37**, 1483 (2004).
- [36] B. Wylie-Van Eerd, D. Damjanovic, N. Klein, N. Setter, and J. Trodahl, *Phys. Rev.*

- B - Condens. Matter Mater. Phys. **82**, 104112 (2010).
- [37] X. Chou, J. Zhai, H. Jiang, and X. Yao, J. Appl. Phys. **102**, 84106 (2007).
- [38] R. Jing, X. Chen, H. Lian, X. Qiao, X. Shao, and J. Zhou, J. Eur. Ceram. Soc. **38**, 3111 (2018).
- [39] P. Mahesh, S. Thota, and D. Pamu, IEEE Trans. Dielectr. Electr. Insul. **22**, 3668 (2015).
- [40] H. Han, C. Davis, and J. C. Nino, J. Phys. Chem. C **118**, 9137 (2014).



Dielectric, Piezoelectric and AC-Conductivity Studies of BNKT and BNT-KNNG Ceramics

4.1 Introduction

In recent years, various lead-free piezoelectric materials with perovskite structure like BaTiO₃ (BT), K_{0.5}Na_{0.5}NbO₃ (KNN), Bi_{0.5}K_{0.5}TiO₃ (BKT), Bi_{0.5}Na_{0.5}TiO₃ (BNT) and etc. have been extensively investigated on account of their superior dielectric and piezoelectric properties. [1–4] Among them, BNT has been explored by the scientific community due to its strong ferroelectric response (remnant polarization (P_r) = 38 $\mu\text{C}/\text{cm}^2$) at RT, high transition temperature ($T_C \sim 320^\circ\text{C}$) and best dielectric properties ($\epsilon_r = 692$ and $\tan\delta = 0.045$ at 1 kHz) [4–6]. However, the BNT ceramics have certain issues like inferior piezoelectric properties and difficult to pole due to the high coercive field and high conductivity, which makes the BNT ceramics less applicable for the practical applications. Also, it is very difficult to densify BNT due to the volatile nature of Na and Bi during the sintering process, which causes the increase in the leakage current and degradation of dielectric, ferroelectric and piezoelectric properties. In order to overcome such drawbacks and to improve the electrical properties, the addition of dopants or other compositions were added to the BNT system. Normally, the improvement in the dielectric and piezoelectric properties are attributable to the formation of a morphotropic phase boundary (MPB) with the substitution of either dopant or composition. Recently, it is reported that BNT-based compositions modified with BT, BKT, KNN, NaNbO₃ (NN) and SrTiO₃ (ST), which have displayed improved dielectric and piezoelectric properties and also eased the poling and density issues [7–11]]. Sasaki and Nagata et al. [12,13] investigated the piezoelectric

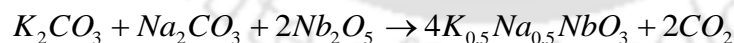
properties ($k_p = 27\%$, $d_{33}=151$ pC/N and $d_{31}=46.9$ pC/N) in $\text{Bi}_{0.5}\text{Na}_{1-x}\text{K}_{x0.5}\text{TiO}_3$ ceramics with an existence of MPB between rhombohedral and tetragonal phases near $x = 0.16$ to 0.20 . In fact, the A-site substitution of ABO_3 perovskites is found to strongly affect its properties. Yan et al. [14] reported that the piezoelectric properties were strongly dependent on the differences in ionic size, atomic weight, and electric-negativity of the A-site and B-site ions of the ABO_3 perovskites. Further, considerable efforts have also been made with the addition of dopants either in A or B-site of BNT ceramics to enhance the ferroelectric and piezoelectric properties [15–21]. Recently, Wu *et al.* [10], reported that the addition of NN into the BNT system, the composite was found to exhibit relaxor behavior with improved dielectric properties. On similar lines, Mahesh *et al.* [22,23] reported that the doping rare-earth Gd^{3+} to KNN [$\text{K}_{0.5}\text{Na}_{0.5}\text{NbO}_3 + 1$ wt. % Gd_2O_3 ; (KNNG)] ceramics have led to the improvement in the electrical properties. However, there are only a few reports available on the effect of A-site substitution in BNT ceramics for studying its effect on the dielectric and piezoelectric properties.

In this chapter, our aim is to study the effect of K and KNNG on the structural, morphological, electrical, dielectric and piezoelectric properties of BNT ceramics and to address the issues related to densification, leakage current and difficulties in the polling process. These ceramics are utilized for fabrication of high-frequency devices such as transformers, ultrasonic motors, actuators and transducers due to their inherent properties like high electromechanical coupling factor (k_p), high piezoelectric coefficient (d_{33}), high dielectric constant (ϵ_r) and low dielectric loss ($\tan\delta$) [24]. Also, most of the studies on BNT were focused on dielectric, piezoelectric and ferroelectric materials. To the best of our knowledge, there have been no reports on AC-conductivity analysis by variable range hopping (VRH) mechanism in BNT based ceramics, which is associated with the hopping of charge carriers between localized states and dielectric behavior of the material.

Moreover, this study also reveals the relaxor behavior with diffuse phase transition present in the system near the transition temperature. The piezoelectric coefficients like elastic compliance, electromechanical coupling factor, piezoelectric charge and voltage coefficients have been estimated from dielectric resonance spectra (i.e., indirect method). Furthermore, the transport mechanism studies in BNT based ceramics are scarce, even though it has been speculated that the volatility of A-site cations and their deficiencies are responsible for the leakage current. This chapter attempts to understand the leakage current mechanism which is by space charge limited conduction (SCLC) and is related to the deep acceptor traps.

4.2 Sample preparation of K doped BNT and BNT-KNNG ceramics

Lead free $\text{Bi}_{0.5}\text{Na}_{1-x}\text{K}_{x0.5}\text{TiO}_3$ (BNKT; $x = 0, 0.1, 0.2$ and 0.3) and $(1-x)\text{Bi}_{0.5}\text{Na}_{0.5}\text{TiO}_3 - x\text{K}_{0.5}\text{Na}_{0.5}\text{NbO}_3 + 1 \text{ wt. } \% \text{Gd}_2\text{O}_3$ (BNT-KNNG; $x = 0, 0.005, 0.01$ and 0.02) ceramics have been synthesized via solid-state reaction method. The high purity powders of Bi_2O_3 , Gd_2O_3 (Alfa-Aesar, USA, 99.999%), Na_2CO_3 , TiO_2 , K_2CO_3 and Nb_2O_5 (Sigma-Aldrich, USA, 99.99%) were weighed according to stoichiometric equations and prepared as follows.



The mixed powders were milled by using a planetary ball mill (Pulverisette 6, Fritsch GmbH, Germany,) for 5h with ZrO_2 balls with isopropanol (Sigma Aldrich, USA) as a media. The obtained slurry was then dried at 120°C . The dried BNT, BNKT and KNNG powders were calcined at 800°C for 3h and 750°C for 5h, respectively. Both the BNT and KNNG calcined powders were mixed to form BNT-KNNG composites and all the samples were again ball milled for 10h to reduce the initial particle size. Further, these

powders were granulated with polyvinyl alcohol and pressed into discs of 10 mm diameter and 1 mm thickness. The prepared discs were subsequently sintered in the temperature range of 900 °C to 1100 °C for 2h/5h and optimized at a temperature of 1050°C for 2h for BNKT and 1050°C for 5h for BNT-KNNG to achieve 90 – 96 % of relative density, as measured by the Archimedes principle. For the electrical measurements, a silver paste was applied on both surfaces of the sintered samples and dried at 150°C for 10 minutes to remove the moisture before making electrical measurements.

4.3 Results and discussion of K doped BNT ceramics

The X-ray diffraction (XRD) patterns of BNKT ($x = 0 - 0.3$) ceramics, sintered at 1050°C for 2h are shown in Figure 4.1(a). All the samples ($x < 0.2$) revealed a pure perovskite structure with rhombohedral crystal symmetry, indicating the formation of the BNKT solid solution. Figure 4.1(b) depicts detailed XRD analysis in the 2θ range of $39.2 - 41.5^\circ$ and $56.5 - 60^\circ$, respectively. At room temperature, the BNT system exhibits a rhombohedral structure while BKT shows tetragonal structure [25]. The BNT–BKT and $\text{Bi}_{0.5}\text{Na}_{1-x}\text{K}_{x0.5}\text{TiO}_3$ (BNKT) system displays the morphotropic phase boundary (MPB) near $x = 0.16 - 0.20$ [26,27]. The MPB of the BNKT system is confirmed by the splitting of (021)/(111) peaks at 2θ around 40° and (122)/(211) peaks around 58° . Therefore, $x = 0.2$ and 0.3 samples demonstrated the coexistence of rhombohedral and tetragonal phases in the BNKT system. However, there is no peak splitting occurred due to the dilute substitution of K.

Furthermore, the relative amounts of rhombohedral and tetragonal phases have been calculated from XRD patterns of the samples ($x \geq 0.2$) by the following expression [28].

$$\text{Tetragonal (\%)} = \frac{100 \times I_{\text{Tetra}}}{I_{\text{Tetra}} + I_{\text{Rhomb}}} \quad (4.1)$$

where, I_{Tetra} is the relative intensity of (211) tetragonal peak and I_{Rhomb} is the intensity of (122) rhombohedral peak. The obtained tetragonal phase intensity is 36.98% and 38.79% for the samples $x = 0.2$ and 0.3 , respectively. The tetragonal phase found to be improved

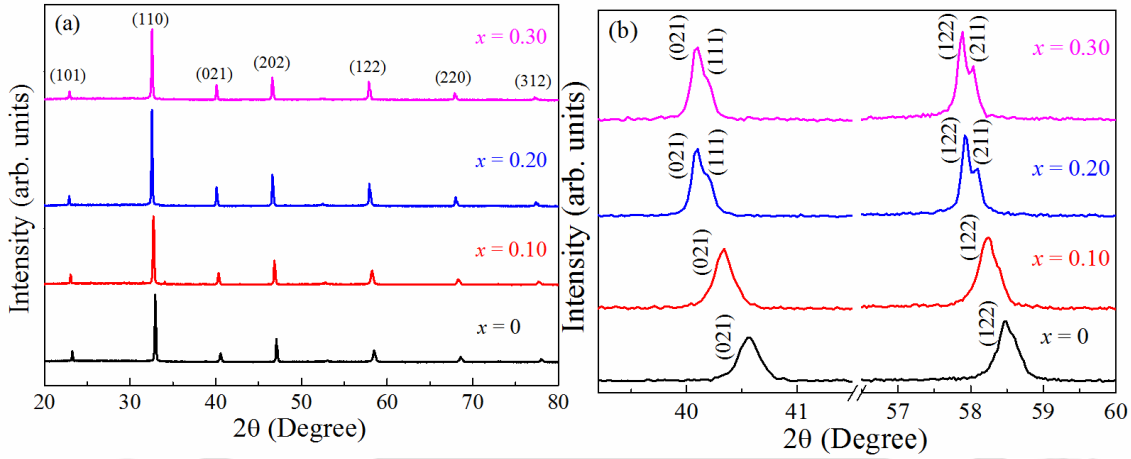


Figure 4.1: (a) XRD pattern of $\text{Bi}_{0.5}(\text{Na}_{(1-x)}\text{K}_x)_{0.5}\text{TiO}_3$ ceramics in the 2θ range of $20 - 80^\circ$ and (b) Splitting of (021) and (122) peaks in the 2θ range of $39.2 - 41.5^\circ$ and $56.5 - 60^\circ$, respectively.

with an increase in x concentration. In addition, an increase in K intensified the separation of the (122) and (211) peaks, suggests an enhancement in the tetragonality of the BNKT lattice.

The RT Raman spectra of BNKT ceramics, recorded over the wavenumber range $50 - 1000 \text{ cm}^{-1}$ are shown in Figure 4.2. There are 12 Raman active modes observed in the spectrum, which are fitted with Gaussian function using origin software. The obtained Raman modes and their corresponding full width at half maxima (FWHM) are listed in Table 4.1. According to group theory, the rhombohedral $R3c$ phase consists of 13 Raman active modes ($\Gamma_{\text{Raman}} = 4A_1 + 9E$). Where, A_1 and E modes are Raman and IR active [29]. The Raman active A_1 (TO_1) modes ($\leq 170 \text{ cm}^{-1}$) are related to the displacement of Bi-O,

Na-O and K-O vibrations. The Raman active E (TO₂) modes at 188 cm⁻¹ to 387 cm⁻¹, are corresponding to Ti-O vibrations and were observed in many perovskites [30]. The high frequency (TO₃) modes observed at 516 – 629 cm⁻¹, are related to the stretching and symmetric vibrations of the TiO₆ octahedra. The LO₃ modes were observed at 750 – 860 cm⁻¹, which are associated with the A₁ (LO) and E (LO) overlapping modes [31].

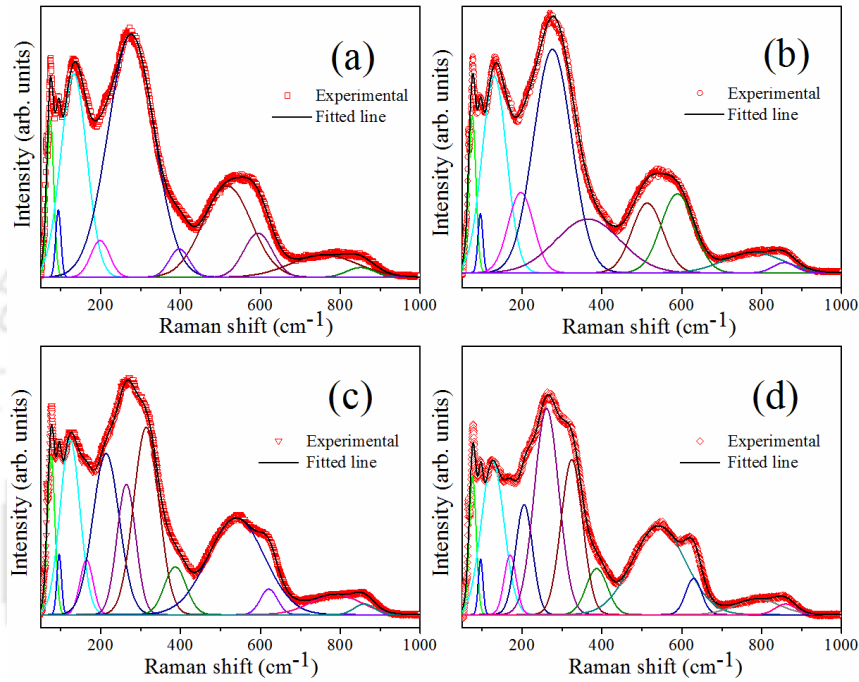


Figure 4.2: Raman spectra of Bi_{0.5}(Na_(1-x)K_x)_{0.5}TiO₃ ceramics for (a) $x = 0$, (b) $x = 0.1$, (c) $x = 0.2$ and (d) $x = 0.3$.

The strong vibrational modes detected at 132 and 276 cm⁻¹ for $x = 0$, are found to shift gradually towards lower wavenumber (redshift) with increasing K⁺ concentration (i.e. for $x = 0.1, 0.2$ and 0.3). The mode appearing at 132 cm⁻¹ is related to the vibration of Na⁺TiO₃ and K⁺TiO₃ clusters rather than Bi³⁺TiO₃ clusters due to the larger mass of Bi [32]. The vibrations modes appeared within the range 261–276 cm⁻¹ for all the samples are mostly dominated by TiO₆ octahedra. Consequently, the changes are associated with the displacement of Ti cation or TiO₆ octahedral distortions. Thus, due to the substitution of larger ions (K⁺) in the A- site (Na⁺) of the investigated perovskite, the redshift is expected

from the relation between the frequency and the reduced mass [33]. All the remaining modes are shifted to higher wavenumbers (blue shift) with an increase in x concentration. Meanwhile, two additional modes noticed at 169 cm^{-1} and 314 cm^{-1} are also shifted to higher wavenumbers (170 cm^{-1} and 324 cm^{-1}) for $x = 0.0$ and 0.3 samples, respectively. This might be due to the change in crystal structure from rhombohedral to tetragonal phase, which causes the change in TiO_6 octahedral vibrations. These results are in line with the conclusion obtained from the XRD patterns. Earlier reports [34,35], have shown that binding strength and compressive strain of the ceramics increased due to short distance between Ti and oxygen atoms in TiO_6 octahedra, as a result, the blue shift of these modes occurs in the systems. The FWHM of all modes is also decreasing with the substitution of K indicating the structural changes in the BNKT system.

Table 4.1: Raman shift and FWHM of the modes for $\text{Bi}_{0.5}(\text{Na}_{(1-x)}\text{K}_x)\text{TiO}_3$ ceramics ($x = 0 - 0.3$).

Modes	$x = 0$		$x = 0.1$		$x = 0.2$		$x = 0.3$	
	Raman shift (cm^{-1})	FWHM (cm^{-1})	Raman shift (cm^{-1})	FWHM (cm^{-1})	Raman shift (cm^{-1})	FWHM (cm^{-1})	Raman shift (cm^{-1})	FWHM (cm^{-1})
1	73.94	19.90	75.51	20.94	75.953	21.957	76.413	20.35
2	93.78	15.46	95.61	14.57	95.973	13.73	96.254	13.84
3	132.58	76.90	130.51	72.68	127.09	58.81	126.26	66.88
4	188.52	55.59	197.00	74.72	169.42	38.56	170.17	35.48
5	276.20	135.60	276.27	111.72	204.97	63.79	205.14	49.92
6	382.23	84.18	384.97	189.75	264.21	55.00	261.42	72.27
7	516.81	83.85	519.30	118.50	314.14	74.54	324.67	63.56
8	593.98	196.01	598.85	89.42	386.86	64.32	387.00	62.81
9	758.95	82.21	776.89	174.24	539.56	165.35	542.40	155.93
10	850.79	59.10	855.74	67.83	621.12	50.02	629.66	47.042
11	–	–	–	–	788.92	147.08	789.67	130.25
12	–	–	–	–	859.681	58.859	860.25	59.484

Figure 4.3 shows the FESEM micrographs of the BNKT ceramics with $x = 0 - 0.3$, sintered at 1050 °C for 2h. All the samples have highly densified and the relative density is in the range of 92-94% of the theoretical density (5.84 g/cm^3) [36]. The average grain size has been calculated by the linear intercept method using image-J software. The grain size decreased from $1.405 \pm 0.39 \text{ }\mu\text{m}$ – $0.667 \pm 0.18 \text{ }\mu\text{m}$, with an increase in x from 0 to 0.3, respectively. As the K concentration increases, grain growth is inhibited, which leads to a decrease in the grain size. The decrease in the grain size with increasing K can be understood by the reduction in the grain boundary mobility and mass transportation [35,37]. From the SEM micrographs of all compositions, the sample with $x = 0.2$ sample was found to have a well-crystallized microstructure with uniform grain growth.

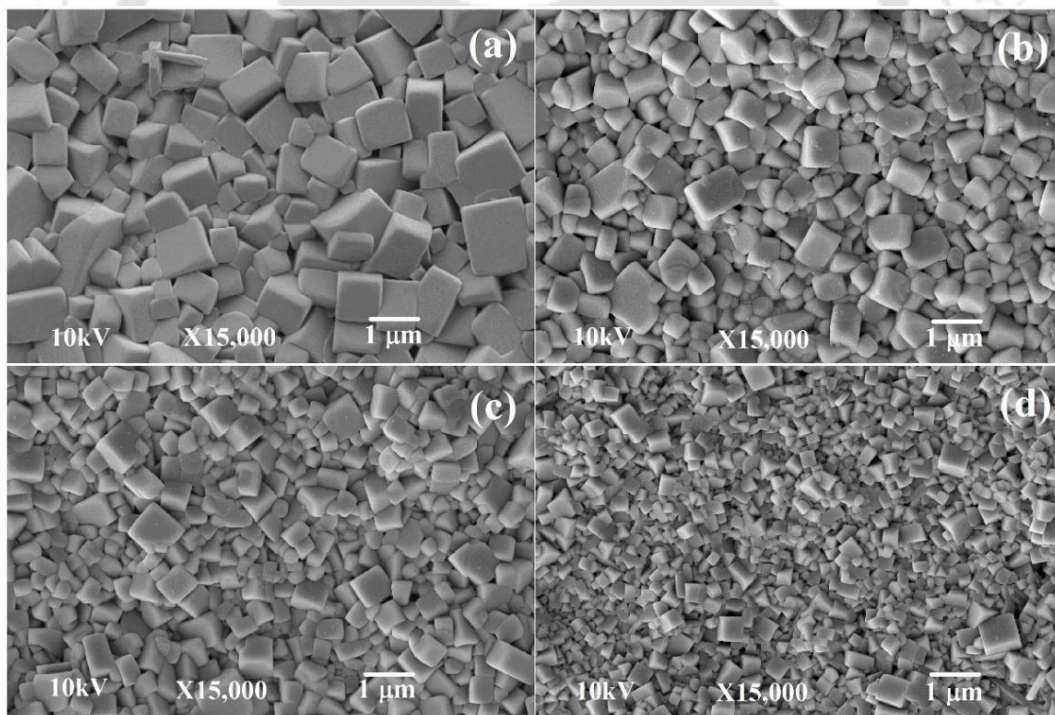


Figure 4.3: FESEM micrographs of $\text{Bi}_{0.5}(\text{Na}_{(1-x)}\text{K}_x)_{0.5}\text{TiO}_3$ ceramics for (a) $x = 0$, (b) $x = 0.1$, (c) $x = 0.2$ and (d) $x = 0.3$.

Figure 4.4 illustrates the FETEM images for $x = 0$ and 0.2 compositions and the segregation of K at the grain boundary is shown in Figure 4.4 (b). It is noticed that the grain growth leads to the homogeneous and uniform microstructure as compared to the pure sample (Figure 4.4 (a); $x = 0$). The substitution of K^+ into the Na^+ site (A-site) of the BNT system helps the mass transport and grain boundary mobility during the sintering process, which is responsible for the enhancement of the grain growth with the incorporation of K [38,39].

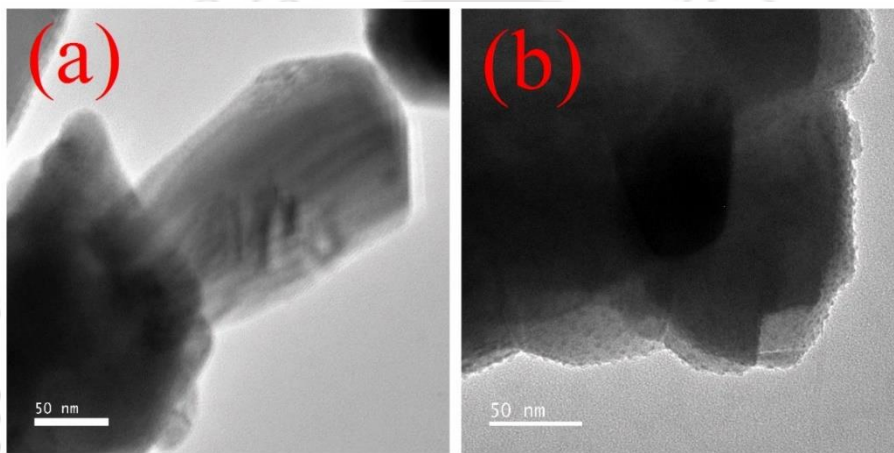


Figure 4.4: FETEM images of $Bi_{0.5}(Na_{(1-x)}K_x)_{0.5}TiO_3$ ceramics for (a) $x = 0$ and (b) 0.2 samples.

Further, in order to confirm the elemental composition and microstructure of BNKT ceramics, the typical microstructure and elemental composition mapping were investigated, which are shown in Figure 4.5 (a_1, a_2 and b_1, b_2) for $x = 0$ and 0.2, respectively. The BNKT ($x = 0.2$) sample was highly densified with uniform grain growth and smaller grains as compared to the pure BNT. It is noticed that the Bi, Na and Ti occupied the same areas, which are connected with each other. However, the remaining and isolated areas were occupied by K concentration. The substituted K gathered together at the grain boundaries of the BNT system by forming the BNKT composition. The observed elemental distribution was shown in Figure 4.5 (a_3 and b_3). The experimental volume fraction of K

for BNKT is 1.6 % and is approximately equal to the theoretical volume fraction (2 %), which confirms the formation of BNKT perovskite. The above results conclude that the segregation of the K at the grain-boundary inhibited the grain-growth.

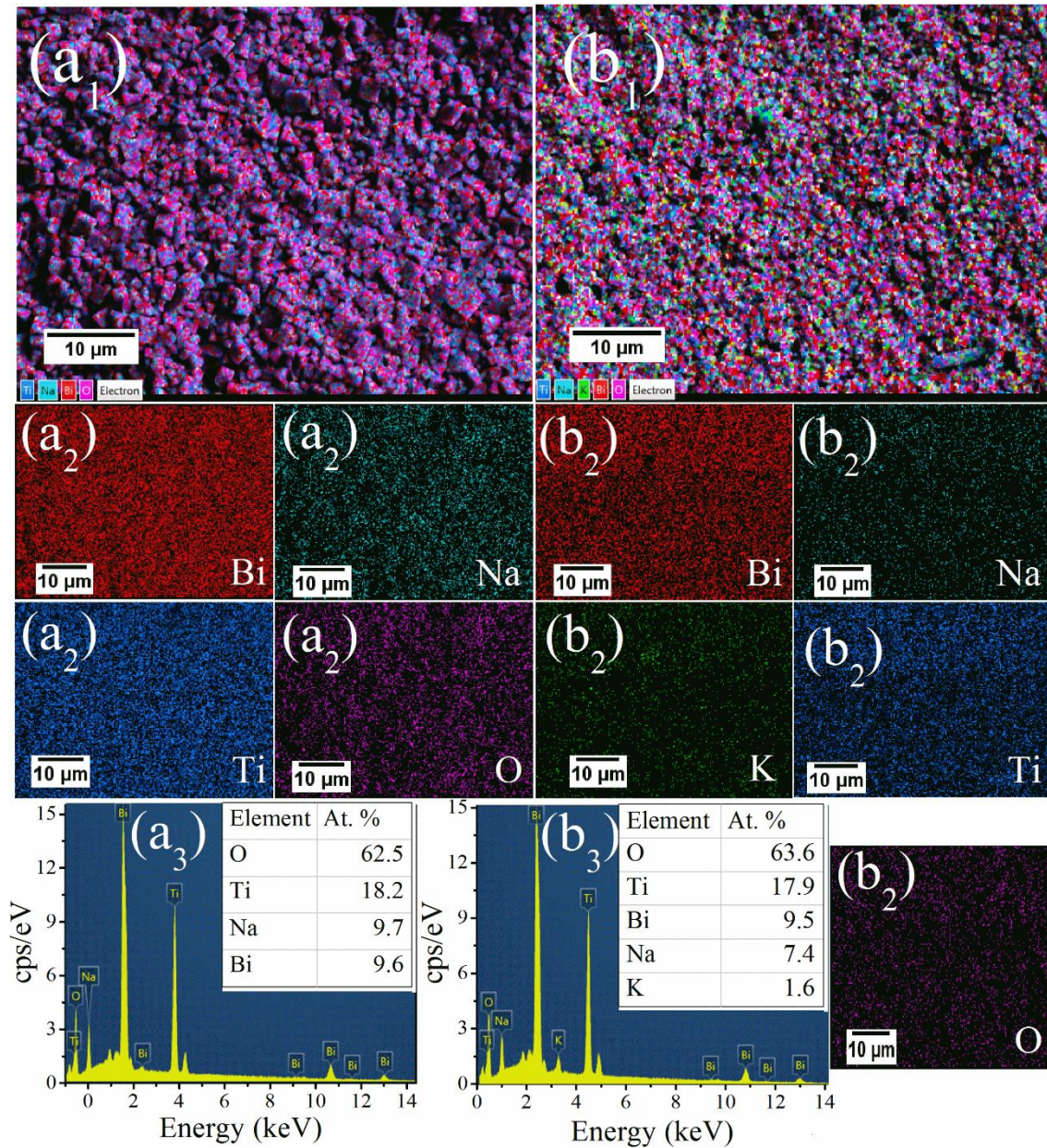


Figure 4.5: The typical microstructure, elemental mapping and composition distribution for (a₁), (a₂), (a₃) and (b₁), (b₂), (b₃) for $x = 0$ and 0.2 samples, respectively.

Figure 4.6 illustrates the temperature-dependent dielectric constant (ϵ_r) and loss tangent ($\tan\delta$) of BNKT ($x = 0 - 0.3$) ceramics, measured at frequencies 100Hz to

1MHz. The ϵ_r values were found to increase with K concentration up to $x = 0.2$ and beyond that, it decreased. The maximum ϵ_r (1273) and lowest $\tan\delta$ (0.047) at 1 kHz was obtained

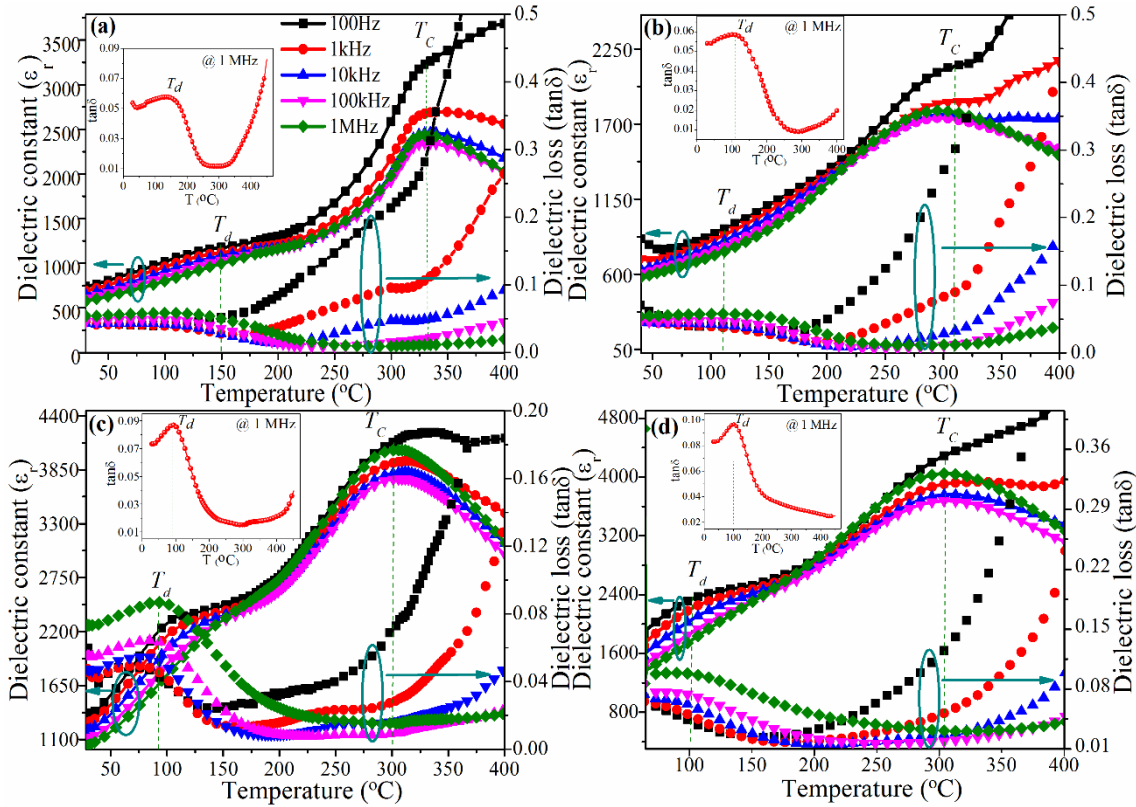


Figure 4.6: The temperature dependence of ϵ_r and $\tan\delta$ of $\text{Bi}_{0.5}(\text{Na}_{(1-x)}\text{K}_x)_{0.5}\text{TiO}_3$ ceramics for (a) $x = 0$, (b) $x = 0.1$, (c) $x = 0.2$ and (d) $x = 0.3$, measured at 100 Hz – 1 MHz, respectively. Insets of (a), (b), (c) and (d) show the variation of depolarization temperature (T_d) at 1 MHz.

for $x = 0.2$ sample. The ϵ_r of all the ceramics exhibited two dielectric anomalies corresponding to the structural phase-transitions from rhombohedral to tetragonal (T_d) and ferroelectric tetragonal to paraelectric cubic phase (T_c), respectively. Vijayeta Pal *et al.* [38] defined the T_d in Nd-doped BNT ceramics as the phase transition from ferroelectric (FE) to anti-ferroelectric (AFE) and also dielectric anomaly in a dielectric loss versus temperature corresponds to T_d which is also called as the dielectric method. In this study,

we have determined the T_d by using the dielectric method. The obtained T_d values measured at 1MHz are 150, 110, 91 and 100 °C for $x = 0, 0.1, 0.2$ and 0.3 , respectively and which are shown in inset of Figure 4.6 (a) to (d). These phase transitions were intrinsically coming from pure BNT ceramics [40]. However, $T_d (=150^\circ\text{C})$ and $T_C (=330^\circ\text{C})$ for Pure BNT ($x = 0$) decreased to 91°C and 300°C with an increase in the concentration for $x = 0.2$. With a further increase in the x values, both the T_d and T_C increased to 100°C and 305°C . Hence, the enhancement in dielectric permittivity and shifting of phase transitions occur due to the incorporation of K into BNT matrix. At higher concentration of $x (> 0.2)$, the dielectric permittivity values decreased and loss tangent increased mainly because of crystal cell distortions and it also led to the decrease of net dipole moment. At the same time, the T_d peaks gradually shifted towards higher temperature and magnitude of transition decreased with the increase in frequency. This was also accompanied by a significant shift in T_C . The loss tangent curves also clearly exhibited the frequency dispersive behaviour. This type of behaviour is a characteristic of relaxor ferroelectrics [41]. It can be understood that the substitution of K into BNT lattice disturbs the long-range ferroelectric order. This process can force to reduce the transition temperature and leads to the formation of polar nano regions due to the difference in ionic radius of K^+ (1.38 \AA) and Na^+ (1.02 \AA). The formation of polar nano regions embedded in the BNKT disorder in the system [42,43]. These results indicate that the relaxor behavior is present in the system. A similar kind of behaviour was also observed in $\text{Ba}(\text{Zr}_x\text{Ti}_{1-x})\text{O}_3$, $\text{Na}_{0.5}\text{Bi}_{0.5}\text{TiO}_3\text{-PbTiO}_3$ and $\text{Na}_{0.5}\text{Bi}_{0.5}\text{TiO}_3\text{-K}_{0.5}\text{Bi}_{0.5}\text{TiO}_3$ systems [44,45].

The temperature-dependent dielectric constant of BNKT ceramics exhibited the diffuse phase transitions near the T_C , which is the typical signature of relaxor ferroelectrics [46]. Therefore, a modified Curie-Weiss law is used to describe the relaxor behavior of the BNKT ceramics, which was first proposed by Uchino and Nomura [47].

$$(1/\varepsilon_r) - (1/\varepsilon_r^m) = (T - T_m)^\gamma / C \quad (4.2)$$

where, C is a Curie constant, γ is the diffuseness coefficient and ε_r^m is the maximum dielectric constant at a temperature T_m . For normal ferroelectrics, γ should be equal to unity but varies between 1 and 2 for relaxor ferroelectrics [47]. The diffuseness coefficient (γ) was evaluated at 1 MHz for all the samples by finding the slope of the Eq. 4.2 as shown in Figure 4.7. The calculated γ values are found to be 1.48 – 1.89 for $x = 0 - 0.3$, which indicates that the BNKT system exhibits the relaxor behavior. In the present study, the γ values were found to increase with x . The γ value was found to be 1.48 for $x = 0$ and increases with K concentration. The increase in γ with the substitution of K might be due to the strong distortion of the BNT system. It can be understood that the difference in ionic radii of K^+ and Na^+ causes the disorder at the A-site of the BNT system, which leads to the formation of polar nano regions. The relaxor behavior is mostly decided by the response of polar nano regions to the applied AC field.

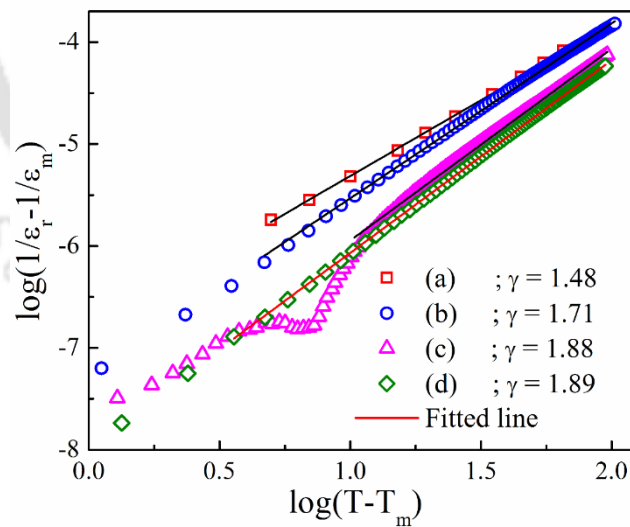


Figure 4.7: The logarithmic variation of $(1/\varepsilon_r - 1/\varepsilon_r^m)$ as a function of $\log(T - T_m)$ of $Bi_{0.5}(Na_{(1-x)}K_x)_{0.5}TiO_3$ ceramics for (a) $x = 0$, (b) $x = 0.1$, (c) $x = 0.2$ and (d) $x = 0.3$.

Further, Vogel-Fulcher law was used to confirm the relaxation mechanism in BNKT ($x = 0.0$ and 0.2) ceramics by following equation, as shown in Figure 4.8 [48].

$$f = f_0 \exp(-E_A / (k_B(T_P - T_o))) \quad (4.3)$$

where, f_0 is attempt frequency, E_A is activation energy, k_B is Boltzmann constant, T_P is the critical temperatures and T_o is the freezing temperature of polarized domains. The obtained parameters are $f_0 = 6.774 \times 10^{15}$ Hz (2.882×10^{12} Hz), $T_o = 303^\circ\text{C}$ (300°C) and $E_A = 0.162$ eV (0.016 eV) for $x = 0.0$ ($x = 0.2$), respectively. These results confirm the strong relaxation behaviour for $x = 0.2$ sample. Such low values of activation energy signify the presence of not only oxygen vacancies also deep acceptors in the present system.

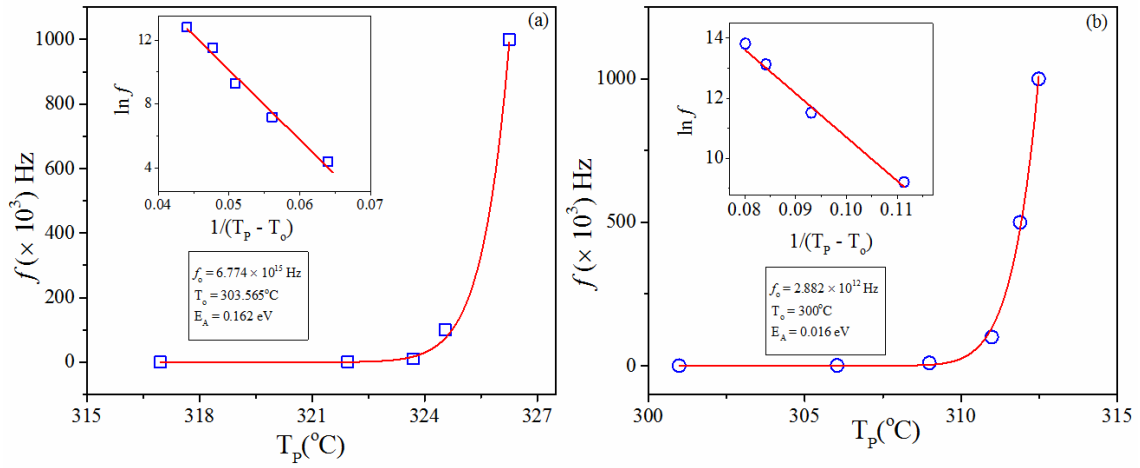


Figure 4.8: Frequency variation of critical temperature of BNKT ceramics, for (a) $x = 0$ and (b) $x = 0.2$ samples fitted with Vogel-Fulcher law.

The Activation energies (E_A) of BNKT ceramics were calculated at 1 MHz by using Arrhenius relation [49],

$$\sigma_{ac} = \sigma_0 \exp(-E_A / k_B T) \quad (4.4)$$

where, σ_0 is the pre-exponential factor, k_B is the Boltzmann constant, and T is the absolute temperature. The E_A values evaluated from the slope of Eq. 4.4 in different regimes are shown in Figure 4.9. The calculated E_A values of all samples are shown in Table 4.2. The E_A values are found to be enhanced from 0.058 – 0.112 for $x = 0$ to 0.2 in the regime 1(302 – 392K) and beyond that it decreased ($x > 0.2$). It can be understood from the increasing

random hopping of charge carriers between the localized states. The E_A values are found to be higher (0.417 eV) in regime 2 (562 – 592K) for pure BNT as compared to regime 1 due to release of more number of charge carriers from the oxygen vacancies, which creates excess amount of electrons in the A-site and as a result, crystallographic phase changes from anti-ferroelectric to paraelectric phase. This also strongly affects AC-conductivity. The E_A value is found to decrease (0.077 eV) for $x = 0.2$ sample due to the overcoming of oxygen vacancies as well as an excess amount of electrons with an increase in K concentration. The E_A values of all samples are below 1 eV and they are consistent with the earlier reports [50]. Furthermore, it also shows that the conduction is due to the thermal motion of oxygen vacancies and residual cations in the grain boundary of the BNKT ceramics [50]. In the present case, the E_A values were found to be (0.05 to 0.41 eV) below 1 eV for all the samples. These orders of E_A values are also due to some relaxing charge carriers like mobile dipoles and holes or defects ion complexes and with the deep acceptor traps.

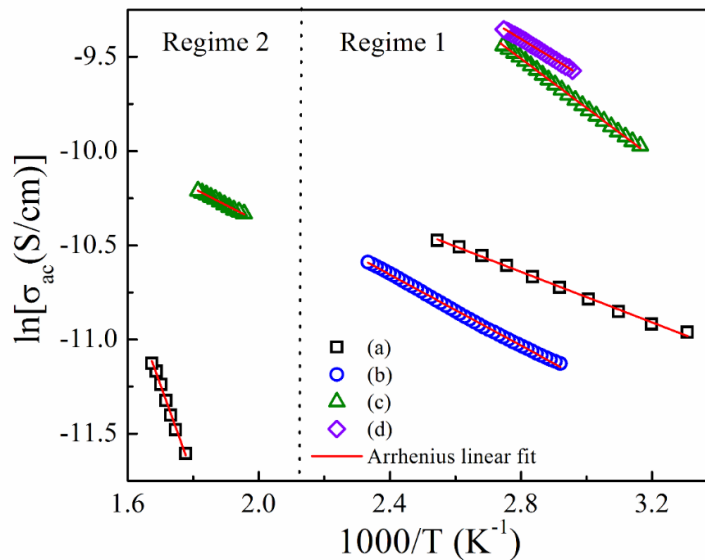


Figure 4.9: Temperature-dependent of AC-conductivity of $\text{Bi}_{0.5}(\text{Na}_{(1-x)}\text{K}_x)_{0.5}\text{TiO}_3$ ceramics, analyzed with Arrhenius relation in R1 (302 – 392K) and R2 (562 – 592K) regimes.

In order to understand the hopping conduction mechanism with the substitution of K into the BNT system, the AC-resistivity has been analyzed by using Mott's variable range hopping (VRH) model [51,52]. Figure 4.10 shows the variation of $\ln(\rho_{ac})$ with respect to $T^{-1/4}$ at 1 MHz for Pure BNT and optimized sample ($x = 0.2$) in R1 and R2 regions and fitted with the following equation,

$$\rho_{ac} = \rho_0 \exp(T_0 / T)^{1/4} \quad (4.5)$$

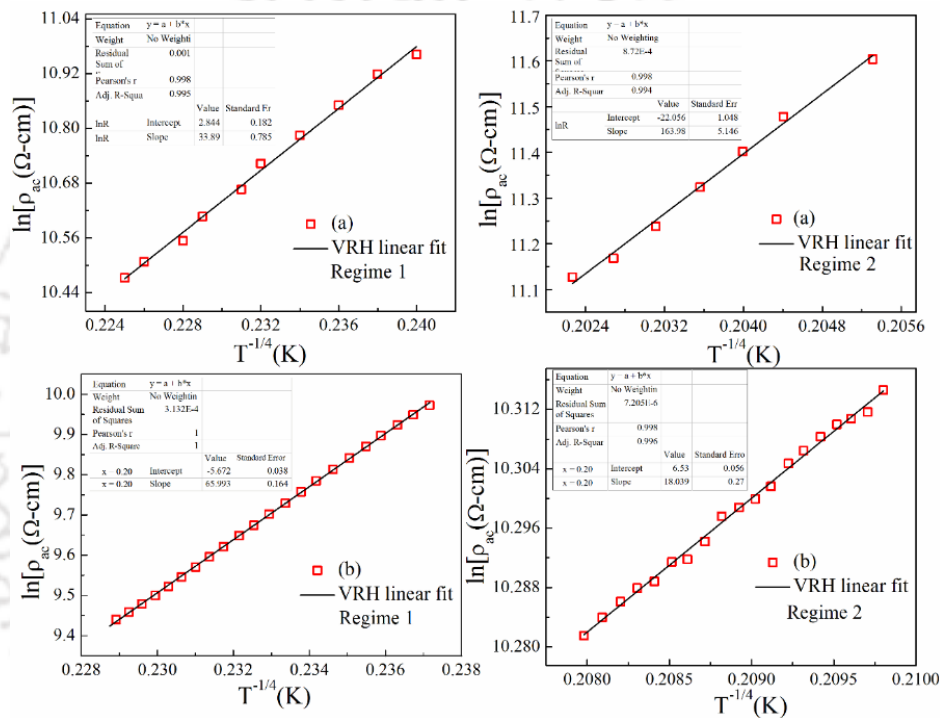


Figure 4.10: The $\ln(\rho_{ac})$ versus reciprocal temperature of $\text{Bi}_{0.5}(\text{Na}_{(1-x)}\text{K}_x)_{0.5}\text{TiO}_3$ ceramics for (a) $x = 0$ and (b) $x = 0.2$ in R1 (302 – 392K) and R2 (562 – 592K) regimes. Insets of (a) and (b) show the VRH linear fit parameters in tabular form.

where, ρ_0 is the pre-exponential factor and T_0 is the temperature coefficient, which is extracted from the slope of Figure 4.10. The power of the exponential factor varies based on the nature of the hopping process. Reports suggest that it should be equal to -1/4 [52]. The linear variation of logarithmic graphs $\ln[\ln(\rho_{ac})]$ with respect to $\ln(T)$ at R1 and R2 regimes are shown in Figure 4.11. Interestingly, all the samples showed the linear behavior

with a slope value of -0.25, which confirms the typical signature of the VRH process of charge carriers in the BNKT system. Further, the density of charge carriers near the Fermi level ($N(E_F)$) is determined by using the following expression,

$$N(E_F) = 16\alpha^3 / k_B T_0 \quad (4.6)$$

where, α is the localized wave function $\exp(-\alpha R)$ and k_B is the Boltzmann constant. Han *et al.* [53], assumed the decay length α^{-1} (0.6 nm) to be the distance between the nearest B site atoms of the perovskite structure. The obtained $N(E_F)$ values of all the samples are shown in Table 4.2. The $N(E_F)$ of BNKT ceramics at regime R1 is found to decrease with an increase in K concentration up to $x = 0.2$. The obtained $N(E_F)$ values are low for a lower concentration of x might be due to the decrease in the A-site defects caused by the volatile nature of alkali elements during the high-temperature sintering process. The small value of $N(E_F)$ could be the reason for a decrease in grain size. The $N(E_F)$ values are also found to be increased for $x = 0.3$ sample, which is due to the rise of defect states and crystal distortion across the Fermi level. The $N(E_F)$ values are low for pure BNT as compared to $x = 0.2$ sample in Regime 2 might be due to changes in the crystal structure. Furthermore, the conduction behavior of the BNKT ceramics is analyzed in terms of most probable hopping length R_H and the average hopping energy W_H between localized sites by using the following Equations [54].

$$R_H = 0.75 \times [3 / (2\pi\alpha N(E_F) k_B T)]^{1/4} \quad (4.7)$$

$$W_H = [3 / (4\pi R_H^3 N(E_F))] \quad (4.8)$$

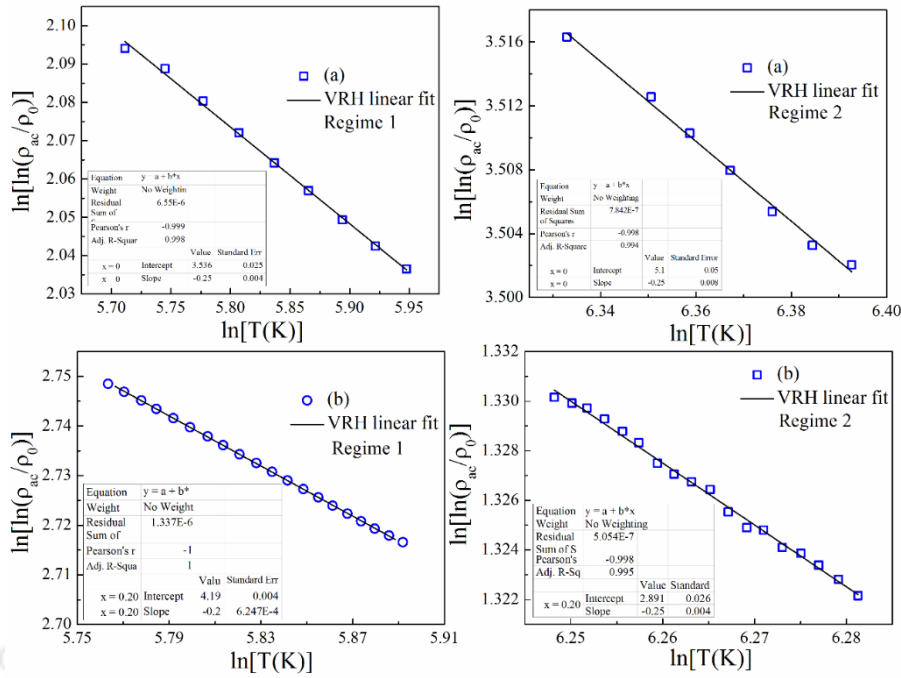


Figure 4.11: The $\ln[\ln(\rho_{AC}/\rho_0)]$ versus $\ln[T(K)]$ of $\text{Bi}_{0.5}(\text{Na}_{(1-x)}\text{K}_x)_{0.5}\text{TiO}_3$ ceramics for (a) $x = 0$ and (b) $x = 0.2$ in R1 (302 – 392K) and R2 (562 – 592K) regimes. Insets of (a) and (b) show the VRH linear fit parameters in tabular form.

The calculated Mott's parameters for all samples at R1 and R2 regimes satisfied the VRH condition $W_H \geq k_B T$ and $\alpha R_H \geq 1$ [51,54]. The obtained R_H and W_H values are shown in Table 4.2. It can be seen that the R_H decreases whereas W_H increases with an increase in temperature are shown in Figure 4.12, which is attributed to the increase in disorder in the BNKT system. In the regime R2, R_H and W_H values decreased from 6.29-0.70 nm and 0.80–0.08 eV whereas $N(E_F)$ values increased to $81.18 \times 10^{20} \text{ eV}^{-1} \text{ cm}^{-3}$ for $x = 0 - 0.2$ samples, respectively. The hopping energy and hopping length reduced with the addition of K significantly indicate the formation of additional localized states owing to the incorporation of K into BNT lattice.

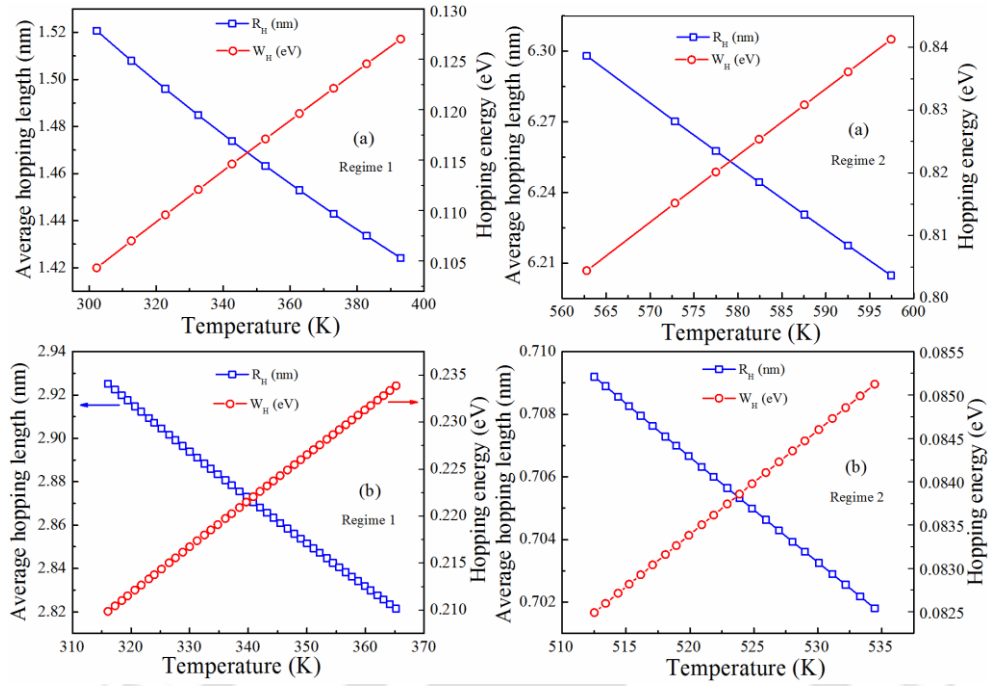


Figure 4.12: Temperature variation of Mott's variable range hopping parameters (R_H and W_H) of $\text{Bi}_{0.5}(\text{Na}_{(1-x)}\text{K}_x)_{0.5}\text{TiO}_3$ ceramics, for (a) $x = 0$ and (b) $x = 0.2$ in R1 (302 – 392K) and R2 (562 – 592K) regimes.

Table 4.2: Activation Energy (E_A) and Mott's parameters of $\text{Bi}_{0.5}(\text{Na}_{(1-x)}\text{K}_x)_{0.5}\text{TiO}_3$ ($x = 0 - 0.3$) ceramics, in R1 (302 – 392K) and R2 (562 – 592K) regimes.

Composition	E_A (eV)		$N(E_f)$ ($10^{20} \text{ eV}^{-1} \text{ cm}^{-3}$)		R_H (nm)		W_H (eV)	
	R1	R2	R1	R2	R1	R2	R1	R2
$x = 0$	0.058	0.417	6.510	0.0118	1.521–1.424	6.298–6.205	0.104–0.127	0.804–0.841
$x = 0.1$	0.081	–	2.368	–	1.898–1.795	–	0.148–0.175	–
$x = 0.2$	0.112	0.077	0.454	81.180	2.925–2.821	0.709–0.702	0.210–0.234	0.082–0.085
$x = 0.3$	0.091	–	1.167	–	2.272–2.231	–	0.174–0.184	–

Furthermore, the piezoelectric properties have been estimated from the fundamental resonance (f_r) and anti-resonance frequencies (f_a). Figure 4.13 shows the resonance and anti-resonance frequency of dielectric permittivity for BNKT ceramics

measured at room temperature in the frequency range from 1 MHz to 20 MHz. As the characteristic features of the piezoelectric constants are anisotropic, the resonant frequency is determined by the composition of piezoelectric material, the shape and volume of the sintered pellets. The physical constants are related to the applied mechanical or electric force directions and perpendicular to the applied electric force direction. Thus, the piezoelectric constants have two subscripts and refer to the direction of the two related quantities. The direction X, Y and Z quantities are denoted by the subscript 1, 2 and 3 respectively.

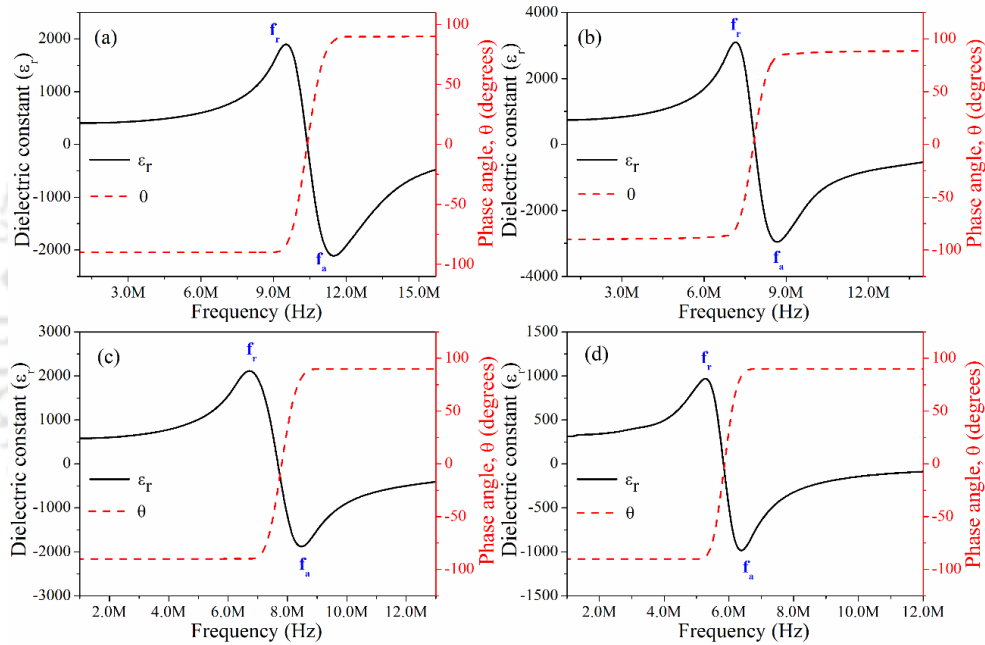


Figure 4.13: Resonance and anti-resonance curve for $\text{Bi}_{0.5}(\text{Na}_{(1-x)}\text{K}_x)_{0.5}\text{TiO}_3$ ceramics with (a) $x = 0$, (b) $x = 0.1$, (c) $x = 0.2$ and (d) $x = 0.3$, measured at room temperature.

The electromechanical coupling factor (k) is one of the most important parameters in piezoelectric materials, which converts the electrical energy into mechanical energy or vice versa and also describes the electromechanical coupling strength. The high electromechanical coupling factor of materials is suitable for efficient energy conversion. In electromechanical coupling factors k_{ij} , the suffix i indicates the direction of the applied

electric field and j indicates the direction of mechanical energy. The electromechanical coupling factors (k_{ij}), elastic compliance (S_{ij}), piezoelectric charge constants (d_{ij}), and piezoelectric voltage constants (g_{ij}) have been calculated from dielectric permittivity of resonance and anti-resonance frequency of disc-shaped BNKT ceramics, using the following equations [55].

$$k_{33}^2 = \frac{\frac{\pi}{2}}{1 + \frac{(f_a - f_r)}{f_r}} \tan \left[\frac{\frac{\pi(f_a - f_r)}{2f_r}}{1 + \frac{(f_a - f_r)}{f_r}} \right] \quad (4.9)$$

$$k_{31}^2 = \frac{\psi}{1 + \psi} \quad (4.10)$$

$$\psi = \frac{\pi}{2} \left(1 + \frac{(f_a - f_r)}{f_r} \right) \tan \left(\frac{\pi(f_a - f_r)}{2f_r} \right) \quad (4.11)$$

where, k_{33} and k_{31} are the coupling factor for the electric field in direction 3 and longitudinal vibration in 3 and 1 direction, respectively.

The thickness of electromechanical coupling factor (k_t) can be estimated following expression,

$$k_t^2 = \frac{\pi}{2} \left(\frac{f_r}{f_a} \right) \cot \left(\frac{\pi f_r}{2f_a} \right) \quad (4.12)$$

where, electromechanical coupling factor for the electric field and vibration are along direction 3.

The planar coupling coefficient (k_p) (planar mode vibration when applied electric field along the sample polarization direction) have been approximately calculated using the following expression,

$$k_p = \frac{f_a^2 - f_r^2}{f_r^2} \quad (4.13)$$

Elastic compliance can be defined as the amount of strain generated in a piezoelectric material per unit of applied stress, which is calculated using the following equations,

$$s_{33}^D = \frac{1}{4\rho f_a^2 t^2} \quad (4.14)$$

$$s_{33}^E = \frac{s_{33}^D}{1-k_{33}^2} \quad (4.15)$$

$$s_{11}^D = \frac{1}{4\rho f_a^2 d^2} \quad (4.16)$$

$$s_{11}^E = s_{11}^D(1-k_{31}^2) \quad (4.17)$$

where, ρ is the density of the sintered sample in kg/m^3 is obtained from Archimedes principle and t is the thickness and d is the diameter of the sample.

The piezoelectric charge coefficient d_{33} and d_{31} are proportional to the electromechanical coupling factor k_{33} and k_{31} , respectively.

$$d_{33} = k_{33} \sqrt{\varepsilon_0 \varepsilon_r s_{33}} \quad (4.18)$$

$$d_{31} = k_{31} \sqrt{\varepsilon_0 \varepsilon_r s_{11}} \quad (4.19)$$

where, piezoelectric charge coefficient for the induced polarization in the direction of sample polarization per unit stress in the direction perpendicular to the polarization.

The piezoelectric voltage constant g_{33} and g_{31} were calculated by using the following expressions,

$$g_{33} = \frac{d_{33}}{\varepsilon_0 \varepsilon_r} \quad (4.20)$$

$$g_{31} = \frac{d_{31}}{\varepsilon_0 \varepsilon_r} \quad (4.21)$$

where, piezoelectric voltage constant for the induced field in the direction of sample polarization per unit stress applied in a perpendicular direction.

Table 4.3: Dielectric, electromechanical, elastic and piezoelectric parameters of $\text{Bi}_{0.5}(\text{Na}_{(1-x)}\text{K}_x)_{0.5}\text{TiO}_3$ ceramics ($x = 0 - 0.3$).

Parameters	$x = 0$	$x = 0.1$	$x = 0.2$	$x = 0.3$
ϵ' (1 kHz)	692	752	1273	920
$\tan\delta$ (1 kHz)	0.045	0.206	0.047	0.081
f_r (MHZ)	9.8545	7.3564	6.7593	5.5246
f_a (MHZ)	10.9303	8.3091	8.1835	6.1750
k_{33}	0.469	0.503	0.603	0.484
k_{31}	0.481	0.518	0.629	0.497
K_t	0.469	0.503	0.603	0.484
k_p	0.230	0.275	0.465	0.249
S_{33}^D (m^2/N)	2.089×10^{-13}	5.348×10^{-13}	6.407×10^{-13}	16.92×10^{-13}
S_{33}^E (m^2/N)	2.68×10^{-13}	7.16×10^{-13}	10.068×10^{-13}	22.10×10^{-13}
S_{11}^D (m^2/N)	3.547×10^{-15}	6.173×10^{-15}	5.231×10^{-15}	12.47×10^{-15}
S_{11}^E (m^2/N)	4.617×10^{-15}	8.431×10^{-15}	8.647×10^{-15}	16.56×10^{-15}
d_{33} (C/N)	19.03×10^{-12}	34.73×10^{-12}	64.234×10^{-12}	64.98×10^{-12}
d_{31} (C/N)	2.560×10^{-12}	3.877×10^{-12}	6.205×10^{-12}	5.775×10^{-12}
g_{33} (Vm/N)	3.10×10^{-3}	5.21×10^{-3}	5.69×10^{-3}	7.97×10^{-3}
g_{31} (Vm/N)	4.179×10^{-4}	5.824×10^{-4}	5.506×10^{-4}	7.089×10^{-4}

The obtained piezoelectric parameters are listed in Table 4.3. The d_{33} and k_{33} values of BNT ceramics are found to be 19 pC/N and 0.46, respectively. These values are in good agreement with the earlier reports [55]. The values of electromechanical coupling factors

(k_{33} , k_{31} , k_t and k_p), elastic compliance ($s_{33}^D, s_{33}^E, s_{11}^D$ and s_{11}^E) piezoelectric charge constants (d_{33} and d_{31}), and piezoelectric voltage constants (g_{33} and g_{31}) were found to improve with an increase in K concentrations. Further, the resonance and anti-resonance frequencies are shifted towards lower frequency with increasing K concentration. All the above results obtained from the dielectric resonance spectra indicate that the solid solution of K substituted BNT ceramics exhibits soft dielectric behavior.

In order to understand leakage current conduction mechanism in the present system, the current density (J) versus electric field (E) measurement of the pure BNT and optimized BNKT ($x = 0.2$) ceramics were measured at room temperature and is shown in Figure 4.14(a). The value of J increases with the applied electric field up to 1 kV/cm and above that, it saturated for both the samples. Higher leakage current density is around $\sim 4.625 \times 10^{-5}$ A/cm² observed for pure BNT, which is attributed to the hopping of electrons from Ti^{+4} to Ti^{+3} . There is a slight decrease in leakage current density (1.215×10^{-5} A/cm²) with the substitution of K for $x = 0.2$ sample and is attributed to the increase of Ti valence state from Ti^{+3} to Ti^{+4} . The lower leakage current is attributed to K doping strengthening bonding energy and results in the decrease in the oxygen vacancies and Ti valence transition.

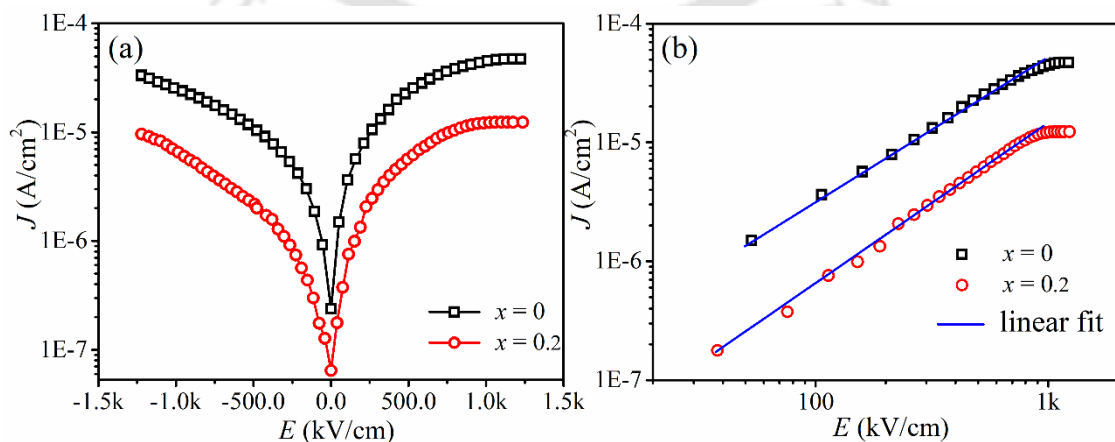


Figure 4.14: (a) Leakage current density (J) versus electric field (E), (b) $\ln(E)$ versus $\ln(J)$ of BNKT ceramics for $x = 0$ and 0.2 , measured at RT.

Furthermore, the space-charge-limited conduction (SCLC) mechanism was used to understand the conduction mechanism in the present system and was fitted with observed data by using the following equation.

$$J_{sclc} = \frac{9\mu\epsilon_r\epsilon_o\theta}{8t} E^2 \quad (4.22)$$

where μ is the carrier mobility, ϵ_r is the dielectric constant, ϵ_o is the dielectric constant of free space, θ is the fraction of free to total carrier density and t is the thickness of sample [56,57]. The linear fitting of $\ln(J)$ versus $\ln(E)$ of the pure BNT and BNKT ($x = 0.2$) ceramics are shown in Figure 4.14(b). The slope of BNKT ($x = 0.2$) is found to be increased from 1.18 to 1.42 and is indicating the space charge limited conduction mechanism, which corresponds to discrete trap carriers assisted discrete conduction mechanism. It is one of the leading factors to control the conduction process in BNKT ceramics. These studies suggested that the substitution of K^+ ions at A-sites can redistribute the oxygen vacancies and defects which are trapped across grains and grain boundaries. The reduction in leakage current and improvement in dielectric and piezoelectric properties are attributed to the incorporation of K at A-site in BNKT ceramics.

4.4 Results and discussion of BNT-KNNG composite ceramics

Figure 4.15 illustrates the X-ray diffraction (XRD) patterns of BNT-KNNG ($x = 0 - 0.02$) along with their Rietveld refinements. The Rietveld refined XRD patterns were obtained using Full-prof software, in which the pseudo-Voigt function used to describe the peak profiles. The fitting quality was confirmed by the goodness of the fit (χ^2) values. From the refinement analysis, it was observed that all the samples exhibited a single phase with rhombohedral crystal symmetry and belonged to the R3c space group (JCPDS No. 01-085-

0530) [58]. The obtained lattice parameters, unit-cell volume and χ^2 values are listed in Table 4.4. There is no significant variation in lattice parameters was observed with an

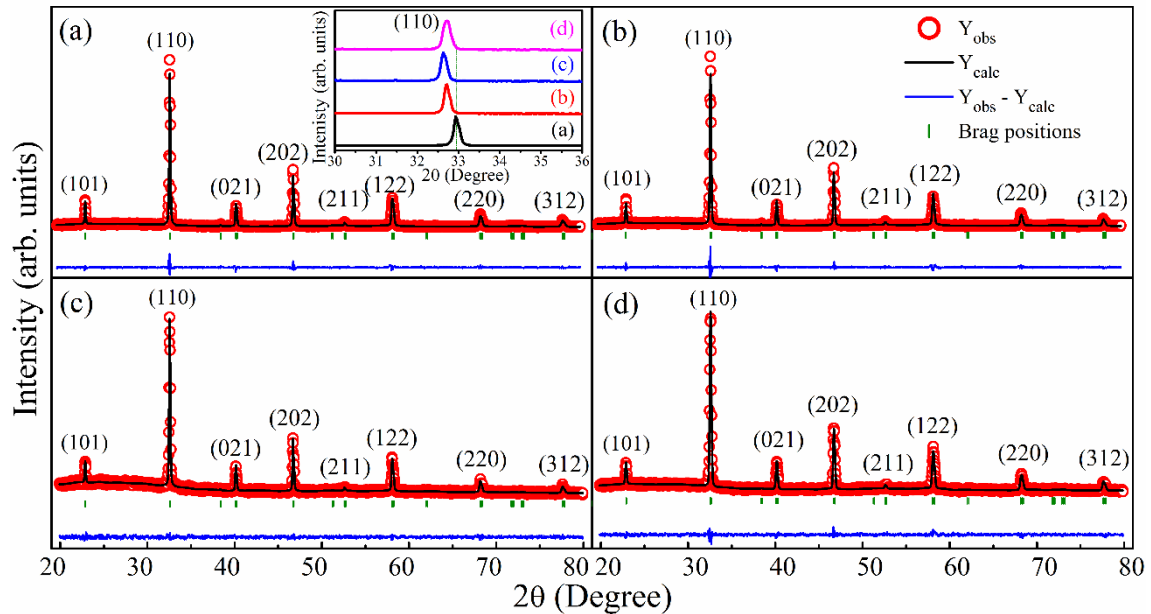


Figure 4.15: Rietveld refined XRD patterns of BNT-KNNG composites for (a) $x = 0$, (b) $x = 0.005$, (c) $x = 0.01$ and (d) $x = 0.02$. Inset of Figure 4.15(a) represents the shift in (110) diffraction peak in the 2θ range of 30° to 36° .

increase in x concentration. However, a slight enhancement in the unit cell volume was observed with an increase in x from 0 to 0.01 but the volume decreased for $x = 0.02$. The inset of Figure 4.15 (a) shows the position of (110) diffraction peak, which is shifted to a lower Bragg angle for $x = 0$ to 0.01, and beyond that, it shifted towards higher Bragg's angle. The shift towards the lower Bragg angle signifies the lattice expansion whereas the shift towards higher Bragg angle implies the shrinkage. The shift in the diffraction peak also supports the increase/decrease in the lattice parameter as well as the unit cell volume. The increase/decrease of lattice parameters was attributed to the incorporation of KNNG in the BNT matrix. For $x \leq 0.01$, the Nb^{5+} (0.64 \AA) ions occupied the Ti^{4+} (0.60 \AA) site, whereas the Na^+ (1.02 \AA), K^+ (1.38 \AA) and Gd^{3+} (0.93 \AA) ions occupied the Na^+ (1.02 \AA) and Bi^{3+} (1.03 \AA) site of BNT composition at higher concentrations of x (≥ 0.02) due to a

mismatch of ionic radii and valency [10,22]. When Na⁺ (KNNG) occupied in Na⁺ (BNT) and Bi³⁺ sites, there is no evidence of lattice variation in the present composition, as the ionic radius of Na⁺ is very close to Bi³⁺. However, for $x \geq 0.02$ composition, the decrease in the lattice parameters is mainly caused by the smaller ionic radius of Gd³⁺ as compared to Na⁺ and Bi³⁺ ions.

The crystallite size (D) of all the compositions was calculated by using the Scherrer equation (Eqn. 3.1) [59,60]. The obtained crystallite sizes of the samples are listed in Table 4.4. For $x = 0$, the crystallite size is found to be 47 nm. With increasing the KNNG composition, there is a slight enhancement in crystallite size for $x = 0.01$ and further, it decreases to 38 nm for $x = 0.02$ composition due to the substitution of smaller Gd³⁺ ions at the A- (Na⁺ and Bi³⁺) site of BNT system.

Table 4.4: Lattice parameters and average grain sizes of BNT-KNNG ceramics ($x = 0 - 0.02$).

Parameters	$a=b$ (Å)	c (Å)	$V(\text{Å}^3)$	χ^2	Crystallite size (nm)	Grain size (μm)
$x = 0$	5.5016	13.4474	352.4916±0.03	2.29	47±2.35	1.7±0.48
$x = 0.005$	5.4942	13.4840	352.4953±0.05	2.38	51±2.55	1.0±0.31
$x = 0.01$	5.4956	13.4809	352.6016±0.04	2.28	47±2.35	0.9±0.24
$x = 0.02$	5.4913	13.4863	352.1811±0.06	2.55	38±1.9	1.0±0.31

The FESEM micrographs of the sintered BNT-KNNG compositions ($x = 0 - 0.02$) are shown in Figure 4.16. All the samples displayed rectangular-shaped grains with uniform microstructure. From Figure 4.16(c), one can clearly see that the $x = 0.01$ composite exhibited a highly dense microstructure and was found to be more compact with smaller grain size as compared with the pure BNT sample. The relative density of all compositions

was estimated by using the Archimedes principle and was found to be in the range of 90-95% of the theoretical density. The average grain size was calculated by the linear intercept method using Image-J software and are shown in Table 4.4. The average grain size of BNT system ($x = 0$) was found to be larger ($1.7 \mu\text{m}$) as compared to other compositions ($x = 0.005, 0.01$ and 0.02). With the addition of KNNG, the grain size is found to be decreased ($0.9 \mu\text{m}$) up to $x = 0.01$ and increased for $x \geq 0.02$. The reduction in the grain size is due to the incorporation of KNNG that lead to the inhibition of grain growth [61]. The obtained small grains and uniform microstructure with a maximum density would improve the mechanical strength of piezoelectric ceramics, which was also reported by Matsubara et al. [62].

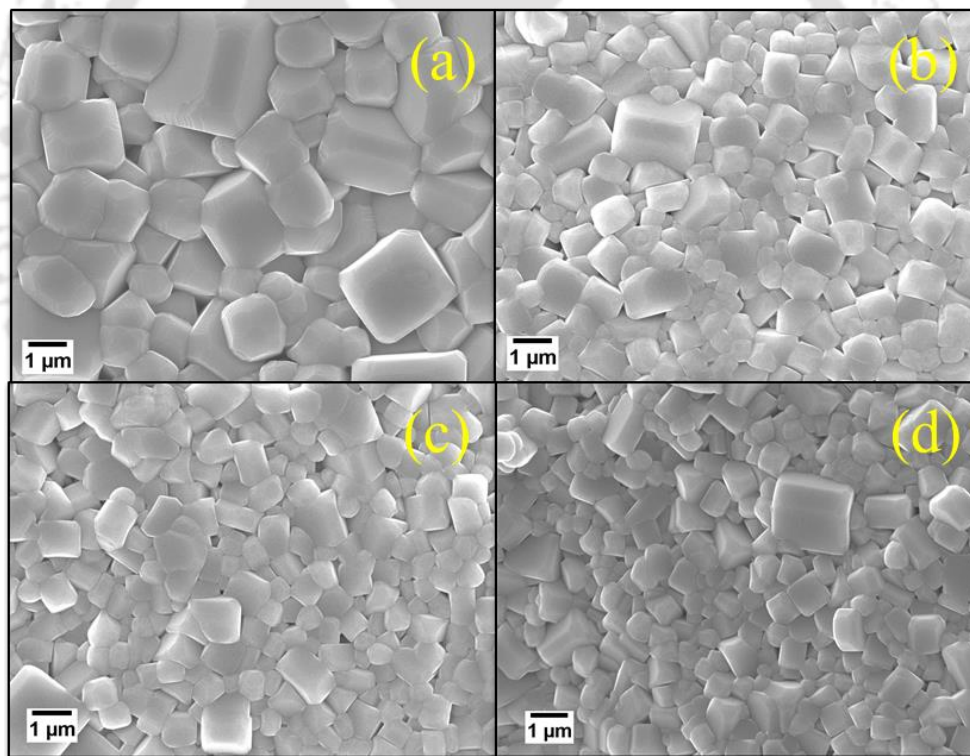


Figure 4.16: FESEM micrographs of BNT-KNNG composites for (a) $x = 0$, (b) $x = 0.005$, (c) $x = 0.01$ and (d) $x = 0.02$.

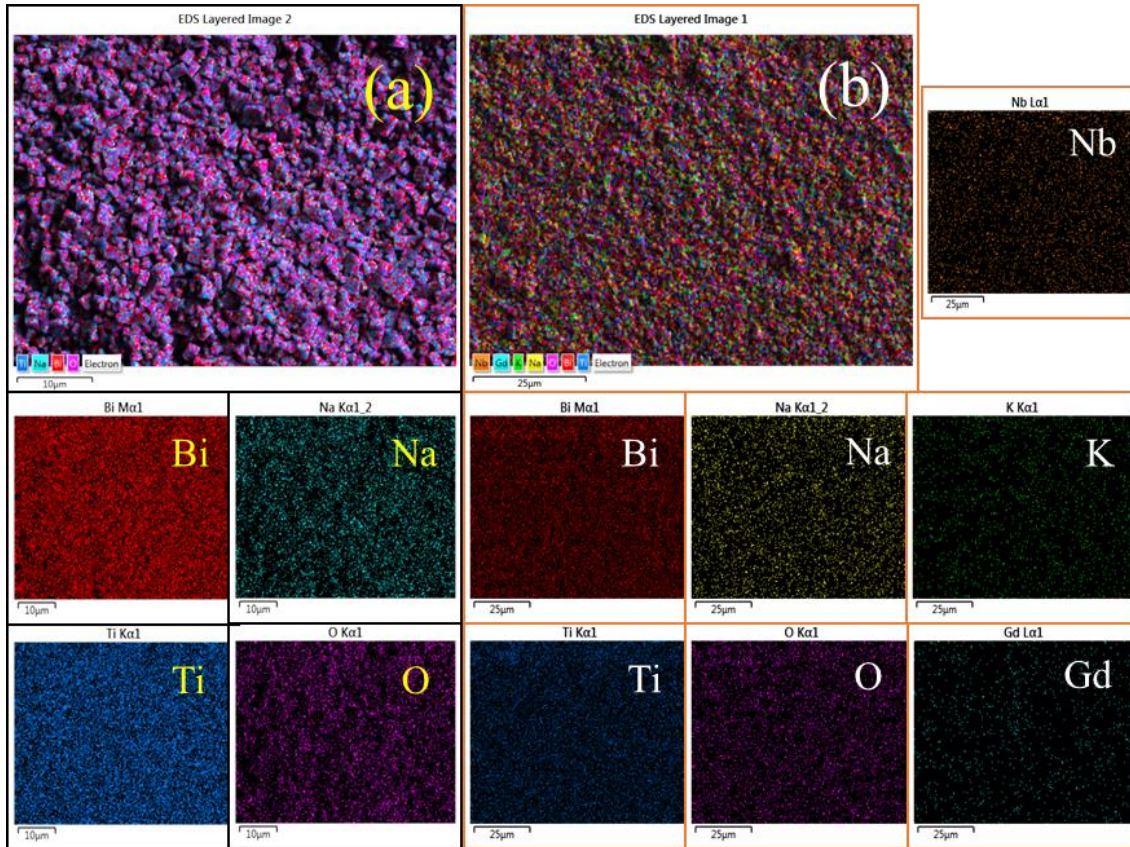


Figure 4.17: The typical microstructure and elemental mapping for (a) $x = 0$ and (b) $x = 0.01$ of BNT-KNNG ceramics.

The composition of BNT-KNNG composite ceramics have been analyzed in terms of the elemental composition mapping using EDAX, which are shown in Figure 4.17 (a) (yellow text) and (b) (white text) for $x = 0$ and 0.01, respectively. It is noticed that the Bi, Na, Ti and O occupied the same areas and are well connected to each other. However, the Na, K, Nb, Gd and O occupied the remaining isolated areas. These results indicate that all the elements of KNNG enter into grains and are homogeneously distributed. Moreover, the EDAX technique is used to confirm the elemental distribution of BNT-KNNG composition for $x = 0$ and 0.01, and are shown in Figure 4.18 (a) and (b), respectively. The experimental volume fraction of BNT-KNNG (Bi=9.5%, Na=9.2%, Ti=18.7%, O=62.2%, Nb=0.2%, K=0.1%, Gd=0.1%) composition is in line with the theoretical volume fractions (Bi=9.9%, Na=9.9995%, Ti=19.8%, O=60%, Nb=0.199%, K= 0.0995%, Gd=0.095%), which

confirms the stoichiometry of the BNT-KNNG composite. However, the experimental volume fraction of Na and Bi is slightly lower than the theoretical value due to the volatile nature of Na and Bi during sintering the process [63].

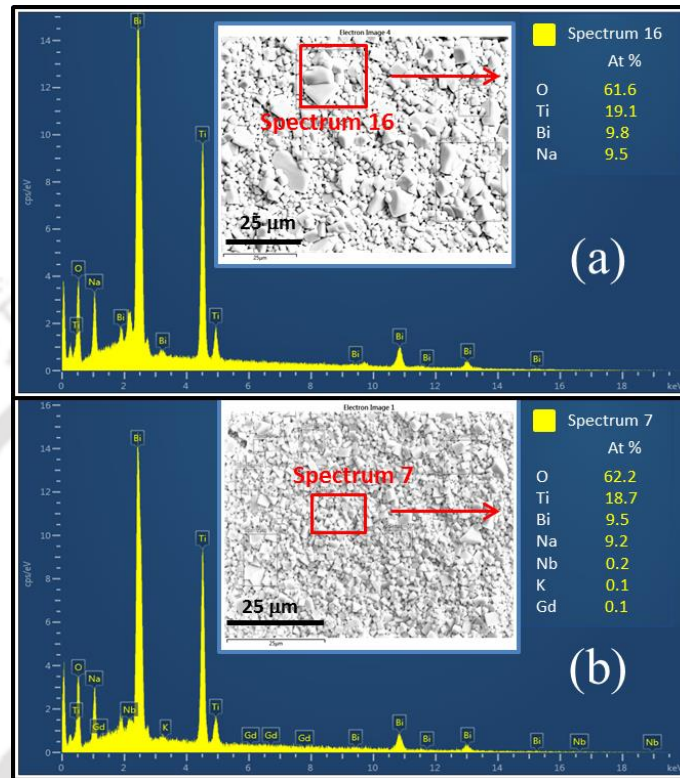


Figure 4.18: The EDAX spectra of BNT-KNNG composites for (a) $x = 0$ and (b) $x = 0.021$ samples.

In addition, the TEM analysis is used to identify the rhombohedral phase of BNT-KNNG composition. The bright-field mode transmission electron microscopy images, selected area electron diffraction (SAED) pattern and corresponding high-resolution transmission electron microscopy (HRTEM) images of the BNT-KNNG compositions have been investigated and depicted in Figure 4.19. The TEM images (Figure 4.19 (a) and (e)) of BNT-KNNG shows that the powder is composed of polyhedral shaped particles with an average size of ~ 411 nm and ~ 463 nm for $x = 0$ and 0.01 samples, respectively. The clear lattice fringes can be seen from the SAED pattern of Figure 4.19 (b) and (f), which confirms the polycrystalline nature of the prepared sample ($x = 0$ and 0.01). Further, the

interplanar spacing' for all crystallographic planes is determined from lattice fringes by using Gatan software, which is listed in Table 4.5.

Table 4.5: Crystal planes and corresponding inter planer spacing (d) of BNT-KNNG ceramics for $x = 0$ and 0.01 compositions.

Plane	$d(\text{nm}); x=0$	$d(\text{nm}); x=0.01$	$d(\text{nm}); x=0$	$d(\text{nm}); x=0.01$	$d(\text{nm}); x=0$
	(SAED)	(SAED)	(XRD)	(XRD)	(JCPDS#00-036-0340)
101	0.3886	0.3887	0.3887	0.3887	0.3900
110	0.2710	0.2750	0.2750	0.2748	0.2740
021	0.2267	0.2159	0.2245	0.2246	0.2240
202	0.1906	0.1958	0.1943	0.1943	0.1945
211	0.1710	0.1658	0.1739	0.1738	0.1733
122	0.1591	0.1588	0.1587	0.1586	0.1584
220	0.1372	0.1472	0.1375	0.1373	0.1369
312	0.1216	0.1228	0.1228	0.1229	0.1227

The insets of Figure 4.19 (d) and (h) are the inverse fast Fourier transform (IFFT) HRTEM images of yellow squared box regions of BNT-KNNG ceramics for $x = 0$ and 0.01, respectively. The obtained interplanar spacing of the BNT-KNNG compositions is 0.3867 nm and 0.2570 nm corresponding to (101) and (110) planes for $x = 0$ and 0.01. The obtained d values are in good agreement with BNT-0.06BT composites reported by Zhou et al. [64]. It is noticed that the interplanar spacing of (110) crystallographic plane is slightly higher for KNNG composite with $x = 0.01$, which can be attributed to the substitution of larger Nb^{+5} ion in Ti^{4+} site. The extracted' values from both HRTEM and SAED patterns closely match the calculated interplanar spacing of the rhombohedral phase (R3c space group) of BNT-KNNG as obtained from the XRD analysis using Rietveld refinement and standard JCPDS file #00-036-0340.

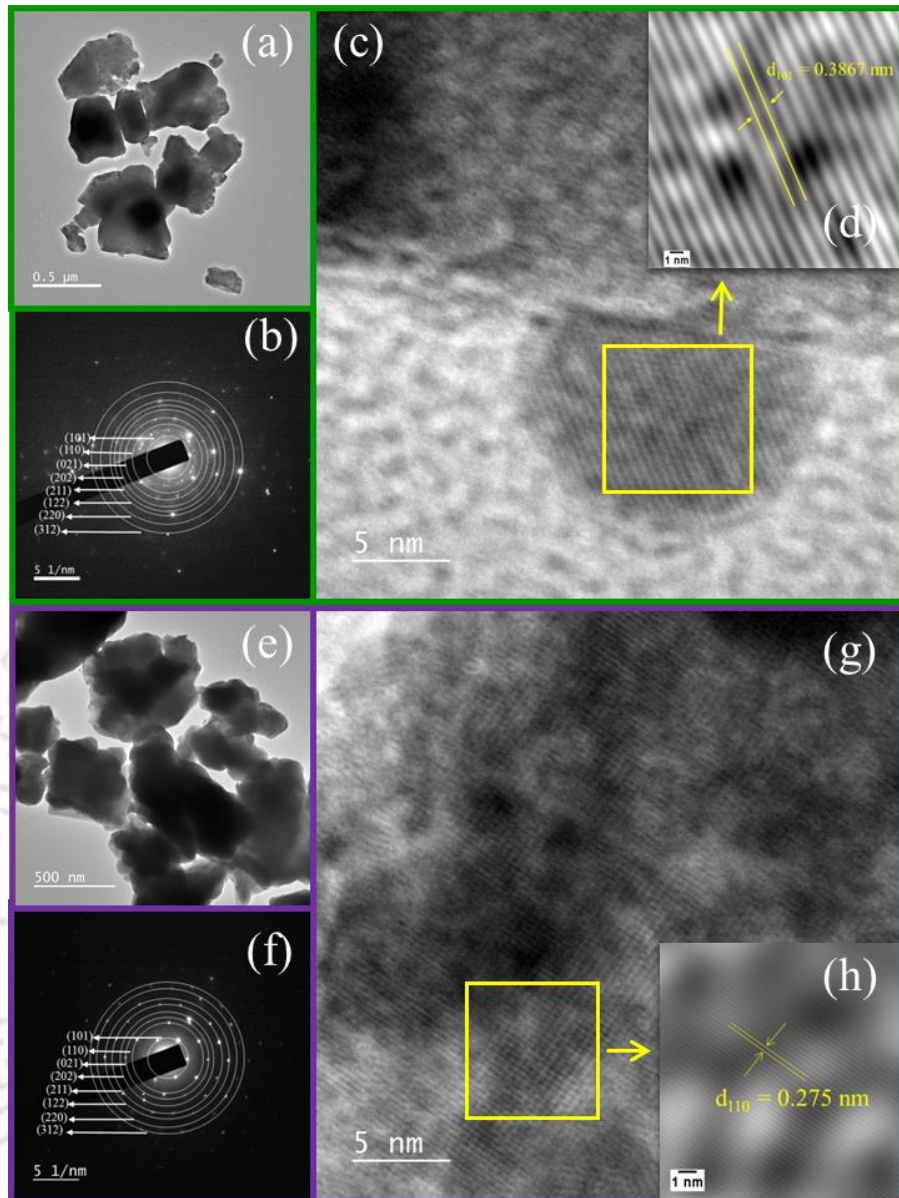


Fig. 19: (a) and (e) represents the bright-field TEM images, (b) and (f) the SAED patterns, (c) and (g) HRTEM images, (d) and (h) the IFFT images (insets) of BNT-KNNG ceramics for $x = 0$ and 0.01 , respectively.

Figure 4.20 shows the RT Raman spectra of BNT-KNNG composites recorded in the wavenumber range of $50 - 1000 \text{ cm}^{-1}$ along with their spectral de-convolution, which are fitted with Gaussian function using the origin software. Nine Raman active modes were observed for all the compositions. The obtained Raman modes and full width at half maxima (FWHM) are reported in Table 4.6. The broadening of all the vibrational modes

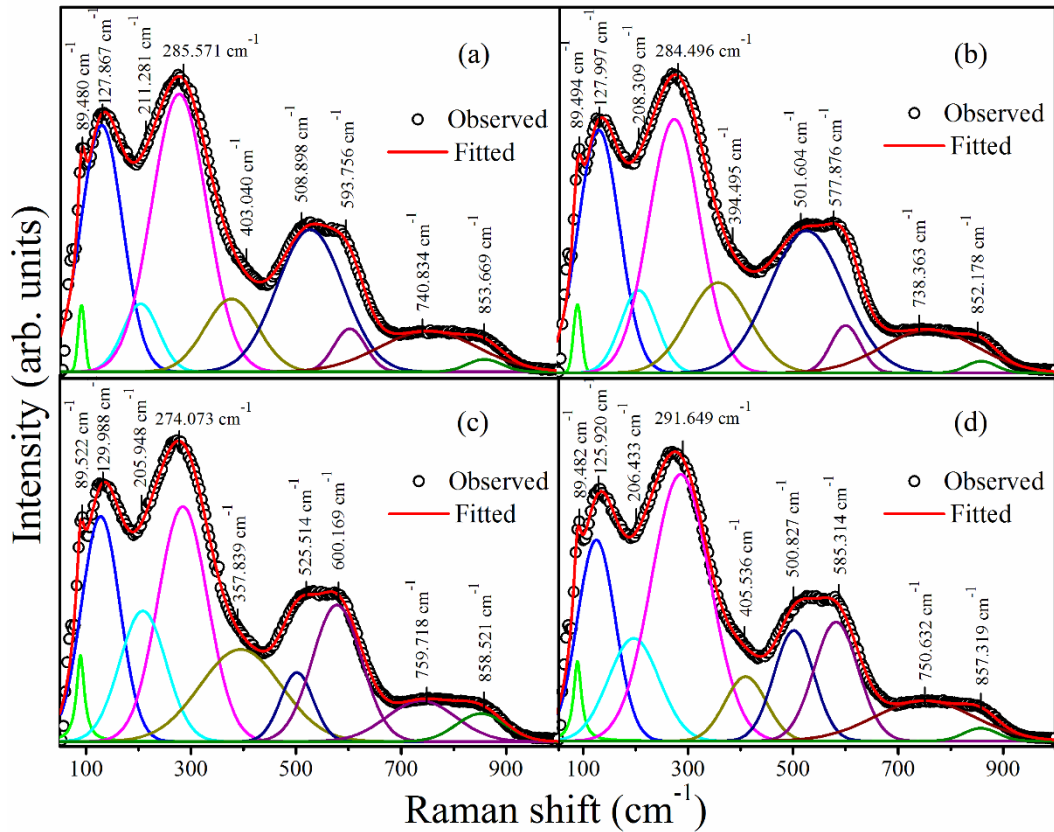


Figure 4.20: Raman spectra of BNT-KNNG composites for (a) $x = 0$, (b) $x = 0.005$, (c) $x = 0.01$ and (d) $x = 0.02$.

signifies the disorder in the BNT lattice and the overlapping of Raman modes with each other. From the group theory, the BNT system having a rhombohedral crystal structure with an $R3c$ space group consists of 13 Raman active modes: $\Gamma_{Raman} = 4A_1 + 9E$. Where A_1 (non-degenerate) and E (doubly degenerate) optical modes and all these modes are Raman as well as IR active [29]. The Raman active A_1 (TO_1) modes found in the region of 89 - 129 cm^{-1} are associated with the displacement of Bi-O and Na-O vibrations. Whereas, the doubly degenerated Raman active E (TO_2) modes located between 211 cm^{-1} to 403 cm^{-1} corresponds to Ti-O vibrations, which were observed in many perovskites [30]. The high frequency (TO_3) modes situated between 501 – 600 cm^{-1} are associated with the vibrations of the TiO_6 octahedra. The LO_3 modes observed between 738 – 858 cm^{-1} are corresponding to the A_1 (LO) and E (LO) overlapping modes [31].

Table 4.6: Raman shift and FWHM of the modes for BNT-KNNG ceramics ($x = 0 - 0.02$).

Modes	$x = 0$		$x = 0.005$		$x = 0.01$		$x = 0.02$	
	Raman shift (cm ⁻¹)	FWHM (cm ⁻¹)	Raman shift (cm ⁻¹)	FWHM (cm ⁻¹)	Raman shift (cm ⁻¹)	FWHM (cm ⁻¹)	Raman shift (cm ⁻¹)	FWHM (cm ⁻¹)
1	89.480	14.968	89.494	18.156	89.522	17.934	89.482	18.329
2	127.867	94.082	127.997	86.469	129.988	93.079	125.920	85.629
3	211.281	92.737	208.309	104.176	205.948	81.135	206.433	126.093
4	285.571	137.701	284.496	111.576	274.073	115.176	291.649	131.591
5	403.040	74.864	394.495	182.884	357.839	137.339	405.536	77.797
6	508.898	119.647	501.604	73.782	525.514	168.043	500.827	101.657
7	593.756	86.891	577.876	110.286	600.169	67.158	585.314	97.174
8	740.834	222.309	738.363	153.855	759.718	213.341	750.632	222.758
9	853.669	84.867	852.178	110.265	858.521	67.482	857.319	74.442

However, the strong vibrational modes of pure BNT observed at 211, 285 and 403 cm⁻¹ are gradually shifted towards lower wavenumber with an increase in KNNG composition up to $x = 0.01$ and further shifted towards higher wavenumber region. This can be attributed to the enhancement in the B-site disorder in BNT-KNNG composite, induced by the substitution of smaller Ti⁴⁺ by larger Nb⁵⁺ ions. Consequently, the size of (Bi_{0.5}Na_{0.5})TiO₃ clusters increased. This can also be understood from the relation between the frequency and the reduced mass of ion [33]. Similarly, the vibration modes appearing in the 89 – 129 cm⁻¹ regions and above 500 cm⁻¹ are slightly shifted towards higher wavenumber with an increase in KNNG composition. These modes correspond to the A-site, TiO₆ and A₁ + E vibrations and are attributed to the A-site disorder in the present system. Such disorders are induced by the substitution of Na⁺ and Bi³⁺ by K⁺ and Gd³⁺ ions. The results obtained from the Raman analysis agree with the XRD and microstructural studies.

Figure 4.21 represents the temperature-dependent dielectric constant (ϵ_r) and dielectric loss ($\tan\delta$) of BNT-KNNG ($x = 0 - 0.02$) composites, measured in the frequency range of 1 kHz to 1 MHz. From Figure 4.21(a), it is observed that a clear dielectric anomaly $\sim 330^\circ\text{C}$ corresponding to the ferroelectric tetragonal to paraelectric cubic phase, which is called the critical temperature (T_C) along with a feeble anomaly $\sim 200^\circ\text{C}$ corresponding to the structural phase transitions from rhombohedral to tetragonal often referred as the depolarization temperature (T_d) of pure BNT ceramics [38]. A gradual shift in T_d as well as T_C is observed towards lower temperatures $\sim 180^\circ\text{C}$ and $\sim 317^\circ\text{C}$ due to the incorporation of KNNG with $x = 0.02$. It can be attributed to the substitution of KNNG into the BNT system, which disturbs the long-range ferroelectric order and causes the reduction of transition temperature (T_d and T_C). This reduction of the transition temperature leads to the formation of polar nano-regions (PNR) due to the differences in ionic radius of A and B-sites of BNT-KNNG system. The formation of PNR embedded in the BNT-KNNG causes the disorder in the system [43]. The maximum dielectric constant ($\epsilon_{r,\text{max}}$) at T_C is found to be ~ 2312 (@ $f = 100$ kHz) for pure BNT which is enhanced to ~ 2729 for $x = 0.01$. It further decreased for $x \geq 0.02$ which is shown in the inset of Figure 4.21(a). A similar trend was also observed in ϵ_r values measured at RT. The enhancement in ϵ_r (~ 1074) and lowering of $\tan\delta$ (~ 0.059) at 1 kHz was noticed for the $x = 0.01$ sample. The improvement in ϵ_r values can be attributed to the incorporation of KNNG into the BNT matrix and to the maximum relative density. However, the damaged ferroelectric order and lower relative densities causes the lowering of ϵ_r values at RT and slight increase in the $\tan\delta$ for $x \geq 0.02$ composition.

Furthermore, the T_C values were slightly shifted towards higher temperatures (similar to the ϵ_r versus T) and the peaks were diffused with a rise in frequency from 1 kHz

to 1 MHz. The loss tangent also clearly exhibited the frequency dispersive behavior, which is popularly known as the signature of ferroelectric relaxor behavior [65]. This frequency

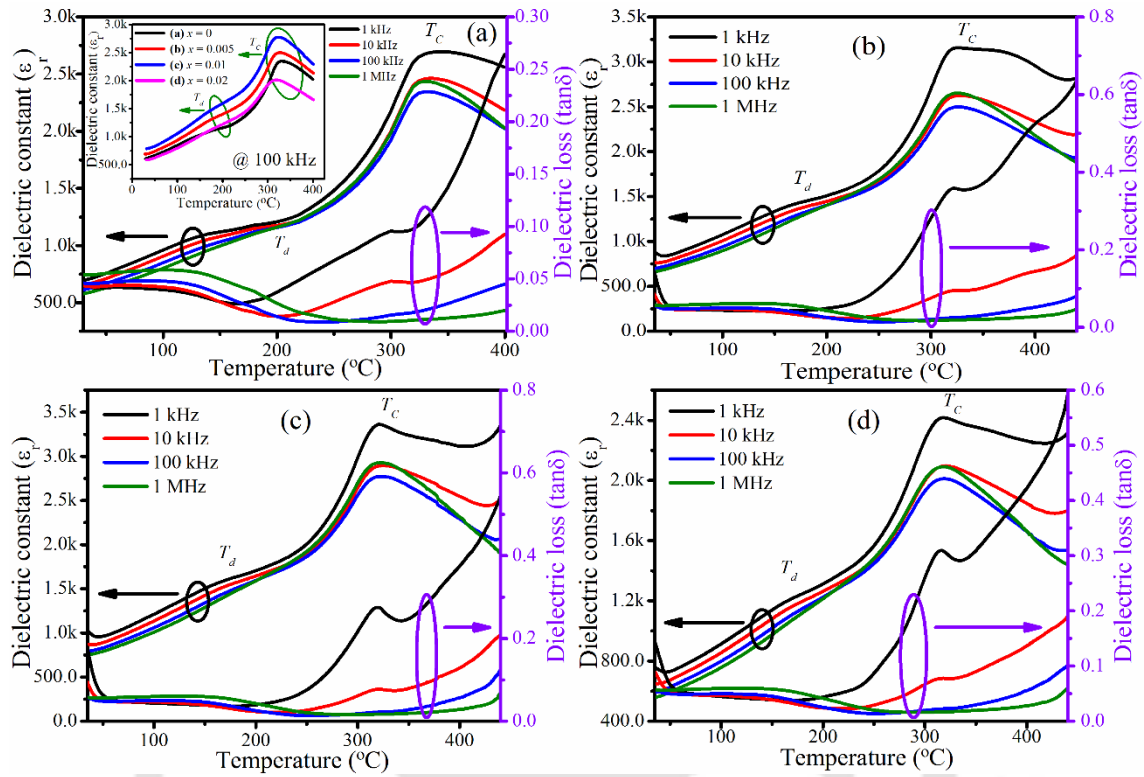


Figure 4.21: The temperature dependence of ϵ_r and $\tan\delta$ of BNT-KNNG composites for (a) $x = 0$, (b) $x = 0.005$, (c) $x = 0.01$ and (d) $x = 0.02$, measured from 1 kHz – 1 MHz. The inset of Figure 4.21(a) represents the temperature dependence of ϵ_r at 100 kHz for all the compositions.

dispersion behavior indicates the existence of the relaxor behavior of the dipoles in all the compositions that are associated with the domain wall motion, domain reorientation and dipolar orientations of the ferroelectric materials. Therefore, the observed relaxor behavior with diffuse phase transition of the BNT-KNNG compositions can be described by the modified Curie-Weiss law by using Eq. 4.2 [47]. The value of γ is equal to unity for normal ferroelectrics and it lies in between 1 to 2 for relaxor ferroelectrics [47]. Figure 4.22 represents the log-log plots of $(1/\epsilon_r - 1/\epsilon_r^m)$ vs. $(T - T_m)$ at 1 MHz. The γ values obtained from the above analysis lies in the range of 1.48 – 1.73 for all the samples, indicating the

existence of relaxor behavior. The increase in γ with the substitution of Nb might be due to a strong distortion in the BNT system.

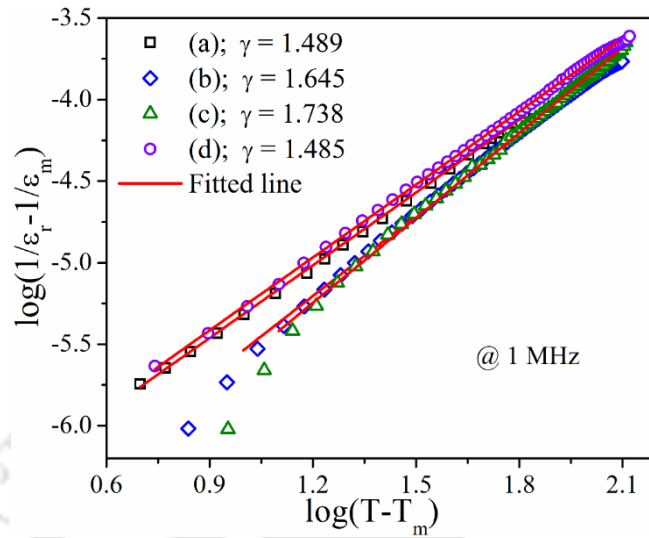


Figure 4.22: The logarithmic variation of $(1/\epsilon_r - 1/\epsilon_r^m)$ as a function of $\log(T - T_m)$ of BNT-KNNG composites for (a) $x = 0$, (b) $x = 0.005$, (c) $x = 0.01$ and (d) $x = 0.02$.

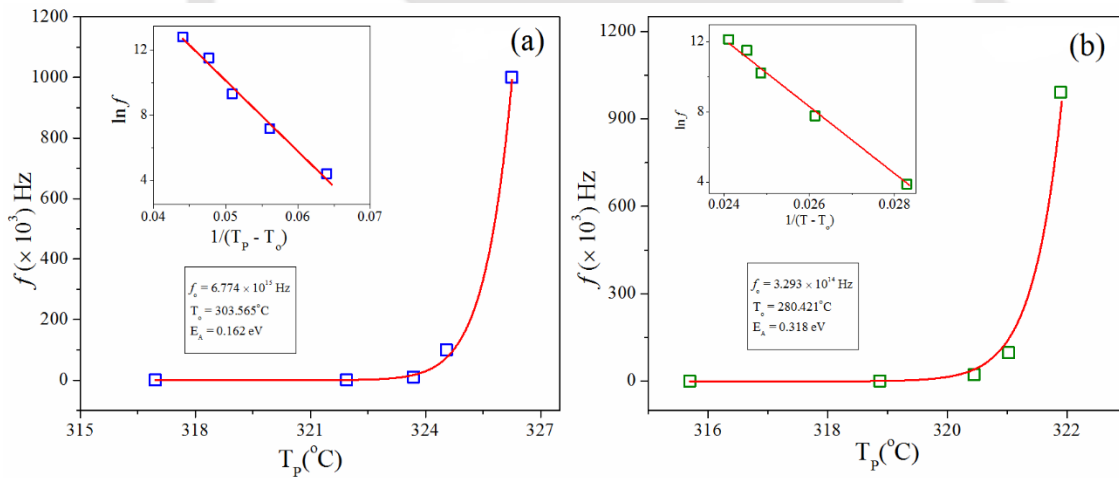


Figure 4.23: Frequency variation of critical temperature of BNT-KNNG ceramics for (a) $x = 0$ and (b) $x = 0.01$ fitted with Vogel-Fulcher law.

In order to confirm the existence of relaxor behavior in BNT-KNNG for $x = 0$ and 0.01 compositions were analyzed using Vogel-Fulcher (V-F) law by Eq. 4.3 [48]. The scattered symbol indicates the critical temperatures (T_p), and the solid line represents the fitted line of the V-F equation as shown in Figure 4.23. The evaluated fitting parameters

from this analysis are $f_0 = 6.774 \times 10^{15}$ Hz, $E_A = 0.162$ eV, and $T_0 = 303.565^\circ\text{C}$ and $f_0 = 3.293 \times 10^{14}$ Hz, $E_A = 0.318$ eV, and $T_0 = 280.421^\circ\text{C}$ for $x = 0$ and 0.01 , respectively. For ideal relaxor behavior, the attempt frequency should lie in-between $10^9 - 10^{16}$ Hz [66]. Further, the variation in the $\ln(f)$ versus $1/(T_P - T_0)$ graph is displayed in the inset of Figure 4.23 and showed a good agreement with the obtained results.

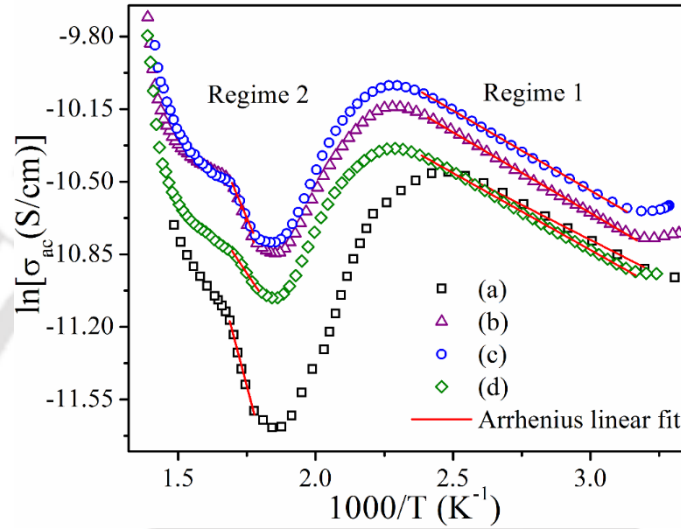


Figure 4.24: Temperature-dependent of AC-conductivity of BNT-KNNG composites fitted with Arrhenius equation for (a) $x = 0$, (b) $x = 0.005$, (c) $x = 0.01$ and (d) $x = 0.02$.

The activation energies (E_A) of all compositions have been evaluated from the temperature dependence of ac conductivity (σ_{ac}) by using the Arrhenius equation by Eq. 4.4 [67]. The E_A values calculated from the slope of $\ln\sigma_{ac}$ versus $1000/T$ plots at different regimes have been shown in Figure 4.24. The calculated E_A values of all the compositions are listed in Table 4.7. These values were found to enhance from $0.058 - 0.067$ eV for $x = 0$ to 0.01 in the regime 1 ($302 - 419$ K) and decreased further for $x > 0.01$. This behavior can be understood from the enhancement in a random distribution of hopping charge carriers between the localized states. In regime 2 ($562 - 589$ K), the activation energy values are found to be higher (0.433 eV) for pure BNT than in regime 1 which is attributed to the presence of oxygen vacancies, that can create an excess amount of electrons in both A and

B-sites of the present composition. As a result, a phase transition from the anti-ferroelectric to para electric phase occurs $\sim 330^\circ\text{C}$. Further, with an increase in the KNNG composition, the E_A value decreased to 0.172 eV for $x = 0.02$ sample and is attributed to the redistribution of oxygen vacancies and other charge carriers (electrons and holes). However, the obtained activation energy values are less than 1 eV which signifies the presence of oxygen vacancies due to relaxation of charge carriers or defects of ion in complexes along with the presence of deep acceptor traps in the system.

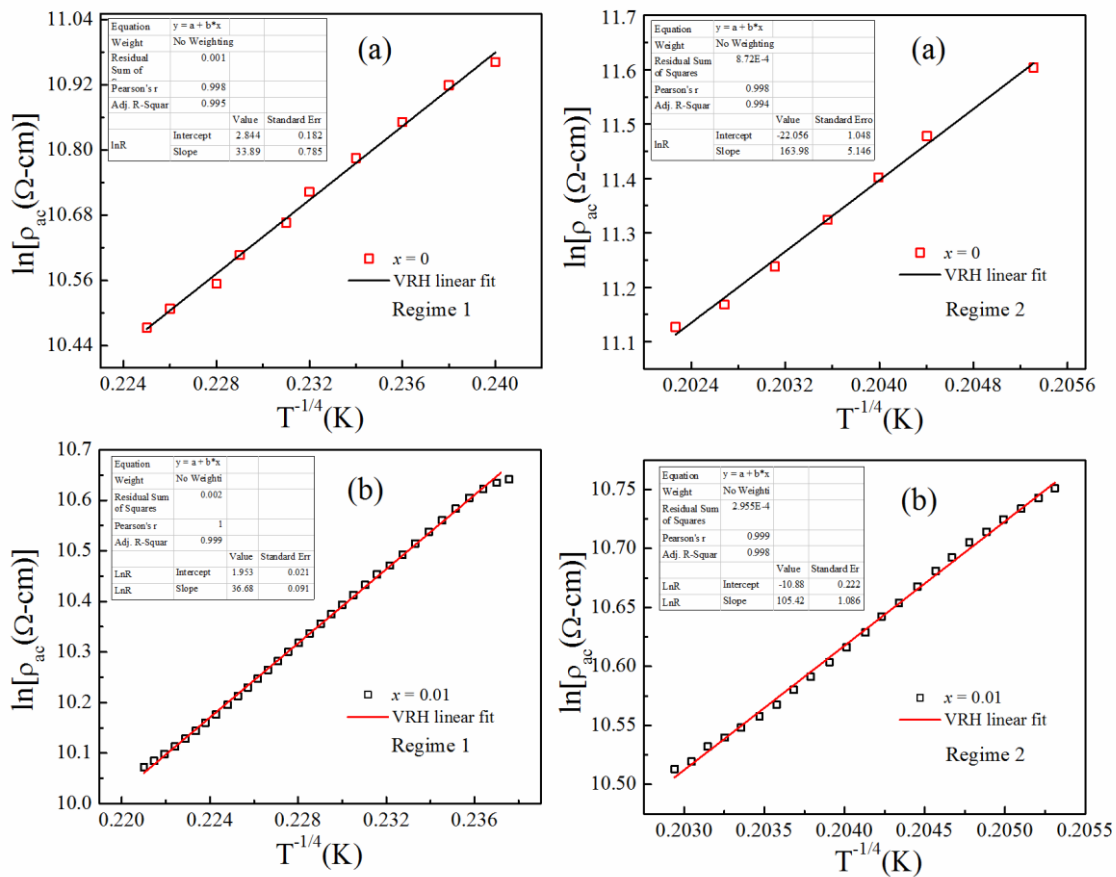


Figure 4.25: The $\ln(\rho_{ac})$ versus reciprocal temperature of BNT-KNNG composites for (a) $x = 0$ and (b) $x = 0.01$ in different regimes (R1 and R2).

Further, the nature of the hopping conduction mechanism and the temperature dependence of AC-resistivity in BNT-KNNG compositions were analyzed using variable-range-hopping (VRH) model, proposed by Mott [52,68]. According to the VRH model,

the variation of $\ln(\rho_{ac})$ versus $T^{-1/4}$ for BNT-KNNG compositions ($x = 0$ and 0.02) measured at 1 MHz in R1 and R2 regions are shown in Figure 4.25 and are fitted with the Eq. 4.5.

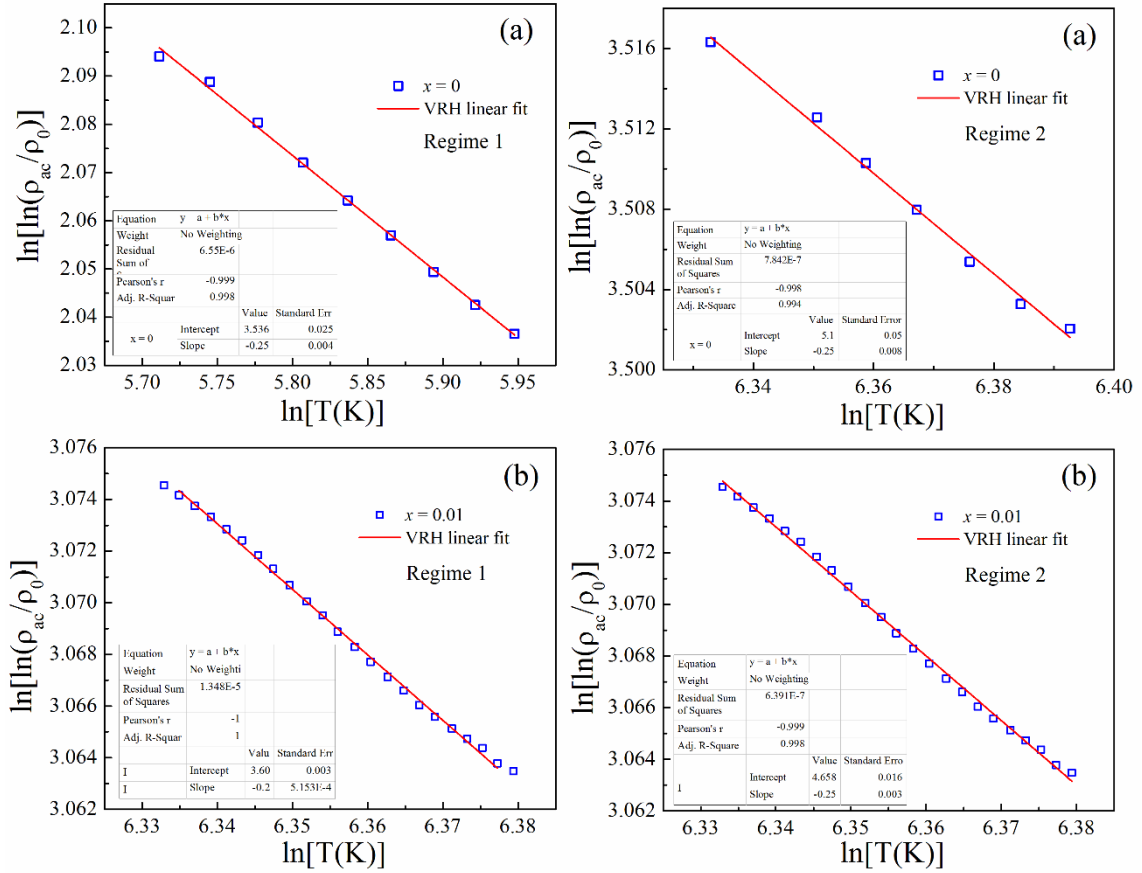


Figure 4.26: The $\ln[\ln(\rho_{ac}/\rho_0)]$ versus $\ln[T(K)]$ of BNT-KNNG composites for (a) $x = 0$ and (b) $x = 0.01$ in different regimes (R1 and R2).

The power of the exponential factor can vary depending on the nature of the hopping process. There are a few earlier reports, which suggested that it should be equal to $-1/4$ [51]. The linear plots of $\ln[\ln(\rho_{ac})]$ with respect to $\ln(T)$ for the BNT-KNNG system in both (R1 and R2) regimes are presented in Figure 4.26. It can be seen that all the compositions exhibited the linear behavior with the slope of $'-0.25'$, which confirms the signature of the VRH mechanism and is valid in both R1 and R2 regimes. Further, the density of states across the Fermi level ($N(E_F)$) is calculated using the Eq. 4.6. The obtained $N(E_F)$ values of all compositions are listed in Table 4.7 and are found to be decreased in

R1 region due to an increase in the resistivity of the KNNG composition. The lower values of $N(E_F)$ (at R2) found for low substitution of KNNG composition and is due to the reduction in the A or B-site defects caused by the volatilization of alkali elements (Na/K) as well as Bi during the high-temperature sintering process. The diminution in the grain size is also one of the reasons for the small value of $N(E_F)$. In the R2 regime, the $N(E_F)$ values are enhanced with an increase in x concentration due to the increase in crystal distortion and defect states across the Fermi level.

Furthermore, the electrical conduction response of the BNT-KNNG ceramics have been analyzed in terms of hopping length (R_H) and hopping energy (W_H) between localized states as given by the Eq. 4.7 and 4.8 [54].

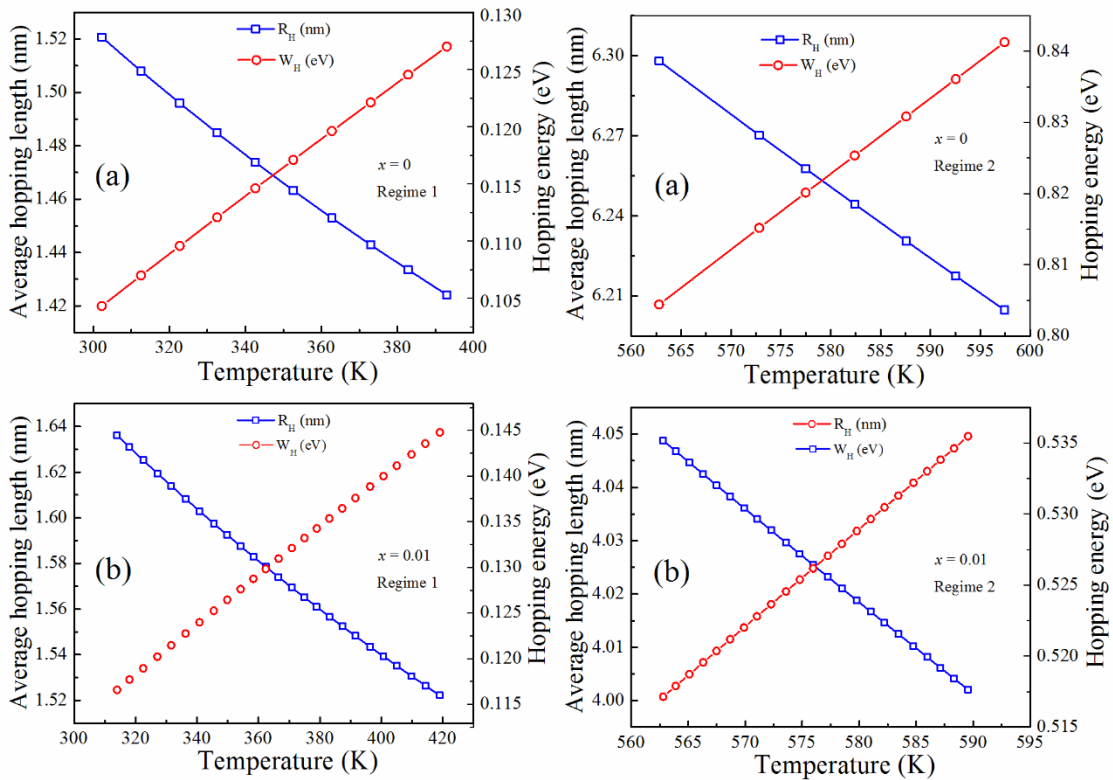


Figure 4.27: Temperature variation of Mott's variable range hopping parameters (R_H and W_H) of BNT-KNNG composites for (a) $x = 0$ and (b) $x = 0.01$ in different regimes (R1 and R2).

The obtained R_H and W_H values are listed in Table 4.7. These values for all compositions at R1 and R2 regimes satisfy the VRH mechanism conditions, i.e. $W_H \geq k_B T$ (0.025 eV) and $\alpha R_H \geq 1$ [22,53]. Temperature variation of Mott's variable range hopping parameters (R_H and W_H) of BNT-KNNG compositions for (a) $x = 0$ and (b) $x = 0.01$ in different regimes (R1 and R2) are shown in Figure 4.27. The R_H values diminished whereas W_H values rise with the temperature, which is attributed to the increase in disorder in the BNT-KNNG system. With an increase in x concentration, the R_H and W_H values reduced from 6.29 to 2.67 nm and 0.80 to 0.33 eV whereas $N(E_F)$ values increased from 0.01×10^{20} to $0.37 \times 10^{20} \text{ eV}^{-1} \text{ cm}^{-3}$ in the R2 regime. The reduction in average hopping length and hopping energy with the KNNG composition signifies the formation of additional localized states due to the incorporation of KNNG into the BNT system.

Table 4.7: Activation energy (E_A) and Mott's parameters of BNT-KNNG ($x = 0 - 0.02$) ceramics, in different regimes (R1 and R2).

Composition	E_A (eV)		$N(E_F)$ ($10^{20} \text{ eV}^{-1} \text{ cm}^{-3}$)		R_H (nm)		W_H (eV)	
	R1	R2	R1	R2	R1	R2	R1	R2
$x = 0$	0.058	0.433	6.510	0.011	1.521–1.424	6.298–6.205	0.104–0.127	0.804–0.841
$x = 0.005$	0.066	0.308	4.323	0.037	1.669–1.550	4.707–4.655	0.119–0.147	0.603–0.624
$x = 0.01$	0.067	0.269	4.678	0.069	1.634–1.522	4.049–4.004	0.117–0.145	0.517–0.535
$x = 0.02$	0.064	0.172	5.291	0.372	1.582–1.476	2.671–2.638	0.114–0.140	0.339–0.351

The resonance (f_r) and anti-resonance frequencies (f_a) of dielectric spectra for BNT-KNNG compositions ($x = 0 - 0.02$) measured at RT in the frequency range from 1 MHz to 20 MHz are shown in Figure 4.28. The electromechanical coupling factors (k_{33} , k_{31} , k_p and k_t), elastic compliance (S_{33} and S_{11}), piezoelectric charge constants (d_{33} and d_{11}), and piezoelectric voltage constants (g_{33} and g_{11}) were estimated from dielectric permittivity of

resonance and anti-resonance frequency of BNT-KNNG ceramics using the ANSI/IEEE standards on piezoelectricity expressions (Eq. 4.9 – 4.21) [69]. The calculated piezoelectric

Table 4.8: Dielectric, electromechanical, elastic and piezoelectric parameters of BNT-KNNG ceramics ($x = 0 - 0.02$).

Parameters	$x = 0$	$x = 0.005$	$x = 0.01$	$x = 0.02$
ϵ' (1 KHz)	692	918	1074	758
$\tan\delta$ (1 KHz)	0.045	0.054	0.059	0.057
f_r (MHZ)	2.847	4.263	6.016	3.199
f_a (MHZ)	2.998	4.583	6.699	3.403
k_{33}	0.343	0.401	0.477	0.373
k_{31}	0.347	0.408	0.489	0.379
K_t	0.343	0.401	0.477	0.373
k_p	0.364	0.434	0.533	0.400
S_{33}^D (m ² /N)	7.944×10^{-12}	4.152×10^{-12}	4.203×10^{-12}	7.630×10^{-12}
S_{33}^E (m ² /N)	9.005×10^{-12}	4.948×10^{-12}	5.441×10^{-12}	8.866×10^{-12}
S_{11}^D (m ² /N)	5.974×10^{-14}	3.041×10^{-14}	1.339×10^{-14}	4.228×10^{-14}
S_{11}^E (m ² /N)	6.795×10^{-14}	3.649×10^{-14}	1.761×10^{-14}	4.938×10^{-14}
d_{33} (C/N)	80.614×10^{-12}	80.435×10^{-12}	108.518×10^{-12}	91.065×10^{-12}
d_{31} (C/N)	70.939×10^{-12}	70.314×10^{-12}	63.323×10^{-12}	69.013×10^{-12}
g_{33} (Vm/N)	1.316×10^{-2}	0.990×10^{-2}	1.141×10^{-2}	1.357×10^{-2}
g_{31} (Vm/N)	1.160×10^{-3}	0.865×10^{-3}	0.665×10^{-3}	1.030×10^{-3}

constants are reported in Table 4.8. For pure BNT, the d_{33} , and k_p values are found to be 80.61 pC/N and 0.40 respectively, which are in good agreement with the earlier reports [55]. The addition of KNNG significantly enhanced the k_{33} , k_{31} , k_t , k_p , S_{33}^D , S_{33}^E , S_{11}^D , S_{11}^E , d_{33} , d_{31} , g_{33} and g_{31} coefficients. The enhanced k_p (53%) and d_{33} (108 pC/N) values of

BNT-KNNG ($x = 0.01$) ceramics make it a viable candidate for lead-free piezoelectric applications.

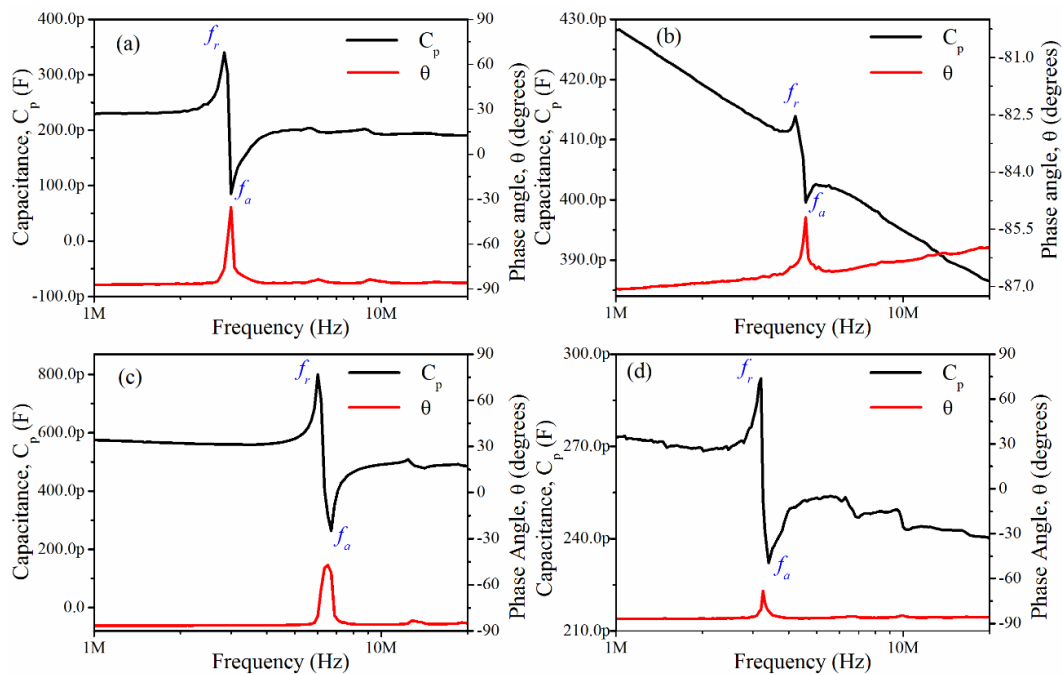


Figure 4.28: Resonance and anti-resonance frequency characteristics of capacitance and loss tangent of poled BNT-KNNG composites for (a) $x = 0$, (b) $x = 0.005$, (c) $x = 0.01$ and (d) $x = 0.02$.

The addition of K (0.20) on BNT effectively increased electromechanical coupling factor (k_{33}) and piezoelectric charge coefficient (d_{33}) to 0.603 and 64 pC/N due to formation of morphotropic phase boundary between rhombohedral and tetragonal phase at $x=0.20$. Similarly, the addition of KNNG (0.01) on BNT effectively increased electromechanical coupling factor (k_{33}) and piezoelectric charge coefficient (d_{33}) to 0.477 and 108 pC/N due to incorporation of KNNG composition in to BNT system at $x=0.01$. The electromechanical coupling factor is basically depending on their resonance frequencies (f_r and f_a), there difference (Δf) and are vary with material to material. The difference between resonance frequencies of BNKT for $x=0.20$ ($\Delta f \sim 1.4$) is approximately double than BNT-KNNG for $x=0.01$ ($\Delta f \sim 0.69$), resulting in lowered k_{33} value for BNKT-KNNG ($x=0.01$) as compared

to BNKT ($x=0.20$). The improved piezoelectric properties; electromechanical coupling factors ($k_{33} \sim 47.7\%$), and piezoelectric constants ($d_{33} = 108$ pC/N and $g_{33} = 1.14 \times 10^{-2}$ Vm/N) are observed for BNT-KNNG with $x = 0.01$ sample than BNKT, which is a potential candidate for high power electromechanical applications.

In general, the oxygen vacancies can play an important role in the conduction process in perovskites. The activation energy for conduction is around 1 eV, which is related to the enthalpy of migration for oxygen vacancies in perovskites [70]. In the present study, the activation energy is found to be much below 1 eV for all the compositions. The obtained E_A values are due to some other relaxing charge carriers (electrons and holes or defects ion complexes) and are also associated with deep acceptor traps. In this regard, the dc transport mechanism also plays an important role. Therefore, the leakage current density (J) of all the samples was measured as a function of electric field (E) for $x = 0, 0.005, 0.01$ and 0.02 at RT and are shown in Figure 4.29(a), which showed asymmetric behavior under an applied electric field of ± 1.2 kV/cm. The value of J is found to increase gradually with the electric field up to 1kV/cm and beyond that it saturates. Pure BNT ceramics exhibited higher leakage current ($\sim 4.51 \times 10^{-5}$ A/cm²) due to the hopping of electrons from Ti^{+4} to Ti^{+3} . The addition of KNNG significantly decreased the leakage current for $x = 0.01$, and increased further beyond $x > 0.01$. The lower J value obtained for $x = 0.01$ (8.83×10^{-6} A/cm²) is due to an increase of Ti valance state from Ti^{+3} to Ti^{+4} and is effectively reduced by the substitution of KNNG (especially Nb) into BNT matrix.

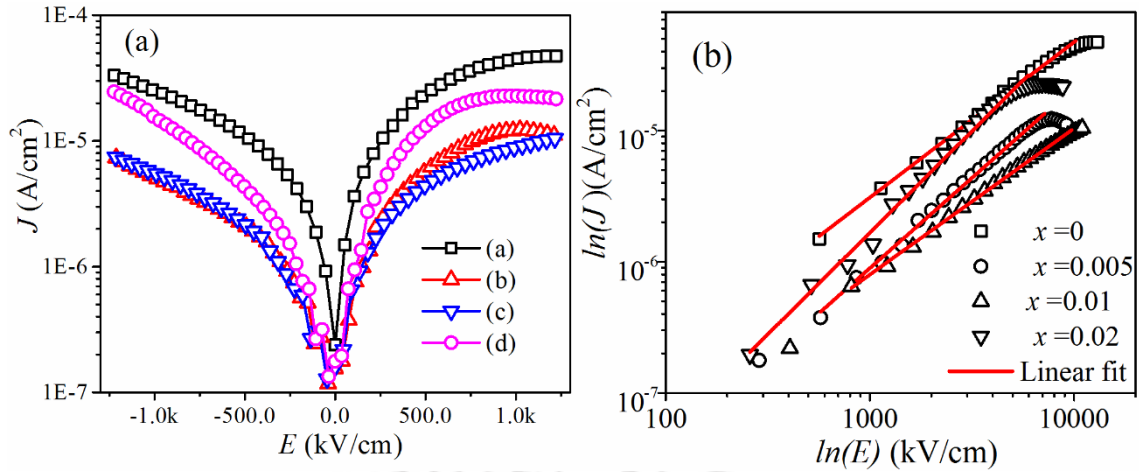


Figure 4.29: (a) Leakage current density (J) versus electric field (E), (b) $\ln(E)$ versus $\ln(J)$ of BNT-KNNG composites for (a) $x = 0$, (b) $x = 0.005$, (c) $x = 0.01$ and (d) $x = 0.02$, measured at RT.

Moreover, four mechanisms were proposed to understand the conduction mechanism/carrier transport phenomena in perovskite oxides: (i) ohmic conduction, (ii) space-charge-limited conduction (SCLC), (iii) bulk-controlled Poole–Frenkel emission, and (iv) interface–controlled Schottky emission [60]. Among them, the SCLC mechanism perfectly fitted with observed data and is analyzed using the $(J \propto E^n)$ Eq. 4.22 [56,57]. Figure 4.29(b) shows the linear fitting of $\ln(J)$ versus $\ln(E)$ of the BNT-KNNG ceramics. The slope of all the samples is found to be between 1.16 to 1.56 (>1) indicating the space charge limited conduction mechanism, which corresponds to discrete trap carriers. Thus, the trap carriers assisted discrete conduction mechanism might be one of the leading factors in controlling the conduction process in BNT-KNNG ceramics. These results suggest that the addition of KNNG cations (Gd^{+3}/Nb^{+5}) at A/B-sites can redistribute the oxygen vacancies and defects that are trapped across grains and grain boundaries. Reduction in the leakage current and improvement in electrical properties are attributed to the incorporation of KNNG at A/B-site in the BNT system.

4.5. Conclusions

BNKT and BNT-KNNG ceramics were prepared by the solid-state reaction method. The crystal structure, microstructure, Raman, dielectric, piezoelectric properties, AC-conductivity and leakage current density analysis of BNKT and BNT-KNNG ceramics were systematically investigated. The average grain size was found to decrease with the substitution of both K and KNNG inhibited the grain growth. The structural and microstructural properties were co-related with Raman and electrical properties. All the samples have displayed two phase transitions: (i) rhombohedral to tetragonal transition temperature (T_d) and (ii) tetragonal to cubic transition (T_C). The T_d and T_C values shifted towards lower temperatures with the addition of K and KNNG compositions. The frequency dispersion with a diffuse transition in T_d and T_C exhibited relaxor behavior, which is confirmed by the conclusion drawn from modified Curie Weiss and Vogel-Fulcher laws. Temperature dependence of resistivity analysis provides the evidence of the variable range hopping mechanism between charge carriers of BNKT and BNT-KNNG systems. The average distance between the two successive hops, associated with hopping energy decreased and density of states near the Fermi level increased with x in both the systems. The leakage current density effectively reduced with the substitution of K and KNNG in the BNT system and improved the dielectric and piezoelectric properties. The leakage current conduction mechanism of both compositions followed space charge limited conduction which is related to deep acceptor traps. A composition of BNKT with $x = 0.2$ has shown high dielectric constant ($\epsilon' = 1273$) and low loss tangent ($\tan\delta = 0.047 @ 1 \text{ kHz}$) as compared to other samples in the respective system as well as BNT-KNNG system. The improved piezoelectric properties; electromechanical coupling factors (k_{33} , k_{31} , $k_t \sim 48\%$ and $k_p = 53\%$), and piezoelectric constants ($d_{33} = 108 \text{ pC/N}$ and $g_{33} = 1.14 \times 10^{-2} \text{ Vm/N}$) are

observed for BNT-KNNG with $x = 0.01$ sample than BNKT, which is a potential candidate for high power electromechanical applications.

4.6. References

- [1] Y. Huan, X. Wang, J. Fang, and L. Li, *J. Eur. Ceram. Soc.* **34**, 1445 (2014).
- [2] J. Wu, D. Xiao, and J. Zhu, *Chem. Rev.* **115**, 2559 (2015).
- [3] Y. Hiruma, R. Aoyagi, H. Nagata, and T. Takenaka, *Japanese J. Appl. Physics, Part 1 Regul. Pap. Short Notes Rev. Pap.* **44**, 5040 (2005).
- [4] G. A. Smolenskii, V. A. Isupov, A. I. Agranovskaya, and N. N. Krainik, *Fiz. Tverd. Tela Sanktpeterbg.* **2**, 2982 (1960).
- [5] C. S. Tu, I. G. Siny, and V. H. Schmidt, *Phys. Rev. B* **49**, 11550 (1994).
- [6] Y. Hiruma, H. Nagata, and T. Takenaka, *J. Appl. Phys.* **104**, 124106 (2008).
- [7] B. Wylie-Van Eerd, D. Damjanovic, N. Klein, N. Setter, and J. Trodahl, *Phys. Rev. B - Condens. Matter Mater. Phys.* **82**, 104112 (2010).
- [8] T. Kainz, M. Naderer, D. Schütz, O. Fruhwirth, F. A. Mautner, and K. Reichmann, *J. Eur. Ceram. Soc.* **34**, 3685 (2014).
- [9] A. B. Kounga, S.-T. Zhang, W. Jo, T. Granzow, and J. Rödel, *Appl. Phys. Lett.* **92**, 222902 (2008).
- [10] C.-C. Wu and C.-F. Yang, *CrystEngComm* **15**, 9097 (2013).
- [11] Y. Hiruma, Y. Imai, Y. Watanabe, H. Nagata, and T. Takenaka, *Appl. Phys. Lett.* **92**, 262904 (2008).
- [12] A. Sasaki, T. Chiba, Y. Mamiya, and E. Otsuki, *Jpn. J. Appl. Phys.* **38**, 5564 (1999).
- [13] H. Nagata, M. Yoshida, Y. Makiuchi, and T. Takenaka, *Jpn. J. Appl. Phys.* **42**, 7401

- (2003).
- [14] H. Yan, D. Xiao, P. Yu, J. Zhu, D. Lin, and G. Li, *Mater. Des.* **26**, 474 (2005).
- [15] P. Y. Chen, C. C. Chou, T. Y. Tseng, and H. Chen, *Jpn. J. Appl. Phys.* **49**, 0615061 (2010).
- [16] N. D. Quan, V. N. Hung, N. Van Quyet, H. V. Chung, and D. D. Dung, *AIP Adv.* **4**, 17122 (2014).
- [17] A. M. Balakt, C. P. Shaw, and Q. Zhang, *J. Alloys Compd.* **709**, 82 (2017).
- [18] V. Chauhan, S. K. Ghosh, A. Hussain, and S. K. Rout, *J. Alloys Compd.* **674**, 413 (2016).
- [19] F. Han, J. Deng, X. Liu, T. Yan, S. Ren, X. Ma, S. Liu, B. Peng, and L. Liu, *Ceram. Int.* **43**, 5564 (2017).
- [20] J. Yin, X. Lv, and J. Wu, *Ceram. Int.* **43**, 13541 (2017).
- [21] A. Hussain, C. W. Ahn, J. S. Lee, A. Ullah, and I. W. Kim, *Sensors Actuators, A Phys.* **158**, 84 (2010).
- [22] P. Mahesh, S. Thota, and D. Pamu, *IEEE Trans. Dielectr. Electr. Insul.* **22**, 3668 (2015).
- [23] M. Peddigari and P. Dobbidi, *AIP Adv.* **5**, 107129 (2015).
- [24] S. Zhang, R. Xia, L. Lebrun, D. Anderson, and T. R. Shrout, *Mater. Lett.* **59**, 3471 (2005).
- [25] A. Moosavi, M. A. Bahrevar, A. R. Aghaei, P. Ramos, M. Algueró, and H. Amorín, *J. Phys. D. Appl. Phys.* **47**, 55304 (2014).
- [26] K. Yoshii, Y. Hiruma, H. Nagata, and T. Takenaka, *Jpn. J. Appl. Phys.* **45**, 4493

- (2006).
- [27] Y.-R. Zhang, J.-F. Li, B.-P. Zhang, and C.-E. Peng, *J. Appl. Phys.* **103**, 74109 (2008).
- [28] L. Liu, H. Fan, S. Ke, and X. Chen, *J. Alloys Compd.* **458**, 504 (2008).
- [29] J. Kreiselt, A. M. Glazer, G. Jones, P. A. Thomas, L. Abello, and G. Lucazeau, *J. Phys. Condens. Matter* **12**, 3267 (2000).
- [30] M. K. Niranjana, T. Karthik, S. Asthana, J. Pan, and U. V. Waghmare, *J. Appl. Phys.* **113**, 194106 (2013).
- [31] D. Rout, K.-S. Moon, S.-J. L. Kang, and I. W. Kim, *J. Appl. Phys.* **108**, 84102 (2010).
- [32] J. Kreisel, A. M. Glazer, P. Bouvier, and G. Lucazeau, *Phys. Rev. B* **63**, 174106 (2001).
- [33] V. Pal, O. P. Thakur, and R. K. Dwivedi, *J. Phys. D: Appl. Phys.* **48**, 55301 (2015).
- [34] K. Kakimoto, K. Akao, Y. Guo, and H. Ohsato, *Jpn. J. Appl. Phys.* **44**, 7064 (2005).
- [35] D. Lin, K. W. Kwok, and H. L. W. Chan, *J. Phys. D: Appl. Phys.* **40**, 6778 (2007).
- [36] Y.-R. Zhang, J.-F. Li, and B.-P. Zhang, *J. Am. Ceram. Soc.* **91**, 2716 (2008).
- [37] P. Fu, Z. Xu, R. Chu, W. Li, Q. Xie, Y. Zhang, and Q. Chen, *J. Alloys Compd.* **508**, 546 (2010).
- [38] V. Pal, R. K. Dwivedi, and O. P. Thakur, *Mater. Res. Bull.* **51**, 189 (2014).
- [39] Z. Yang, Y. Hou, B. Liu, and L. Wei, *Ceram. Int.* **35**, 1423 (2009).
- [40] E.-M. Anton, W. Jo, D. Damjanovic, and J. Rödel, *J. Appl. Phys.* **110**, 94108 (2011).
- [41] X. Chou, J. Zhai, H. Jiang, and X. Yao, *J. Appl. Phys.* **102**, 84106 (2007).

- [42] and Z.-G. Y. A. A. Bokov, *J. Mater. Res.* **41**, 31 (2006).
- [43] V. Bobnar, J. Holc, M. Hrovat, and M. Kosec, *J. Appl. Phys.* **101**, 74103 (2007).
- [44] N. K. Karan, R. S. Katiyar, T. Maiti, R. Guo, and A. S. Bhalla, *J. Raman Spectrosc.* **40**, 370 (2009).
- [45] S. Saed and J. P. Mercurio, *J. Eur. Ceram. Soc.* **21**, 1333 (2001).
- [46] L. E. Cross, *Ferroelectrics* **151**, 305 (1994).
- [47] K. Uchino and S. Nomura, *Ferroelectrics* **44**, 55 (1982).
- [48] R. Pirc and R. Blinc, *Phys. Rev. B* **76**, 20101 (2007).
- [49] Y. Zhuang, S. O. Ural, A. Rajapurkar, S. Tuncdemir, A. Amin, and K. Uchino, *Jpn. J. Appl. Phys.* **48**, 41401 (2009).
- [50] K. Kumar and B. Kumar, *Ceram. Int.* **38**, 1157 (2012).
- [51] R. M. Hill, *Phys. Status Solidi* **34**, 601 (1976).
- [52] J. J. Hauser, *Phys. Rev. B* **9**, 2623 (1974).
- [53] H. Han, C. Davis, and J. C. Nino, *J. Phys. Chem. C* **118**, 9137 (2014).
- [54] I. Rawal and A. Kaur, *J. Appl. Phys.* **115**, 43717 (2014).
- [55] T. Takenaka and H. Nagata, *J. Eur. Ceram. Soc.* **25**, 2693 (2005).
- [56] H. Borkar, V. Rao, M. Tomar, V. Gupta, J. F. Scott, and A. Kumar, *RSC Adv.* **7**, 12842 (2017).
- [57] B. Nagaraj, S. Aggarwal, T. K. Song, T. Sawhney, and R. Ramesh, *Phys. Rev. B* **59**, 16022 (1999).
- [58] V. Pal, R. K. Dwivedi, and O. P. Thakur, *Curr. Appl. Phys.* **14**, 99 (2014).
- [59] U. Holzwarth and N. Gibson, *Nat. Nanotechnol.* **6**, 534 (2011).

- [60] F. T. L. Muniz, M. A. R. Miranda, C. dos Santos, and J. M. Sasaki, *Acta Crystallogr. Sect. A* **72**, 385 (2016).
- [61] K. Ramam and M. Lopez, *J. Phys. D. Appl. Phys.* **39**, 4466 (2006).
- [62] M. Matsubara, K. Kikuta, and S. Hirano, *J. Appl. Phys.* **97**, 114105 (2005).
- [63] R. Wang, D. Wang, Y. Zhang, and X. Zheng, *Sensors Actuators, B Chem.* **190**, 305 (2014).
- [64] X. Zhou, C. Jiang, H. Luo, C. Chen, K. Zhou, and D. Zhang, *Ceram. Int.* **42**, 18631 (2016).
- [65] V. V Shvartsman and D. C. Lupascu, *J. Am. Ceram. Soc.* **95**, 1 (2012).
- [66] B. Hu, M. Zhu, J. Guo, Y. Wang, M. Zheng, and Y. Hou, *J. Am. Ceram. Soc.* **99**, 1637 (2016).
- [67] R. Jing, X. Chen, H. Lian, X. Qiao, X. Shao, and J. Zhou, *J. Eur. Ceram. Soc.* **38**, 3111 (2018).
- [68] S. Ke, P. Lin, H. Fan, H. Huang, and X. Zeng, *J. Appl. Phys.* **114**, 104106 (2013).
- [69] S. Pattipaka, A. R. James, and P. Dobbidi, *J. Electron. Mater.* **47**, 3876 (2018).
- [70] K. Kumar and B. Kumar, *Ceram. Int.* **38**, 1157 (2012).

Nonlinear Optical and Microwave Dielectric Studies of BNT and BNT-KNNG Thin Films

5.1 Introduction

BNT ferroelectric ceramics have been explored more in the bulk form due to its excellent ferroelectric and piezoelectric properties that can lead to the fabrication of thin-film devices for energy storage, sensor, actuator and nonlinear optical applications [1,2]. However, to deposit a single phase of BNT, maintain its stoichiometry and better crystallinity in the thin film is a challenging task due to the volatile nature of the elements in the present composition. The volatilization of Bi and Na is leading to the formation of secondary phases, oxygen deficiencies, and higher leakage currents resulting in poor dielectric, ferroelectric and piezoelectric properties. To the best of the author's knowledge, there are very few reports available on BNT thin films. Therefore, the processing deposition parameters are critical, especially in thin films, to optimize its single-phase, stoichiometry, and better crystallinity. In this chapter, our aim is to deposit BNT thin films by using pulsed laser deposition (PLD) technique, which provides necessary freedom to play with many parameters such as oxygen partial pressure, substrate temperature, energy fluence, etc. to obtain the phase, stoichiometry and crystallinity of complex oxide thin films [3,4]. Therefore, the underlying benefits of PLD motivated us to deposit a single phase of BNT thin films with an excess of Bi and Na with 5 mol %.

In order to improve the dielectric, ferroelectric and piezoelectric properties and overcome such drawbacks of BNT thin films, the BNT-BT, BNT-ST, BNT-BKT, and BNT-

BKT-BT composite thin films were investigated [5–8]. Recently, an attempt has been made to prepare $1-x$ $[\text{Bi}_{0.5}\text{Na}_{0.5}\text{TiO}_3] - x$ $[\text{K}_{0.5}\text{Na}_{0.5}\text{NbO}_3 + 1 \text{ wt. } \% \text{ Gd}_2\text{O}_3]$ (where $x = 0 - 0.02$) composite ceramics due to their superior dielectric and piezoelectric properties which lead to the development of thin-film devices for the above-mentioned applications [9]. The composition ($x = 0.01$) with the best dielectric and piezoelectric properties have been chosen for the deposition of thin films. Microwave dielectric and nonlinear optical properties of films have been widely reported for microwave communication, radiofrequency and photonic devices due to their fast response, lower operation voltage, better compatibility, and larger nonlinearity. Till date, $\text{Pb}_{0.92}\text{La}_{0.08}(\text{Zr}_{0.65}\text{Ti}_{0.35})\text{O}_3$, Rh and Fe doped BaTiO_3 , SrTiO_3 , $\text{Bi}_{1.95}\text{La}_{1.05}\text{TiNbO}_9$, $\text{Bi}_{3.75}\text{Nd}_{0.25}\text{Ti}_3\text{O}_{12}$, $(\text{Na}_{1-x}\text{K}_x)_{0.5}\text{Bi}_{0.5}\text{TiO}_3$ and BNT-BKT thin films were explored for the above applications [10–17]. Nevertheless, there are limited studies available involving microwave dielectric and nonlinear optical properties of BNT based thin films. Therefore, the present chapter provides the influence of O_2 partial pressure on microwave dielectric and nonlinear optical properties of BNT and BNT-KNNG thin films systematically and is divided into two parts: (i) BNT thin films and (ii) BNT-KNNG composite thin films.

5.2 Deposition of thin films

Pure $\text{Bi}_{0.5}\text{Na}_{0.5}\text{TiO}_3$ (BNT) and $1-x$ $[\text{Bi}_{0.5}\text{Na}_{0.5}\text{TiO}_3] - x$ $[\text{K}_{0.5}\text{Na}_{0.5}\text{NbO}_3 + 1 \text{ wt. } \% \text{ Gd}_2\text{O}_3]$ (where $x = 0.01$) targets were made by a conventional solid-state reaction method. The chemical equations of these samples were presented in 2.1.2 and 4.2 sections and page#111 and 40–41, respectively. The high purity powders of Bi_2O_3 , Gd_2O_3 (Alfa-Aesar, USA, 99.999%), Na_2CO_3 , TiO_2 , K_2CO_3 and Nb_2O_5 (Sigma-Aldrich, USA, 99.99%) were weighed according to stoichiometry. 5 mol % excess Bi, Na, and K were added to the BNT-KNNG powder to compensate for the loss of Bi, Na, and K during high-temperature sintering and deposition process. These powders were mixed with ZrO_2 balls in the zirconia vessel by using the planetary ball mill (Pulverisette 6, Fritsch GmbH, Germany) for 5h. Further, the mixed

powder of BNT/KNNG was calcined at 800/750 °C for 3h/5h. The calcined powders were re-milled to reduce the particle size and to enhance the density of the target. Further, polyvinyl alcohol was added to them and pressed into BNT and BNT-KNNG targets using KBr Press (M-20, Technosearch Instruments, India) in the form of a circular disc having 20mm diameter and 4 mm thickness. These were sintered at 1100/1050 °C for 3h/5h. The deposition of BNT and BNT-KNNG thin films were carried out on Pt(111)/Ti/SiO₂/Si and quartz substrates by PLD for electrical and optical studies, respectively. The films were deposited by using a KrF excimer laser of 248 nm wavelength, 5 Hz pulse repetition rate and 225 mJ of pulse energy. The optimized PLD parameters such as the target to substrate distance of 4 cm, a substrate temperature of 700 °C and laser fluence of ~2J/cm² were maintained during the deposition process. Further, the films were deposited under various oxygen partial pressures from 0.1 Pa to 50 Pa. For extracting the electrical properties, Al is deposited on the surface of the films (Ag/BNT and BNT-KNNG/Pt(111)/Ti/SiO₂/Si) as electrodes using thermal evaporator (Lab Coater Auto 500, Hind High Vacuum, India).

5.3 Results and discussions of BNT thin films

Figure 5.1 (a - d) illustrates the Rietveld refined X-ray diffraction (XRD) patterns of BNT thin films deposited on a quartz substrate at various oxygen (O₂) pressures from 1 Pa to 50 Pa. The Rietveld refinement of the XRD spectra has been carried to confirm the presence of phases, peak profiles, and fitting quality by considering Pseudo-Voigt function using Full-proof software. From Rietveld refinement of XRD spectra, the films deposited at lower (1 Pa) and higher oxygen pressure (50 Pa) exhibited BNT phase along with the secondary phase of Bi₄Ti₃O₁₂ (BIT1), and Bi₂Ti₂O₇ (BIT2) which belong to rhombohedral, orthorhombic and cubic crystal symmetry with R3c, Aba2 and $Fd\bar{3}m$, respectively. With an increase in the O₂ pressure, the secondary phase of BIT1 and BIT2 was suppressed, whereas a single phase of

BNT observed for the film grown at 10 Pa. The single phase of BNT (R3c space group) film structure is generated by VESTA software using crystallographic information file (CIF) from Rietveld refinement XRD analysis, which is shown in the inset of Figure 5.1(c). The calculated phase fraction and their lattice parameters are listed in Table 5. 1. The phase fraction of rhombohedral symmetry is found to be increased from 37.2 % to 100 %, whereas the secondary phases BIT1 and BIT2 are diminished with an increase in oxygen partial pressure from 1 Pa to 10 Pa. The oxygen vacancies and interstitials oxygen ions can create charge fluctuations, which are leading to the variation of Bi, Na, and Ti to maintain BNT stoichiometry. Consequently, the secondary phases (BIT1 and BIT2) have appeared in BNT thin films deposited at lower and higher oxygen pressure other than 10 Pa are shown in Figure 5.1. Zhao et al. [18] also observed similar defects like oxygen vacancies and interstitials oxygen ions in BaTiO₃ thin films deposited at lower oxygen partial pressure. The estimated lattice volume and phase fraction of BNT films were found to be increased with a rise in the oxygen pressure as shown in Figure 5.1 (e). The oxygen vacancies can influence the nearest-neighbor distance by decreasing the Coulomb attraction force between anion and cations. As a result, an increase in the lattice parameter and volume of the film [19,20].

Debye-Scherrer's relation [21] is used to estimate the average crystallite size of thin films deposited at various pressures by using Eq. 3.23 and is shown in Figure 5.1(e). The estimated average crystallite size is in the range of 17 – 25 nm. The film deposited at lower oxygen pressure for 1 Pa having a smaller crystalline size of 17 nm, which is increased to 25 nm with a rise in oxygen pressure for the film deposited at 50 Pa. In the present study, the oxygen partial pressure plays an important role to stabilize the phase and improvement in the crystallinity of the deposited films. The oxygen pressure could change the dynamics of the plasma, which leads to a decrease in the mean free path of the molecules and atoms. The nucleation and particle sizes are smaller at lower oxygen pressure, which would enhance with

an increase in oxygen pressure. The oxygen vacancies in the film also decrease with O₂ pressure. As a result,

Table 5. 1: Lattice constants, lattice volume, and phase fraction of BNT thin films deposited at various oxygen pressures.

O ₂ Pressure (Pa)	Lattice parameters (Å)			V(Å ³)	Phase fraction (%)
	Rhombohedral (R3c)	Orthorhombic (Aba2)	Cubic (Fd $\bar{3}m$)		
1	a=b=5.47	a=5.53	a=b=c=10.27	V _R =349.89	R = 37.2
	c= 13.45	b=32.90	$\alpha=\beta=\gamma=90^\circ$	V _O =968.48	O=62.3
	$\alpha=\beta=90^\circ$ $\gamma=120^\circ$	c= 5.31 $\alpha=\beta=\gamma=90^\circ$		V _C =1085.19	C=0.5
5	a=b=5.50	a=5.46			
	c= 13.50	b=32.92	----	V _R =354.16	R = 48.7
	$\alpha=\beta=90^\circ$ $\gamma=120^\circ$	c= 5.31 $\alpha=\beta=\gamma=90^\circ$		V _O =957.47	O=51.3
10	a=b=5.21				
	c= 13.57	----	----	V _R =358.32	R = 100
	$\alpha=\beta=90^\circ$ $\gamma=120^\circ$				
50	a=b=5.49	a=5.33	a=b=c=10.26	V _R =353.40	R = 18.4
	c= 13.53	b=32.11	$\alpha=\beta=\gamma=90^\circ$	V _O =956.86	O=34.8
	$\alpha=\beta=90^\circ$ $\gamma=120^\circ$	c= 5.42 $\alpha=\beta=\gamma=90^\circ$		V _C =1081.74	C=46.8

the increase in collision rate leads to coalescence of formed clusters with bigger size indicating the significant improvement in the crystallinity in the films [22].

The surface morphology of BNT thin films was investigated by AFM to study the surface microstructure, scaling behavior, and growth dynamics of the films. The AFM 3D, 2D images, and their height profiles of BNT thin films deposited on quartz substrate at various

oxygen partial pressures from 1 Pa to 50 Pa over a scan area of $5\mu\text{m} \times 5\mu\text{m}$ are shown in Figure 5.2. The AFM images are indicating the homogenous distribution of grains within the film

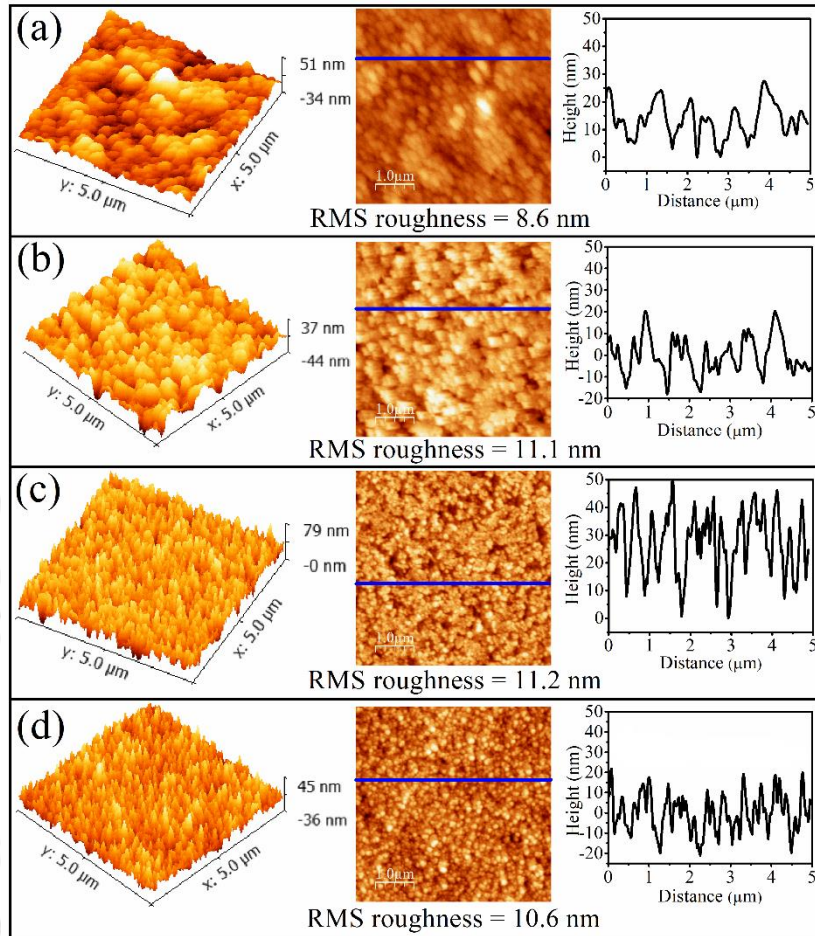


Figure 5.2: AFM 3D (left side) and 2D (centre) images of BNT films for (a) 1 Pa (b) 5 Pa, (c) 10 Pa and (d) 50 Pa. Height profile of each image is shown at the right side of the respective images.

surface. The root-means-square (RMS) surface roughness of the deposited films is in the range of 8.6 – 11.2 nm estimated by WSxM 5.0 software. At lower pressure (1 Pa), the RMS roughness is lower of 8.6 nm and is increased to 11.2 nm for the film deposited at 10 Pa. Further, it is slightly decreased to 10.6 nm for a film deposited at 50 Pa. The obtained RMS roughness of deposited films is in line with crystallite sizes. In order to understand the dynamic scaling behavior and growth mechanism of films, the scaling parameters; α_{loc} , ω and ξ are

calculated from AFM images using height–height correlation function (HHCF), $H(r, t)$. It is a statistical average of the mean square of height difference between pair points (x, y) and (x', y') , separated by a distance r is given by the following equation [23,24].

$$H(r, t) = \langle |h(r + r', t) - h(r', t)|^2 \rangle \quad (5.1)$$

where, $h(r + r', t)$ and $h(r', t)$ is the heights of a surface at a point (x, y) and (x', y') . The HHCF can be estimated by spatial averaging over one or many regions of a large extent, and it should be much larger than r to avoid edge effects. It can also be defined by the exponential correlation model satisfies the condition for self-affine surface and manifests anisotropic scale invariance by following equation [24].

$$H(r) = 2\omega^2 \left[1 - \exp \left[- \left(\frac{r}{\xi} \right)^{2\alpha} \right] \right] \quad (5.2)$$

The HHCF exhibits two distinct behaviors depends on the relative magnitude of r and lateral correlation length (ξ) as follows:

$$\text{For } r \ll \xi, \quad H(r < \xi) = 2\omega^2 \left(\frac{r}{\xi} \right)^{2\alpha} \quad (5.3)$$

$$\text{For } r \gg \xi, \quad H(r > \xi) = 2\omega^2 \quad (5.4)$$

where, ω is the RMS roughness (interface width), α ($0 \leq \alpha_{loc} \leq 1$) is the local roughness scaling exponent, which represents short-range roughness of a self-affine surface and ξ is the lateral correlation length. The log-log plot of HHCF versus distance r along with fitted curve by Eq. (5.2) of BNT thin films for various oxygen partial pressures from 1 Pa – 50 Pa is shown in Figure 5.3(a). The oscillatory behavior is observed for the film deposited higher pressures for $r \gg \xi$ signifying the formation of the mounded surface [24,25]. The $H(r, t)$ is shifted upward as oxygen pressure (P) increases with growth rate, which indicates the enhancement in RMS roughness. The α_{loc} , ω , ξ parameters are extracted from HHCF for the film deposited at different

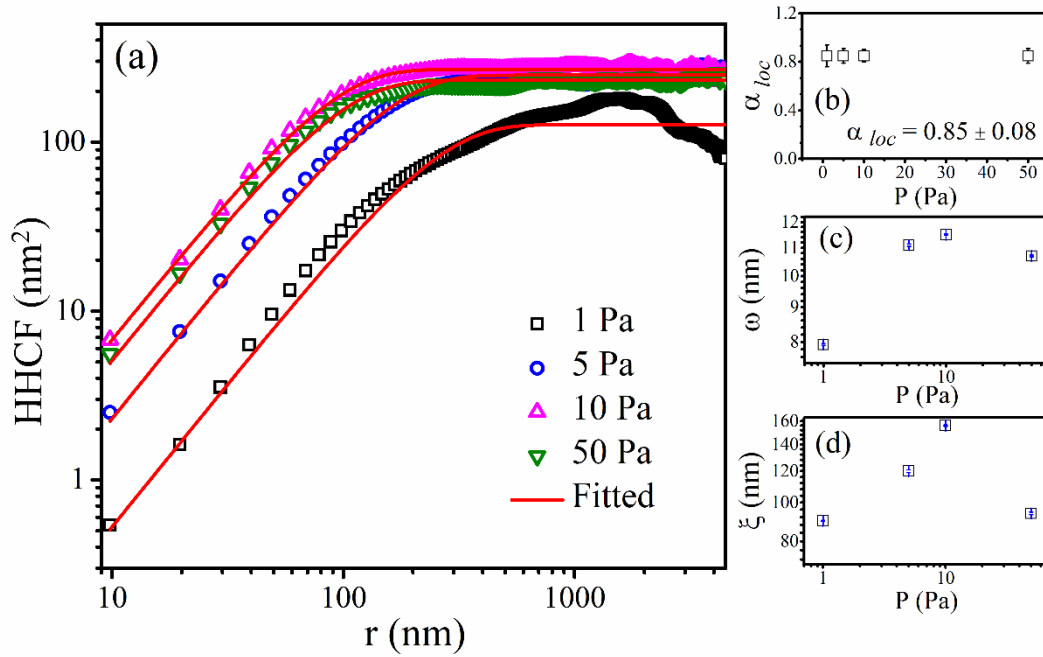


Figure 5.3: (a) log-log plot of HHCF, $H(r)$ as a function of distance r with fitted theoretical curve for BNT thin films at various pressures from 1 – 50 Pa. The plot of (b) roughness exponent α_{loc} , (c) surface roughness ω and (d) correlation length ζ as a function of pressure (P).

pressures to understand the scaling behavior and growth dynamics. The variation of α_{loc} , ω , ζ with P was shown in Figure 5.3(b), (c), and (d). The α_{loc} value of all the deposited films found to be 0.85 ± 0.08 , which is in-between 0 and 1. The smaller and larger value of α_{loc} indicates a more locally rough and locally smooth surface, respectively. The value of ω increases from 7.9 – 11.5 nm for the film grown at various pressure form 1 – 10 Pa confirm that the film is roughening during the growth process and is reduced (10.7 nm) for the film deposited at high pressure (50 Pa). The high ω value because of the various non-local effects such as shadowing, high stickiness of substrate, bulk diffusion of incoming particles. The ζ value is increased from 90 to 156 nm with the rise in O_2 pressure from 1 – 10 Pa and beyond that, it decreases to 94 nm for 50 Pa, which signifies the lateral growth of the islands varies with pressure. It indicates that as the pressure increases, the islands grow in both vertical and lateral, and the total film turn into rough. The lateral growth is due to the improvement in the nucleation of more incoming flux and the enhance in crystallite size with O_2

pressure. The sudden decrease in ζ at higher pressure (50 Pa) might be due to appearance of the secondary phase of BIT1 and BIT2 can be seen from XRD results, where the film growth orientation shifts from (110) to (117). During nucleation and growth stage only vertical growth takes place while with an increase in oxygen pressure (> 10 Pa), the vertical growth of the BIT phase dominates over the lateral growth and the RMS roughness slightly decreases as shown in Figure 5.3(d) [26].

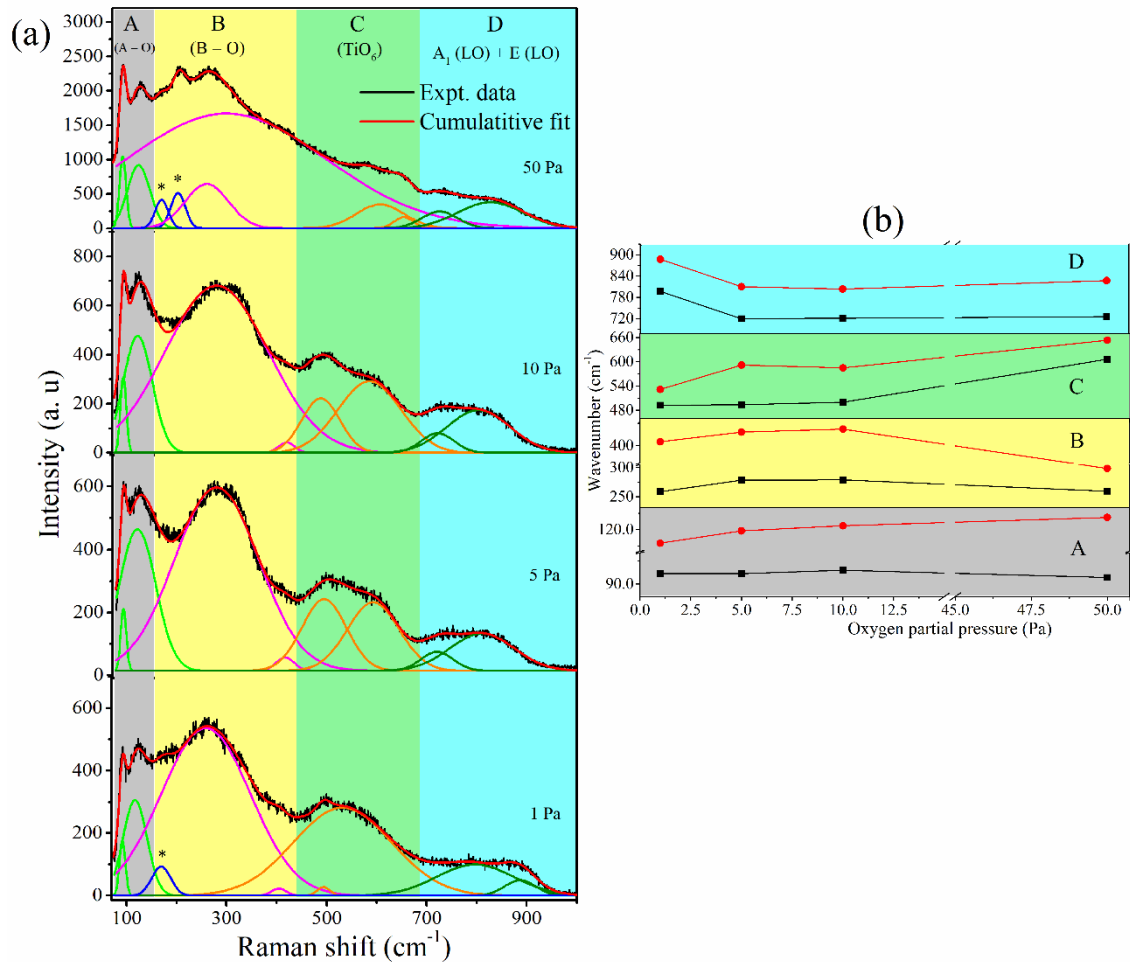


Figure 5.4: (a) Raman spectra and (b) Wavenumber versus oxygen partial pressure of BNT films, deposited at 1 Pa, 5 Pa, 10 Pa and 50 Pa.

Figure 5.4(a) shows the Raman spectra of BNT films deposited on a quartz substrate at different O_2 pressures measured from 50 – 1200 cm^{-1} . In this study, nine Raman modes fitted by considering Gaussian function using OriginPro 8.5 software. BNT has 13 Raman active modes based on group theory: $\Gamma_{\text{Raman}} = 4A_1 + 9E$, where A_1 and E modes are Raman and IR

active [9]. Raman active A_1 (TO_1) modes located at $88.59 - 123.83 \text{ cm}^{-1}$ are associated with the Bi-O and Na-O vibrations. The Raman active E (TO_2) modes located at $159.66 - 409.63 \text{ cm}^{-1}$ are associated with the Ti-O vibrations. The TO_3 modes located at $481.94 - 637.10 \text{ cm}^{-1}$ are associated with TiO_6 octahedral vibrations. The LO_3 modes located at $719.06 - 885.41 \text{ cm}^{-1}$ are corresponding to the overlapping of A_1 (LO) and E (LO) modes. The TO_1 , TO_2 and TO_3 modes are shifted to the higher wavenumber, and the intensity of all the modes increased with an increase in O_2 pressure (in Figure 5.4(b)) from 1 – 10 Pa which indicates the improved degree of crystallinity in the films. In the case of a film deposited at 50 Pa, all modes shifted to lower wavelength, whereas the BNT modes are suppressed due to the appearance of BIT1 and BIT2 phases. However, the Raman spectrum of the film deposited at 10 Pa is similar to that of the BNT target and earlier reports [27,28].

Figure 5.5(a) shows the optical transmittance spectra of BNT thin films deposited on quartz substrates at various O_2 partial pressures in the wavelength range of 200 to 2500 nm. The oscillations in the spectra due to multiple reflections between air to film and film to substrate interfaces. The spectra of all the films found to be 50 to 85 % of transmission in the visible region, which is relatively high transmittance confirming the low surface roughness and better homogeneity of films. A sharp drop in optical transmission at the wavelength of 300 - 400 nm region corresponds to strong absorption, which is the fundamental absorption of the film. It can be seen that the transmittance of deposited films is decreased, where the transmittance spectra shifted to higher wavelength in the absorption region with increasing oxygen pressure. The thickness (d) and refractive index (n_f) of the thin films for different O_2 pressures calculated using Swanepoel's envelope method by following equations [29].

$$n_f = [N + (N^2 - n_s^2)^{0.5}]^{0.5} \quad (5.5)$$

$$N = 2n_s^2 \left(\frac{T_{max} - T_{min}}{T_{max} T_{min}} \right) + \frac{n_s^2 + 1}{2} \quad (5.6)$$

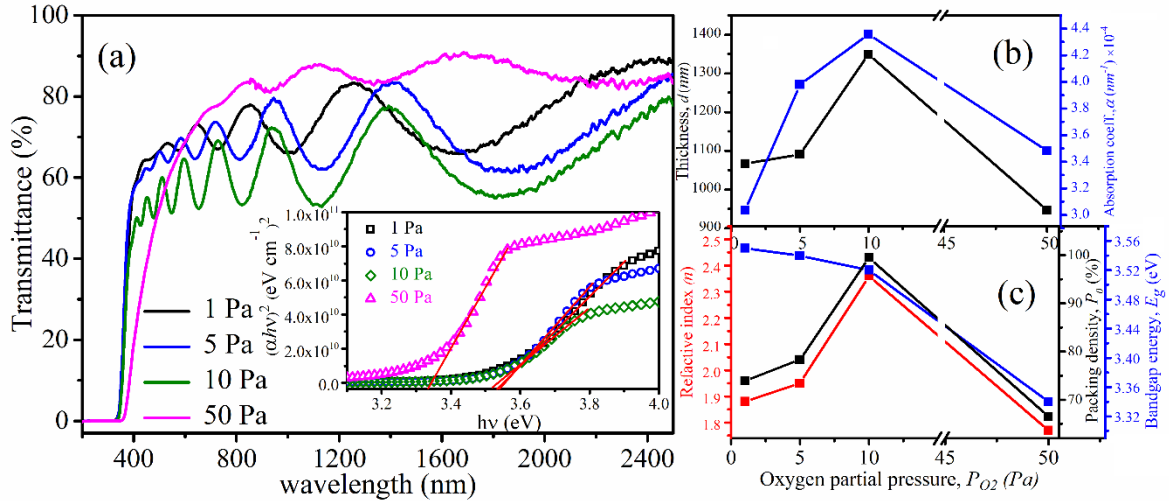


Figure 5.5: (a) Optical transmittance spectra, inset of Figure 5.5(a) optical bandgap energy of BNT films deposited at various pressures. (b) d , α , n , P_0 , and E_g values as a function of oxygen pressure.

$$d = \frac{\lambda_1 \lambda_2}{2(\lambda_1 n_2 - \lambda_2 n_1)} \quad (5.7)$$

where, n_s is the substrate refractive index, T_{max} and T_{min} are transmission maximum and minimum at a certain wavelength (λ), n_1 and n_2 are refractive indices at two adjacent maximum or minimum at λ_1 and λ_2 . The estimated t , n_f , absorption coefficient (α), and the extinction coefficient (k) values are listed in Table 5. 2. The d and n_f values are found to be increased from 1067, 1091, and 1349 nm and 1.83, 1.90, and 2.31 with the rise in the O_2 pressure from 1, 5 and 10 Pa as shown in Figure 5.5(b) and (c). The increase in thickness with oxygen pressure is due to the confinement of plasma, which leads to an increase in the particle flux. Consequently, a higher deposition rate. The thickness of the film deposited at 50 Pa, O_2 pressure is very thick, producing over confinement of the plasma, which limiting the incoming flux impinging on the substrate and hence, the decrease in film thickness [30]. Further, the optical packing density (P_0) of thin films is calculated by the following expression.

$$P_0 = \left(\frac{n_f^2 - 1}{n_f^2 + 2} \right) \left(\frac{n_b^2 + 2}{n_b^2 - 1} \right) \quad (5.8)$$

where, n_b is the refractive index of the bulk BNT (2.32) [31]. The estimated optical packing density lies in the range of 73.94 – 99.52 % and is increased with O₂ pressure. The improvement in crystallinity, optical packing density, decrease in oxygen vacancies and change in the phase (BIT to BNT)) could be the reason for larger n_f and k values at film deposited for 10 Pa.

Table 5. 2: The estimated refractive index (n_f), absorption coefficient (α), and bandgap (E_g) of BNT films.

O ₂ Pressure (Pa)	Film thickness	n_f (at 633nm)	P (%)	α (nm ⁻¹) ($\times 10^{-4}$)	k	E_g (eV)
1	1067 nm	1.83	73.94	3.0346	0.0152	3.55
5	1091 nm	1.90	78.33	3.9791	0.0200	3.54
10	1349 nm	2.31	99.52	4.3581	0.0219	3.52
50	947 nm	1.72	66.50	3.4831	0.0175	3.34

The optical bandgap energy (E_g) of BNT thin films can be calculated using Tauc relation in strong absorption region for direct bandgap by following expression [32].

$$(\alpha h\nu)^2 = A(h\nu - E_g) \quad (5.9)$$

Where, A is a constant, and $h\nu$ is the photon energy. The Tauc plot: $h\nu$ vs. $(\alpha h\nu)^2$ is shown in the inset of Figure 5.5(a). The intersection of the tangent line with the X-axis provides the bandgap of films are listed in Table 5. 2. The E_g values are slightly decreased (Figure 5.5(c)) with the rise in O₂ pressure from 1 to 50Pa due to the improvement in crystallinity and reduction in the oxygen vacancies in the films which turn in narrowing bandgap. The obtained bandgap energy values of BNT thin films are close to the reported values deposited by similar PLD technique [31,33].

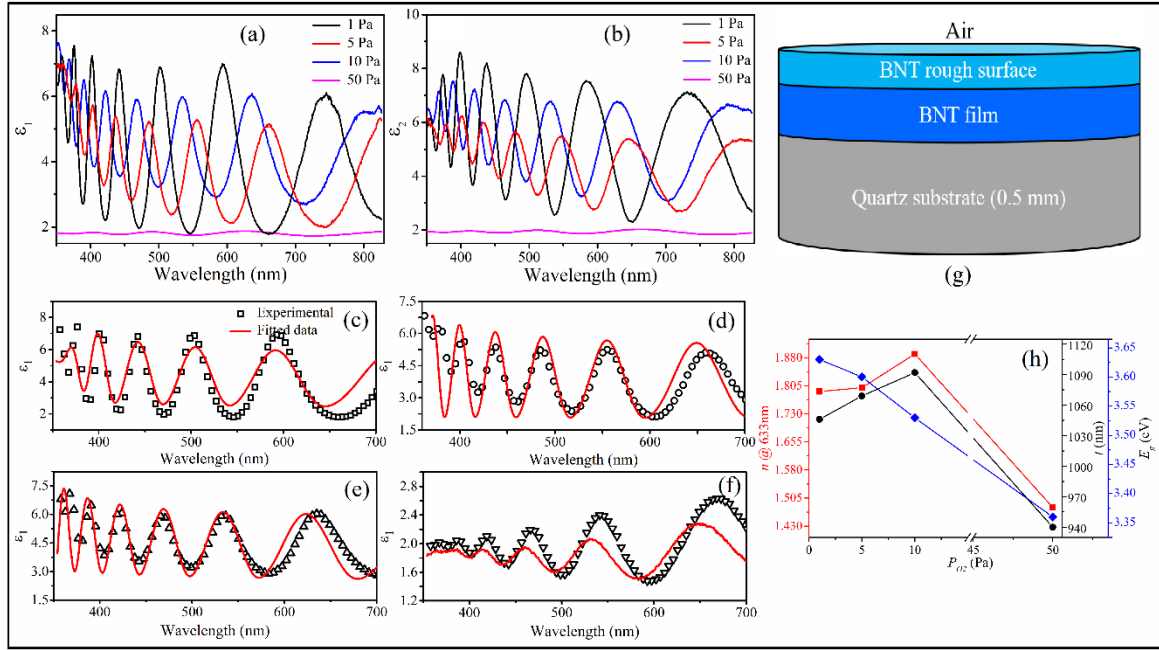


Figure 5.6: (a) and (b) The measured real and imaginary part of the dielectric permittivity of BNT thin films for various pressures. (c - f) The real part of the dielectric function of BNT thin films along with the fitted curve. (g) A schematic diagram of layer structure for SE analysis. (h) n , d and E_g as a function of oxygen pressure.

The spectroscopic ellipsometry (SE) measurements have been performed to investigate the relevance of linear optical properties of BNT thin films in terms of complex dielectric function ($\epsilon^* = \epsilon_1 + i\epsilon_2$) and refractive index ($n^* = n + ik$). The characteristics of SE is related to surface morphology, crystallinity, chemical composition, and conductivity of the films [34]. It is one of the best techniques to estimate the optical properties of thin films by an adequate optical model with more accuracy. The real (ϵ_1) and imaginary (ϵ_2) part of the dielectric function of BNT thin films measured at $\phi = 70^\circ$ in the wavelength range of 300 – 700 nm. Figure 5.6 shows the experimentally measured ϵ_1 and ϵ_2 as a function of wavelength for the film deposited at various oxygen pressures from 1 Pa – 50 Pa. In the current study, the measured ϵ_1 and ϵ_2 of spectra were fitted with the Tauc-Lorentz dispersion model by using Spectroscopy ellipsometry analyzer (SEA) software. Figure 5.6(c-f) shows the ϵ_1 of spectra as

a function of wavelength along with fitted data. It provided the goodness of fit root-mean-square error (RMSE ~ 1) for deposited BNT films on a quartz substrate. In this approach, the ϵ_1 and ϵ_2 of BNT films are performed by assuming four-layers: (i) quartz substrate layer, (ii) BNT film layer, (iii) BNT film Surface roughness layer, and (iv) ambient air and its schematic diagram is shown in Figure 5.6(g). The fitted parameters of BNT films; thickness (d), refractive index (n), and optical bandgap (E_g) as a function of pressures are listed in Figure 5.6(h). The extracted t , n , E_g values are exactly equal to the UV-spectrometer studies derived from Swanepoel's envelope method.

The third-order nonlinear optical properties of the BNT thin films deposited at various pressures are measured using a modified Z-scan technique, which is a sensitive self-focusing technique developed by Sheik-Bahae et al. [35]. A continuous-wave (CW) He: Ne laser beam wavelength of 633 nm is focusing through a film by using a lens of 5 cm focal length. The transmitted light detected by an aperture in the far-field. The transmittance of the far-field aperture is estimated by scanning the film along Z-direction ($\pm Z$), which is called as Z-scan. The effective focal length and incident intensity of the film can be changed by scanning along the beam path. The changes are reflected in the intensity distribution at the aperture in the far-field. The quantity of transmitted energy through aperture depends on film position and sign of nonlinear refractive index [35]. The Z-scan spectra are captured using a charged coupled device camera in the form of a transmitted image. Its data recorded simultaneously from a single scanned image by using Matlab software. The third-order nonlinear optical properties can be measured experimentally by this technique in configurations: (i) open aperture (OA) and (ii) closed aperture (CA). The nonlinear absorption coefficient (β) of BNT films for different oxygen pressures calculated from normalized transmittance ($T(z)$) as a function of film position Z (cm) in OA by the following equation.

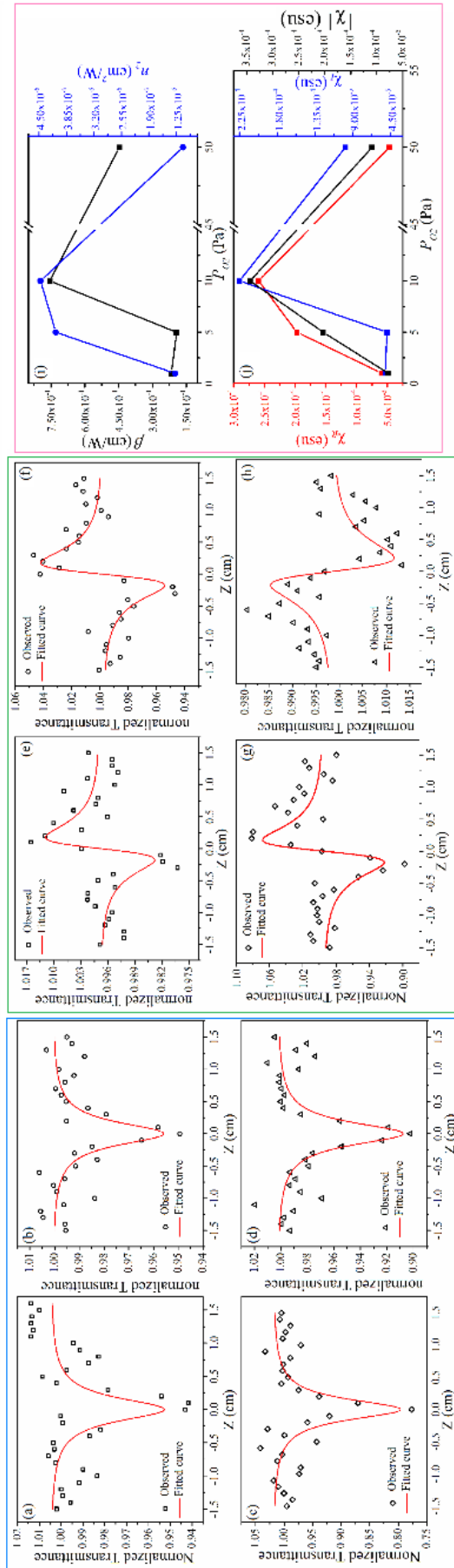


Figure 5.7: (a -d) Open apertures, (e-h) closed apertures normalized transmittance as a function of film position for (a) 1 Pa, (b) 5 Pa, (c) 10 Pa and (d) 50 Pa. (i) and (j) β , n_2 , $\chi_R^{(3)}$, $\chi_I^{(3)}$ and $|\chi^{(3)}|$ values as a function of oxygen partial pressures.

$$T_{open}(z) = 1 - \frac{\beta I_0 T_{eff}}{2^{3/2} [1 + (z/z_0)^2]} \quad (5.10)$$

where, I_0 (7.46 kW/cm²) is intensity of laser beam at focal point ($z = 0$) and $T_{eff} = [1 - \exp(-\alpha t)]/\alpha$ is the effective film thickness, $z_0 = \pi\omega_0^2/\lambda$ is the Rayleigh length of laser beam (2.53 mm) and ω_0 is the beam waist (22.58 μm).

The nonlinear refractive index (n_2) of the films estimated from normalized transmittance ($T(z)$) as a function of film position Z (cm) in CA by using the following equation.

$$T_{closed}(z) = 1 - \frac{4n_2 I_0 T_{eff} (z/z_0) k}{[1 + (z/z_0)^2][9 + (z/z_0)^2]} \quad (5.11)$$

where, k is the magnitude of the wave vector ($k = 2\pi/\lambda$). Figure 5.7 (a) – (d) shows the normalized transmittance of open aperture Z-scan curves of BNT thin films deposited at various O₂ pressures. All the films exhibited transmittance minima at the focal point, indicating the reverse saturation absorption. The increase in temperature due to laser irradiation, which leads to a reduction in the bandgap of the film and therefore enhancing phonon density [36]. It raises the probability of electronic transition rising absorption. As a result, the reverse saturation absorption. Figure 5.7 (e)-(h) represents the normalized transmittance of closed aperture Z-scan curves of the films indicate a pre-focal transmittance minimum followed by a post-focal transmittance maximum, signifying the positive nature of nonlinear refraction caused by self-focusing property in the films. The light is absorbed laser when beam propagates through the film, which gives rise to local heating, generating spatially varying temperature field. The refractive index depends on temperature creating a thermal lens. Thus, the film exhibited self-focusing behavior [37]. The film deposited at higher pressure (50 Pa) with dominant of BIT phase exhibited a negative nature of nonlinear refraction caused by self-defocusing behavior in the films, which can be seen from Figure 5.7(h) [38]. The self-defocusing behavior is due to the local variation of the refractive index with temperature. Since

the film has a negative refractive index, the nature of the film is defocused. It is an important property for the protection of optical sensor application (night vision devices) [39]. The valley to peak separation (Δz_{p-v}) in the closed aperture Z-scan curve estimated to be 3.52 mm which is 1.39 times higher than that of Raleigh length ($z_0 = 2.53$ mm) satisfying the condition of third-order nonlinearity [35]. The real and imaginary parts of third-order nonlinear susceptibilities ($\chi_R^{(3)}$ and $\chi_I^{(3)}$) are estimated by the following expressions [35].

$$\chi_R^{(3)}(esu) = 10^{-4} \frac{\epsilon_0 n_f^2 c^2}{\pi} n_2 (cm^2/W) \quad (5.12)$$

$$\chi_I^{(3)}(esu) = 10^{-2} \frac{\epsilon_0 n_f^2 c^2 \lambda}{4\pi^2} \beta (cm/W) \quad (5.13)$$

where, ϵ_0 is the permittivity of the vacuum, c is the speed of light in vacuum, and λ is the wavelength of the laser. The magnitude of nonlinear susceptibility: $|\chi^{(3)}|$ for all the thin films estimated by the following relation.

$$|\chi^{(3)}| = \sqrt{[(\chi_R^{(3)})^2 + (\chi_I^{(3)})^2]}. \quad (5.14)$$

The calculated n_2 , β , $\chi_R^{(3)}$, $\chi_I^{(3)}$, and $|\chi^{(3)}|$ values are tabulated in Table 5. 3. The n_2 , β , and $|\chi^{(3)}|$ values are found to be increased from $1.283 \times 10^{-6} - 4.464 \times 10^{-6} \text{ cm}^2/\text{W}$, $0.216 - 0.755 \text{ cm/W}$ and $0.926 - 5.198 \text{ esu}$ with increasing oxygen pressure from 1 - 10 Pa, respectively and is shown in Figure 5.7(i) and (j). Higher nonlinearity ($n_2 = 4.464 \times 10^{-6} \text{ cm}^2/\text{W}$), strong nonlinear absorption coefficient ($\beta = 0.755 \text{ cm/W}$) and higher susceptibility ($|\chi^{(3)}| = 5.198 \text{ esu}$) are obtained for the film deposited at 10 Pa. The higher optical packing density in the film is caused by large absorption of laser energy, and thermal agitations of particles lead to the change in the local temperature. Hence, the thermally induced optical nonlinearity [40]. The higher third-order nonlinear optical properties are obtained for the film deposited at 10 Pa pressure with a single phase of BNT is suitable for the in optical photonic devices applications.

Table 5. 3: Nonlinear optical parameters of BNT films deposited under different O₂ pressures.

O ₂ Pressure (Pa)	β (cm/W)	n_2 (cm ² /W) ($\times 10^{-6}$)	χ_R (esu)	χ_I (esu)	$ \chi $ (esu)
1	0.216	1.283	0.010	0.926	0.926
5	0.192	4.104	0.037	0.889	0.890
10	0.755	4.464	0.060	5.197	5.197
50	0.446	1.096	0.008	1.684	1.684

The frequency variation of dielectric constant (ϵ_r) and dielectric loss ($\tan\delta$) of BNT thin films deposited at various O₂ pressures and measured at RT are shown in Figure 5.8(a and b). The ϵ_r values decrease with an increase in frequency due to a decrease in the net polarization in the films, i.e., frequency dispersion behavior. The ϵ_r and $\tan\delta$ values of deposited films are in the range of 295 – 454 and 1.13 – 0.140 @ 1 kHz, respectively. The ϵ_r values of BNT thin films enhanced and $\tan\delta$ values decreased with an increase in O₂ pressure from 1 to 10 Pa as shown in Figure 5.8(c). The film deposited at 10 Pa exhibited the higher ϵ_r (454) and lower $\tan\delta$ (0.140) at 1 kHz. The improvement in the dielectric properties is observed with an increase in the pressure due to reduction in oxygen vacancies, conductivity, improvement in the crystallinity as well as the stabilization of BNT phase. Further, the obtained single-phase BNT thin films deposited at 10 Pa are carried out to study the temperature variation of ϵ_r and $\tan\delta$ at different frequencies from 1 – 100 kHz is shown in Figure 5.8(d). The ϵ_r and $\tan\delta$ values are found to be decreased with an increase in frequency with temperature. It also revealed the two structural phase transitions: (i) ferro to anti-ferro transition, which corresponds to rhombohedral to tetragonal transition, i.e., depolarization transition temperature ($T_d \sim 225$ °C) and (ii) anti-Ferro to para transition corresponds to tetragonal to cubic transition, which is called as Curie transition temperature ($T_C \sim 296$ °C). These results are similar to that of bulk BNT ceramics and are in good agreement with the previous reports [9,41].

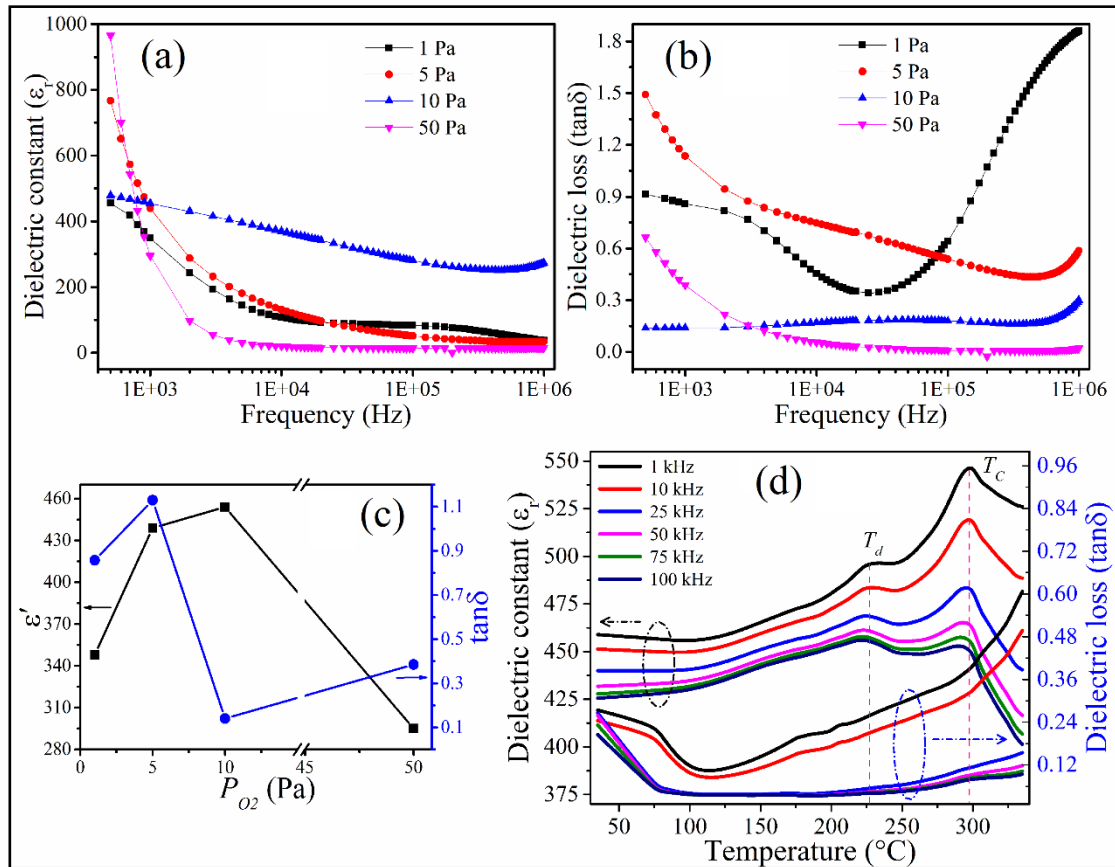


Figure 5.8: (a) and (b) The frequency variation of (a) ϵ_r and (b) $\tan\delta$ of BNT films deposited under various pressures measured at RT. (c) The ϵ_r and $\tan\delta$ values as a function of O_2 pressure. (d) The temperature variation of ϵ_r and $\tan\delta$ of BNT films deposited at 10 Pa pressure measured at different frequencies.

The microwave dielectric properties of BNT thin films deposited on quartz substrates at various oxygen pressures are investigated by the SPDR technique [42]. The SPDR is a familiar, non-destructive, and accurate technique for measuring the microwave dielectric permittivity and loss tangent of thin films at a spot frequency in the microwave region of 5 and 10 GHz. The dielectric resonators use a specific resonant mode with a specific resonant frequency,

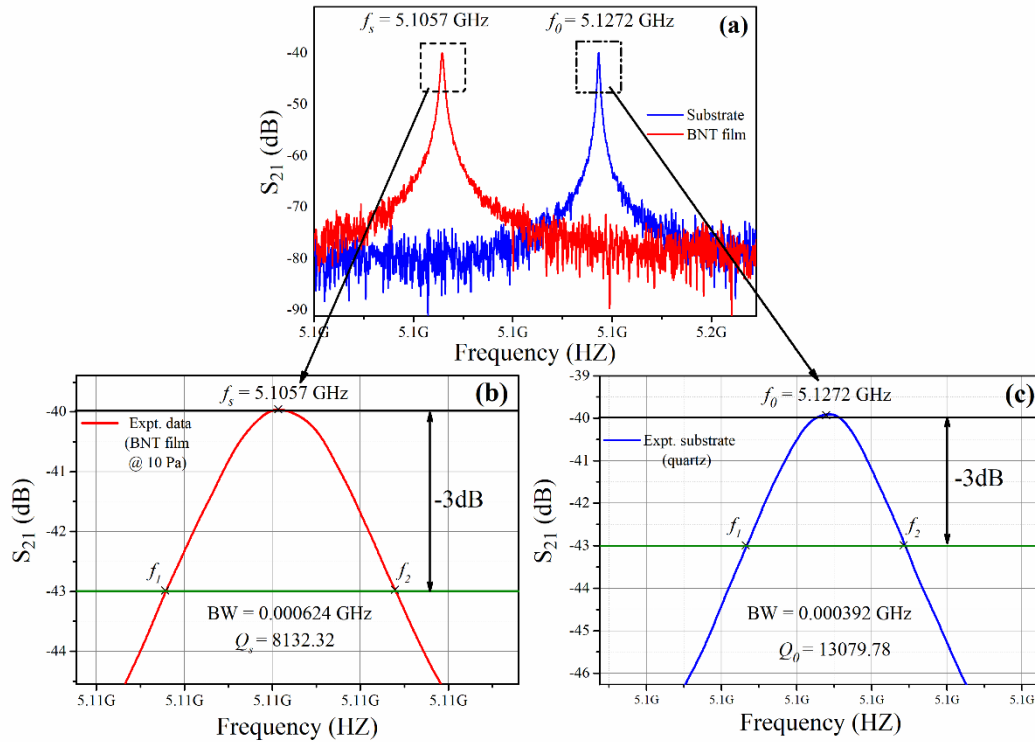


Figure 5.9: (a) Resonance curve of Split Post Dielectric Resonator of nominal frequency 5 GHz with the investigated substrate (quartz) and film (10 Pa). (b) and (c) are the magnified image of Figure 5.9(a) for BNT film and substrate, respectively.

which depends on the SPDR permittivity and its dimensions. The electric field in the SPDR film is parallel to the interface of film. Resonators can operate different modes, and the $TE_{01\delta}$ mode is preferable, which has an azimuthal electric field component. Accordingly, the electric field remains continuous on the test interfaces and is insensitive to the presence of air gaps perpendicular to the z-axis of the fixture [42]. The microwave dielectric permittivity and loss tangent of substrate and film depend on resonant frequency and quality factor. Figure 5.9(a) shows the resonance spectra of the substrate and BNT thin film (10 Pa) measured at 5 GHz. The resonant frequency and quality factor of the empty resonator (f_{01} , Q_{01}) and resonant frequency and quality factor of the substrate (f_0 , Q_0) is measured as shown in Figure 5.9(c). There is a shift in resonant frequency when the thin film placed in SPDR. The shift of resonant frequency and its quality factor (f_s , Q_s) of the film is measured and is shown in Figure 5.9(b).

The resonant frequency, unloaded Q-factor and other parameters are estimated by using the Rayleigh-Ritz method. The real part of dielectric permittivity and loss tangent of deposited films are determined from the measured resonant frequency, quality factor and film thickness by equation 16 and 17.

$$\epsilon_r = 1 + \frac{(f_0 - f_s)}{hf_0 k_s(\epsilon_r, h)} \quad (5.15)$$

$$\tan\delta = \frac{Q^{-1} - Q_{Dr}^{-1} - Q_c^{-1}}{P_{es}} \quad (5.16)$$

where, h is the thickness of the film, f_0 and f_s is the resonance frequency of the substrate (quartz) and film (BNT), K_s is a function of ϵ_r and h . Q is an unloaded quality factor of resonator having the thin film, Q_{Dr} is dielectric losses in the resonator, Q_c is losses of metallic for a resonant cavity having thin film and P_{es} is the electrical energy filling factor of the film [42,43].

Table 5. 4: Microwave dielectric properties of BNT films for various O₂ pressures.

O ₂ Pressure (Pa)	5 GHz		10 GHz	
	ϵ_r	$\tan\delta$	ϵ_r	$\tan\delta$
1	281	0.0028	255	0.0063
5	326	0.0013	258	0.0036
10	336	0.0093	264	0.0154
50	263	0.0083	241	0.0038

The estimated ϵ_r and $\tan\delta$ of deposited thin films at various pressures are displayed in Table 5. 4. The ϵ_r values of BNT thin films gradually improved with the rise in the O₂ pressure from 1 Pa to 10 Pa. It is due to an increase in the optical packing density, crystallinity, refractive index, and stabilization of BNT phase with O₂ partial pressure. It is also observed that the ϵ_r values of BNT thin films decreased with a rise in the frequency from 5 GHz to 10 GHz due to

decrease in polarization and increase in conductivity. The loss tangent of thin films deposited at lower O₂ pressure is slightly higher than higher pressure due to the presence of O₂ deficiencies. Overall, the loss is found to be decreased with rising in O₂ pressure. The improvement in microwave dielectric properties of BNT thin films is obtained due to the minimization of oxygen vacancies. The higher ϵ_r (336 and 264) and low $\tan\delta$ (0.0093 and 0.0015) values are obtained at 5, and 10 GHz frequencies for the film deposited at 10 Pa pressure is promising for the applications of tunable microwave and high-frequency devices.

5.4 Results and discussions of BNT-KNNG thin films

The X-ray diffraction (XRD) patterns of BNT-KNNG composite thin films grown on a Pt(111)/Ti/SiO₂/Si substrate under various oxygen partial pressures from 0.1 Pa to 10 Pa shown in Figure 5.10. The thin films deposited at 0.1 Pa, exhibited a single phase of BNT-KNNG with smaller crystallinity, which corresponds to rhombohedral symmetry with R3c space group (JCPDF of BNT#00-036-0340) [13]. A small fraction of secondary phase of Bi₄Ti₃O₁₂ (BIT) appeared with a rise in the O₂ partial pressure that corresponds to orthorhombic symmetry with Aba2 space group as confirmed from JCPDF data (BIT#35-0795) which can be due to decomposition of BNT-KNNG and/or volatilization of alkaline Na than K in the present composition. In the present films, O₂ vacancies and interstitials of O₂ ions are created at higher pressures because of charge fluctuations that lead to the composition fluctuation of A and B-sites ions in order to maintain stoichiometry. Further, the weight percentage of both the phases have been calculated by using the following expression [44].

$$\text{weight percentage of BNT} = \frac{I_{110}}{I_{171} + I_{110}} \times 100 \quad (5.17)$$

where, the I_{110} and I_{171} are the predominant peak intensities of BNT-KNNG and BIT phases. The estimated wt% of BNT-KNNG composite thin films were found to be 100%, 85.07%, 84.56% and 69.08% for 0.1 Pa, 1 Pa, 5 Pa and 10 Pa pressures respectively. However, it is

seen that the appearance of the secondary phase is minimal and also contributed to enhancing the crystallinity of the films along with the BIT phase.

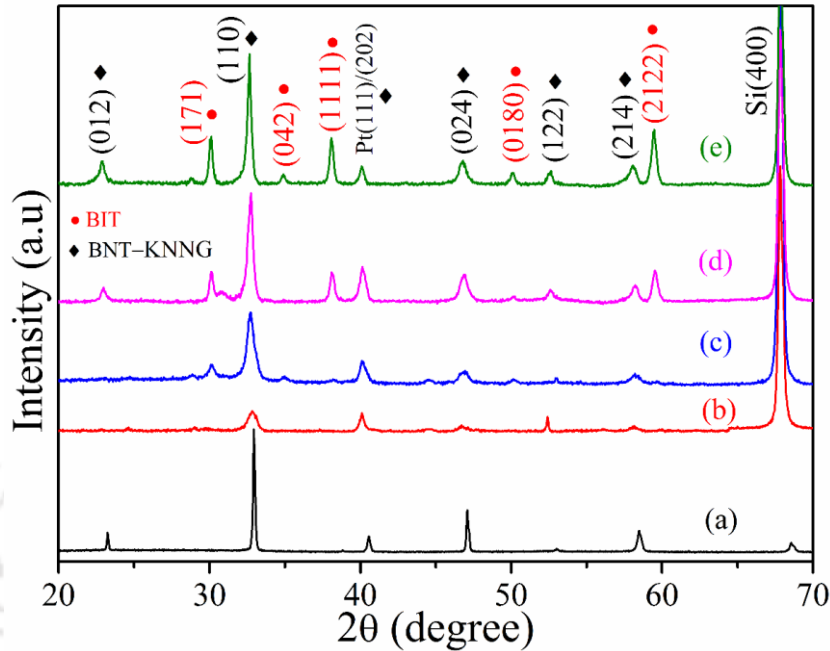


Figure 5.10: XRD pattern of BNT-KNNG thin films for (a) BNT-KNNG target (b) 0.1 Pa, (c) 1 Pa (d) 5 Pa and (e) 10 Pa.

The crystallite size of thin films was calculated by Scherrer's relation (Eq. 3.23) [45]. where, β is the full width at half maximum of diffraction peak (FWHM), θ is Bragg angle, k is shape factor ($k = 0.89$), λ is the wavelength of X-ray ($\text{Cu-K}\alpha = 1.5406 \text{ \AA}$), and D is average crystallite size. The obtained crystallite size is found to be in the range of 11 nm to 26 nm. The film deposited at 0.1 Pa having a smaller crystalline size of 11 nm, is increased with the increase in oxygen pressure and is found to be 26 nm for 10 Pa. A significant improvement in the crystallinity of films also observed with the rise in O_2 pressure, especially the degree of orientation in (110) and (012) direction. In the present study, oxygen partial pressure is an important parameter for the growth of oxide thin films deposited by PLD technique, which can improve the quality of the film. It is well-known that film crystallization is affected by atomic kinetic energy [46]. The oxygen partial pressure mostly governs the atomic kinetic energy

when the rest of the deposition parameters such as substrate temperature, laser energy and etc. are fixed. The atomic kinetic energy in plasma plume can be changed by varying the oxygen partial pressure through the collisions with oxygen atoms. At low oxygen pressure (0.1 Pa), the target ablated species are having a large mean-free-path and directly impinging on to the substrate. The adatoms on the surface have maximum kinetic energy because of weak collisions between atoms in plasma plume and oxygen atoms. The maximum kinetic energy induces the backscattering of adatoms which results in poor crystallization. At relatively high oxygen pressure (10 Pa), the atoms in the plasma plume having smaller mean-free-path and lower kinetic energy. They could gain sufficient energy by scattering oxygen atoms and is prompting the adatoms to reach thermodynamically suitable locations through surface migration. The surface adatoms can migrate quickly to look for the lower energy sites and form the low energy structure, which leads to enhancement of the film crystallinity and quality. Hence, the crystallinity of film is increased with an increase in oxygen pressure. Wang et al. [47] reported that the vanadium oxide thin films deposited at lower oxygen pressure (0.008 Pa) exhibited amorphous and increasing oxygen pressure the film becomes crystallized. Yang et al. [48] observed poor crystallization in $Ta_{0.1}W_{0.9}O_x$ films at low oxygen pressure due to a large number of defects (i.e. oxygen vacancies), which prevent the crystallization of the thin film. A relatively high oxygen pressure causes an enormous reduction in the mean-free-path of target ablated species [49]. Therefore, the oxygen pressure influences crystallization, orientation, nucleation, grain the growth morphology, optical and electrical properties of films. The crystalline quality of film is probably related to the nucleation and growth kinetics of the BNT-KNNG composition.

The surface morphologies obtained from FESEM and AFM analysis of the BNT-KNNG composite films deposited at different O_2 partial pressures are depicted in Figure 5.11. The FESEM images of all the films exhibited dense and uniform microstructures. Furthermore,

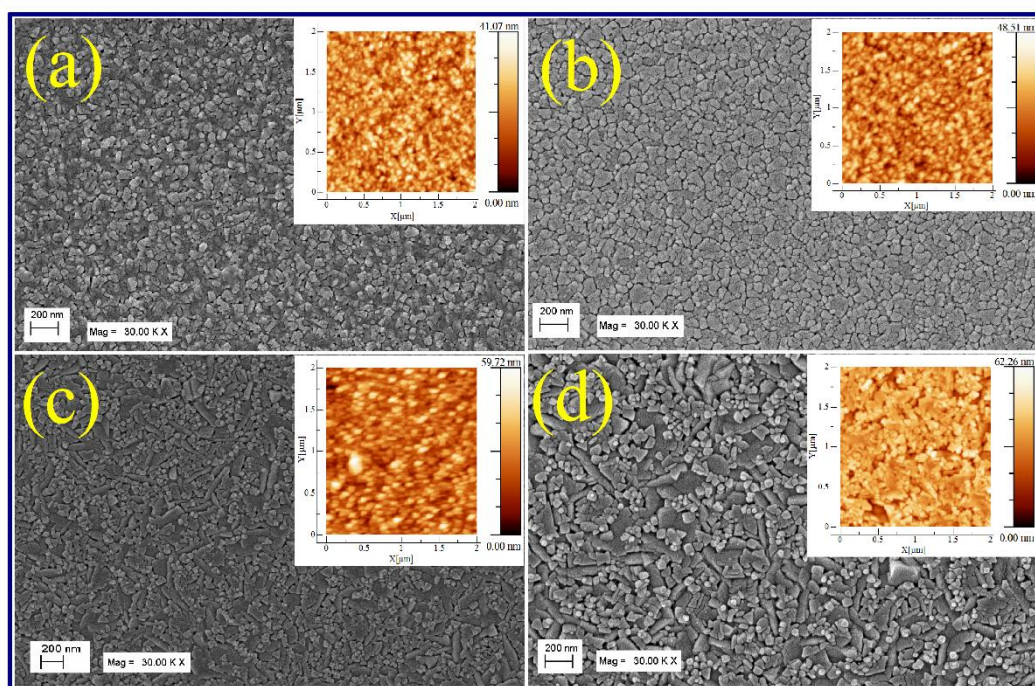


Figure 5.11: FESEM micrographs of BNT-KNNG films for (a) 0.1 Pa, (b) 1 Pa (c) 5 Pa and (d) 10 Pa. Inset AFM images represents the BNT-KNNG films for various pressures.

with an increase in O_2 partial pressure, the average particle sizes of the films were found to be increased. However, the films deposited at 5 Pa and 10 Pa exhibited dual microstructure along with spherical and rectangular particles. It is believed that these rectangular particles correspond to the BIT phase. The variations in the shape and sizes are distributed according to the changes in the rate of deposition, nucleation of the atoms, which are caused by the interaction between oxygen and laser-ablated ions [44]. The average grain sizes were calculated by using image-J software and were found to be 36, 43, 106 and 136 nm for 0.1, 1, 5, and 10 Pa, respectively. It is gradually increased from 36 nm to 136 nm from 0.1 Pa to 10 Pa, which is in line with the obtained crystallite sizes from XRD results. The 10 Pa film, as shown in Figure 5.11(d) exhibited a more uniform microstructure, more compact and have higher grain size as compared to the other films. The increase in grain size and appearance of uniform microstructure could be the reason of favorable conditions for grain growth and nucleation [50].

The AFM image of BNT-KNNG composite thin films grown on Pt(111)/Ti/SiO₂/Si substrate at various oxygen partial pressures over a scan area of 2 μm × 2 μm is shown in the inset of Figure 5.11. The root-mean-square (RMS) of the roughness of deposited films was calculated by WSxM 5.0 software and is found to enhanced from 5.6 – 7.7 nm with O₂ pressure, which is in line with grain size and crystallite sizes. The enhancement of grain growth in the films is attributable to the improvement of crystallization with oxygen pressure. The dense surface morphology with higher roughness and grain size is obtained for the film deposited at 10 Pa.

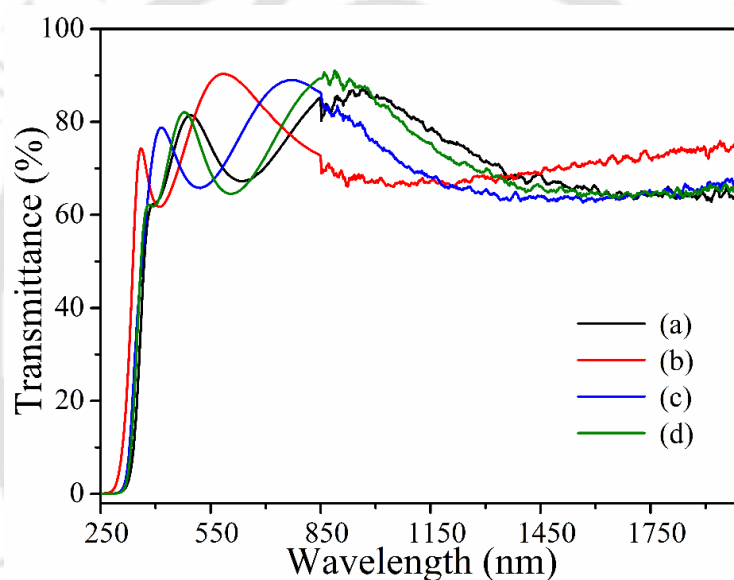


Figure 5.12: Optical transmittance spectra of BNT-KNNG films for (a) 0.1 Pa, (b) 1 Pa (c) 5 Pa and (d) 10 Pa.

The optical transmittance spectra of BNT-KNNG films deposited on quartz substrates at various O₂ partial pressures are displayed in Figure 5.12. These films exhibited high transmission (60 to 90 %) in the visible region and its spectra show interference fringes caused by multi-reflections between air-film and substrate-film interfaces. A sudden decrease in the transmittance to zero in the wavelength range of 334–307 nm is attributed to the fundamental absorption of the films. Every material/film/solvent has a UV-vis absorbance cut-off

wavelength. The cut-off wavelength is the wavelength where the film itself absorbs all of the light (UV or Visible). The film deposited at 1 Pa is having a lower cut-off of wavelength at 307 nm (Figure 5.12(b)) corresponding to higher bandgap energy (4.08 eV) which is related to the amorphous nature of the films deposited at low oxygen pressure. The refractive index (n_f) and thickness (t) of the thin films estimated using Swanepoel's envelope method (Eq. 5.5 – 5.7) [29,51]. The thicknesses of the various films estimated to be in the range of 215 nm to 240 nm. The estimated n_f at a wavelength of 633 nm is found to be in the range of 2.18 – 2.28 for the films deposited at various O₂ partial pressures. The estimated values of the absorption coefficient (α) and the extinction coefficient (k) are shown in Table 5.5. A significant improvement in refractive index and absorption coefficient observed with O₂ partial pressure are due to a decrease in the inter-atomic space, which leads to densification as well as the crystallization of the films and are correlated with the XRD results.

Table 5. 5: The refractive index (n_f), absorption coefficient (α), extinction coefficient (k) and bandgap (E_g) of BNT-KNNG composite thin films deposited at various pressures.

O ₂ Pressure	n_f (at 633nm)	α (nm ⁻¹) ($\times 10^{-4}$)	k	E_g (eV)
0.1 Pa	2.18	4.776	0.0240	3.70
1 Pa	2.24	5.258	0.0264	4.08
5 Pa	2.25	12.01	0.0603	3.80
10 Pa	2.28	18.24	0.0915	3.76

The bandgap energy (E_g) of BNT-KNNG composite thin films estimated using Tauc relation (Eq. 5.9) [32]. The E_g values are estimated by considering direct bandgap ($m= 2$). The intersection of a slope with the horizontal axis ($h\nu$) of Figure 5.13 provides the bandgap energy (E_g) of deposited films, which are shown in Table 5. 5. The optical energy bandgap of the BNT-KNNG thin films is 3.7 eV for the film deposited at low oxygen partial pressure of 0.1 Pa.

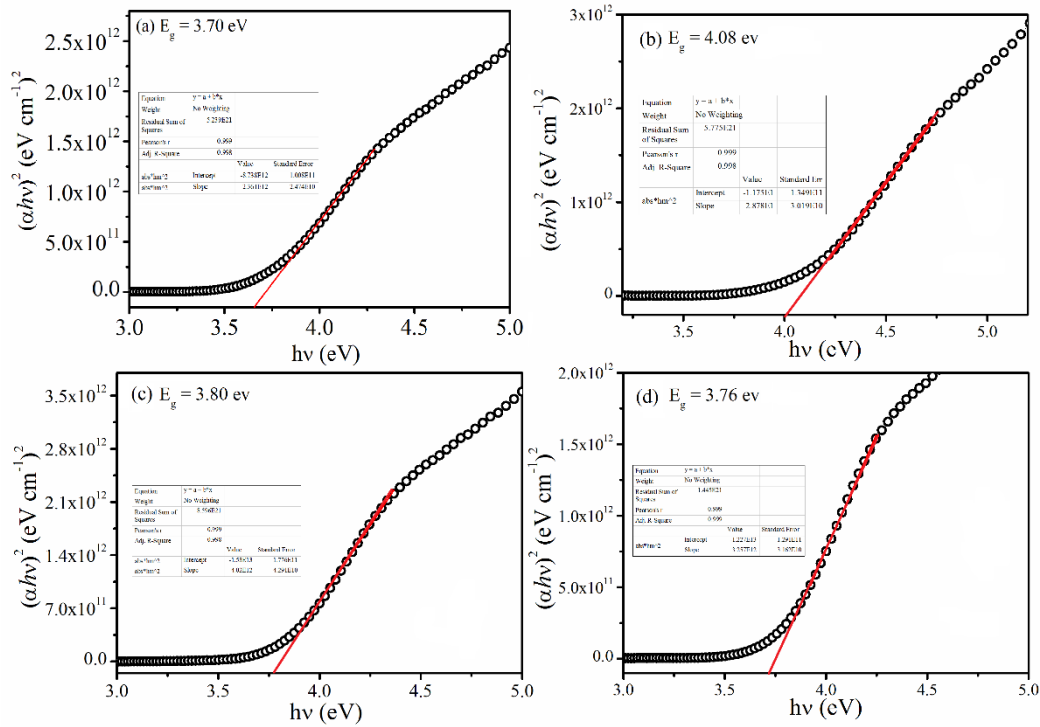


Figure 5.13: Optical bandgap energy of BNT-KNNG films deposited at (a) 0.1 Pa, (b) 1 Pa (c) 5 Pa and (d) 10 Pa.

There is a small increase in energy bandgap of 4.08 eV for 1 Pa film. At lower oxygen pressure, the film has oxygen deficiency. Therefore, the bandgap energy increased with increasing oxygen partial pressure from 0.1 to 1 Pa. Kim et al. [52] also observed similar observations in Ga₂O₃ thin films deposited by PLD. Further, an increase in oxygen pressure to 10 Pa, the optical bandgap found to be reduced which is following quantum confinement effect (>1Pa), i.e. bandgap energy decreases with an increase in the crystallite size. The mean free path decreases as the oxygen partial pressure increases. Consequently, an increase in collision frequency. The ablated atoms have a higher probability of agglomerate due to a large number of collisions (i.e. increase in particle size) before arriving at the substrate surface. Therefore, the particle size, grain size, crystallite size increases and decrease in the oxygen vacancies in the films with an increase in the oxygen partial pressure which leads to the narrowing bandgap in the films. The reduction in bandgap for BNT-KNNG films is more prominent with oxygen partial pressure.

The estimated fundamental optical coefficients (n_f , α , k , and E_g) are correlated to the crystal structure and morphological properties of deposited films and are consistent with earlier reports [53].

The nonlinear optical properties of BNT-KNNG composite thin films were performed by the modified Z-scan technique [53,54]. A continuous-wave (CW) He:Ne laser ($\lambda=633$ nm) is focused to illuminate the thin films by using a lens of 5 cm focal length. The nonlinear optical signal is captured by a charged coupled device (CCD) camera in the form of a transmitted image. The beam waist (ω_0) and its Rayleigh length ($z_0 = \pi\omega_0^2/\lambda$) were estimated to be 22.58 μm and 2.53 mm. The Z-scan data collected simultaneously from a single scanned image using a Matlab software in open aperture (OA) and closed aperture (CA). The nonlinear absorption coefficient (β) and nonlinear refractive index (n_2) of BNT-KNNG composite films deposited at 1 and 10 Pa have been estimated from normalized transmittance ($T(z)$) versus film position Z (cm) graph and by fitting with the Eq. 5.10 and 5.11 and are shown in Figure 5.14 [54].

The obtained OA Z-scan curves shown in Figure 5.14(a). It exhibits the transmittance minima at the focal point ($z = 0$) of the lens, signifying the reverse saturation absorption (RSA) behavior. The nonlinear optical effects arising from the absorption of incident radiation fall under the category of nonlinear absorption (NLA). There are various mechanisms for nonlinear absorption such as multiphoton absorption (MPA), free carrier absorption (FCA), excited-state absorption (ESA), nonlinear scattering, etc. [55]. For multiphoton absorption (two-photon absorption), the incident photon energy should be more than half of the bandgap energy of the sample. In the present z-scan experiment the excitation energy ($h\nu=1.96$ eV corresponding to 633 nm of He:Ne laser) is close to half of the bandgap energies, Table 5. 5, of the samples. Therefore, the NLA shown by the samples is dominated by the two-photon absorption (TPA) process. However, considering the low intensity, continuous-wave He:Ne laser beam, the

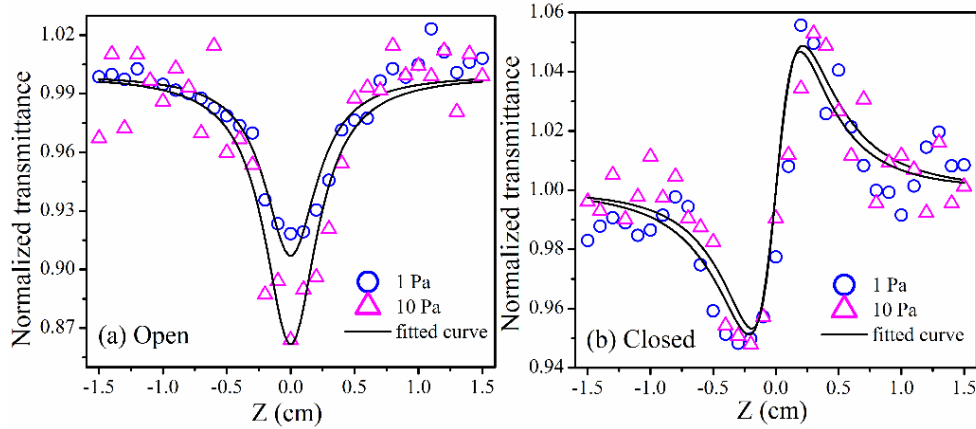


Figure 5.14: The normalized transmittance as a function of film position in (a) open apertures and (b) closed apertures for the deposited films at 1 and 10 Pa.

contribution from FCA and other effects are also prominent. The overall contribution from all the effects has been assigned as a nonlinear absorption coefficient. The CA Z-scan curves shown in Figure 5.14(b) indicates a pre-focal transmittance minimum followed by a post-focal transmittance maximum, demonstrating the positive nature of nonlinear refraction caused due to self-focusing behavior in the films. The estimated n_2 and β values are in the range of $4.019 \times 10^{-6} - 6.188 \times 10^{-6} \text{ cm}^2/\text{W}$ and $0.775 - 1.043 \text{ cm/W}$ for 1 and 10 Pa films, respectively. The film deposited at higher pressure (10 Pa) exhibited better nonlinearity and nonlinear absorption coefficient as compared to that of pure BNT thin ($n_2 = 4.62 \times 10^{-6} \text{ cm}^2/\text{W}$ and $\beta = 0.796 \text{ cm/W}$) [53]. The magnitude of nonlinear susceptibility: $|\chi^{(3)}|$ for the films estimated by Eq. 5.12 – 5.14 [54,56]. The $|\chi^{(3)}|$ values are found to be increased from $0.77 - 1.05 \times 10^{-3} \text{ esu}$ with increasing oxygen pressure from 1 - 10 Pa. The third-order nonlinear optical susceptibility ($|\chi^{(3)}|$) strongly depends on the crystalline quality of the film [57]. Higher the crystallinity, larger be the nonlinear optical susceptibility. The present work demonstrates an improvement in the crystalline quality with an increase in the O_2 pressure (Figure 5.10). Therefore, the film deposited at 10 Pa displays larger $|\chi^{(3)}|$ value as compared to that of the film deposited at 0.1 Pa pressure. In addition, the linear absorption coefficient and the linear

refractive index increase with an increase in the oxygen pressure (Table 5. 5) which also contributes towards the increasing behavior of $\chi^{(3)}$.

It can be clearly understood on the basis of thermal effects considering the CW laser for nonlinearity investigations. The thermal effect in nonlinear optical phenomenon arises if the interaction time (τ) between the light and mater is quite large i.e. within the range of $1 \text{ sec} < \tau < 100 \mu\text{s}$ [58]. In the present case, the experiment was carried out under the illumination of continuous-wave He: Ne laser and so, the thermal-induced optical nonlinearity plays a major role as compared to that of electronic nonlinearity [59]. The longer interaction time between the sample and laser beam increases the local temperature of the sample resulting into the thermal-induced nonlinear refractive index (n_2^{th}) which is expressed as [58].

$$n_2^{\text{th}} = \left(\frac{dn}{dT} \right) \frac{\alpha R^2}{k} \quad (5.18)$$

where, dn/dT is the variation of linear refractive index with temperature, α is linear absorption coefficient, R is the radius of the incident beam and k is the thermal conductivity of the material. This expression suggests that the thermally induced nonlinear refractive index increases with a linear absorption coefficient. Therefore, the film deposited for 10 Pa exhibits greater χ^3 as compared to the rest of the samples. The obtained large third-order nonlinearity, strong absorption coefficient and greater χ^3 in the present films are promising for the applications in optical photonic devices.

Figure 5.15 shows the variation of dielectric constant (ϵ_r) and dielectric loss ($\tan\delta$) of BNT-KNNG composite thin films deposited at various O_2 pressures and were measured in the range of 100 Hz – 300 kHz at RT. The ϵ_r value were found to be 227, 335, 373, and 411 (@ 1 kHz) for 0.1, 1, 5, 10 Pa, respectively. The dielectric response of films was improved with a rise in O_2 pressure. The film deposited at higher O_2 pressure (10 Pa) exhibited the best dielectric

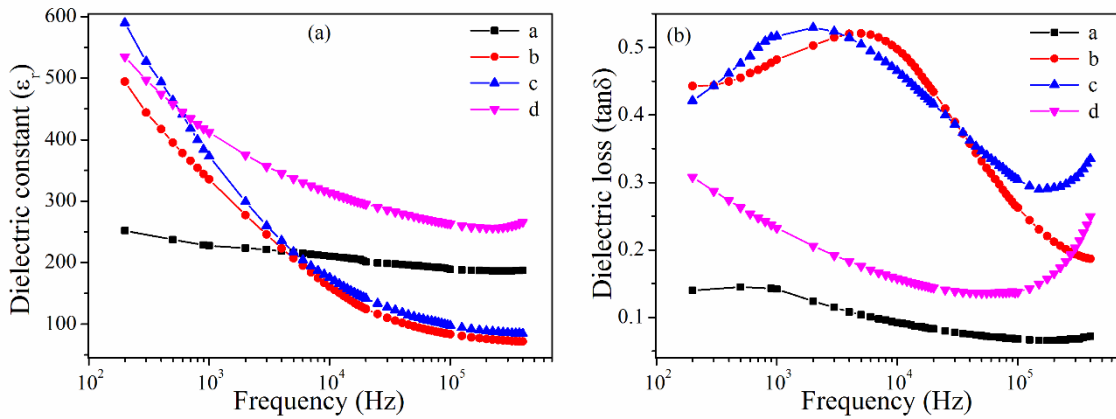


Figure 5.15: The frequency variation of (a) ϵ_r and (b) $\tan\delta$ of BNT-KNNG films for various O_2 pressures measured.

constant ($\epsilon_r = 411$) and lower loss tangent ($\tan\delta = 0.156$) at 1 kHz. The obtained $\tan\delta$ values are in the range of 0.092 – 0.512. In this study, enhancement in the dielectric constant was observed with a rise in the pressure. Therefore, improvement in ϵ_r and decrease in $\tan\delta$ with the rise in O_2 pressure might be attributable to the reduction in oxygen vacancies, conductivity, improvement in the crystallinity and the average particle size of the film. The temperature-

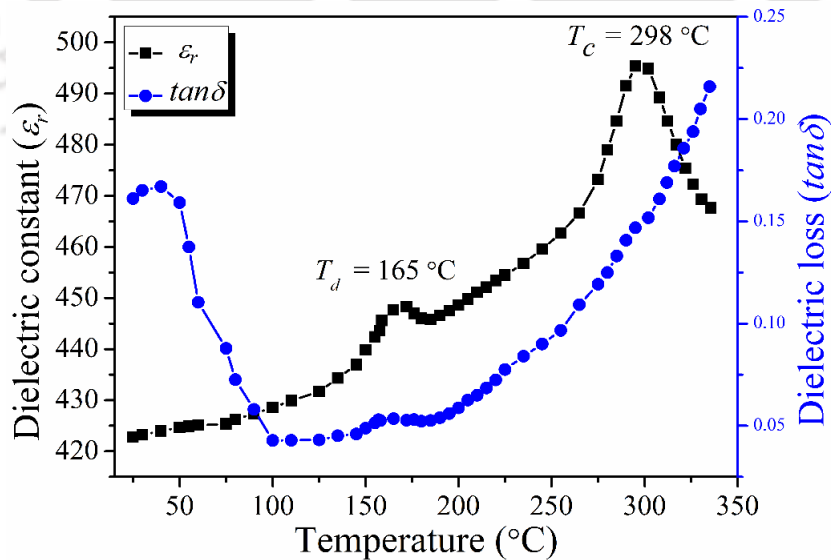


Figure 5.16: Temperature dependence of (a) ϵ_r and (b) $\tan\delta$ of BNT-KNNG film deposited at 10 Pa.

dependent dielectric constant and loss tangent of the film (10 Pa) measured at 1 kHz is shown in Figure 5.16. It exhibited the two-phase transitions from Ferro - anti-Ferro corresponding to rhombohedral to tetragonal structural phase transition (T_d) around 165 °C and anti-Ferro - para corresponding to tetragonal to cubic structural phase (T_c) around 298 °C which is in good agreement with the earlier results [9].

The MWD properties of BNT-KNNG composite thin films grown on quartz substrate at various oxygen pressures by the SPDR method [42]. It is a well-known and non-destructive method for evaluating the MWD properties of thin films at a discrete frequency microwave region. The SPDR operates with $TE_{01\delta}$ a mode that has only an azimuthal electric field component. Subsequently, the electric field remains continuous on the test interfacing, which makes the estimation heartless to the presence of air gaps perpendicular to the z-axis of the test fixture [43]. The resonant frequency, unloaded Q-factor and other parameters have been calculated by the Rayleigh-Ritz method. The ϵ_r and $\tan\delta$ of the substrate as well as film depend on resonant frequency and quality factor. First, the resonant frequency and quality factor (f_{01} , Q_{01}) of the empty resonator and the resonant frequency and quality factor of the substrate (f_0 , Q_0) were measured. Later, the deposited film quality factor (f_s , Q_s) was also estimated and it was seen that there is a shift in resonant frequency when the film placed.

The ϵ_r and $\tan\delta$ of deposited thin films at various pressures were investigated at 5 GHz, and 10 GHz and are shown in Table 5. 6. The ϵ_r values of deposited thin films for various pressures were found to be enhanced. It is attributable to an increase in the packing density as well as a refractive index with O_2 partial pressure. The films deposited at lower O_2 pressure displayed high dielectric losses due to the presence of O_2 vacancies. The loss is reduced with an increase in O_2 pressure. It was also seen that the dielectric constant of deposited films was decreased and $\tan\delta$ values were slightly increased with a rise in the frequency from 5 GHz to

10 GHz, caused by reduction in polarization and high conductivity. Mahesh and Saravanan et al. [60,61] also observed an improvement in MWD properties in KNN and BST films with oxygen pressure by RF sputtering technique. The enhanced MWD properties of BNT-KNNG thin films are achieved in comparison to pure BNT thin films due to the minimization of oxygen vacancies [53]. The higher ϵ_r and low $\tan\delta$ values obtained for the film deposited at 10 Pa are important parameters for the development of tunable microwave and high-frequency device applications.

Table 5. 6: Microwave dielectric properties of BNT-KNNG composite thin films for various pressures.

O ₂ Pressure	5 GHz		10 GHz	
	ϵ_r	$\tan\delta$	ϵ_r	$\tan\delta$
0.1 Pa	71	0.0018	59	0.0873
1 Pa	287	0.0037	216	0.0294
5 Pa	318	0.0035	223	0.0091
10 Pa	330	0.0021	317	0.0074

Figure 5.17 shows the RT polarization-electric field (P-E) loops of 1 and 10 Pa deposited films measured at 1 kHz for different voltages. These films exhibited well-saturated P-E loops with the applied electric field up to 200 kV/cm. The remnant polarization (P_r) was found to be $6.94 \mu\text{C}/\text{cm}^2$ at 11.12 kV/cm for 1 Pa and $1.52 \mu\text{C}/\text{cm}^2$ at 3.57 kV/cm for 10 Pa at 1 V. With an increase in the voltage, the P_r value was found to be enhanced for both the films. The film deposited at higher O₂ pressure (10 Pa) exhibited a higher remnant polarization ($P_r = 25.31 \mu\text{C}/\text{cm}^2$ and $E_C = 42.62 \text{ kV}/\text{cm}$) at 5 V which is slightly higher than the film deposited at 1 Pa ($P_r = 20.39 \mu\text{C}/\text{cm}^2$ and $E_C = 72.37 \text{ kV}/\text{cm}$). Therefore, the enhancement in ferroelectric-properties in this film might be due to the decrease of charge defects like oxygen vacancies with rising in O₂ pressure, which plays a primary role in the pinning domain walls [62].

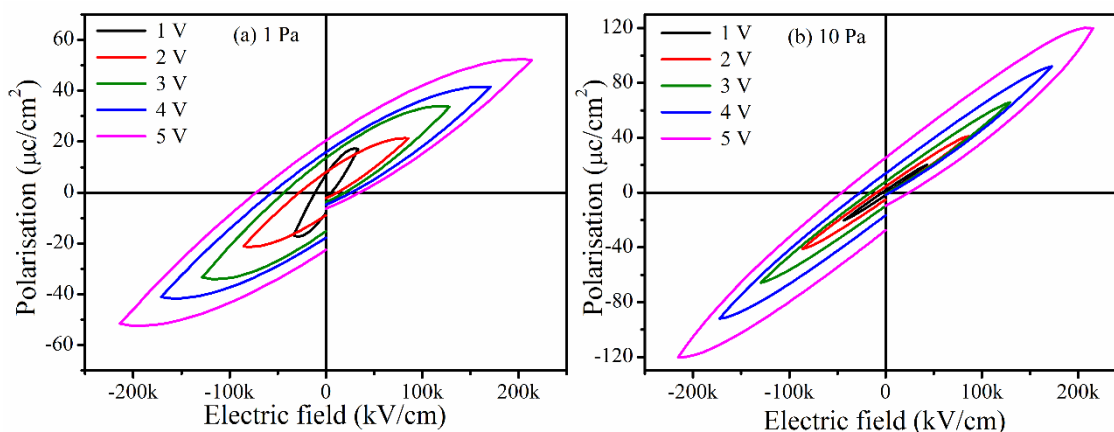


Figure 5.17: Hysteresis loops of BNT-KNNG thin film at a different voltage for the films deposited at (a) 1 Pa and (b) 10 Pa film.

In the present study, both crystalline size and grain sizes are found to be increased with increasing oxygen partial pressure. Normally, the crystallite size can be either equal or less than the grain size. Here, crystallite size is following a similar trend to that of the grain size. The average grain size of BNT-KNNG thin film is an important parameter in the evaluation of dielectric, ferroelectric and piezoelectric properties. The larger grain size is desired for ceramics applications due to the grain boundary barrier effect on mobility [63]. It is found that the remnant polarization increases and the coercive field decrease with oxygen pressure as shown in Figure 5.17. The ferroelectric property (remnant polarization and coercive field) of material generally depends on film thickness and grain size. Since all the deposited thin films are having the almost same thickness of $227\text{nm} \pm 13\text{nm}$, then the grain sizes are only responsible for variation in ferroelectric properties. As the grain size increases, the repulsive force between the neighboring domain walls decreases, which leads to smaller activation energy required for the reorientation of the domains. Consequently, enhancement in the remnant polarization and the reduction in the coercive field [64]. Wei et al. [65] investigated that as the grain size increases, the energy barrier for switching the ferroelectric domain must be broken through and the energy barrier decreases. Thus, the reversal polarization process of

a ferroelectric domain or domain switching is much easier in a large grain than that of small grain. Ohihara et al. [66] investigated the response of P-E loops to the grain size by the following expression.

$$f = f_0[1 - \exp(-G_a d^3 / kT)] \quad (5.19)$$

Where, fractions (f) of grains give rise to polarization reversal or domain switching, f_0 is the initial polarization or domain of ferroelectric materials, G_a is a constant it denotes grain anisotropy energy density and d is the grain size of the sample. Based on the expression 5.19, f strongly depends on the grain size (d). Therefore, the fraction of grains contributing to the polarization reversal increases as the grain size increases, which leads to an enhancement in the ferroelectric properties of the sample. Therefore, the larger grain size is good for ferroelectric as well as piezoelectric properties and their applications. It can be concluded that the improvement in ferroelectric properties is a combined effect of an increase in grain size and improvement in the film crystallinity.

The RT leakage current density (J) versus electric field (E) measurement was carried out for 1 and 10 Pa films, as shown in Figure 5.18(a). It shows symmetric nature under the applied electric fields (± 200 kV/cm). The current density J value increased with an applied field of ~ 180 kV/cm and above that, it is saturated. With an increase in O_2 pressure, the J values were found to be decreased from 5.71×10^{-3} A/cm² to 2.94×10^{-3} A/cm² for 1 and 10 Pa films, respectively. The estimated J value is slightly higher than the BNT-KNNG target sample or previous reports due to deficiency Bi and Na [9]. Yang et al. [67] also observed the same order J values in BNT-KNNG-ST composite thin films grown by PLD technique. Furthermore, leakage current density of thin films deposited at 1 and 10 Pa was analyzed by the space-charge-limited conduction (SCLC) mechanism using Eq. 4.22 [68]. The linear fitting of $\ln(J)$ versus $\ln(E)$ curve of the BNT-KNNG composite films for various O_2 pressures is shown in Figure

5.18(b). The estimated slope found to be increased from 0.98 to 1.59 for 1 and 10 Pa films, which indicates the ohmic and SCLC mechanism (i.e., highly nonlinear J-E characteristics). The SCLC behavior is influenced by trapped charge carriers and is assisted in discrete conduction mechanism. It is one of the significant characteristics to govern the conduction process in films. Therefore, the leakage current effectively reduced with an increase in O₂ pressure in BNT-KNNG films and improved structural, microstructural, optical, dielectric as well as ferroelectric properties.

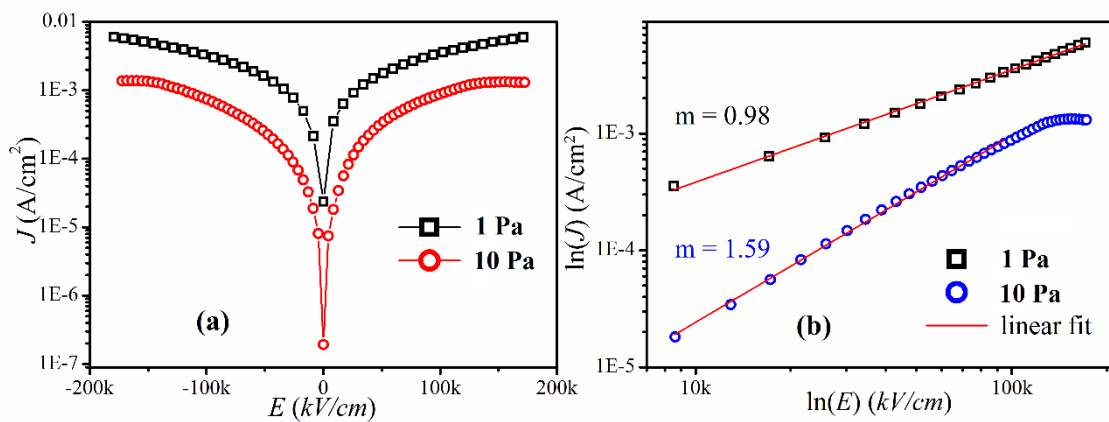
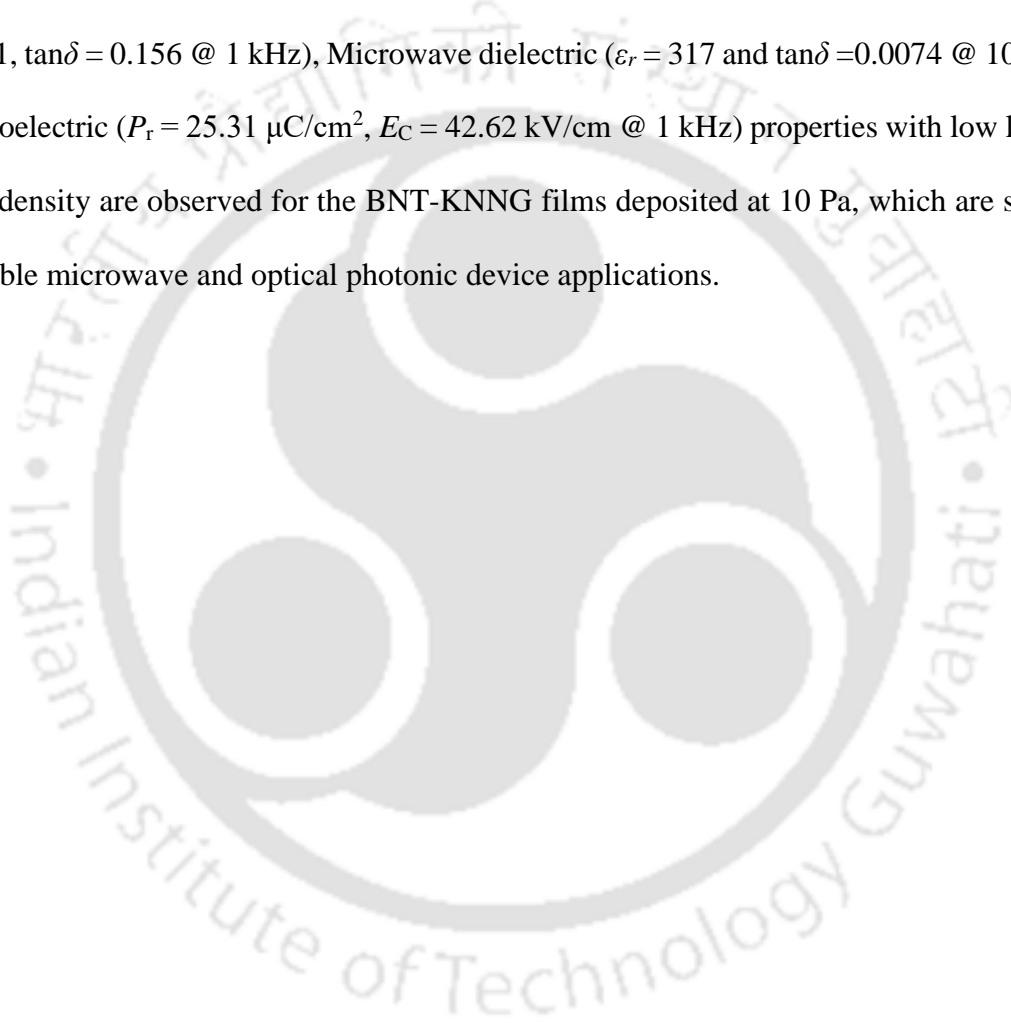


Figure 5.18: (a) Current density (J) versus Electric field (E) and (b) linear fitting of $\ln(J)$ versus $\ln(E)$ for films deposited at 1 and 10 Pa.

5.5 Conclusions

The effect of oxygen partial pressure on structural, morphological, linear and nonlinear optical, electrical properties of BNT and BNT-KNNG composite thin films were investigated in detail and are deposited by the PLD technique. The oxygen partial pressure plays an important role to stabilize the single phase of BNT and BNT-KNNG, controlling the crystallinity, surface roughness, optical and dielectric properties of thin films. XRD pattern of BNT and BNT-KNNG thin films deposited at 10 Pa and 0.1 Pa revealed a single phase of rhombohedral crystal symmetry with the R3c space group. The optical studies revealed an increase in the refractive index and a decrease in the optical bandgap energy with O₂ partial

pressure. The enhancement in the dielectric, MWD and ferroelectric properties with a reduction in the leakage current is observed with the rise in the O₂ pressure. The BNT-KNNG films deposited at 10 Pa exhibited higher nonlinear refractive index ($n_2 = 6.188 \times 10^{-6} \text{ cm}^2/\text{W}$) and strong absorption coefficient ($\beta = 1.043 \text{ cm/W}$) than pure BNT films. The temperature-dependent dielectric response displayed two structural phase transitions from rhombohedral to tetragonal phase at $\sim 200 \text{ }^\circ\text{C}$ and tetragonal to cubic phase at $\sim 300 \text{ }^\circ\text{C}$. The enhanced dielectric ($\epsilon_r = 411$, $\tan\delta = 0.156$ @ 1 kHz), Microwave dielectric ($\epsilon_r = 317$ and $\tan\delta = 0.0074$ @ 10 GHz), and ferroelectric ($P_r = 25.31 \text{ } \mu\text{C}/\text{cm}^2$, $E_C = 42.62 \text{ kV}/\text{cm}$ @ 1 kHz) properties with low leakage current density are observed for the BNT-KNNG films deposited at 10 Pa, which are suitable for tunable microwave and optical photonic device applications.



5.6 References

- [1] M. Li, M. J. Pietrowski, R. A. De Souza, H. Zhang, I. M. Reaney, S. N. Cook, J. A. Kilner, and D. C. Sinclair, *Nat. Mater.* **13**, 31 (2014).
- [2] Y. Yao, Y. Li, N. Sun, J. Du, X. Li, L. Zhang, Q. Zhang, and X. Hao, *J. Alloys Compd.* **750**, 228 (2018).
- [3] M. N. R. Ashfold, F. Claeysens, G. M. Fuge, and S. J. Henley, *Chem. Soc. Rev.* **33**, 23 (2004).
- [4] H. Fujioka, in *Handb. Cryst. Growth Thin Film. Ep. Second Ed.* (2014), pp. 365–397.
- [5] A. Andrei, N. D. Scarisoreanu, R. Birjega, M. Dinescu, G. Stanciu, F. Craciun, and C. Galassi, *Appl. Surf. Sci.* **278**, 162 (2013).
- [6] P. Li, J. Zhai, H. Zeng, B. Shen, W. Li, and K. Zhao, *J. Eur. Ceram. Soc.* **36**, 3139 (2016).
- [7] K. S. Yang, M. J. Choi, J. S. Choi, J. H. Eom, B. J. Park, S. Y. Lee, and S. G. Yoon, *Sensors Actuators, A Phys.* **243**, 117 (2016).
- [8] M. Abazari, A. Safari, S. S. N. Bharadwaja, and S. Troler-McKinstry, *Appl. Phys. Lett.* **96**, 82903 (2010).
- [9] S. Pattipaka, A. R. James, and P. Dobbidi, *J. Alloys Compd.* **765**, 1195 (2018).
- [10] W. Leng, C. Yang, H. Ji, J. Zhang, J. Tang, H. Chen, and L. Gao, *J. Phys. D: Appl. Phys.* **40**, 1206 (2007).
- [11] G. Yang, H. Wang, G. Tan, A. Jiang, Y. Zhou, and Z. Chen, *Appl. Opt.* **41**, 1729 (2002).
- [12] W. T. Wang, G. Yang, P. Duan, Y. L. Zhou, and Z. H. Chen, *Chinese Phys. Lett.* **19**, 1122 (2002).

- [13] Y. Deng, Y. L. Du, M. S. Zhang, J. H. Han, and Z. Yin, *Solid State Commun.* **135**, 221 (2005).
- [14] H. Chen, B. Yang, M. Zhang, F. Wang, K. Cheah, and W. Cao, *Thin Solid Films* **518**, 5585 (2010).
- [15] Y. H. Wang, B. Gu, G. D. Xu, and Y. Y. Zhu, *Appl. Phys. Lett.* **84**, 1686 (2004).
- [16] T. Zhang, W. Zhang, Y. Chen, and J. Yin, *Opt. Commun.* **281**, 439 (2008).
- [17] T. Zhang, C. Jia, Y. Bai, and W. Zhang, in *Adv. Mater. Res.* (Trans Tech Publications Ltd, 2013), pp. 340–348.
- [18] T. Zhao, Z. H. Chen, F. Chen, H. Bin Lu, G. Z. Yang, and H. S. Cheng, *Appl. Phys. Lett.* **77**, 4338 (2000).
- [19] W. J. Kim, W. Chang, S. B. Qadri, J. M. Pond, S. W. Kirchoefer, D. B. Chrisey, and J. S. Horwitz, *Appl. Phys. Lett.* **76**, 1185 (2000).
- [20] A. G. Ali, B. F. Dejene, and H. C. Swart, *Phys. B Condens. Matter* **480**, 174 (2016).
- [21] V. Kumar, C. S. S. Sandeep, R. Philip, V. Kumar, and C. S. S. Sandeep, **98**, 661 (2011).
- [22] S. R. Emani and K. C. J. Raju, *Appl. Surf. Sci.* **397**, 49 (2017).
- [23] G. Pradhan, P. P. Dey, and A. K. Sharma, *RSC Adv.* **9**, 12895 (2019).
- [24] *Evolution of Thin Film Morphology* (2008).
- [25] R. Kesarwani, P. P. Dey, and A. Khare, *RSC Adv.* **9**, 7967 (2019).
- [26] K. Chopra and J. Klerrer, *Thin Film Phenomena* (McGraw-Hill, New York; London, 1970).
- [27] S. Pattipaka, A. R. James, and P. Dobbidi, *J. Electron. Mater.* **47**, 3876 (2018).
- [28] F. Yang, P. Wu, and D. C. Sinclair, *J. Mater. Chem. C* **5**, 7243 (2017).

- [29] R. Swanepoel, J. Phys. E. **16**, 1214 (1983).
- [30] A. T. T. Mostako and A. Khare, Laser Part. Beams **30**, 559 (2012).
- [31] M. Bousquet, J. R. Duclère, E. Orhan, A. Boule, C. Bachelet, and C. Champeaux, J. Appl. Phys. **107**, (2010).
- [32] J. Tauc, Opt. Prop. Solids 277 (1972).
- [33] A. Joseph, J. P. Goud, S. R. Emani, and K. C. J. Raju, AIP Conf. Proc. **1731**, 80039 (2016).
- [34] H. Fujiwara, *Spectroscopic Ellipsometry: Principles and Applications* (John Wiley & Sons, 2007).
- [35] M. Sheik-Bahae, A. A. Said, T. H. Wei, D. J. Hagan, and E. W. Van Stryland, IEEE J. Quantum Electron. **26**, 760 (1990).
- [36] Y. Choi, J. H. Park, M. R. Kim, W. Jhe, and B. K. Rhee, Appl. Phys. Lett. **78**, 856 (2001).
- [37] F. L. S. Cuppo, A. M. Figueiredo Neto, S. L. Gómez, and P. Palffy-Muhoray, J. Opt. Soc. Am. B **19**, 1342 (2002).
- [38] S. Shettigar, G. Umesh, K. Chandrasekharan, and B. Kalluraya, Synth. Met. **157**, 142 (2007).
- [39] Y. S. Zhou, E. B. Wang, J. Peng, J. Liu, C. W. Hu, R. D. Huang, and X. You, Polyhedron **18**, 1419 (1999).
- [40] G. P. Bharti and A. Khare, Opt. Mater. Express **6**, 2063 (2016).
- [41] Y. Zhao, X. Hao, and M. Li, J. Alloys Compd. **601**, 112 (2014).
- [42] J. Krupka, J. Eur. Ceram. Soc. **23**, 2607 (2003).

- [43] J. Krupka, A. P. Gregory, O. C. Rochard, R. N. Clarke, B. Riddle, and J. Baker-Jarvis, *J. Eur. Ceram. Soc.* **21**, 2673 (2001).
- [44] A. S. Daryapurkar, J. T. Kolte, and P. Gopalan, *Thin Solid Films* **579**, 44 (2015).
- [45] A. L. Patterson, *Phys. Rev.* **56**, 978 (1939).
- [46] Z. G. Zhang, F. Zhou, X. Q. Wei, M. Liu, G. Sun, C. S. Chen, C. S. Xue, H. Z. Zhuang, and B. Y. Man, *Phys. E Low-Dimensional Syst. Nanostructures* **39**, 253 (2007).
- [47] Y. L. Wang, X. K. Chen, M. C. Li, R. Wang, G. Wu, J. P. Yang, W. H. Han, S. Z. Cao, and L. C. Zhao, *Surf. Coatings Technol.* **201**, 5344 (2007).
- [48] D. Yang and L. Xue, *Thin Solid Films* **494**, 28 (2006).
- [49] S. J. Wang, L. Lu, M. O. Lai, and J. Y. H. Fuh, *J. Appl. Phys.* **105**, 84102 (2009).
- [50] J. Pundareekam Goud, S. Ramakanth, A. Joseph, K. Sandeep, G. Lakshminarayana Rao, and K. C. James Raju, *Thin Solid Films* **626**, 126 (2017).
- [51] D. Dorranean, L. Dejam, and G. Mosayebian, *J. Theor. Appl. Phys.* **6**, 13 (2012).
- [52] T. K. Oanh Vu, D. U. Lee, and E. K. Kim, *J. Alloys Compd.* **806**, 874 (2019).
- [53] S. Pattipaka, A. Joseph, G. P. Bharti, K. C. J. Raju, A. Khare, and D. Pamu, *Appl. Surf. Sci.* **488**, 391 (2019).
- [54] G. P. Bharti and A. Khare, *Opt. Mater. Express* **6**, 2063 (2016).
- [55] E. W. Van Stryland, M. Sheik-Bahae, A. A. Said, and D. J. Hagan, *Prog. Cryst. Growth Charact. Mater.* **27**, 279 (1993).
- [56] M. Peddigari, S. Pattipaka, G. P. Bharti, A. Khare, and P. Dobbidi, *Opt. Mater. (Amst.)* **58**, 9 (2016).
- [57] G. P. Bharti, P. P. Dey, and A. Khare, *Mater. Chem. Phys.* **216**, 206 (2018).

- [58] P. Yang, L. Zhang, Y. Zhao, J. Gong, and Y. Tang, *Int. J. Appl. Ceram. Technol.* **12**, 399 (2015).
- [59] R. W. Boyd, *Acad. Press* (2011).
- [60] K. V. Saravanan, K. Sudheendran, M. G. Krishna, and K. C. J. Raju, *Ferroelectrics* **356**, 158 (2007).
- [61] M. Peddigari, V. Patel, G. P. Bharti, A. Khare, and D. Pamu, *J. Am. Ceram. Soc.* **100**, 3013 (2017).
- [62] F. Xu, S. Trolier-McKinstry, W. Ren, B. Xu, Z.-L. Xie, and K. J. Hemker, *J. Appl. Phys.* **89**, 1336 (2001).
- [63] Y. Y. Ma and R. H. Bube, *J. Electrochem. Soc.* **124**, 1430 (1977).
- [64] S. H. Hu, G. J. Hu, X. J. Meng, G. S. Wang, J. L. Sun, S. L. Guo, J. H. Chu, and N. Dai, *J. Cryst. Growth* **260**, 109 (2004).
- [65] W. Cai, C. Fu, J. Gao, and H. Chen, *J. Alloys Compd.* **480**, 870 (2009).
- [66] H. Orihara, S. Hashimoto, and Y. Ishibashi, *J. Phys. Soc. Japan* **63**, 1031 (1994).
- [67] K.-S. Yang, M.-J. Choi, J.-S. Choi, J.-H. Eom, B.-J. Park, S.-Y. Lee, and S.-G. Yoon, *Sensors Actuators A Phys.* **243**, 117 (2016).
- [68] H. Borkar, V. Rao, M. Tomar, V. Gupta, J. F. Scott, and A. Kumar, *RSC Adv.* **7**, 12842 (2017).

Summary and Future Scope of Work

6.1 Summary

A summary of interesting results and highlights of the present thesis work are concluded in this chapter. This thesis is mainly focused on the lead-free piezoelectric bulk ceramics and thin films, which are highly interesting from the point of view of scientific, research, and industrial applications. The fundamental aspects of lead-free doped piezoelectric ceramics, composites, thin films and the details of synthesis methods and characterization techniques of the prepared ceramics and thin films were presented in chapters 1 and 2, respectively. Successful efforts have made to improve the structural, dielectric, piezoelectric, and other physical properties BNT ceramics with suitable dopants and compositions are presented in chapters 3 and 4. Further, the BNT based thin films have been deposited by PLD technique to investigate their microwave dielectric, and nonlinear optical properties for microwave tunable and nonlinear photonic applications are presented in chapter 5. A brief summary of the key results with important findings as follows:

6.1.1 Pure $\text{Bi}_{0.5}\text{Na}_{0.5}\text{TiO}_3$, $\text{Bi}_{0.5}(\text{Na}_{(1-x)}\text{Ce}_x)_{0.5}\text{TiO}_3$, and $\text{Bi}_{1-x}\text{Gd}_x\text{Na}_{0.5}\text{TiO}_3$ Ceramics

Initially, the pure BNT ceramics were prepared by the conventional solid-state reaction method. The processing parameters such as milling time, milling speed, the ball to powder ratio, calcination, sintering temperatures, and sintering duration were optimized. The effect of sintering temperature on structural, microstructural, dielectric, and AC-conductivity behavior of BNT ceramics studied. These properties are significantly enhanced with the sintering temperature, the samples sintered at 1100 °C showed

high dielectric constant ($\epsilon_r = 692$ @ 1 kHz), and low dielectric loss ($\tan\delta = 0.045$) as compared to samples sintered at 1000 °C and 1050 °C due to the maximum relative density (~94%), dense microstructure (grain size of 1.40 μm) with larger crystallite size (52 nm). The high-frequency dielectric analysis revealed that weak relaxor behavior is presented in the system.

In this study, an attempt has been made to synthesis of $\text{Bi}_{0.5}\text{Na}_{1-x}\text{Ce}_{x0.5}\text{TiO}_3$ ($x = 0 - 0.035$) and $\text{Bi}_{1-x}\text{Gd}_{x0.5}\text{Na}_{0.5}\text{TiO}_3$ ($x = 0.02 - 0.06$) ceramics to study the structural, microstructural, and electric properties. Rietveld refinement of both Ce and Gd doped BNT ceramics revealed the rhombohedral crystal symmetry with improved dielectric properties as compared to the pure BNT ceramics. In both cases, the average grain size reduced and improved density with substitution of Ce and Gd concentrations is observed. The temperature dependence of dielectric permittivity of all the samples exhibited two phase transitions; the transition from ferroelectric to antiferroelectric is known as T_d , and the transition from antiferroelectric to paraelectric is known as T_C . All the samples showed the relaxation behavior with a diffuse phase transition due to compositional heterogeneity in the BNT system, which is analyzed by modified Curie-Weiss law. The dielectric properties of the Gd ($\epsilon_r = 809$ and $\tan\delta = 0.201$ at 1 kHz) and Ce ($\epsilon_r = 775$ and $\tan\delta = 0.032$ at 1 kHz) doped BNT ceramics improved for the composition of $x = 0.025$ and 0.06, respectively. The temperature-dependent of AC-conductivity is analyzed using a variable range hopping (VRH) model to study the hopping conduction mechanism in terms of the density of states ($N(E_F)$), hopping length (R_H), and hopping energies (W_H). It has been observed that both R_H and W_H values decreased with Gd and Ce doping, which is due to the enhancement of defect states near the Fermi level. It indicates that Gd^{3+} and Ce^{3+} assisted the hopping of charge carriers from one localized state to another in the BNT system.

6.1.2 $\text{Bi}_{0.5}(\text{Na}_{1-x}\text{K}_x)_{0.5}\text{TiO}_3$ and $(1-x)$ BNT – x $[(\text{K}_{0.5}\text{Na}_{0.5})\text{NbO}_3 + 0.01 \text{ wt.}\% \text{ Gd}_2\text{O}_3]$

Ceramics

In this study, the structural, microstructural, piezoelectric, dielectric and AC conductivity studies of $\text{Bi}_{0.5}(\text{Na}_{1-x}\text{K}_x)_{0.5}\text{TiO}_3$ (BNKT; $x = 0 - 0.3$) and $(1-x)$ BNT – x $[(\text{K}_{0.5}\text{Na}_{0.5})\text{NbO}_3 + 0.01 \text{ wt.}\% \text{ Gd}_2\text{O}_3]$ (BNT-KNNG; $x = 0 - 0.02$) piezoelectric ceramics investigated systematically. The XRD analysis of BNKT ceramics and BNT-KNNG composites exhibited a morphotropic phase boundary between rhombohedral and tetragonal structures for $x = 0.2$ and rhombohedral structure for all the samples, respectively. The local structure of both the compositions were analyzed by Raman spectroscopy; two additional modes appeared at 169 and 314 cm^{-1} are shifted to higher wavenumbers for $\text{Bi}_{0.5}(\text{Na}_{0.8}\text{K}_{0.2})_{0.5}\text{TiO}_3$ and $\text{Bi}_{0.5}(\text{Na}_{0.7}\text{K}_{0.3})_{0.5}\text{TiO}_3$ samples due to the change in crystal structure from rhombohedral to tetragonal phase, which causes the change in TiO_6 octahedral vibrations. In the case of BNT-KNNG, a significant shift ($\sim 11 \text{ cm}^{-1}$) towards the lower wavenumber as the Nb occupies in TiO_6 octahedral sites of the $\text{Bi}_{0.5}\text{Na}_{0.5}\text{TiO}_3$ matrix. The density is improved with increasing K and KNNG, whereas the average grain size reduced, which inhibited grain growth. All the samples exhibited two transitions (T_C and T_d), shifted towards the lower temperature with a rise K and KNNG, which are compositional dependent. Frequency dispersion of T_d and T_C suggests that BNKT and BNT-KNNG ceramics exhibit a relaxor behavior with a diffuse phase transition, which is confirmed by Uchino-Nomura criteria and Vogel-Fulcher law. Temperature dependence of resistivity $\rho_{ac}(T)$ analysis provides the evidence of the variable range hopping mechanism between charge carriers of BNKT and BNT-KNNG system. The average distance between the two successive hops R_H ($\sim 0.709 \text{ nm}$ and 2.67 nm), associated with hopping energy W_H ($\sim 0.082 \text{ eV}$ and 0.33 eV) decreased and density of states near the Fermi level [$\sim N(E_F) = 81.180 \times 10^{20} \text{ eV}^{-1} \text{ cm}^{-3}$ and $0.37 \times 10^{20} \text{ eV}^{-1} \text{ cm}^{-3}$] increased for BNKT ($x =$

0.2) and BNT-KNNG ($x = 0.01$) compositions are signifying the formation of additional localized states due to the incorporation of K and KNNG into BNT system. A significant enhancement of dielectric and piezoelectric properties were observed for BNKT ($x = 0.2$) system: dielectric constant ($\epsilon' = 1273$), dielectric loss ($\tan\delta = 0.047$) at 1 kHz, planar electromechanical coupling coefficient ($k_p \sim 46\%$), elastic coupling coefficients ($S_{33}^D = 6.40 \times 10^{-13} \text{ m}^2/\text{N}$ and $S_{33}^E = 10.06 \times 10^{-13} \text{ m}^2/\text{N}$) and piezoelectric constants ($d_{33} = 64.23 \text{ pC/N}$ and $g_{33} = 5.69 \times 10^{-3} \text{ Vm/N}$). The addition of KNNG effectively reduced grain size, transition temperature, leakage current and improved dielectric ($\epsilon' = 1074$ and $\tan\delta = 0.059$ @ 1 kHz) and piezoelectric properties; planar electromechanical coupling factor ($k_p = 53\%$), and piezoelectric constants ($d_{33} = 108 \text{ pC/N}$ and $g_{33} = 1.14 \times 10^{-2} \text{ Vm/N}$) are observed for BNT-KNNG ($x = 0.01$) sample. The BNT-KNNG sample shows larger d_{33} and k_p values as compared to BNKT, which is a potential candidate for high power electromechanical applications.

6.1.3 BNT and BNT-KNNG Composite Thin Films

Thin films of BNT and BNT-KNNG composite ceramics were deposited on Pt(111)/Ti/SiO₂/Si and quartz substrates by PLD technique. BNT thin films are grown at different oxygen partial pressures (P) and investigated their structural, morphological, linear, and nonlinear optical, dielectric, and microwave dielectric properties in detail. The suitable O₂ pressure is optimized to obtain a pure BNT phase. The growth dynamics of BNT thin films are studied by scaling theory as a function of P using height–height correlation function analysis from atomic force microscopy images. All the films exhibited a local roughness exponent; $\alpha_{loc} = 0.85 \pm 0.08$. The linear optical properties of the films extracted from ellipsometric analysis using a Tauc-Lorentz dispersion model and are in the same order as compared to the parameters extracted from the Swanepoel envelope and Tauc

relation. The thickness, refractive index, extinction coefficient, packing density values increased, whereas the bandgap energy values reduced with a rise in oxygen pressure due to the improvement in crystallinity and reduction in the oxygen vacancies. The third-order nonlinear optical and microwave dielectric properties are enhanced with O₂ pressure. The film (50 Pa) with a rich BIT phase displayed self-defocusing behavior for the application in the protection of optical sensor devices. The film deposited at 10 Pa exhibited higher nonlinearity ($n_2 = 4.62 \times 10^{-6} \text{ cm}^2/\text{W}$), strong absorbance ($\beta = 0.755 \text{ cm/W}$) and higher dielectric constant ($\epsilon_r = 336$) with lower loss tangent ($\tan\delta = 0.0093 @ 5 \text{ GHz}$).

Further, $1-x [\text{Bi}_{0.5}\text{Na}_{0.5}\text{TiO}_3] - x [\text{K}_{0.5}\text{Na}_{0.5}\text{NbO}_3 + 1 \text{ wt. \% Gd}_2\text{O}_3]$ (BNT-KNNG); ($x = 0.01$) composite thin films are deposited at various O₂ pressures from 0.1 Pa to 10 Pa by PLD technique and investigated their structural, optical, dielectric, and ferroelectric properties. X-ray diffraction analysis of films deposited at 0.1 Pa revealed a single phase of BNT-KNNG, and further ($> 0.1 \text{ Pa}$), film crystallinity gradually increased with a rise in O₂ pressure. The increase in the refractive index and a decrease in optical bandgap is observed with O₂ pressure and are in the range of 2.18 – 2.28, and 4.08 – 3.70 eV, respectively. The larger nonlinear refractive index ($n_2 = 5.775 \times 10^{-6} \text{ cm}^2/\text{W}$) and strong absorption coefficient ($\beta = 0.973 \text{ cm/W}$) observed with the rise in oxygen pressure, which are higher than BNT films. The temperature-dependent dielectric response displayed two structural phase transitions from rhombohedral to tetragonal phase at 165 °C and tetragonal to cubic phase at 298 °C. The enhanced dielectric ($\epsilon_r = 411$, $\tan\delta = 0.156 @ 1 \text{ kHz}$), microwave dielectric ($\epsilon_r = 317$ and $\tan\delta = 0.0074 @ 10 \text{ GHz}$), and ferroelectric ($P_r = 25.31 \mu\text{C}/\text{cm}^2$, $E_C = 42.62 \text{ kV}/\text{cm} @ 1 \text{ kHz}$) properties with low leakage current density are observed for the film deposited at 10 Pa followed a space charge limited conduction behaviour.

From these studies, we have concluded that the obtained best dielectric and piezoelectric properties of bulk BNKT and BNT-KNNG ceramics are good candidates for

the high performance of electromechanical applications. Furthermore, the optimized best linear, nonlinear optical properties and microwave dielectric properties with low leakage current density properties of the BNT-KNNG composite thin films are making the material suitable for antireflection, nonlinear photonics, optoelectronic, integrated electronic and microwave tunable device applications.

6.1.4 Future Scope of Work

In the present study, it has been observed that the modified lead-free BNT ceramics and thin films have shown better dielectric, piezoelectric, and nonlinear optical responses with interesting results than pure BNT ceramics, respectively. However, further studies are essential for the complete characterization of the modified BNT ceramics and thin films. Here, we proposed some future work of the present study as follows:

- So far, we have explored only the dielectric and piezoelectric properties of modified BNT ceramics. The ferroelectric properties of these materials will be studied systematically. In order to understand the ferroelectric domain switching and local polarization mechanisms of ferroelectric/nanostructure bulk and thin films, it is necessary to probe these properties at the atomic-level of grain and domain using piezoelectric force microscopy (PFM) for various electronic, optical and optoelectronic device applications.
- Also, we have investigated only the electrical properties of modified BNT ceramics and thin films. It will be interesting to study with the substitution of magnetic elements in the B-site of the BNT system (e.g., $\text{Bi}(\text{M}_x\text{Ti}_{1-x})\text{O}_3$, where $\text{M} = \text{Ni}, \text{Co}, \text{Mn}, \text{Mg}, \text{and Fe}$), or multiferroics either doping or composition method. These materials are much attracted to the potential applications in advanced technological devices that involve a

coupling between ferroelectric and magnetic response, which leads to the formation of new mechanisms for supporting ferroelectricity.

- We have studied the piezoelectric properties of modified BNT ceramics using the indirect method. It can be considered fatigue, piezoelectric, and pyroelectric properties using the direct method.
- The temperature-dependent XRD and Raman spectroscopy of the BNKT ceramics will be helpful in understanding the structural properties near the MPB.
- Various synthesis (sol-gel, hydrothermal, and combustion method) and sintering methods (microwave, spark plasma, and hot-pressing sintering) will be helpful to reduce the particle size, sintering temperature, and improve the density and physical properties of these bulk materials. The structural and ferroelectric domains properties of nanostructured materials can be studied with the help of high-resolution transmission electron microscopy (HRTEM) analysis.
- The photoluminescence properties of modified BNT ceramics and thin films can be studied and compared with the pure BNT.
- In the present study, we have fabricated mono layer BNT and BNT-KNNG thin films by PLD technique. It will be interesting to study the bilayer or multilayer thin films. The pulsed-laser deposition has been widely used for the fabrication of ferroelectric multilayers and heterostructures. The properties of multilayer ferroelectric films vary as a function of periodicity, which can be useful for the development of various electronic devices.
- The essential findings in the present study suggest that the modified lead-free BNT ceramics and thin films are suitable candidates for the development of device applications such as microwave tunable and piezoelectric sensor and actuator devices

(energy harvesters). The device fabrication is possible once device characteristics optimized.



List of publications

Thesis Related Publications

- 1) **Srinivas Pattipaka**, J. Pundareekam Goud, Gyan Prakash Bharti, K. C. James Raju, Alike Khare and Pamu D, Effect of oxygen partial pressure on nonlinear optical and electrical properties of BNT-KNNG composite thin films, *Journal of Materials Science: Materials in Electronics* **31**, 2986–2996 (2020).
- 2) **Srinivas Pattipaka**, A.R. James and D. Pamu, Enhanced dielectric and piezoelectric properties of BNT-KNNG piezoelectric ceramics, *Journal of Alloys and Compounds* **765**, 1195–1208 (2018).
- 3) **Srinivas Pattipaka**, A.R. James and D. Pamu, Dielectric, Piezoelectric and Variable Range Hopping Conductivity Studies of $\text{Bi}_{0.5}(\text{Na}, \text{K})_{0.5}\text{TiO}_3$ Ceramics, *Journal of Electronic Materials* **47(7)**, 3876–3890 (2018).
- 4) **Srinivas Pattipaka**, P. Mahesh and D. Pamu, Structural, Dielectric and AC-Conductivity Studies of Gd Doped Lead-Free $\text{Bi}_{0.5}\text{Na}_{0.5}\text{TiO}_3$ Ceramics, *Ferroelectrics* **518**, 1-7 (2017).
- 5) **Srinivas Pattipaka**, P. Mahesh and D. Pamu, Effect of Ce on Structural and Dielectric Properties of Lead-Free $(\text{Bi}_{0.5}\text{Na}_{0.5})\text{TiO}_3$ Ceramics, *Ceramics International* **43**, S151–157 (2017).
- 6) **Srinivas Pattipaka**, J. Pundareekam Goud, Gyan Prakash Bharti, Gobinda Pradhan, K. C. James Raju, Alike Khare and Pamu D, Surface scaling, ellipsometric and nonlinear optical studies of $\text{Bi}_{0.5}\text{Na}_{0.5}\text{TiO}_3$ thin films deposited by PLD (Communicated).
- 7) **Srinivas Pattipaka**, P. Mahesh and D. Pamu, Structural and dielectric properties of lead free $\text{Bi}_{0.5}\text{Na}_{0.5}\text{TiO}_3$ ceramics, *AIP Conference Proceedings* **1728**, 020352 (2016)
- 8) **Srinivas Pattipaka** and D. Pamu, Raman spectroscopy and low temperature dielectric properties of $(\text{Bi}_{0.5}\text{Na}_{0.5})\text{TiO}_3$ ceramics, *IOP Conference Series: Material science and engineering-B* **360**, 012024 (2018).

Outside Thesis Publications

- 1) **Srinivas Pattipaka**, Sweety Bora, Pamu D, Structural, Electrical, and AC-Resistivity Studies of BNT-KN Piezoelectric Ceramics, *Ferroelectrics* **557 (1)**, 28-42 (2020).
- 2) **Srinivas Pattipaka**, Mahesh Peddigari, Pamu D, Dielectric and ferroelectric properties of Gd^{3+} doped $(K_{0.5}Na_{0.5})_{0.96}Li_{0.04}(Nb_{0.8}Ta_{0.2})O_3$ piezoelectric ceramics, *Materials Science and Engineering: B* **252**, 114470 (2020).
- 3) **Srinivas Pattipaka**, Andrews Joseph, Gyan Prakash Bharti, K. C. James Raju, Alike Khare, and D. Pamu, Thickness-dependent microwave dielectric and nonlinear optical properties of $Bi_{0.5}Na_{0.5}TiO_3$ thin films, *Applied Surface Science* **488**, 391–403 (2019).
- 4) Prajna P Mohapatra, **Srinivas Pattipaka**, Pamu Dobbidi, The effect of Sr substitution on the electrical, dielectric and magnetic behavior of lithium ferrite, *Ceramics International* **45(18)**, 25010-25019 (2019).
- 5) Maneesh Kumar Poddar, Sachin Sharma, **Srinivas Pattipaka**, D Pamu, Vijayanand S Moholkar, Ultrasound-assisted synthesis of poly (MMA-co-BA)/ZnO nanocomposites with enhanced physical properties, *Ultrasonics sonochemistry* **39**, 782-791 (2017).
- 6) Mahesh Peddigari, **Srinivas Pattipaka**, Gyan Prakash Bharti, Alike Khare, Pamu Dobbidi, Nonlinear optical properties of pulsed laser deposited Gd_2O_3 and Dy_2O_3 doped $K_{0.5}Na_{0.5}NbO_3$ thin films, *Optical Materials* **58**, 9-13 (2016).
- 7) Pallabi Gogoi, **Srinivas Pattipaka**, Pramod Sharma, D. Pamu, Optical, Dielectric Characterization and Impedance Spectroscopy of Ni-Substituted $MgTiO_3$ Thin Films, *Journal of Electronic Materials* **45(2)**, 899-909 (2015).

Research work presented in conferences and workshops

Thesis related

- 1) **Srinivas Pattipaka**, P. Mahesh, and D. Pamu, Structural and dielectric properties of lead free $(Bi_{0.5}Na_{0.5})TiO_3$ ceramics, Presented in *International Conference on Condensed Matter and Applied Physics (ICC-2015)*, during 30-31 October 2015 at Bikaner, Rajasthan, India.

- 2) **Srinivas Pattipaka**, Mahesh Peddigari and D. Pamu, Raman and Impedance Spectroscopy Analysis of $(\text{Bi}_{0.5}\text{Na}_{0.5})\text{TiO}_3$ Ceramics, Presented in *International conference on materials science and technology (ICMST-2016)*, during 5-8 June 2016, at Kottayam, Kerala, India.
- 3) **Srinivas Pattipaka**, P. Mahesh and D. Pamu, Structural, Dielectric and AC-Conductivity Studies of Gd Doped Lead-Free $(\text{Bi}_{0.5}\text{Na}_{0.5})\text{TiO}_3$ Ceramics, Presented in *International Conference on Technologically Advanced Materials & Asian Meeting on Ferroelectricity (ICTAM-AMF10)*, during 7-11 November, 2016 at University of Delhi, Delhi, India.
- 4) **Srinivas Pattipaka**, A.R. James and D. Pamu, Synthesis and characterization of $\text{Bi}_{0.5}(\text{Na}, \text{K})_{0.5}\text{TiO}_3$ Ceramics Presented in *RESEARCH CONCLAVE (RC-2018)* held on 08-17th March 2018, IIT Guwahati, India.
- 5) **Srinivas Pattipaka** and D. Pamu, Effect of Fe on structural, dielectric and magnetic properties of $(\text{Bi}_{0.5}\text{Na}_{0.5})\text{TiO}_3$ ceramics, Presented in *International Conference on Advanced ceramics and Nanomaterials for sustainable development (ACeND-2018)*, during 19-21 September, 2018 at Christ University Bangalore, India.
- 6) **Srinivas Pattipaka** and D. Pamu, Nonlinear optical and dielectric properties $(\text{Bi}_{0.5}\text{Na}_{0.5})\text{TiO}_3$ thin films deposited by PLD technique, Presented in *International Conference on Nano Science & Engineering Applications (ICONSEA-2018)*, during 4-6 October, 2018 at Jawaharlal Nehru Technological University Hyderabad, India.
- 7) **Srinivas Pattipaka**, J Pundarikam Goud, Gyan Prakash Bharti, K. C. James Raju, Alike Khare, and Pamu Dobbidi, Nonlinear Optical and Electrical Properties of $(\text{Bi}_{0.5}\text{Na}_{0.5})\text{TiO}_3$ -Based Thin Films Grown by PLD, Presented in **2019 ISAF-ICE-FEM-IWPM-PFM Joint Conference - $f^2c\pi^2$** at the Swiss Tech Convention Center, EPFL, Lausanne, Switzerland during July 14 to 19, 2019.
- 8) **Srinivas Pattipaka**, Sweety Bora and Pamu Dobbidi, Structural, Electrical and AC-Resistivity Studies of BNT-KNNG Piezoelectric ceramics, Presented in **2019 ISAF-ICE-FEM-IWPM-PFM Joint Conference - $f^2c\pi^2$** at the Swiss Tech Convention Center, EPFL, Lausanne, Switzerland during July 14 to 19, 2019.

Outside Thesis

- 1) Participated in National Workshop on ***Advanced Probing Techniques in TEM***, Organized by Indian Institute of Technology Guwahati & Electron Microscopy Society of India Venue: Conference Center, IIT Guwahati held on 15 – 16 February 2016, IIT Guwahati, India.
- 2) Played an important role and given a talk in short-term course on ***Nanomaterials and Smart Devices*** conducted under the Technical Education Quality Improvement Programme (TEQIP) Sponsored by the Ministry of Human Resource Development, Government of India, held on 17-21 September, 2018.
- 3) Participated in ***National Conference on Emerging Trends in Vacuum Electronic Devices & Applications (VEDA-2018)*** held on during November 22-24, 2018, SAMEER, IIT Guwahati, India.



Curriculum Vitae

Dr. Srinivas Pattipaka

Ph.D., Department of Physics
Indian Institute of Technology Guwahati Guwahati-781 039
Assam, INDIA,
Mobile: +91-9085885740
E-mail: s.pattipaka@iitg.ac.in / cnuphy444@gmail.com
LinkedIn: <https://www.linkedin.com/in/dr-srinivas-pattipaka-5a3aa3193/>



Research experience

Thesis: “[Studies on Bismuth Sodium Titanate-based Lead-Free Piezoelectric Bulk Ceramics and Thin Films](#)”

Supervisor: [Dr. D Pamu](#)

Research Interests: Materials Science & Experimental Condensed Matter Physics

Key findings and expertise:

- Electro Ceramics: Dielectric, Ferroelectric & Piezoelectrics, Perovskite (ABO_3) oxides, Relaxor ferroelectrics and composites, Nano-structured materials
- Expertise in synthesis of bulk ceramics and nanostructured materials: solid-state reaction and sol-gel process
- Experience in fabrication of oxide thin films: RF magnetron sputtering and pulsed laser deposition techniques
- Experience in analytical methods to characterize ceramic compounds, nanomaterials and thin films
- Piezoelectric and relaxor ferroelectric materials for energy harvesting and storage applications

Academic background

- Ph.D.** Title: Studies on Bismuth Sodium Titanate-based Lead-Free Piezoelectric Bulk Ceramics and Thin Films, **Indian Institute of Technology Guwahati (IIT Guwahati)**, Assam, India. CPI: 6.77 (Dated: 17/06/2020)
- B.Ed.** Physical Science, **Osmania University**, Hyderabad, Telangana, 63% (Dated: 06/2012)
- M.Sc.** Physics (*Specialization: Applied electronics*), **University College of Science (Campus), Osmania University**, Hyderabad, Telangana, CPI: 6.71 (Dated: 11/2011)
- B.Sc.** M.P.C. (Maths, Physics & Chemistry), **Kakatiya University**, Telangana, India, 62.5% (Dated: 09/2008)
- 10+2** M.P.C (Mathematics, Physics & Chemistry), **Board of Intermediate Education**, Telangana, India, 81.3% (Dated: 03/2005)
- 10th Class** **Secondary Board of Education**. Telangana, India, 83.1% (Dated: 03/2003)

Teaching experience

- Teaching experience for guiding B. Tech, M. Tech and M.Sc. students and supervised 12 students for final year projects.
- Teaching assistant for B. Tech Engineering Physics (Electronics Laboratory/PH411) during July - Dec 2015.

Technical skills

Analytical/Characterization XRD, DSC-TGA, Raman spectrometer, FESEM, FETEM, LCR meter, RF Impedance Analyzer, P-E Tester, VSM, RF Sputtering Units, Pulsed laser deposition, Thermal evaporator, Profilometer, UV-Vis Spectrometer (UV-Vis), spectroscopic ellipsometer, Atomic Force Microscope, Vector Network Analyzer, AC/DC-Probe, Krupka resonator cavity, Split Post Dielectric Resonator, and Z-scan technique.

Publications ([Google Scholar](#) & [Research Gate](#))

Number of publications: 14

- (1) **Srinivas Pattipaka**, J. Pundareekam Goud, Gyan Prakash Bharti, K. C. James Raju, Alika Khare, and D Pamu, Effect of oxygen partial pressure on nonlinear optical and electrical properties of BNT-KNNG composite thin films, *Journal of Materials Science: Materials in Electronics* 31, 2986–2996 (2020), <https://doi.org/10.1007/s10854-019-02842-4>
- (2) **Srinivas Pattipaka**, Mahesh Peddigari, and D. Pamu, Dielectric and ferroelectric properties of Gd³⁺ doped (K_{0.5}Na_{0.5})_{0.96}Li_{0.04}(Nb_{0.8}Ta_{0.20})O₃ piezoelectric ceramics, *Materials Science and Engineering: B* 252, 114470 (2020), <https://doi.org/10.1016/j.mseb.2019.114470>
- (3) **Srinivas Pattipaka**, Sweetly Bora, Pamu D, Structural, Electrical, and AC- Resistivity Studies of BNT-KN Piezoelectric Ceramics, *Ferroelectrics* 557 (1), 28-42 (2020), <https://doi.org/10.1080/00150193.2020.1713360>
- (4) **Srinivas Pattipaka**, Andrews Joseph, Gyan Prakash Bharti, K. C. James Raju, Alika Khare, and D. Pamu, Thickness-dependent microwave dielectric and nonlinear optical properties of Bi_{0.5}Na_{0.5}TiO₃ thin films, *Applied Surface Science* 488, 391–403 (2019), <https://doi.org/10.1016/j.apsusc.2019.05.264>
- (5) Prajna P Mohapatra, **Srinivas Pattipaka**, Pamu Dobbidi, The effect of Sr substitution on the electrical, dielectric and magnetic behavior of lithium ferrite, *Ceramics International* 45(18), 25010-25019 (2019), <https://doi.org/10.1016/j.ceramint.2019.04.040>
- (6) **Srinivas Pattipaka**, A.R. James and D. Pamu, Enhanced dielectric and piezoelectric properties of BNT-KNNG piezoelectric ceramics, *Journal of Alloys and Compounds* 765, 1195–1208 (2018), <https://doi.org/10.1016/j.jallcom.2018.06.138>
- (7) **Srinivas Pattipaka**, A.R. James and D. Pamu, Dielectric, Piezoelectric and Variable Range Hopping Conductivity Studies of Bi_{0.5}(Na, K)_{0.5}TiO₃ Ceramics, *Journal of Electronic Materials* 47(7), 3876–3890 (2018), <https://doi.org/10.1007/s11664-018-6263-0>
- (8) **Srinivas Pattipaka** and D. Pamu, Raman spectroscopy and low temperature dielectric properties of (Bi_{0.5}Na_{0.5})TiO₃ ceramics, *IOP Conference Series: Material science and engineering-B* 360, 012024 (2018), <https://doi.org/10.1088/1757-899X/360/1/012024>
- (9) Maneesh Kumar Poddar, Sachin Sharma, **Srinivas Pattipaka**, D Pamu, Vijayanand S Moholkar, Ultrasound-assisted synthesis of poly (MMA-co-BA)/ZnO nanocomposites with enhanced physical properties, *Ultrasonics sonochemistry* 39, 782-791 (2017), <https://doi.org/10.1016/j.ultsonch.2017.05.040>
- (10) **Srinivas Pattipaka**, P. Mahesh and D. Pamu, Structural, Dielectric and AC-Conductivity Studies of Gd Doped Lead-Free Bi_{0.5}Na_{0.5}TiO₃ Ceramics, *Ferroelectrics* 518, 1-7 (2017), <https://doi.org/10.1080/00150193.2017.1360122>
- (11) **Srinivas Pattipaka**, P. Mahesh and D. Pamu, Effect of Ce on Structural and Dielectric Properties of Lead-Free Bi_{0.5}Na_{0.5}TiO₃ Ceramics, *Ceramics International* 43, S151–S157 (2017), <https://doi.org/10.1016/j.ceramint.2017.05.185>
- (12) Mahesh Peddigari, **Srinivas Pattipaka**, Gyan Prakash Bharti, Alika Khare, Pamu Dobbidi, Nonlinear optical properties of pulsed laser deposited Gd₂O₃ and Dy₂O₃ doped K_{0.5}Na_{0.5}NbO₃ thin films, *Optical Materials* 58, 9-13 (2016), <https://doi.org/10.1016/j.optmat.2016.05.007>
- (13) **Srinivas Pattipaka**, P. Mahesh and D. Pamu, Structural and dielectric properties of lead free Bi_{0.5}Na_{0.5}TiO₃ ceramics, *AIP Conference Proceedings* 1728, 020352 (2016), <https://doi.org/10.1063/1.4946403>
- (14) Pallabi Gogoi, **Srinivas Pattipaka**, Pramod Sharma, D. Pamu, Optical, Dielectric Characterization and Impedance Spectroscopy of Ni-Substituted MgTiO₃ Thin Films, *Journal of Electronic Materials* 45(2), 899-909 (2015), <https://doi.org/10.1007/s11664-015-4209-3>

Selected Conference/ Workshop Presentations:

Number of Presentations During Ph.D.: 11

- (1) **Srinivas Pattipaka**, P. Mahesh, and D. Pamu, “*Structural and dielectric properties of lead free $Bi_{0.5}Na_{0.5}TiO_3$ ceramics*”, Presented in **International Conference on Condensed Matter and Applied Physics (ICC-2015)**, during 30-31 October 2015 at **Bikaner**, Rajasthan, India.
- (2) **Srinivas Pattipaka**, Mahesh Peddigari and D. Pamu, “*Raman and Impedance Spectroscopy Analysis of $(Bi_{0.5}Na_{0.5})TiO_3$ Ceramics*”, Presented in **International Conference on Materials Science and Technology (ICMST-2016)**, during 5-8 June 2016, at **Kottayam**, Kerala, India.
- (3) **Srinivas Pattipaka**, P. Mahesh and D. Pamu, Structural, “*Dielectric and AC-Conductivity Studies of Gd Doped Lead-Free $Bi_{0.5}Na_{0.5}TiO_3$ Ceramics*”, Presented in **International Conference on Technologically Advanced Materials & Asian Meeting on Ferroelectricity (ICTAM-AMF10)**, during 7-11 November 2016 at University of Delhi, **Delhi**, India.
- (4) **Srinivas Pattipaka**, J Pundarikam Goud, Gyan Prakash Bharti, K. C. James Raju, Alike Khare, and Pamu Dobbidi, “*Nonlinear Optical and Electrical Properties of $Bi_{0.5}Na_{0.5}TiO_3$ -Based Thin Films Grown by PLD*”, Presented in **2019 ISAF-ICE-FEM-IWPM-PFM Joint Conference - $f^2c\pi^2$** at the Swiss Tech Convention Center, EPFL, **Lausanne, Switzerland** during July 14 to 19, 2019.
- (5) **Srinivas Pattipaka**, Sweety bora and Pamu Dobbidi, “*Structural, Electrical and AC- Resistivity Studies of BNT-KNNG Piezoelectric ceramics*”, Presented in **2019 ISAF-ICE-FEM-IWPM-PFM Joint Conference - $f^2c\pi^2$** at the Swiss Tech Convention Center, EPFL, **Lausanne, Switzerland** during July 14 to 19, 2019.

Awards and achievements

- Mar 2014** Qualified and secured All India 905 Rank in Graduate Aptitude Test in Engineering (GATE) in Physics, organized by the Ministry of Human Resource and Development, Govt. of India.
- July 2019** Grant from Science and Engineering Research Board (SERB), India for presentation of paper in International Conference “2019 ISAF-ICE-FEM-IWPM-PFM Joint Conference - $f^2c\pi^2$ ” at the Swiss Tech Convention Center, EPFL, Lausanne, Switzerland during July 14 to 19, 2019.

References

- | | |
|---------------------------------------------------------------------------------------------------------------------------------------------------------------------------------------------------------------------------------------------------------------|------------------------------------------------------------------------------------------------------------------------------------------------------------------------------------------------------------------------------------------------------------------------------------------|
| (1) Dr. D. Pamu (Ph.D. Supervisor)
Associate Professor
Department of Physics
Indian Institute of Technology Guwahati
Guwahati-781039, Assam, India.
Phone: +91-361 258 2721 (O)
Email: pamu@iitg.ac.in | (3) Prof. Dilip Pal
Professor
Department of Physics
Indian Institute of Technology Guwahati
Guwahati-781039, Assam, India.
Phone: +91-361 258 2720 (O)
Email: dpal@iitg.ac.in |
| (2) Prof. S. Ravi
Professor
Department of Physics
Indian Institute of Technology Guwahati
Guwahati-781039, Assam, India.
Phone: +91- 361 258 2707 (O)
Email: sravi@iitg.ac.in | (4) Prof. Roy Paily Palathinkal
Professor
Department of Electronics and Electrical Engineering,
Indian Institute of Technology Guwahati
Guwahati-781039, Assam, India.
Phone: +91-361 258 2512 (O)
Email: roypaily@iitg.ac.in |